



THE UNIVERSITY
of ADELAIDE

On The Effects of Roughness Parameters on Turbulent Boundary Layer Flows

by

Misarah Abdelaziz

A thesis submitted in total fulfillment for the
degree of Doctor of Philosophy

School of Electrical & Mechanical Engineering
Adelaide, South Australia 5005
Australia

June 27, 2023

Ph.D. Thesis

June 27, 2023

School of Electrical & Mechanical Engineering

The University of Adelaide

Adelaide, South Australia 5005

Typeset by the author using L^AT_EX

Printed in Australia

Copyright © 2022 Misarah Abdelaziz, and The University of Adelaide, Australia

All rights reserved. No part of this report may be used or reproduced in any form or by any means, or stored in a database or retrieval system without prior written permission of the university except in the case of brief quotations embodied in critical articles and reviews.

To my beloved parents: “As I complete this important milestone in my academic journey, I cannot help but feel immense gratitude for all that you have done for me. Your unwavering love, support, and encouragement have been the bedrock upon which I have built my success. No words can truly express how much you mean to me, but I hope this dedication serves as a small token of my love and gratitude. Thank you for being the best parents a child could ask for.”

To Aisha: “I dedicate this PhD thesis to my loving wife. Your unwavering faith in me, and your constant encouragement, have been my driving force. Your sacrifices and understanding have made it possible for me to pursue my dreams and achieve this milestone. I cannot express how grateful I am for you. This achievement is as much yours as it is mine. I love you with all my heart.”

Layal & Eiad: “Your arrival has brought me so much joy and inspiration. Your innocent and pure presence in my life has given me a new perspective on the importance of hard work and determination. To my daughter, I promise to be your best role model and make you proud. To my nephew, thank you for always being a source of joy and laughter. I hope that my journey will serve as an inspiration to both of you to pursue your dreams and aspirations. I love you both with all my heart.”

Abstract

Turbulent boundary layers (TBLs) are a well-known phenomenon in fluid dynamics and are observed in various transport, such as ships and aeroplanes. The majority of wall-bounded flows in engineering applications possess a rough surface, such as the growth of bio-fouling on ship hulls or surface erosion of wind turbine blades. The existence of surface roughness significantly influences the boundary layer flow and affects the heat and momentum transfer. The increase in drag caused by roughness leads to greater fuel consumption and emissions in transportation. Therefore, comprehending the impact of roughness on boundary layer flows is vital for enhancing energy efficiency and decreasing environmental impact across multiple industries. One of the principal objectives of rough wall fluid dynamics research is to determine the drag penalty of surfaces exclusively based on their topographical characteristics. Nevertheless, there is no consensus regarding the most important length scale or roughness parameter that accurately describes a surface in relation to friction drag, and several studies have attempted to identify it.

This study investigates the impact of various two-dimensional (2D) and three-dimensional (3D) roughness geometries on turbulence statistics and drag coefficient (C_f) in a zero pressure gradient (ZPG) turbulent boundary layer (TBL), using single hotwire anemometry (HWA). The research involves the use of three types of 2D roughness elements, namely circular rods, 3D printed triangular ribs, and computerised numerical control (CNC) machined sinewave surfaces with different heights and streamwise spacings. Additionally, three types of 3D sinewave roughness are examined, including isotropic 3D sinewave surfaces with equal streamwise and spanwise wavelengths, anisotropic 3D sinewave surfaces with different streamwise and spanwise wavelengths, and isotropic 3D sinewave surfaces with different roughness skewness values (positive, negative, and zero). The turbulence statistics and drag coefficient are evaluated to determine the effects of the various 2D and 3D roughness geometries in the ZPG-TBL flows.

In the fully rough regime, the friction Reynolds number (Re_τ) no longer affects C_f . Compared to smooth wall profiles, all types of roughness cause a downward shift in the wall-unit normalised streamwise mean velocity profile. When the roughness height and streamwise spacing are the same, 2D roughness has higher C_f and roughness functions (ΔU^+) than 3D roughness. This is due to the larger blockage area imposed by 2D roughness, which forces the fluid to flow over the roughness elements. Conversely, the fluid can flow around and above the roughness elements of 3D roughness. As TBL develops from a transitionally to a fully rough regime, the inner peak of turbulence intensity profiles for 2D surface roughness gradually reduces with increasing Reynolds number. However, the inner peak disappears entirely in the fully rough regime, and the profiles only exhibit an outer peak, located at a wall-normal location of approximately $y/\delta \approx 0.06$ where δ represents the boundary layer thickness. These findings suggest that Townsend's similarity hypothesis for 2D surface roughness is relatively well approximated in the outer region of the flow, as evidenced by the collapse of velocity defect, turbulence intensity, skewness, and flatness distributions when scaled with δ ,

The streamwise spacing to height ratio (s_x/k) has a greater impact on ΔU^+ and C_f than the spanwise spacing to height ratio (s_z/k) for 3D sinewave roughness. However, s_z/k substantially affects streamwise turbulence intensities in the log and outer layer. Surfaces with positive roughness skewness (k_{sk}) exhibit higher drag, resulting in a more significant downward shift compared with zero and negative roughness skewness. C_f decreases as k_{sk} decreases. The increase in the percentage of C_f and ΔU^+ is significantly higher when moving from negative to zero roughness skewness than when moving from zero to positive roughness skewness. The shape factor (H) was identified as a suitable scaling parameter for improving the data collapse of the diagnostic plot for both 2D and 3D roughness.

Numerous studies have been conducted to determine the most significant surface parameter in wall-bounded turbulence. The concept of equivalent sand-grain roughness (k_s) was introduced by Nikuradse (1933) to standardise different types of roughness and serve as an input parameter for predictions of ΔU^+ . A chronological compilation of roughness correlations is presented, providing details on the parameter ranges and types of roughness used during their development.

The research findings indicate that in the fully rough regime, for 2D roughness, the roughness skewness k_{sk} and the streamwise effective slope (ES_x) are significant parameters that influence the drag coefficient C_f . These parameters have been incorporated into a new expression for k_s that is normalised with the maximum peak to valley roughness height (k_t). Similarly, for 3D roughness in the fully rough regime, a correlation has been developed based on k_{sk} and ES_x to predict k_s normalised with the root mean square roughness height (k_q). Despite the fact that this correlation is restricted to 3D surface roughness, which is a more realistic representation, the model demonstrated a high level of accuracy in predicting k_s for over 120 distinct rough surfaces, with a coefficient of determination (R^2) of 0.96. The R^2 value, is a statistical measure that represents the proportion of the variance in the dependent variable that is explained by the independent variable(s) in a regression model. It is a measure of how well the regression line fits the data.

Declaration of Authorship

I certify that this work contains no material which has been accepted for the award of any other degree or diploma in my name in any university or other tertiary institution and, to the best of my knowledge and belief, contains no material previously published or written by another person, except where due reference has been made in the text. In addition, I certify that no part of this work will, in the future, be used in a submission in my name for any other degree or diploma in any university or other tertiary institution without the prior approval of the University of Adelaide and, where applicable, any partner institution responsible for the joint award of this degree.

The author acknowledges that copyright of published works contained within this thesis resides with the copyright holder(s) of those works.

I give permission for the digital version of my thesis to be made available on the web, via the University's digital research repository, Library Search and also through web search engines, unless permission has been granted by the University to restrict access for a period of time.

I acknowledge the support I have received for my research through the provision of an Australian Government Research Training Program Scholarship.

Signed:

Misarah Abdelaziz

Acknowledgements

First and foremost, I would like to praise Allah the Almighty, the Most Gracious, the Most Merciful, and the Most Compassionate. for His blessing. I am forever thankful for the opportunities and experiences that have been bestowed upon me.

I express my sincere gratitude to my supervisors, Dr Rey Chin, Dr Mergen Ghayesh and Prof Lyazid Djenidi, for their unwavering support for almost four years of my PhD. Their invaluable insights and expertise have shaped my research and enabled me to bring this thesis to fruition. It was an exclusive privilege to work with them. They were not only my academic supervisors but a role model in many aspects of life. Without their guidance, support, constructive feedback and motivation, this PhD would be more challenging, if not impossible, to complete. I am indebted to them, and hopefully, I can pay this debt back by following their steps and attitude toward younger students and researchers in the future.

I would like to express my deepest gratitude to my wife, Aisha, for her unwavering love and support throughout my PhD journey. Her encouragement and understanding have been a constant source of motivation and strength for me. Her constant belief in me and my abilities, her patience and understanding during the long nights and weekends spent working on my thesis, and her willingness to sacrifice so much for my success have meant more to me than words can express. I could not have completed this endeavour without her by my side. Thank you, Aisha, for always believing in me and being my rock.

I would like to extend my heartfelt appreciation to my family overseas, my wife and my parents, brother and sisters for their dedicated support and encouragement throughout my PhD journey. Despite the distance and time difference, they have always been there for me, offering words of encouragement and motivation when I needed it the most. Their love and support have been invaluable, and I am forever grateful for their presence in my life. I would also like to thank them for their sacrifices and for understanding the long hours and dedication required for me to complete this degree. I am truly blessed to have such a loving and supportive family.

I also want to express my deepest gratitude to my colleagues and friends overseas for their support and guidance throughout my PhD journey. Your contributions, both professional and personal, have been invaluable to my success. I am incredibly grateful for the time we spent together in the lab and for the friendship and camaraderie we shared. Thank you for being a part of my academic and personal growth.

Finally, I would like to acknowledge the funding agencies and organizations that supported this research, The University of Adelaide and The Australian Research Council (ARC). Without their support, this work would not have been possible.

Contents

Abstract	v
Declaration of Authorship	vii
Acknowledgements	viii
List of Figures	xiii
List of Tables	xxi
1 Introduction	1
1.1 MOTIVATION	2
1.2 AIMS AND OBJECTIVES	3
1.2.1 Aims	4
1.2.2 Objectives	4
1.3 THESIS OUTLINE	5
2 Literature Review	7
2.1 WALL-BOUNDED TURBULENT FLOWS	7
2.2 BASIC PRINCIPLES OF SMOOTH WALL TBL	8
2.2.1 Classical description	9
2.2.2 Ryenolds number similarity	11
2.2.3 Spectral scaling arguments	12
2.2.4 Taylor’s frozen turbulence hypothesis	14
2.3 PRINCIPLES OF ROUGH WALL TBL	15
2.3.1 k -type and d -type Roughness	16
2.3.2 Classical description	18
2.3.3 Outer layer similarity	19
2.3.4 Roughness function	20
2.3.5 Equivalent sand grain roughness height, k_s	20
2.3.6 Rough flow regimes	21
2.3.7 k_s Predictive correlations based on roughness parameters	23
3 Methodology	47
3.1 WIND TUNNEL FACILITY	47
3.2 SURFACE ROUGHNESS	47
3.3 MEASURING STATION	56

4	Outer Turbulent Boundary Layer Similarities	59
4.1	CHAPTER OVERVIEW	59
4.2	OUTER TURBULENT BOUNDARY LAYER SIMILARITIES FOR DIFFERENT 2D SURFACE ROUGHNESSES AT MATCHED REYNOLDS NUMBER	60
4.3	INTRODUCTION	62
4.4	EXPERIMENTAL DETAILS	64
4.4.1	Wind tunnel facility	64
4.4.2	Surface roughness	64
4.4.3	Measurement rig	66
4.4.4	Experiments	66
4.5	FRICION VELOCITY	67
4.6	RESULTS	68
4.6.1	Mean velocity profile	68
4.6.2	Turbulence intensities	71
4.6.3	Velocity skewness and flatness factor	73
4.6.4	Autocorrelations	74
4.6.5	Pre-multiplied energy spectra	75
4.7	CONCLUSIONS	76
5	A New Equivalent Sand Grain Roughness Relation For 2-D Rough Surfaces	81
5.1	CHAPTER OVERVIEW	81
5.2	A NEW EQUIVALENT SAND GRAIN ROUGHNESS RELATION FOR TWO-DIMENSIONAL ROUGH SURFACES	82
5.3	INTRODUCTION	84
5.4	EXPERIMENTAL DETAILS	87
5.4.1	Wind tunnel facility	87
5.4.2	Surface roughness	87
5.4.3	Measurement rig	89
5.4.4	Experiments	90
5.5	FRICION VELOCITY	91
5.6	RESULTS	93
5.6.1	Validation	93
5.6.2	Second set of experiments	96
5.6.2.1	Mean velocity profile	96
5.6.2.2	Roughness function	98
5.7	CONCLUSIONS	103
6	Streamwise And Spanwise Effective Slopes Effect on Turbulent Boundary Layers	109
6.1	CHAPTER OVERVIEW	109
6.2	ON THE EFFECT OF STREAMWISE AND SPANWISE SPACING TO HEIGHT RATIOS OF THREE-DIMENSIONAL SINUSOIDAL ROUGHNESS ON TURBULENT BOUNDARY LAYERS	110
6.3	INTRODUCTION	112
6.4	EXPERIMENTAL DETAILS	115
6.4.1	Wind tunnel facility	115
6.4.2	Surface roughness	115
6.4.3	Measurement rig	117
6.4.4	Experiments	120
6.5	FRICION VELOCITY	120

6.6	RESULTS	123
6.6.1	2D roughness vs 3D roughness	123
6.6.2	Streamwise spacing vs spanwise spacing in 3D sinusoidal roughness	125
6.6.3	TBL over different rough surfaces at matched friction Reynolds number	132
6.6.4	Energy spectra	135
6.7	CONCLUSION	136
7	Roughness Skewness Effect on Turbulent Boundary Layers	143
7.1	CHAPTER OVERVIEW	143
7.2	INFLUENCE OF SKEWED THREE-DIMENSIONAL SURFACE ROUGHNESS ON TURBULENT BOUNDARY LAYERS	144
7.3	INTRODUCTION	146
7.4	EXPERIMENTAL DETAILS	149
7.4.1	Wind tunnel and test section facilities	149
7.4.2	3D Sinusoidal roughness and roughness parameters	150
7.4.3	Hotwire and measurements apparatus	151
7.4.4	Experiments	152
7.5	RESULTS AND DISCUSSION	155
7.5.1	Friction Velocity	155
7.5.2	Mean velocity profile	156
7.5.3	Turbulence intensity profiles	161
7.5.4	Velocity skewness and kurtosis factor	165
7.5.5	Autocorrelations	165
7.5.6	Energy Spectra	169
7.6	CONCLUSIONS	170
8	A New Equivalent Sand Grain Roughness Relation For 3D Rough Surfaces	175
8.1	CHAPTER OVERVIEW	175
8.2	ON PREDICTIVE MODELS FOR THE EQUIVALENT SAND GRAIN ROUGHNESS FOR WALL-BOUNDED TURBULENT FLOWS	176
8.3	INTRODUCTION	178
8.3.1	Motivation	179
8.3.2	Roughness function	180
8.3.3	Equivalent sand grain roughness height, k_s	180
8.3.4	Rough flow regimes	181
8.3.5	k_s predictive correlations based on roughness parameters	182
8.4	SURFACE ROUGHNESS	192
8.5	RESULTS AND DISCUSSION	196
8.5.1	Existing k_s correlations	196
8.5.2	New k_s correlation	202
8.6	CONCLUSIONS	203
9	Conclusions	209
9.1	FUTURE WORK	210

List of Figures

1.1	(a) The fall of a stream of water as depicted by Leonardo da Vinci's(c.1510-12). The bottom part of the sheet RCIN 912660. Royal Collection Trust Copyright Her Majesty Queen Elizabeth II 2021, (b) The final configuration of SPH simulation using an air-water model Colagrossi <i>et al.</i> (2021).	2
2.1	Cross-sections of flow geometry for turbulent bounded flows with contours of premultiplied energy spectra of streamwise velocity fluctuations. Adapted from Monty <i>et al.</i> (2009).	8
2.2	A simple schematic for developing boundary layer, displacement and momentum thickness of TBL over a flat plate with free-stream velocity, U_∞	9
2.3	Mean streamwise velocity profile over smooth surface showing the different regions of the profile with the DNS smooth TBL data from Chan <i>et al.</i> (2021) at $Re_\tau \approx 2000$	11
2.4	Different spectral regions of u in TBL. Adapted from Perry <i>et al.</i> (1986)	13
2.5	A schematic of different regimes of the mean flow over 2D roughness (a) k -type roughness, (b) d -type roughness.	17
2.6	Mean streamwise velocity profile over rough surface showing the different regions of the profile with the DNS smooth TBL data from Chan <i>et al.</i> (2021) at $Re_\tau \approx 2000$	19
2.7	Moody chart for calculation of the friction factor in pipe flows Moody (1944).	22
2.8	The roughness function ΔU^+ as a function of the roughness Reynolds number k_s^+ for Nikuradse and Colebrook behaviour roughness.	24
3.1	A schematic of the University of Adelaide wind tunnel. The air is guided from (1) the fan through a series of turning vanes into (2) the settling chamber consists of a honeycomb flow straightener, and three screens, then enter (3) the nozzle and (4) the test section before redirecting back through (5) the diffuser to the fan.	48
3.2	The main roughness heights parameters on a sampling length L_s . The dashed line represents the mean line m , the reference line about which the profile deviations are measured.	49
3.3	Sketch of rough surface illustrates how frontal and plan solidity are calculated. The red area is the frontal projection of the rough element. The yellow area represents the plan projection of the rough element. The blue area is the projection of the total area of the surface.	50
3.4	Sketches of different configurations of 3D isotropic sinusoidal surfaces with equal streamwise and spanwise roughness effective slopes. (a) Low ES value. (b) High ES value. The contours are plotted with the same coordinates for ease of comparison.	51
3.5	Sketches of different configurations of 3D isotropic sinusoidal surfaces with equal streamwise and spanwise roughness skewness. (a) Positive skewness value. (b) Negative skewness value. (c) Zero skewness roughness. The contours are plotted with the same coordinates for ease of comparison.	52

3.6	Roughness chart shows the schematic variation in roughness parameters for all rough surfaces used in the thesis.	54
3.7	Output signals from CTA, LDA and PIV	56
3.8	A schematic of the streamwise velocity measurement procedures.	57
4.1	Schematic of different surfaces setups where $p = 8, 12,$ or 16 . The red dotted line shows the measurement location at $x \approx 1.5$ m downstream. The coordinate system used in experiments and $y = 0$ as a reference point are indicated in the schematic.	67
4.2	Streamwise mean velocity profiles over different rough surfaces at matched Reynolds number $Re_\tau = 2800 \pm 300$ for each surface are normalised by the friction velocity U_τ . Our smooth wall measurements are represented in blue triangle symbols. The symbols of our rough wall measurements are detailed in Table 4.1. The blue hexagram symbols are smooth TBL data from Marusic et al. (2015) at $Re_\tau = 2800$. The cyan line is DNS smooth TBL data from Chan et al. (2021) at $Re_\tau \approx 2000$. The inner length scale ν/U_τ normalises the wall-normal position y	69
4.3	Comparison of streamwise mean velocity deficit profiles over a smooth wall and different rough wall surfaces at $Re_\tau = 2800 \pm 300$ for each rough surface. The symbols are the same as in Figure 4.2. The magenta and green triangle symbols are smooth TBL from (Marusic et al., 2015) at $Re_\tau \approx 3600$ with different tripping conditions. The cyan line is DNS smooth TBL data from Chan et al. (2021) at $Re_\tau \approx 2000$. (a) The deficit profiles are normalised by U_∞ . (b) The deficit profiles are normalised by U_τ	70
4.4	The mean streamwise turbulence intensities profiles at $Re_\tau = 2800 \pm 300$ for each surface are normalised by U_τ . (a), (c), & (e): y is normalised by the inner length scale ν/U_τ . (b), (d), & (f): y is normalised by the outer length scale δ . The symbols of our measurements are detailed in Table 4.1. (a), & (b): shows all the profiles, while, (c), & (d): are the rods roughness compared to the smooth wall, and (e), & (f): compare the smooth wall with the sinewave roughness. The blue triangle symbols represent our smooth TBL at $Re_\tau = 2000$, while the blue hexagram symbols represent the smooth TBL from Marusic et al. (2015) at $Re_\tau = 2800$. The cyan line is DNS smooth TBL data from Chan et al. (2021) at $Re_\tau \approx 2000$	72
4.5	(a), (c), & (e): u' is normalised by U and plotted against U normalised by U_∞ . (b), (d), & (f): u' is normalised by $U\sqrt{H}$ and plotted against U normalised by U_∞ . The symbols of our measurements are detailed in Table 4.1. (a), & (b): shows all the profiles, while, (c), & (d): are the rods roughness compared to the smooth wall, and (e), & (f): compare the smooth wall with the sinewave roughness. The solid straight magenta line corresponds to the linear relationship $u'/U = 0.286 - 0.255 U/U_\infty$ (see Alfredsson et al., 2012).	73
4.6	(a) The smooth and rough wall streamwise velocity skewness comparisons. (b) The smooth and rough wall streamwise velocity kurtosis comparisons. The wall-normal position y is normalised by the outer length scale δ . The blue triangle symbols represent our smooth TBL at $Re_\tau = 2000$. The blue hexagram symbols represent the smooth TBL from Marusic et al. (2015) at $Re_\tau = 2800$. The cyan line is DNS smooth TBL data from Chan et al. (2021) at $Re_\tau \approx 2000$	74
4.7	Autocorrelation R_{uu} of streamwise velocity fluctuations at different wall-normal locations for each rough surface as well as the smooth wall surface. The smooth wall surface is plotted in a blue line. The symbols of our rough wall measurements are detailed in Table 4.1. Marks are only for surface differentiation and does not indicate any specific data. (a) $y/\delta = 0.06$, (b) $y/\delta = 0.1$, (c) $y/\delta = 0.2$, (d) $y/\delta = 0.5$. The dashed grey line represents R_{uu} of 0.05.	76

4.8	Pre-multiplied energy spectra of different rough and smooth surfaces at four different wall-normal locations. The wavelength λ_x is normalised by the outer length scale δ . (a) $y/\delta = 0.06$. (b) $y/\delta = 0.1$. (c) $y/\delta = 0.2$. (d) $y/\delta = 0.5$. The coloured lines and symbols represent the different rough surfaces, as indicated in Table 4.1. The blue line is our smooth wall measurement at $Re_\tau = 1930$	76
5.1	Schematic of different surface geometry set-ups with the same $k = 1.6$ mm and $s_x = 8k$. The red dotted line shows the measurement location. The coordinate system used in the experiments and $y = 0$ as a reference point are indicated in the schematic.	90
5.2	Friction velocity and least square error of TBL measurement over the R24-06 surface at $Re_\tau = 5700$ (a) Contours of U_τ calculated from the modified Clauser chart. (b) Contours of least square error from fitting data to the modified Clauser chart. The plus mark (+) refers to $\kappa = 0.405$ and $\epsilon = k/2 = 1200$ μm	94
5.3	The streamwise mean velocity profiles over the R16-08 surface at different free-stream velocities normalised by the friction velocity U_τ . The unfilled symbols represent data from Djenidi et al. (2018) at the closest Re_τ . Our smooth wall TBL measurements are plotted in grey symbols and are detailed in Table 5.3. The dot-dashed line shows the smooth DNS data from Schlatter & Örlü (2010) at $Re_\tau = 1040$. The dashed line shows the smooth DNS data from Sillero et al. (2014) at $Re_\tau = 2000$. The black and blue hexagram symbols are smooth TBL data from Marusic et al. (2015) at $Re_\tau = 3500$ and 4000 , respectively. The wall-normal position y is normalised by the inner length scale ν/U_τ	95
5.4	Profiles of u' over the R16-08 surface at different free-stream velocities normalised by the friction velocity U_τ . The symbols are the same as indicated in Figure 5.3. (a) The wall-normal position y is normalised by the outer length scale δ . (b) The wall-normal position y is normalised by the inner length scale ν/U_τ	95
5.5	Streamwise mean velocity profiles over different rough surfaces at matched Reynolds number $3300 < Re_\tau < 4300$ where each surface is normalised by the friction velocity U_τ . The symbols of our measurements are detailed in Table 5.3. The black hexagram symbols are smooth TBL data from Marusic et al. (2015) at $Re_\tau = 3500$. The wall-normal position y is normalised by the inner length scale ν/U_τ . The vertical lines indicate the roughness heights in terms of viscous length scale units k^+	96
5.6	The streamwise mean velocity profiles over different rough surfaces at matched Reynolds number $3300 < Re_\tau < 4300$ where each surface is normalised by the friction velocity U_τ . The wall-normal position y is normalised by different outer length scales. The symbols of the different rough surfaces are detailed in Table 5.3. (a) The wall-normal position y is normalised by the outer roughness length scale k . (b) The wall-normal position y is normalised by the outer length scale δ . (c) The wall-normal position y is normalised by the outer roughness length scale k_s	97
5.7	Roughness function ΔU^+ as a function of maximum peak-to-valley roughness height, k normalised by the inner length scale ν/U_τ . The filled symbols are the different surfaces roughness symbols indicated in Table 5.3.	98
5.8	Roughness function ΔU^+ as a function of effective slope, ES . The filled symbols are the different surfaces roughness symbols indicated in Table 5.3. The blue pentagram symbols are channel flow data over various irregularly distributed sinusoidal roughness from Napoli et al. (2008)	99

5.9	The streamwise mean velocity profiles over three different roughnesses with the same height, k , and effective slope, ES , but different geometries normalised by the friction velocity U_τ . Cases $R16-08$, $S16-08$ and $T16-08$ are compared with The smooth TBL data from Marusic <i>et al.</i> (2015) . The symbols of our different surfaces are indicated in Table 5.3.	100
5.10	Roughness function ΔU^+ as a function of roughness skewness, k_{sk} . The filled symbols are the different surfaces roughness symbols indicated in Table 5.3. . . .	101
5.11	The roughness function for 2-D roughness as a function of equivalent sand grain roughness height k_s , normalised by the inner length scale ν/U_τ . The filled symbols are the different surface roughness symbols indicated in Table 5.3. The unfilled symbols are the predicted k_s^+ from (5.18) for the same rough surface. The black solid line is the fully rough asymptote of Nikuradse (1933) . The values of k_s of Krogstad & Antonia (1999) , Kamruzzaman <i>et al.</i> (2015) and Djenidi <i>et al.</i> (2018) are reported in the figure for comparison and validation.	102
5.12	Comparison between actual k_s measured from mean velocity profiles and the calculated k_s from (5.18) for our surfaces along with previous experimental and numerical results of 2-D roughness only.	102
5.13	Comparison between actual k_s from literature and the calculated k_s from (5.19) for 3-D roughness only.	104
5.14	Comparison between actual k_s and the calculated k_s from (5.20) for 2-D and 3-D roughnesses	104
6.1	The experimental setup of the adjustable sidewalls test section of the wind tunnel with the hot-wire probe and the 3D sinewave rough surface.	118
6.2	Pre- and-post calibration of hot-wire example with an intermediate calibration curve. Circle symbols are pre-calibration, while plus symbols are post-calibration points. The blue line represents the intermediate calibration curve.	119
6.3	A schematic of a 3D sinewave roughness. $S24-12-06$, represented in this figure, is a 3D sinusoidal surface with a roughness height of 2.4 mm and a streamwise spacing between two consecutive roughness peaks of $12k$ and a spanwise spacing of $6k$. The red mark shows the hot-wire measurement location.	120
6.4	Streamwise mean velocity deficit profiles over different rough wall surfaces at four different Reynolds numbers for each surface. The symbols of our measurements are detailed in Table 6.2. Solid black line: DNS smooth TBL data from Chan <i>et al.</i> (2021) at $Re_\tau \approx 2000$	122
6.5	Variation of C_f as a function of θ/y_o . The dashed and dashed-dotted curves represent the standard two-parameter family results with wake strengths of $\Pi = 0.7$ and $\Pi = 0.55$, respectively.	123
6.6	(a) Mean streamwise velocity profiles over 2D and 3D sinewave roughness. (b) Mean streamwise turbulence intensity profiles over 2D and 3D sinewave roughness. The symbols of the 3D roughness are indicated in Table 6.2, and the same symbols are used for the 2D sinewave roughness with a magenta color. Solid black line: DNS smooth TBL data from Chan <i>et al.</i> (2021) at $Re_\tau \approx 2000$	124
6.7	Mean streamwise velocity profiles over different rough surfaces at a free-stream velocity of $U_\infty = 20$ m/s. The symbols of our measurements are detailed in Table 6.2. Solid black line: DNS smooth TBL data from Chan <i>et al.</i> (2021) at $Re_\tau \approx 2000$. The profiles over rough surfaces with constant $s_x/k = 6, 8, \text{ and } 12$ are shown in (a), (c) and (e), respectively. The profiles over rough surfaces with constant $s_z/k = 6, 8, \text{ and } 12$ are shown in (b), (d) and (f), respectively. The profiles over smooth and rough surfaces at four different free-stream velocities U_∞ are shown for one surface in panel (b), the same symbol with different colors, as the other profiles have the same trend.	126

6.8	(a) ΔU^+ as a function of the spanwise spacing to height ratio s_z/k for different values of s_x/k . (b) ΔU^+ as a function of the streamwise spacing to height ratio s_x/k for different values of s_z/k . The symbols of each roughness are indicated in Table 6.2.	127
6.9	(a) C_f and H as a function of the spanwise spacing to height ratio s_z/k for different values of s_x/k . (b) C_f and H as a function of the streamwise spacing to height ratio s_x/k for different values of s_z/k . The symbols of each roughness are indicated in Table 6.2. Black lines represent the linear approximation of C_f , while blue lines represent the linear approximation of H . The solid lines are for s_x/k , and $s_z/k = 6$ in (a) and (b), respectively. The dashed lines are for s_x/k , and $s_z/k = 8$ in (a) and (b), respectively. The dotted lines are for s_x/k , and $s_z/k = 12$ in (a) and (b), respectively.	128
6.10	Mean streamwise velocity profiles over different rough surfaces at different Reynolds numbers for each surface. The wall-normal location y is normalized by k . The symbols of the different rough surfaces are detailed in Table 6.2. The profiles over rough surfaces with constant $s_x/k = 6, 8,$ and 12 are shown in (a), (c), and (e), respectively. The profiles over rough surfaces with constant $s_z/k = 6, 8$ and 12 are shown in (b), (d), and (f), respectively.	129
6.11	Mean streamwise turbulence intensity profiles over different rough surfaces at a free-stream velocity of $U_\infty = 20$ m/s. The symbols of our measurements are detailed in Table 6.2. The profiles over the smooth wall at different Reynolds numbers and the DNS smooth TBL data from Sillero <i>et al.</i> (2014) at approximately matched Reynolds numbers are also shown in (b). The profiles over the rough surface S24-06-08 at four different free-stream velocities U_∞ , the same symbol with different colors, are shown in (d) only, as the other profiles have the same trend. The profiles over rough surfaces with constant $s_x/k = 6, 8,$ and 12 are shown in (a), (c), and (e), respectively. The profiles over rough surfaces with constant $s_z/k = 6, 8,$ and 12 are shown in (b), (d), and (f), respectively.	130
6.12	Mean streamwise turbulence intensity profiles over smooth and rough surfaces are compared using the diagnostic plot. The symbols of our measurements are detailed in Table 6.2. Solid black line: DNS smooth TBL data from Chan <i>et al.</i> (2021) at $Re_\tau \approx 2000$. The solid straight magenta line corresponds to the linear relationship $u'/U = 0.286 - 0.255 U/U_\infty$ (Alfredsson <i>et al.</i> , 2012). The profiles over rough surfaces with constant $s_x/k = 6, 8,$ and 12 are shown in (a), (c), and (e), respectively. The profiles over rough surfaces with constant $s_z/k = 6, 8,$ and 12 are shown in (b), (d), and (f), respectively.	133
6.13	(a) Mean streamwise velocity profiles for the different rough surfaces presented in Table 6.2 at matched Reynolds number $Re_\tau = 2500 \pm 400$. (b) Mean streamwise turbulence intensity profiles of the different rough surfaces at matched Reynolds number $Re_\tau = 2500 \pm 400$. The symbols of our measurements are detailed in Table 6.2. Solid black line: DNS smooth TBL data from Chan <i>et al.</i> (2021) at $Re_\tau \approx 2000$	134
6.14	The premultiplied streamwise energy spectrograms at approximately matched Re_τ , for the isotropic surfaces with equal streamwise and spanwise effective slopes, and compared with our smooth wall data as a reference in (d). The vertical solid line in (a)-(C) corresponds to $y = k$ in S24-06-06, S24-08-08 and S24-12-12, respectively.	137

6.15 The premultiplied streamwise energy spectrograms at approximately matched Re_τ for the anisotropic surfaces. The left column represents spectrograms of surfaces with a higher spanwise spacing to height ratios than the streamwise spacing to height ratios [(a): S24-08-16, (c): S24-06-12, (e): S24-08-12, (g): S24-06-08]. The right column represents spectrograms of the same surfaces after rotating them by 90° in the (x, z) plane, a higher streamwise spacing to height ratios than the spanwise spacing to height ratios, [(b): S24-16-08, (d): S24-12-06, (f): S24-12-08, (h): S24-08-06]. The vertical solid line corresponds to $y = k$ 138

7.1 A schematic of the University of Adelaide wind tunnel. The air is guided from (1) the fan through a series of turning vanes into (2) the settling chamber consists of a honeycomb flow straightener, and three screens, then enter (3) the nozzle and (4) the test section before redirecting back through (5) the diffuser to the fan. 149

7.2 A schematic of different 3D sinewave rough surfaces. Plots on the left column are Positive roughness skewness, while plots on the middle column are negative roughness skewness, and the zero roughness skewness are plotted on the right column. Units of x, z and Y are in mm. 151

7.3 A simple schematic of the tripping devices and the rough surface inserted in the test section. This schematic is not to scale. The insert figure is a local view of the sinewave roughness taken by a high-magnification microscope 153

7.4 Streamwise mean velocity deficit profiles over smooth and rough wall surfaces for all the profiles at different Re_τ . The symbols of our measurements are detailed in Table 7.2. Solid black line: DNS smooth TBL data from Chan *et al.* (2021). 156

7.5 (a) Mean streamwise velocity profiles over our smooth wall data and 3D sinewave surfaces with constant $ES = 0.2$. The profiles over smooth and S24-06-06 surfaces at three different freestream velocities U_∞ are shown with the same symbols and different colours. Solid black line: DNS smooth TBL data from Chan *et al.* (2021) at $Re_\tau \approx 2000$. (b) Comparison with velocity profiles over a smooth wall data of Marusic *et al.* (2015), (the black hexagram) at matched $Re_\tau = 3000 \pm 300$. The symbols of our measurements are detailed in Table 7.2. N for negative k_{sk} , Z for zero k_{sk} and P for positive k_{sk} . The blue symbols are at $U_\infty = 10$ m/s. The green symbols are at $U_\infty = 15$ m/s. The red symbols are at $U_\infty = 20$ m/s. 157

7.6 (a) The relation between H and k_{sk} for the different 3D sinewave surfaces that have $ES \approx 0.18 \pm 0.4$ at the three different Re_τ values. (b) The relation between C_f and k_{sk} for the different 3D sinewave surfaces with $ES \approx 0.18 \pm 0.4$ at the three different Re_τ values. The symbols of the rough surface are indicated in Table 7.2. N for negative k_{sk} , Z for zero k_{sk} and P for positive k_{sk} . the left area is for negative roughness skewness, while the right one is for positive roughness skewness values. The blue symbols are at $U_\infty = 10$ m/s. The green symbols are at $U_\infty = 15$ m/s. The red symbols are at $U_\infty = 20$ m/s. 159

7.7 (a) The relation between ΔU^+ and k_{sk} for the different 3D sinewave surfaces that have $ES \approx 0.18 \pm 0.4$ at the three different Re_τ values. (b) The relation between k_s^+ and k_{sk} for the different 3D sinewave surfaces with $ES \approx 0.18 \pm 0.4$ at the three different Re_τ values. The symbols of the rough surface are indicated in Table 7.2. N for negative k_{sk} , Z for zero k_{sk} and P for positive k_{sk} . the left area for negative roughness skewness, while the right one is positive roughness skewness values. The blue symbols are at $U_\infty = 10$ m/s. The green symbols are at $U_\infty = 15$ m/s. The red symbols are at $U_\infty = 20$ m/s. 160

7.8	Equivalent sand grain roughness k_s as a function of roughness skewness k_{sk} for the different 3D sinewave surfaces that have $ES = 0.2 \pm 0.2$ at the three different Re_τ values. The solid black line represents the exponential fitting of the data. The symbols of the rough surface are indicated in Table 7.2. N for negative k_{sk} , Z for zero k_{sk} and P for positive k_{sk} . The blue symbols are at $U_\infty = 10$ m/s. The green symbols are at $U_\infty = 15$ m/s. The red symbols are at $U_\infty = 20$ m/s.	162
7.9	Mean streamwise turbulence intensity profiles over smooth and rough surfaces normalized by inner scaling in (a) and (c) and outer scaling in (b) and (d). The same surfaces used in Figure 7.5(a) are plotted in (a) and (b). The same surfaces used in Figure 7.5(b) are plotted in (c) and (d). The symbols of our measurements are detailed in Table 7.2. Solid black line in (a) and (b): DNS smooth TBL data from Chan <i>et al.</i> Chan <i>et al.</i> (2021) at $Re_\tau \approx 2000$. The smooth wall data of Marusic <i>et al.</i> Marusic <i>et al.</i> (2015) is plotted with a black hexagram in (c) and (d).	163
7.10	(a) and (b): u' is normalized by U and plotted against U normalized by U_∞ . (c) and (d): u' is normalized by $U\sqrt{H}$ and plotted against U normalized by U_∞ . The symbols of our measurements are detailed in Table 7.2. The smooth wall data of Marusic <i>et al.</i> (2015) is plotted with a black hexagram in (b). Solid black line in (a): DNS smooth TBL data from Chan <i>et al.</i> (2021) at $Re_\tau \approx 2000$. The solid straight magenta line corresponds to the linear relationship $u'/U = 0.286 - 0.255 U/U_\infty$ (Alfredsson <i>et al.</i> , 2012).	164
7.11	(a) Streamwise velocity skewness over smooth and rough wall surfaces at different Re_τ . (b) Streamwise velocity kurtosis over smooth and rough wall surfaces at different Re_τ . The symbols of our measurements are detailed in Table 7.2. Solid black line: DNS smooth TBL data from Chan <i>et al.</i> (2021). The wall-normal position y is normalized by the outer length scale δ	166
7.12	Autocorrelation R_{uu} of streamwise velocity fluctuations at $y/\delta = 0.1$ for different smooth and rough surfaces. The same surfaces used in Figures 7.5 (a) and (b) are plotted here in (a) and (b), respectively. The symbols of our measurements are detailed in Table 7.2. Marks are only for surface differentiation and do not indicate any specific data. The black dashed line represents $R_{uu} = 0.05$ as the cutoff R_{uu}	167
7.13	The premultiplied streamwise energy spectrograms contours at approximately matched $Re_\tau = 3000 \pm 300$, for the nine 3D sinusoidal surfaces. The positive roughness skewness rough surfaces are shown in the left column, (a)S24-07-07P33, (d)S24-06-06P48 and (g)S24-05-05P63. The negative roughness skewness rough surfaces are shown in the middle column, (b)S24-07-07N33, (e)S24-06-06N48 and (h)S24-05-05N63. The right column shows the three zero-roughness skewness rough surfaces, (c)S24-06-06, (f)S24-08-08 and (i)S24-12-12.	168
8.1	The roughness function ΔU^+ as a function of the roughness Reynolds number k_s^+ for Nikuradse and Colebrook behaviour roughness.	183
8.2	The main roughness heights parameters on a sampling length L_s . The dashed line represents the mean line m , the reference line about which the profile deviations are measured.	193
8.3	Sketches of different configurations of 3D isotropic sinusoidal surfaces with equal streamwise and spanwise roughness effective slopes. (a) Low ES value. (b) High ES value. The contours are plotted with the same coordinates for ease of comparison.	194
8.4	Sketch of rough surface illustrates how frontal and plan solidity are calculated. The red area is the frontal projection of the rough element. The yellow area represents the plan projection of the rough element. The blue area is the projection of the total area of the surface.	194

8.5	Sketches of different configurations of 3D isotropic sinusoidal surfaces with equal streamwise and spanwise roughness skewness. (a) Positive skewness value. (b) Negative skewness value. (c) Zero skewness roughness. The contours are plotted with the same coordinates for ease of comparison.	195
8.6	Comparison between actual k_s and predicted k_s for regular 3D roughnesses using different correlation from literature: (a) correlation from Boyle & Stripf (2009), (b) correlation from Flack <i>et al.</i> (2016), (c) correlation from Forooghi <i>et al.</i> (2017), (d) correlation from Barros <i>et al.</i> (2018), (e) correlation from Kuwata & Kawaguchi (2019) and (f) correlation from Flack <i>et al.</i> (2020).	197
8.7	Comparison between actual k_s and predicted k_s for irregular 3D roughnesses using different correlation from literature: (a) correlation from Boyle & Stripf (2009), (b) correlation from Flack <i>et al.</i> (2016), (c) correlation from Forooghi <i>et al.</i> (2017), (d) correlation from Barros <i>et al.</i> (2018), (e) correlation from Kuwata & Kawaguchi (2019) and (f) correlation from Flack <i>et al.</i> (2020).	200
8.8	Comparison between actual k_s and predicted k_s for all 3D roughnesses using different correlation from literature: (a) correlation from Boyle & Stripf (2009), (b) correlation from Flack <i>et al.</i> (2016), (c) correlation from Forooghi <i>et al.</i> (2017), (d) correlation from Barros <i>et al.</i> (2018), (e) correlation from Kuwata & Kawaguchi (2019) and (f) correlation from Flack <i>et al.</i> (2020).	201
8.9	Comparison between actual k_s and predicted k_s using the new predicted correlation 8.2 for (a) regular 3D roughnesses, (b) irregular 3D roughnesses, (c) regular and irregular 3D roughnesses.	202

List of Tables

2.1	Previous research on the onsets of transitionally rough and fully rough regimes	23
2.2	Previous research on k_s correlations	33
3.1	Different key surface roughness parameters. The surfaces are defined by the first letter of the geometry: R for rods T for triangular ribs and S for sinewaves, followed by ten times the maximum peak-to-valley height k , then the streamwise spacing to height ratio and the spanwise spacing to height ratio for 3D roughness and followed by the skewness value if it is not equal zero (P for positive and N for negative).	55
4.1	Different key surface roughness parameters. The surfaces are defined by the first letter of the geometry: R for rods and S for sinewaves, followed by ten times the maximum peak to valley height k and finally, the spacing between two consecutive roughness peaks.	65
4.2	Details of the experimental data sets.	67
4.3	Streamwise length of the correlated regions normalised by outer length scale $\Delta x/\delta$ at $R_{uu} = 0.05$ at different wall-normal locations in the log and outer region.	75
5.1	Different key surface roughness parameters.	89
5.2	Details of the first set of rough wall experimental data. $R16-08L$ refer to Djenidi et al. (2018) data.	91
5.3	Details of the second set of rough wall experimental data.	92
6.1	Different key surface roughness parameters.	117
6.2	Details of the experimental datasets. U_∞ , U_τ , and δ units are in m/s, m/s, and mm, respectively.	121
7.1	Statistical parameters of roughness topography for each surface. The surfaces are defined by the first letter of the geometry: S for a sinewave, followed by ten times the maximum peak-to-valley height k , then the streamwise spacing to height ratio and the spanwise spacing to height ratio for 3D roughness and followed by the roughness skewness value if it is not equal zero (P for positive and N for negative). For all the 3D sinewave surfaces, $k_t = k_p - k_v = 2.4$ mm, where k_p is the maximum peak height and k_v is the minimum valley height, and $k_a = 0.47$ mm and $k_q = 0.60$ mm.	152
7.2	Details of the experimental data sets. H is the shape factor.	154
8.1	Previous research on the onsets of transitionally rough and fully rough regimes	182
8.2	Previous research on k_s correlations	188
8.3	Different roughness parameters and their corresponding equations.	195
8.4	The statistical characteristics of different rough surface topographies and k_s values, gathered from literature, are presented. Both experimental and numerical data have been utilised, and the measurements are given in millimetres.	198

Nomenclature

Greek symbols

- α_{rms} = Root-mean-square slope angle of roughness;
 δ = Channel half height or boundary layer thickness;
 δ^* = Displacement thickness;
 ΔU^+ = Hama roughness function;
 Δx = Change in streamwise location;
 ϵ = Origin offset;
 ϵ_d = Average turbulent energy dissipation;
 η = Wall-normal position to boundary layer thickness ratio $\eta = y/\delta$;
 η_K = Kolmogorov length scale;
 θ = Momentum thickness;
 κ = von Kármán constant;
 Λ, Λ_s = Roughness parameters check intervening space between roughness elements;
 λ = Solidarity;
 λ_D = Dirling density parameter;
 λ_f = Frontal solidity;
 λ_p = Plan solidity;
 λ_s = Shelter solidity;
 λ_x = Signal wavelength;
 μ = Micro;
 ν = Kinematic viscosity;
 π = Mathematical constant (the ratio of a circle's circumference to its diameter);
 Π = Wake parameter;
 ρ = Fluid density;
 σ = Standard deviation;
 τ = Time;
 τ_w = Wall shear stress;
 v = Velocity scale;
 ϕ_{xx} = Power spectral density;
 $\omega(\eta)$ = Wake function;

Roman symbols

- A = Parameter in scaling law equations depends on flow geometry;
 A_f = Roughness element frontal projected area;
 A_p = Roughness element plan projected area;
 A_s = Sampling area of roughness;
 A_{sh} = Sheltered plan area of roughness element;
 A_t = Total surface area of a repeated unit of roughness element;
 A_w = Wetted or windward area of roughness element;
 B = Smooth wall intercept;
 b_m = Spanwise width of roughness element;
 C = Waigh & Kind roughness constant;
 C_f = Coefficient of friction ($C_f = 2\tau_w/\rho U_\infty^2$);
 C_{sk} = Skewness constant;
 dB = Decibel;
 D = The inverse square root of the number of roughness elements per unit geometric surface area;
 D_h = Hydraulic diameter;
 E = Voltage;
 E_{int} = The voltage of intermediate calibration curve;
 E_{post} = The voltage of the post-calibration from a polynomial of order six-degree fit;
 E_{pre} = The voltage of the pre-calibration from a polynomial of order six-degree fit;
 ES = Effective slope;
 ES_x = Streamwise effective slope;
 ES_z = Spanwise effective slope;
 f_c = The frequency response;
 H = Shape factor;
 K = Acceleration parameter ($K = (\nu/U_\infty^2)[dU_\infty/dx]$);
 k^+ = Non-dimensional roughness parameter ($k^+ = kU_\tau/\nu$);
 K_0 = Universal Kolmogorov constant;
 k, k_t = Maximum peak to valley roughness height;
 k_t^+ = Roughness Reynolds number based on k_t ($k_t^+ = k_t U_\tau/\nu$);
 k_a = Mean roughness height;
 k_a^+ = Roughness Reynolds number based on k_a ($k_a^+ = k_a U_\tau/\nu$);
 k_{ch} = Characteristic roughness height;

k_{ku}	=	Roughness kurtosis;
k_q, k_{rms}	=	Root-mean-square roughness height ;
k_q^+	=	Roughness Reynolds number based on k_q ($k_q^+ = k_q U_\tau / \nu$);
k_s	=	Equivalent sand grain roughness;
k_s^+	=	Roughness Reynolds number based on k_s ($k_s^+ = k_s U_\tau / \nu$);
$k_s^+ - Smooth, k_s^+ - Rough$	=	Roughness flow regimes margins;
k_{sk}	=	Roughness skewness;
K_u	=	Streamwise velocity kurtosis;
k_x	=	Streamwise wavenumber;
k_z	=	Average peak to valley height;
kHz	=	Kilohertz;
l	=	Hot-wire length;
l^+	=	Non-dimensional hot-wire length ($l^+ = l U_\tau / \nu$);
L_{ch}	=	Characteristic length;
L_s	=	Sampling length of roughness;
L_x^{cor}	=	Streamwise correlation length ;
m	=	Roughness mean line;
m	=	Meter;
mm	=	Millimeter;
R	=	Proportional drift for hot-wire calibration;
R^2	=	Statistical parameter;
R_p	=	Pipe radius;
R_{uu}	=	Autocorrelation of streamwise velocity fluctuations;
Re_τ	=	Friction Reynolds number ($Re_\tau = \delta U_\tau / \nu$);
Re_θ	=	Friction Reynolds number ($Re_\theta = \theta U_\infty / \nu$);
s	=	Seconds;
s_m	=	Streamwise width of roughness element;
s_x	=	Streamwise roughness spacing;
s_z	=	Spanwise roughness spacing;
S_f	=	Total frontal area of roughness;
S_t	=	Total surface area of roughness;
S_u	=	Streamwise velocity skewness;

- t = Time;
 t_i = The time when the data is acquired at each point within the experiment;
 t_{post} = The time when the post-calibration was conducted;
 t_{pre} = The time when the pre-calibration was conducted;
 u = Streamwise velocity fluctuation;
 U = Mean streamwise velocity;
 U^+ = Non-dimensional mean streamwise velocity ($U^+ = U / U_\tau$);
 U_∞^+ = Non-dimensional free-stream velocity ($U_\infty^+ = U_\infty / U_\tau$);
 u' = Rms of streamwise velocity fluctuation;
 u'^+ = Non-dimensional rms of streamwise velocity fluctuation ($u'^+ = u' / U_\tau$);
 u_a = Appropriate velocity scale;
 U_c = Convection velocity;
 U_{ch} = Characteristic velocity;
 U_∞ = Free-stream velocity;
 U_τ = Friction velocity ($U_\tau = \sqrt{\tau_w / \rho}$);
 w = Width of test section;
 x = Streamwise direction;
 y = Wall-normal direction;
 y_b = Appropriate length scale;
 y_o = The roughness length;
 y^+ = Non-dimensional wall normal direction ($y^+ = yU_\tau / \nu$);
 $Y(x, z)$ = 3D roughness elevation from mean line;
 z = Spanwise direction;
 $Z(x)$ = 2D roughness elevation from mean line;

Acronyms

2-D, 2D	=	Two-dimensional;
3-D, 3D	=	Three-dimensional;
ABS	=	Acrylonitrile butadiene styrene;
CNC	=	Computerised numerical control;
CTA	=	Constant temperature anemometer;
DAQ	=	Data acquisition systems;
DMLS	=	Direct metal laser sintering;
DNN	=	Deep neural network;
DNS	=	Direct numerical simulations;
FDM	=	Fused deposition modelling;
FFT	=	Fast Fourier transform;
GPR	=	Gaussian process regression;
HWA	=	Hotwire anemometry;
LDA	=	Laser doppler anemometry;
LES	=	Large eddy simulations;
OHR	=	Overheat ratio;
PIV	=	Particle image velocimetry;
rpm	=	Revolutions per minute;
SPH	=	Smoothed particle hydrodynamics;
SQT	=	Square wave test;
TBL	=	Turbulent boundary layer;
TIG	=	Tungsten inert gas;
ZPG	=	Zero pressure gradient;

Chapter 1

Introduction

*“Turbulence, a force of nature wild and free,
A dance of chaos in the air and sea.
It twists and turns, it swirls and spins,
A tempestuous symphony of winds.*

*It challenges the bravest of pilots bold,
And tests the strength of ships made of gold.
It’s a force of nature that can’t be tamed,
A force that leaves us both awed and maimed.
It can bring destruction in its wake,
But also bring new life in its path to make.”*

The first “picture” of turbulence is a matter of interpretation, as the concept of turbulence has been around for centuries and has been described in various forms in literature and scientific texts. However, the earliest known visual representation of turbulence is a series of sketches made by Leonardo da Vinci in the late 15th century, shown in Figure 1.1(a). He made several drawings of turbulent water flow in rivers and streams. These drawings were not made with the intent of studying turbulence, but they do depict the chaotic and irregular nature of the turbulent flow.

In the late 19th century, the invention of the Schlieren technique and the smoke wire method allowed scientists to make the first photographic images of turbulent flow. These methods involved using a light source to illuminate a thin sheet of smoke or other tracer particles and then capturing the distorted light on a photographic plate. These early images provided valuable insights into the structure and behaviour of turbulent flow, and they continue to be used in scientific research today.

In the 20th century, various experimental techniques such as hotwire anemometry (HWA), particle image velocimetry (PIV) and laser doppler anemometry (LDA) were developed that allowed for more detailed and accurate measurements of turbulent flow, as well as visualisation of the flow with the use of computer simulations. After 500 years of Leonardo da Vinci’s death, Colagrossi *et al.* (2021) reproduced the flow depicted in the drawing using the smoothed particle hydrodynamics (SPH) model, shown in Figure 1.1(b).

The turbulent boundary layer (TBL) is a fundamental concept in fluid dynamics, describing fluid flow in close proximity to a solid boundary. The behaviour of the TBL is crucial in many engineering applications, such as aerodynamics, heat transfer, and drag reduction. A

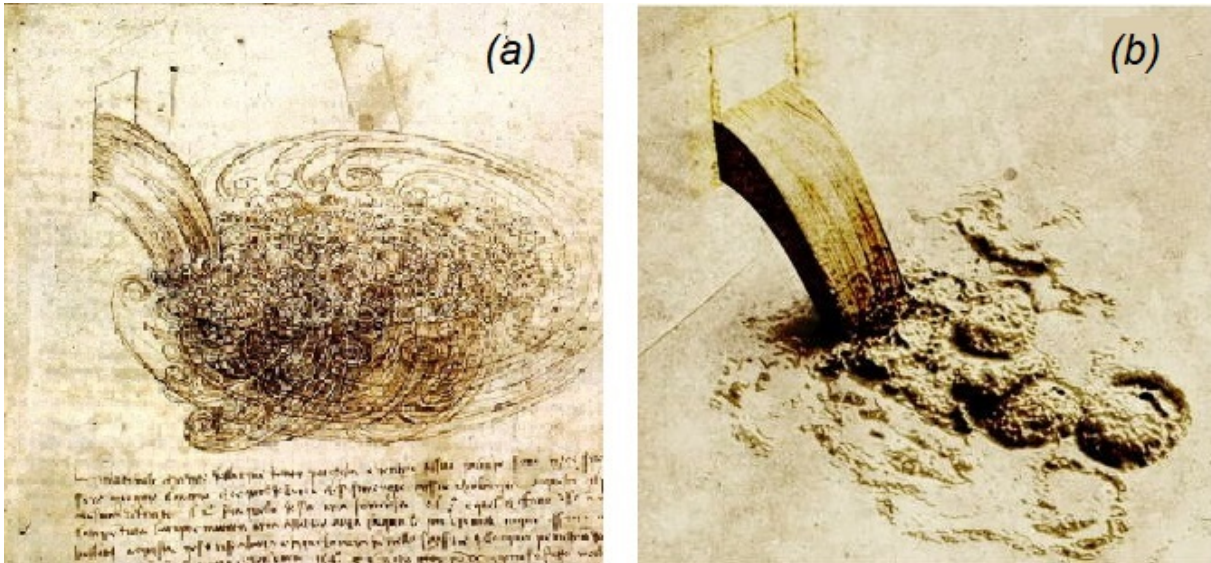


FIGURE 1.1: (a) The fall of a stream of water as depicted by Leonardo da Vinci's (c.1510-12). The bottom part of the sheet RCIN 912660. Royal Collection Trust Copyright Her Majesty Queen Elizabeth II 2021, (b) The final configuration of SPH simulation using an air-water model Colagrossi *et al.* (2021).

smooth surface is often assumed in TBL research, but in many practical situations, surfaces are rough. The roughness elements on a surface can have a significant impact on the TBL, affecting the flow structures, turbulence intensity, and drag forces. A single large container ship can release pollutants equivalent to those emitted by 50 million cars in a single year (Eyring *et al.*, 2010). Even after cleaning, a ship's hull experiences a significant increase in drag when compared to a smooth surface due to imperfections (Nugroho *et al.*, 2017; Utama *et al.*, 2017). For commercial aircraft, skin friction drag accounts for approximately 50% of total drag, while for large carrier ships, it can reach up to 80 – 90%. Therefore, understanding the various roughness parameters and their impact on the drag coefficient is crucial. A longstanding goal in fluid dynamics research is to determine the drag penalty on surfaces based solely on their topographical parameters.

Despite the importance of TBL over rough surfaces, there are still many unresolved questions and gaps in our understanding of the behaviour of TBL over rough surfaces. For example, the effects of different types of roughness (e.g. shape, size, and arrangement) on the TBL are not fully understood. Additionally, the minimum Reynolds number and maximum relative roughness (roughness height to boundary layer thickness height) required to achieve similarity between rough and smooth wall data are still not clear. Furthermore, the dominant roughness parameters that affect the turbulence statistics and drag coefficient over different flow regimes, from hydrodynamically smooth to fully rough regimes, are still unknown.

1.1 MOTIVATION

Predicting the movement of fluids over uneven surfaces is crucial for engineering design, as the surfaces in engineering flows are usually rough. These rough surfaces can be caused by imperfections in the surface finish during production, as well as erosion or corrosion due to aging and fouling processes. Examples include aerodynamic flows over airfoils with icing, ship hull roughness due to organic fouling, and erosion of gas turbine blades by impinging combustor air. It is well known that these rough surfaces can lead to a decrease in performance due to an

increase in wall friction (Kuwata *et al.*, 2019). The examination of roughness in turbulent flows began two centuries ago with the early work of Darcy (1857), who discovered that pressure drop is influenced by roughness in pipe flow. Nikuradse (1933) carried out extensive research on the impact of equivalent sand grain roughness on turbulent pipe flow, greatly advancing knowledge in this area. Moody (1944), building on the work of Colebrook & White (1937), then developed a chart for estimating head losses in smooth and rough pipes, which has been an essential tool in the field of hydraulic engineering. The concept of equivalent sand grain roughness (k_s) was introduced by Nikuradse (1933) as a way to define the grain size of uniform, close-packed sand grains on a hypothetical surface that would cause the same drag as the surface of interest if exposed to the same flow in the fully rough regime. The roughness height listed on the Moody diagram provides a common currency across different roughness for wall-bounded turbulence and serves as an input parameter for predictions. However, it is important to note that k_s is not a physical measure of roughness elevation and should not be used as such. Researchers aim to gain a deeper understanding of the relationship between a surface’s physical characteristics and the flow resistance it creates, specifically in regard to the point at which a rough surface starts to have a greater impact on wall shear stress compared to a smooth surface.

The roughness present on any surface can have a significant effect on boundary layer flow, impacting heat and momentum transfer. Roughness can cause an increase in drag, which can result in higher fuel consumption and emissions in transportation, such as for ships and aeroplanes. By understanding how roughness affects boundary layer flows, it is possible to develop methods for controlling and reducing drag, which can lead to significant cost savings and environmental benefits. A small reduction in drag, as little as 1%, can result in significant fuel savings and emissions reductions over time. Therefore, understanding the effect of roughness on boundary layer flows is crucial for improving energy efficiency and reducing environmental impact in various industries.

This thesis aims to gain a deeper understanding of TBL over rough surfaces by addressing these unresolved questions. The research will be conducted using HWA as the experimental method, with a focus on investigating the effects of different types of roughness on the TBL and determining the dominant roughness parameters that affect the turbulence statistics and drag coefficient over different flow regimes. The research will also aim to derive a general formula for different surface roughnesses based solely on the surface parameters.

There has been no clear agreement on which length scale or roughness parameter best describes a surface in relation to friction drag. It should be mentioned that over the last four decades, many studies have been conducted to try and determine which surface parameter is most important. Many different parameters have been examined, such as mean roughness height (k_a), root-mean-square height (k_q), maximum peak to valley height (k_t), average peak to valley height (k_z), effective slope (ES), solidarity (λ), skewness (k_{sk}), and kurtosis (k_{ku}) (Musker, 1980; Napoli *et al.*, 2008; Forooghi *et al.*, 2017; Flack *et al.*, 2020; Abdelaziz *et al.*, 2022, among many others). However, none of these parameters has been found to be able to be generally applied to all types of roughness.

1.2 AIMS AND OBJECTIVES

There is a lack of consensus among researchers about how different rough surfaces affect the behaviour of turbulent boundary layer flow and the statistics of the flow. It is not clear at what Reynolds number and relative roughness height these similarities occur. Additionally, there has been less research on turbulent boundary layers over rough surfaces compared to smooth surfaces.

The specific roughness parameters that have the greatest impact on turbulence statistics and drag coefficient in different flow regimes, ranging from hydrodynamically smooth to fully rough, have yet to be determined. A physical roughness length scale that can be directly inferred from a surface's topography has not been established. The roughness scales that have been proposed in the literature are not universally applicable to all types of roughness. Therefore, the current research aims to conduct a series of hotwire experiments to investigate turbulent boundary layer flow over rough surfaces with systematic changes in roughness parameters. The aims and objectives of the present research work are summarised in the following section:

1.2.1 Aims

This research aims to gain a comprehensive understanding of turbulent flow over rough surfaces for various flow regimes, including hydrodynamically smooth to fully rough. It aims to validate the Reynolds independence and Townsend's similarity hypothesis over a wide range of relative roughness (k/δ), where δ is the boundary layer thickness. The research also aims to determine the minimum Reynolds number and maximum k/δ required to achieve the outer layer similarity in lower -and higher-order turbulence statistics. To investigate the roughness parameters that have the greatest impact on turbulence statistics and drag coefficient, a systematic study of variations in roughness parameters will be conducted. Additionally, the research aims to establish a link between the surface's hydraulic length scale and its physical topography in order to better understand how frictional drag is affected by different types of roughness in fluid engineering practice.

1.2.2 Objectives

The objectives of this research are:

- To verify Townsend's similarity hypothesis for rough surfaces across a wide range of δ/k . This will involve examining the impact of different roughness types on the distribution of kinetic energy and the extent to which the turbulent boundary layer is affected.
- To conduct experimental studies of turbulent boundary layers over two-dimensional (2D) and three-dimensional (3D) uniformly distributed rough surfaces with zero pressure gradient at different Reynolds numbers using single hotwire probes. This will involve fabricating various types of 2D uniformly distributed rough surfaces and systematically studying the effects of different roughness parameters on lower-order statistics (mean velocity profiles) and higher-order statistics (skewness, flatness, and energy spectrum) of the turbulent boundary layer and comparing them to smooth wall data in order to identify the dominant roughness parameters that affect turbulence statistics and drag coefficient.
- To develop a general formula that can be used to predict drag based solely on surface roughness topography by analysing all our experiments and previous experiments from the literature. This will involve introducing an appropriate roughness length scale based solely on surface topology in order to provide a method for drag prediction based on surface roughness topography alone.

1.3 THESIS OUTLINE

Chapter 2 provides a brief literature review on the prevailing issues in wall-bounded turbulent shear flows, focusing on zero pressure gradient turbulent boundary layer (ZPG-TBL) flow over rough surfaces, and a summary of the large body of work has been undertaken to address the over-lasting issue of how to predict the frictional drag of any rough surface based solely on its roughness topography. Chapter 3 briefly explains the methodology and the experimental details and techniques used for the experiments. Chapter 4 assesses Townsend’s outer layer similarity hypothesis for 2D surface roughness with a wide range of δ/k . Additionally, a comparison of turbulence statistics of TBL flow over two different 2D roughness geometries is analysed. Chapter 5 emphasises the influence of the effective slope ES and the height skewness k_{sk} on the drag coefficient. Furthermore, provides a new predicted correlation of the equivalent sand grain roughness k_s for different 2D rough wall surfaces. Chapter 6 investigates the effect of streamwise and spanwise effective slopes, ES_x and ES_z of 3D sinusoidal roughness on turbulence statistics and drag coefficient. Chapter 7 investigates the effect of roughness skewness, k_{sk} of 3D sinusoidal roughness on turbulence statistics and drag coefficient. Chapter 8 develops a new predicted correlation of the equivalent sand grain roughness k_s as a function of the major roughness parameters, k_t , ES and k_{sk} for different rough wall surfaces used in the previous chapters. Finally, chapter 9 concludes the findings and summarises the future work that can be explored to add to this work.

Bibliography

- ABDELAZIZ, M., DJENIDI, L., GHAYESH, M. H., & CHIN, R. 2022 A new equivalent sand grain roughness relation for two-dimensional rough wall turbulent boundary layers. *Journal of Fluid Mechanics* **940**, A25.
- COLAGROSSI, A., MARRONE, S., COLAGROSSI, P., & LE TOUZÉ, D. 2021 Da vinci’s observation of turbulence: A french-italian study aiming at numerically reproducing the physics behind one of his drawings, 500 years later. *Physics of Fluids* **33** (11), 115122.
- COLEBROOK, C. F. & WHITE, C. M. 1937 Experiments with fluid friction in roughened pipes. *Proceedings of the Royal Society of London. Series A-Mathematical and Physical Sciences* **161** (906), 367–381.
- DARCY, H. 1857 *Recherches expérimentales relatives au mouvement de l’eau dans les tuyaux*, , vol. 1. Mallet-Bachelier.
- EYRING, V., ISAKSEN, I. S., BERNTSEN, T., COLLINS, W. J., CORBETT, J. J., ENDRESEN, O., GRAINGER, R. G., MOLDANOVA, J., SCHLAGER, H., & STEVENSON, D. S. 2010 Transport impacts on atmosphere and climate: Shipping. *Atmospheric Environment* **44** (37), 4735–4771.
- FLACK, K. A., SCHULTZ, M. P., & BARROS, J. M. 2020 Skin friction measurements of systematically-varied roughness: probing the role of roughness amplitude and skewness. *Flow, Turbulence and Combustion* **104** (2), 317–329.
- FOROOGHI, P., STROH, A., MAGAGNATO, F., JAKIRLIĆ, S., & FROHNAPFEL, B. 2017 Toward a universal roughness correlation. *Journal of Fluids Engineering* **139** (12).

- KUWATA, Y., SUGA, K., & KAWAGUCHI, Y. 2019 An extension of the second moment closure model for turbulent flows over macro rough walls. *International Journal of Heat and Fluid Flow* **77**, 186–201.
- MOODY, L. F. 1944 Friction factors for pipe flow. *Trans. Asme* **66**, 671–684.
- MUSKER, A. J. 1980 Universal roughness functions for naturally-occurring surfaces. *Transactions of the Canadian Society for Mechanical Engineering* **6** (01), 1–6.
- NAPOLI, E., ARMENIO, V., & DE MARCHIS, M. 2008 The effect of the slope of irregularly distributed roughness elements on turbulent wall-bounded flows. *Journal of Fluid Mechanics* **613**, 385–394.
- NIKURADSE, J. 1933 Laws of flow in rough pipes. *Translation from German published 1950 as NACA Tech. Memo. 1292* .
- NUGROHO, B., BAIDYA, R., NURROHMAN, M. N., YUSIM, A. K., PRASETYO, F. A., YUSUF, M., SUASTIKA, I. K., UTAMA, I. K. A. P., MONTY, J. P., HUTCHINS, N., ET AL. 2017 In-situ turbulent boundary layer measurements over freshly cleaned ship-hull under steady cruising. In *Proceeding of International Conference on Ship and Offshore Technology (ICSOT), Royal Institution of Naval Architects (RINA) Conference*.
- UTAMA, I. K. A. P., NUGROHO, B., CHIN, C., HAKIM, M. L., PRASETYO, F. A., YUSUF, M., SUASTIKA, I. K., MONTY, J., HUTCHINS, N., & GANAPATHISUBRAMANI, B. 2017 A study of skin friction drag from realistic roughness of a freshly cleaned and painted ship hull. In *International Symposium on Marine Engineering (ISME)*.

Chapter 2

Literature Review

The objective of this review is to establish a strong basis and enhance comprehension of the ongoing investigation of rough wall turbulent boundary layers by providing the essential context. It furnishes an overview of earlier research and advancements on turbulent boundary layers (TBLs) over smooth and rough surfaces. The review concentrates only on the topics that are pertinent to this study, which involves establishing a direct correlation between the primary roughness parameters and drag. Irrelevant cases are briefly mentioned, and readers are directed to the appropriate sources.

Prior to conducting an extensive literature review, it is beneficial to establish the coordinate system and notations that will be employed throughout this thesis. The streamwise, wall-normal and spanwise directions will be represented by x , y and z respectively. Time-averaged quantities are designated with capital letters (e.g. U denote the average streamwise velocity component). On the other hand, u is used to represent the fluctuation in streamwise velocity, and the superscript ($'$) denotes the root-mean-square (rms) value. Quantities that are normalised by viscous scaling are denoted by the superscript ($^+$). The thickness of the boundary layer is symbolised by δ , and is defined as the distance from the wall to the point at which the mean streamwise velocity reaches 99% of the free-stream velocity.

2.1 WALL-BOUNDED TURBULENT FLOWS

The type of flows that arise when a fluid moves over a solid surface are referred to as wall-bounded flows. This category encompasses canonical flows such as those over a flat plate, as well as those through a channel or pipe. The analytical solutions for fluid motions, as documented by [Anderson \(2005\)](#), have been applied to these flows. The Euler equations, which were derived from Newton's second law and the principle of mass conservation, represented a significant step forward in conceptualising fluid flow. However, it was not until the mid-19th century that viscosity was integrated into this description, resulting in the non-linear partial differential equations now known as the Navier-Stokes equations. In theory, these equations enable us to determine the pressure and velocity fields of a fluid at all points in space.

In a landmark contribution, [Prandtl \(1904\)](#) presented the initial explanation of the boundary layer. The model is based on the no-slip condition at the wall, which implies that the velocity of the fluid in contact with the bounding surface is zero because the molecules are "stuck" to the surface. Far from the surface or wall, the flow is not affected by it and adopts the free-stream velocity U_∞ . The boundary layer is situated between these two boundaries, where the fluid's viscosity acts to slow it down. This layer dominates the interaction between

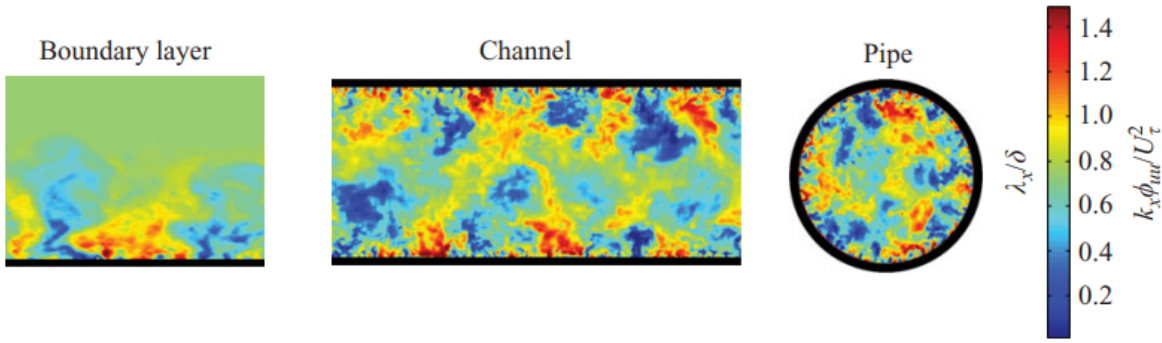


FIGURE 2.1: Cross-sections of flow geometry for turbulent bounded flows with contours of premultiplied energy spectra of streamwise velocity fluctuations. Adapted from [Monty *et al.* \(2009\)](#).

the solid surface and the flow, governing aspects such as the pumping power needed to force gas through pipelines, and the fuel required for planes and ships to overcome drag forces during their movement.

Dimensional analysis of wall-bounded flows leads to the crucial non-dimensional Reynolds number, which is fundamental to characterising turbulent flows. It is expressed as $Re = U_{ch} L_{ch} / \nu$, where U_{ch} represents a characteristic velocity, L_{ch} a characteristic length, and ν the kinematic viscosity of the fluid. The Reynolds number signifies the ratio of inertial forces to viscous forces, and high Reynolds numbers, where inertial forces dominate, are linked to turbulent flows. Although the exact definition of a turbulent flow is ambiguous, [Tennekes *et al.* \(1972\)](#) identifies high Reynolds numbers, irregularity, diffusivity, high levels of fluctuating vorticity, and a dissipative nature as typical characteristics of such flows. Despite their apparent randomness, turbulent wall-bounded flows demonstrate coherent structures and universal scaling, as exemplified by Coles' law of the wall/wake for the turbulent boundary layer ([Coles, 1956](#)). Many articles concur on the similarity between pipe and channel flows, because from locations close enough to the surface, the curvature of the pipe wall is nearly zero ([Tennekes *et al.*, 1972](#)). Consequently, pipes/channels are referred to as “internal” geometries, while boundary layers are called “external.” Figure 2.1 displays the premultiplied energy spectra contours of streamwise velocity fluctuations for the three types of wall-bounded flows from [Monty *et al.* \(2009\)](#). Our primary focus is on ZPG– TBL flows.

2.2 BASIC PRINCIPLES OF SMOOTH WALL TBL

The analysis begins by using the von Kármán integral momentum equation presented in [Jones *et al.* \(2008\)](#),

$$\frac{\tau_w}{\rho} = \frac{\partial}{\partial x} \left[U_\infty^2 \int_0^\infty \frac{U}{U_\infty} \left(1 - \frac{U}{U_\infty} \right) dy \right] + U_\infty \frac{dU_\infty}{dx} \int_0^\infty \left(1 - \frac{U}{U_\infty} \right) dy, \quad (2.1)$$

This equation establishes a relationship between the wall shear stress (τ_w) and different parameters of the fluid flow where ρ is the fluid density. To delve deeper into this equation, two new measures called the displacement thickness (δ^*) and the momentum thickness (θ) are introduced as follows:

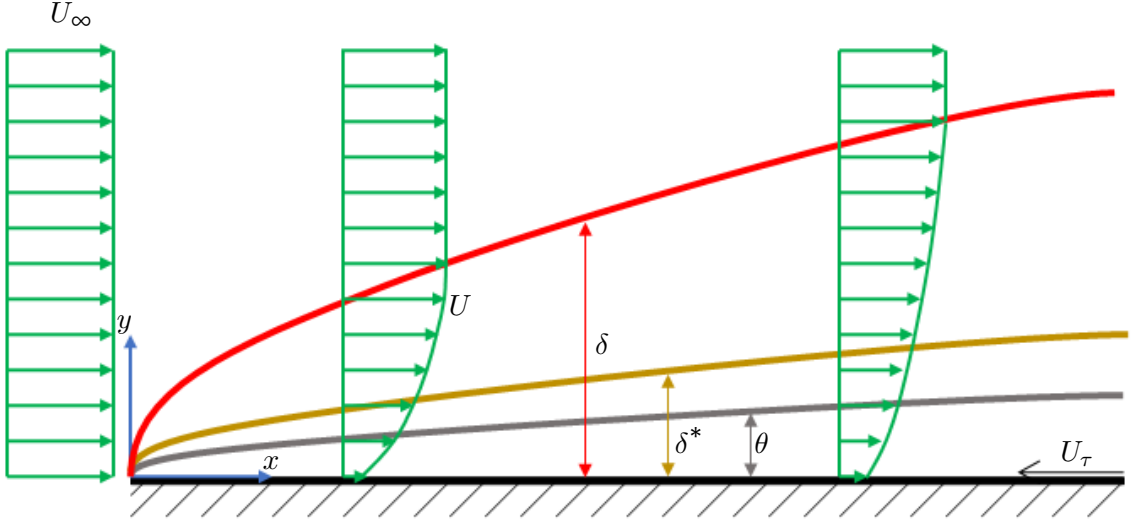


FIGURE 2.2: A simple schematic for developing boundary layer, displacement and momentum thickness of TBL over a flat plate with free-stream velocity, U_∞

$$\delta^* = \int_0^\infty \left(1 - \frac{U}{U_\infty}\right) dy, \quad (2.2)$$

$$\theta = \int_0^\infty \frac{U}{U_\infty} \left(1 - \frac{U}{U_\infty}\right) dy. \quad (2.3)$$

The displacement thickness represents the increase in thickness of the boundary layer caused by the object present in the flow, while the momentum thickness is associated with the transfer of momentum across the boundary layer. The relationship between these two parameters is given by the shape factor (H), which is the ratio of displacement thickness to momentum thickness. Figure 2.2 illustrates a visual depiction of the boundary layer thickness, displacement thickness, and momentum thickness.

2.2.1 Classical description

The mean velocity profile of a turbulent wall-bounded flow can be analysed using dimensional analysis. The profile is influenced by the mean local wall shear stress τ_w , the distance from the wall y , the kinematic viscosity of the fluid ν , and the characteristic large-scale of the wall-bounded geometry δ . δ varies depending on the specific flow, such as being the half-height of the channel for a turbulent channel flow or the radius of the pipe for a turbulent pipe flow. This discussion is generally valid for all canonical flows, but the focus of this thesis is on the TBL. In the region very close to the wall, referred to as the inner region, Prandtl (1925) proposed that the mean streamwise velocity U is influenced by y , ν , and the friction velocity (U_τ), which is defined as $U_\tau = \sqrt{\tau_w/\rho}$. Applying the dimensional analysis to the inner region results in the following relationship:

$$U^+ = \frac{U}{U_\tau} = f(y^+) = f\left(\frac{yU_\tau}{\nu}\right), \quad (2.4)$$

The law of the wall suggests that U_τ and ν/U_τ are the relevant scales for velocity and length, respectively, in the inner region. In contrast, the outer region, which is further from the wall, is influenced by variables including y , U_τ , δ , and U_∞ , as proposed by [von Kármán \(1930\)](#). The relationship between the mean velocity and these variables in the outer region is known as the defect law:

$$U_\infty^+ - U^+ = \frac{U_\infty - U}{U_\tau} = f(\eta) = f\left(\frac{y}{\delta}\right), \quad (2.5)$$

with δ and U_τ respectively the characteristic length and velocity scales in the outer region. A region known as the overlap region was introduced by [Millikan \(1939\)](#). In this region, the derivatives of the velocity defect law for $\eta \ll 1$ and the law of the wall for $y^+ \gg 1$ are collapsed:

$$y^+ \frac{\partial U^+}{\partial y^+} = \eta \frac{\partial (U_\infty^+ - U^+)}{\partial \eta} = \frac{1}{\kappa}, \quad (2.6)$$

where κ is the von Kármán constant. Integration of the two sides of Eq. 2.6 yields:

$$U^+ = \frac{1}{\kappa} \ln y^+ + B, \quad (2.7)$$

$$U_\infty^+ - U^+ = \frac{-1}{\kappa} \ln \eta + A, \quad (2.8)$$

where B is universal constant while A is a parameter which depends on the flow geometry. Equations 2.7 and 2.8 are known as the logarithmic law, which is a widely recognised analytical expression describing the turbulent wall-bounded flows. This law demonstrates the logarithmic relationship between the mean streamwise velocity and the distance from the wall, and as a result, the overlap region is also referred to as the log-region. [Coles \(1956\)](#) adds an additional wake function to cover the defect layer, as follows:

$$U^+ = \frac{1}{\kappa} \ln y^+ + A + \frac{\Pi}{\kappa} \omega(\eta), \quad (2.9)$$

where Π is a profile parameter depends on pressure gradient and ω is the wake function. More recently, [Chauhan *et al.* \(2009\)](#) suggested a complete mean streamwise velocity profile called a composite profile as follows:

$$U^+ = U_{inner}^+ + \frac{2\Pi}{\kappa} \omega(\eta), \quad (2.10)$$

where U_{inner}^+ is a long function of y^+ (see [Chauhan *et al.*, 2009](#), for more details).

After examining the data of mean velocity profiles, [Coles \(1964\)](#) recommended $\kappa = 0.41$ and $A = 5.0$ for Eq. 2.7. However, the literature has debated the value of κ due to the uncertain bounds for the log-region. While classical arguments suggest a fixed fraction of δ for the upper bound and a viscous-scaled wall-normal location y^+ for the lower bound, determining these bounds is difficult due to the slow deviation of the mean velocity profile from Eq. 2.7 ([Marusic *et al.*, 2010](#)). Consequently, there is a wide variation in the estimates for the lower bound in the literature. By analysing the experimental data over a wide range of friction Reynolds number ($2 \times 10^4 < Re_\tau = \delta U_\tau / \nu < 6 \times 10^5$), [Marusic *et al.* \(2013\)](#) suggested that $y^+ > 3\sqrt{Re_\tau}$ and $y/\delta \approx 0.15$ are reasonable approximations for the bounds of the overlap region. Figure 2.3 shows the mean streamwise velocity profile showing the different regions of the profile with the direct numerical simulation (DNS) smooth TBL data from [Chan *et al.* \(2021\)](#) at $Re_\tau \approx 2000$.

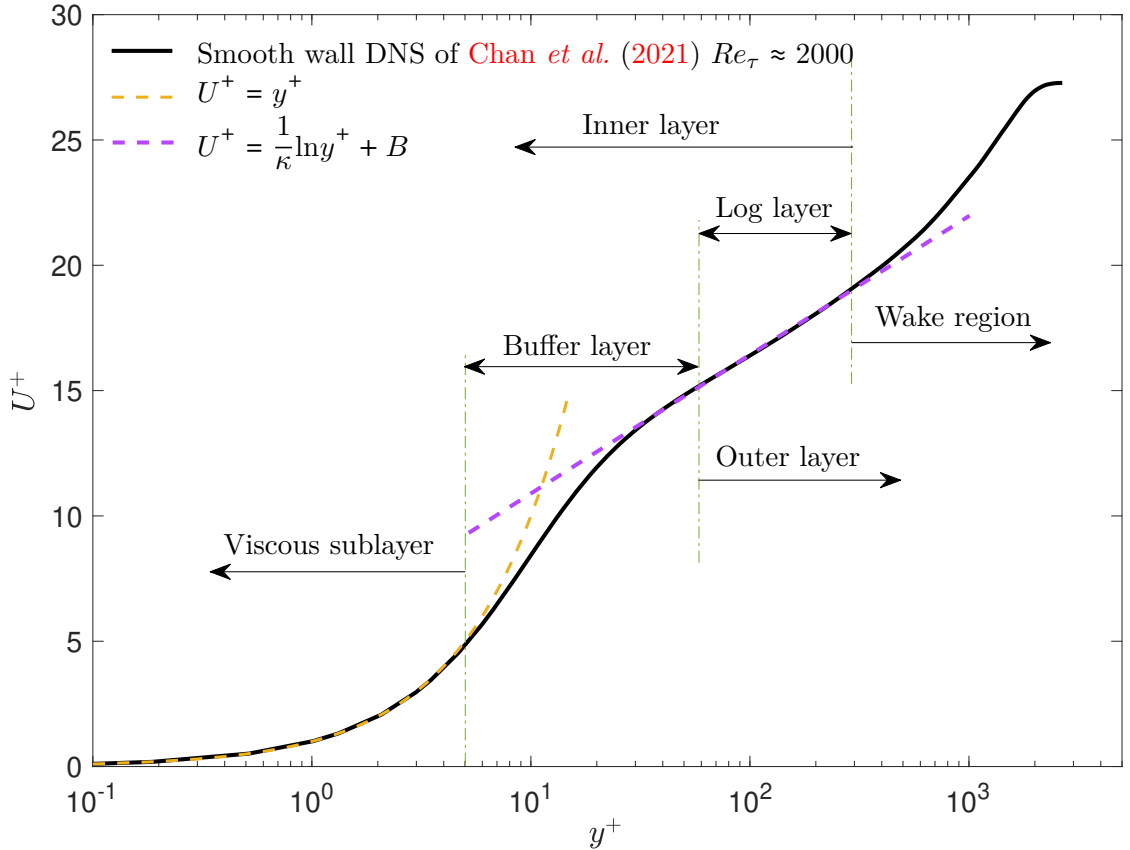


FIGURE 2.3: Mean streamwise velocity profile over smooth surface showing the different regions of the profile with the DNS smooth TBL data from Chan *et al.* (2021) at $Re_\tau \approx 2000$.

2.2.2 Reynolds number similarity

In the study of turbulent shear flows, Townsend (1980) put forward a hypothesis using simple arguments that the turbulence far from the wall in wall-bounded flows can be dependent only on the height of the wall layer and the wall stresses. In channel flows, which can be generalised to other wall-bounded flows, this reasoning suggests that in the region external to the viscous layer, where the effects of the viscous stresses are negligible, the energy input is determined by the pressure gradient whereas in boundary layer flows, advective terms also make a contribution. Neglecting the possibility that the viscous layer may influence the outer flow, it follows that the fully turbulent flow relies only on the height of the wall layer δ and the wall stresses, as shown by U_τ for channels, pipes, and boundary layers. It is important to note that the basis of Townsend's hypothesis is that absolute velocities are not involved, only relative motions in the convecting frame. Although Reynolds decomposed fluctuations are mainly used to scrutinise the hypothesis, the arguments leading to the hypothesis are only relevant across the energy-containing range and do not apply to outer-region motions responsible for the viscous dissipation of energy, nor across different external flow geometries in the low wavenumber range, where the large-scale geometry has an influence.

Empirical support for Townsend's Reynolds number similarity hypothesis in smooth-wall flows is found in a number of studies, although the exact nature and extent of the universality is still under investigation. In turbulent pipe flows, Perry *et al.* (1987) provided evidence for the hypothesis through an analysis of scaling laws for velocity spectra in several overlapping

spectral ranges. Recently, [Kunkel & Marusic \(2006\)](#) presented evidence indicating the similarity of Reynolds numbers in atmospheric boundary layer and pipe flows, particularly at very high Reynolds numbers. However, the scrutiny of Townsend's hypothesis is primarily focused on studies of rough-wall flows, where the hypothesised weak dependence on the wall condition has significant implications. These implications will be discussed in detail in section [2.3](#).

2.2.3 Spectral scaling arguments

In accordance with the scaling arguments presented in subsection [2.2.2](#), [Perry *et al.* \(1986\)](#) utilised such arguments to anticipate the shape of the three velocity components as represented by the velocity spectra. The authors focused on three spectral ranges beyond the viscous layer: the low wavenumber range, where the external flow geometry influences the inactive motions and adheres to Reynolds number similarity for a single type of flow; the intermediate wavenumber range, which comprises active turbulent motions conforming to Townsend's Reynolds number similarity hypothesis; and the high wavenumber range, which involves dissipative motions that are reliant on viscosity. In this thesis, the one-dimensional streamwise spectra are denoted as $\phi_{uu}k_x$, where k_x represents the streamwise wavenumber. Through dimensional analysis of the low and intermediate wavenumber (energy-containing) ranges, the following respective scaling laws were revealed for the streamwise velocity component.

$$\frac{\phi_{uu}(k_x\delta)}{U_\tau^2} = \frac{\phi_{uu}(k_x)}{\delta U_\tau^2} = f_L(k_x\delta), \quad (2.11)$$

$$\frac{\phi_{uu}(k_x y)}{U_\tau^2} = \frac{\phi_{uu}(k_x)}{y U_\tau^2} = f_I(k_x y). \quad (2.12)$$

In the context of high wavenumbers, [Kolmogorov \(1991\)](#) suggested that turbulent fluctuations become locally isotropic and are unaffected by large-scale flow characteristics. Consequently, the energy spectra in this range should adhere to the Kolmogorov length and velocity scales, as these are the only relevant scales.

$$\frac{\phi_{uu}(k_x\eta_K)}{v^2} = \frac{\phi_{uu}(k_x)}{v^2\eta_K} = f_H(k_x\eta_K), \quad (2.13)$$

where η_K is the Kolmogorov length scale and v is the velocity scale. The values of both the Kolmogorov length and velocity scales rely on the average turbulent energy dissipation, denoted as ϵ_d , and the kinematic viscosity, denoted as ν . These scales can be defined as follows:

$$\eta_K = \left(\frac{\nu^3}{\epsilon_d} \right)^{0.25}, \quad (2.14)$$

$$v = (\nu\epsilon_d)^{0.25}. \quad (2.15)$$

Let us consider the possible regions of overlap between the three spectral ranges mentioned earlier. In the overlapping region between the low and intermediate wavenumbers, denoted by LI (refer to Figure [2.4](#)), both equations [2.11](#) and [2.12](#) hold. Hence, f_L and f_I follow the scaling behaviour expressed by:

$$f_L(k_x\delta) = \frac{A_{LI}}{k_x\delta}, \quad (2.16)$$

or

$$f_I(k_x y) = \frac{A_{LI}}{k_x y}, \quad (2.17)$$

where A_{LI} is a universal constant. This scaling behaviour is commonly known as k_x^{-1} scaling. Similarly, in the IH region, equations 2.12 and 2.13 hold. Assuming that the movements in this region are in approximately local equilibrium (i.e., active movements external to the viscous layer), f_I and f_H follow the scaling behaviour expressed by equations:

$$f_I(k_x y) = \frac{K_0}{\kappa^{2/3} (k_x y)^{5/3}}, \quad (2.18)$$

or

$$f_H(k_x \eta_K) = \frac{K_0}{(k_x \eta_K)^{5/3}}, \quad (2.19)$$

where K_0 is the universal Kolmogorov constant. The scaling behaviour of equations 2.17 and 2.18 is commonly referred to as Kolmogorov's $k^{-5/3}$ scaling. The various u spectral regions are depicted in Figure 2.4.

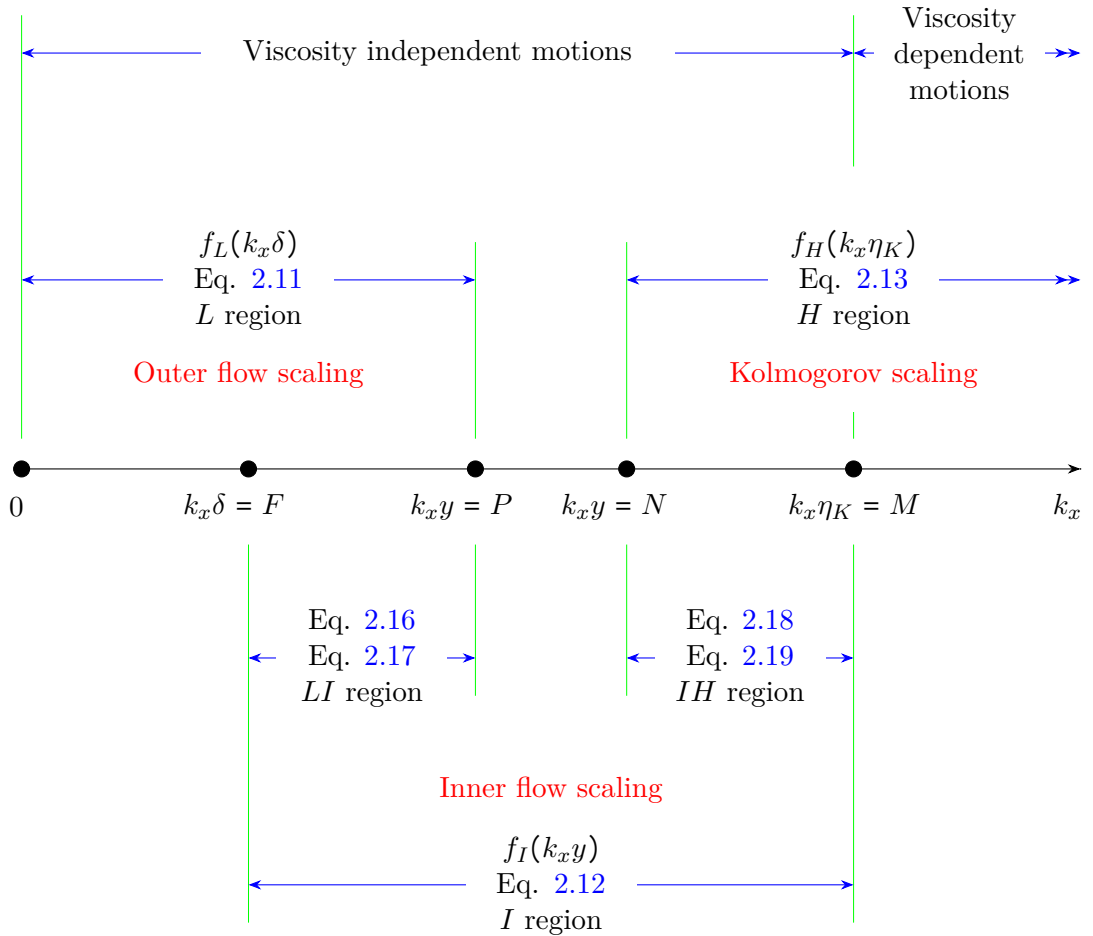


FIGURE 2.4: Different spectral regions of u in TBL. Adapted from Perry *et al.* (1986)

2.2.4 Taylor’s frozen turbulence hypothesis

In investigations of turbulent flows, a common practice is to interchange temporal and spatial flow descriptions by utilising the hypothesis suggested by [Taylor \(1938\)](#), known as the Taylor hypothesis. The Taylor frozen hypothesis is a fundamental concept in fluid mechanics that relates temporal and spatial flow descriptions in turbulent flows. The hypothesis suggests that if a probe is stationary within a turbulent flow, the temporal signal recorded by the probe can be viewed as the result of a spatial pattern of turbulence that is advecting past the probe at a constant mean speed, known as the characteristic convection velocity (U_c). The term “frozen” turbulence is used because it implies that the spatial pattern of turbulence is stationary with respect to the probe, and the temporal variations of the flow are solely due to the movement of this pattern.

The mathematical representation of the Taylor frozen hypothesis is $u(x, t) = u(x - U_c t, 0)$, where $u(x, t)$ is the fluctuating velocity at position x and time t , and U_c is the characteristic convection velocity. This equation suggests that the temporal and spatial variations of the velocity are related, and the temporal signal can be converted into a spatial flow description by using the characteristic convection velocity.

While the Taylor hypothesis was originally proposed for U_c equal to the mean velocity of the flow, more recent studies have shown that U_c can be a function of both the wall-normal location and the scale of the turbulence structure ([Atkinson *et al.*, 2015](#); [Drózdź *et al.*, 2023](#)). The Taylor frozen hypothesis is a crucial concept in fluid mechanics, as it provides a means of relating temporal and spatial flow descriptions and allows for the analysis of complex turbulent flows. Taylor’s hypothesis was initially proposed for grid turbulence in a uniform flow, and its effectiveness in this scenario has resulted in its widespread adoption in shear flows. Nonetheless, there has been extensive debate concerning whether its application in shear flows is appropriate.

[Lin \(1953\)](#) investigated the different terms in the Navier-Stokes equation and showed that extending Taylor’s hypothesis to shear flows is not generally justifiable. According to Lin’s analysis, the Taylor frozen hypothesis can only be applied when the Reynolds number is sufficiently high, the turbulence intensity is small, and the main flow is uniform. In the case of shear flows, it is suggested that there is a limited basis for utilising the hypothesis, but only for small wavelengths (λ_x) and at positions where $y/\delta > 0.2$, with the limitations becoming increasingly restrictive as the distance from the wall reduces.

[Fisher & Davies \(1964\)](#) employed filtered space-time correlations of axial velocity in the mixing region of a jet to estimate convection velocity. [Fisher & Davies \(1964\)](#) found that significant discrepancies between the convection velocity and the local mean velocity arise in areas where turbulence fluctuations are large. Additionally, the measured convection velocity was observed to be a function of frequency. These observations indicate that the scale-dependence of the convection velocity, even when disregarding errors caused by energetic temporal fluctuations, can result in substantial inaccuracies when applying Taylor’s hypothesis using the mean velocity.

[Lumley \(1965\)](#) evaluated the potential sources of error in the application of Taylor’s hypothesis and established criteria that ensure the effect of fluctuating convection velocity is the only factor present. Lumley’s criteria are applicable for high frequencies that lie beyond the energy-containing range. Corrections were also introduced to account for the effect of convection velocity fluctuations within this frequency range.

[Zaman & Hussain \(1981\)](#) investigated the agreement between actual spatial distributions of large-scale coherent motions generated by a controlled jet excitation and those predicted using Taylor’s hypothesis. [Zaman & Hussain \(1981\)](#) found that for an isolated coherent structure, the

hypothesis was accurate when the structure center velocity was used. However, when using the local time-averaged or instantaneous streamwise velocity, significant distortions were observed. [Zaman & Hussain \(1981\)](#) also noted that the presence of structure interactions during advection made it impossible to deduce a successful convection velocity.

According to [Cenedese *et al.* \(1991\)](#); [Romano \(1995\)](#), using two-point laser doppler anemometry measurements, a frequency-dependent convection velocity is needed to accurately convert between temporal and spatial descriptions of the flow. They also found that when characterised in this way, Taylor’s hypothesis can generally be applied in wall-bounded flows, except for very close to the wall, provided that the standard deviation of the streamwise velocity fluctuations is less than 30% of the local streamwise velocity. Similarly, [Lee *et al.* \(1992\)](#) reported a threshold of $\sqrt{u^2}/U < 0.15 - 0.25$ for Taylor’s hypothesis to be suitable for incompressible isotropic turbulent flow, using a similar convection velocity quantification.

[Dennis & Nickels \(2008\)](#) investigate the applicability of Taylor’s hypothesis to long structures, with a focus on its validity in wall-bounded flows. Using time-resolved wall-parallel planar PIV measurements at $y/\delta = 0.16$, they show that the convection velocity is similar to the mean streamwise velocity at this location. [Dennis & Nickels \(2008\)](#) demonstrate that the accuracy of Taylor’s hypothesis decreases linearly with streamwise projection distance and suggest that for large streamwise motions, the hypothesis can be applied with reasonable accuracy for projection distances up to 6δ . Furthermore, recent numerical simulations support the idea that the hypothesis is appropriate for large-scale motions, contrary to the early studies of [Lin \(1953\)](#); [Lumley \(1965\)](#).

[Del Alamo & Jiménez \(2009\)](#) examine the validity of the frozen turbulence approximation by studying the correlation coefficient of spatial and temporal derivatives. They use DNS data from turbulent channels to show that only short, wide eddies in the viscous sublayer and eddies with certain wavelengths can be approximated as frozen, and that these eddies are strongly correlated across the wall-layer and affect the convection velocity accordingly.

Several semi-empirical expressions for $U_c(\lambda_x)$ have been suggested, as it can enhance the precision of spatial estimates from temporal measurements by accounting for the scale-dependent convection velocity. (see, for example, [Del Alamo & Jiménez, 2009](#)). Despite the usefulness of accounting for scale-dependent convection velocity in improving the accuracy of spatial approximations from temporal measurements, the use of Taylor’s original hypothesis, $U_c = U(y)$, which assumes a constant convection velocity equal to the local mean velocity, is still reasonable for the outer layer of a smooth-wall turbulent boundary layer. Nonetheless, it is important to note that temporal fluctuations in a frame advecting at this mean scale-dependent velocity can still introduce additional errors. This choice of hypothesis is used in this thesis since the main focus of the research is on the outer layer of smooth and rough wall flows.

2.3 PRINCIPLES OF ROUGH WALL TBL

In fluid mechanics, the smoothness or roughness of a surface is not determined by its size in microns, but rather by its impact on the adjacent flow. For turbulent flows, a surface is considered rough if its topographical features are large enough to interfere with the smallest eddies near the wall, leading to alterations in the transfer of momentum, heat and mass. In practical terms, this translates to topographical features greater than approximately $10\ \mu\text{m}$ on container ship hulls and passenger aircraft, $1\ \mu\text{m}$ on gas turbine blades, and $0.1\ \text{mm}$ on atmospheric surfaces ([Chung *et al.*, 2021](#)). The study of turbulent boundary layers over rough walls has practical significance and can offer insight into the influence of wall boundary conditions

on turbulence structure. However, uncertainties exist in understanding how rough surfaces affect turbulent quantities and boundary layer structure. The challenges associated with obtaining measurements in rough-wall flows contribute to this uncertainty. High turbulence intensities and large flow angles, especially near the wall, can lead to errors that are difficult to detect and correct. The estimation of wall friction velocity, U_τ , poses a particular challenge in rough-wall flows, as many direct techniques are not feasible. Despite the fact that wall drag is generally significant in rough-wall flows and comprises both a frictional and a pressure component, the standard smooth-wall approaches to determining U_τ rely on assumptions about the flow that lack validation for rough walls. Additionally, defining the origin of the wall-normal location is ambiguous and varies spatially.

Hagen (1854) and **Darcy (1857)** were the first to investigate the effects of roughness on turbulent flows, discovering that it resulted in increased pressure drop due to heightened drag force and blockage effects. The formation of the boundary layer over surfaces plays a crucial role in transport phenomena such as heat and momentum transfer. The roughness of these surfaces can significantly impact the boundary layer flow, thereby influencing heat and momentum transfer over the fluid-surface interface. In the study of roughness effects on turbulent boundary layers, some of the earliest investigations were carried out by **Nikuradse (1933)** who examined pipe flows with graded sand on the pipe wall. The sand grain size was varied, and measurements of pressure drop and bulk velocity were obtained to determine the coefficient of friction (C_f) which is a dimensionless measure of friction losses in the pipe. This coefficient can be calculated as $C_f = 2\tau_w / \rho U_\infty^2$. Further research on rough surfaces was conducted by **Colebrook & White (1937)**, who used commercial pipes with roughness to establish an empirical relationship between the relative roughness, $k/2R_p$, where R_p is the pipe radius, and the coefficient of friction. This culminated in the Moody chart (**Moody, 1944**), which is still widely used in engineering applications and textbooks to estimate the coefficient of friction of various rough surfaces.

2.3.1 k -type and d -type Roughness

Rough-wall flows can be divided into two categories depending on how the mean velocity responds to the roughness. The designations k -type and d -type roughness pertain to two-dimensional roughness, such as spanwise ribs and grooves. **Perry et al. (1969)** introduced the concept of distinguishing between k -type and d -type roughness, based on their observation of flow behaviour resembling the conventional Clauser or Nikuradse scheme for some rough surfaces. For k -type flows, the increment in drag reflected by the mean profile is solely a function of the characteristic roughness height, k_{ch} . In recent times, the term k -type has been extended to describe any flow that exhibits such a dependence on any characteristic roughness length scale (**Raupach et al., 1991**). The flow separation in the k -type flows is strong and the eddies generated by the roughness elements interact with the flow above. Conversely, for d -type roughnesses, the elements are closely spaced, and the flow skims over the roughness elements, with stable vortices being trapped in the grooves. The drag increment is independent of k and is determined by the streamwise roughness spacing, s_x . **Perry et al. (1969)** suggest that in d -type flows, a significant portion of the cavity flow within and around the roughness elements is separated and hence isolated from the primary flow, so that the length scale determining the effective height of the roughness is not k solely but k and s_x . The depicted diagram in Figure 2.5 presents a representation of two distinct types of flow pattern, whereby the distinction is dependent upon the ratio of roughness spacing-to-height. In the case of k -type roughness, illustrated in Figure 2.5 (a), the presence of separation and reattachment zones within the cavity generates a pronounced interaction between the surface roughness and the outer layer flow. Conversely, the

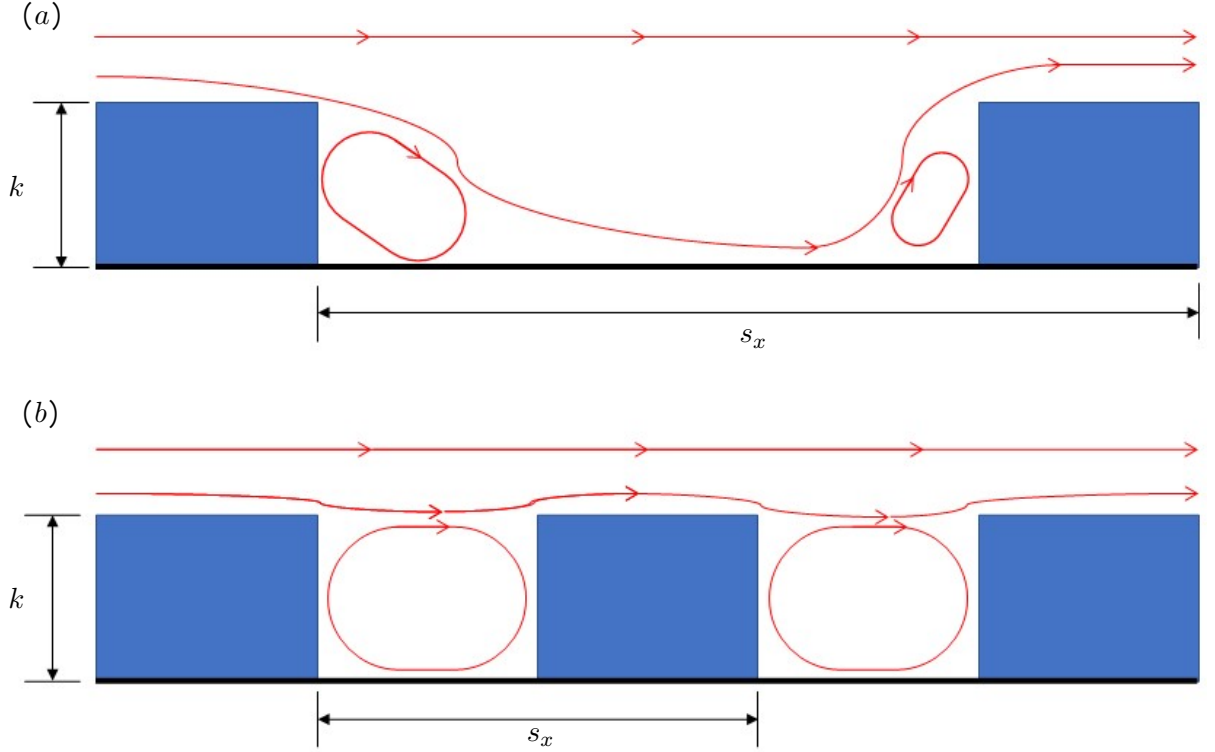


FIGURE 2.5: A schematic of different regimes of the mean flow over 2D roughness (a) *k*-type roughness, (b) *d*-type roughness.

d-type roughness illustrated in Figure 2.5 (b) yields separated vortices that envelop the gaps between the roughness elements.

However, more recent studies have suggested that the explanations for these observations are likely to be more complex. Coleman *et al.* (2007) conducted experiments to investigate flow structures within cavities between consecutive ribs of uniform cross-section. They classified three types of roughness based on the pitch ratio s_x/k , which is the distance between ribs s_x divided by the height of ribs k . The three types of roughness were the *d*-type, intermediate type, and *k*-type. According to Coleman *et al.* (2007), closely spaced *d*-type roughness creates stable separated eddies that occupy the entire cavity between ribs with minimal impact on the outer flow. In contrast, for widely spaced *k*-type roughness, reattachment occurs before the next rib, and eddies are shed from the roughness and penetrate to the boundary-layer edge. The transition from *d*-type flow to interactive *k*-type flow occurs smoothly at a rib spacing of $s_x/k = 5$. Djenidi *et al.* (1994); Leonardi *et al.* (2004) have shown that the flow structure within the cavities changes depending on the Reynolds number, and that the characteristics of *d*-type flows change depending on the relative magnitudes of the pressure drag and frictional drag. Jiménez (2004) introduced the concept of roughness solidity λ to differentiate between *k*-type and *d*-type roughness in which the solidity is the ratio of the total projected frontal roughness area to the wall-parallel projected area. Jiménez (2004) identified two flow regimes based on roughness solidity, namely the sparse regime and dense regime. In the sparse regime, where the solidity is less than $\lambda \approx 0.15$, the roughness impact increases with solidity; however, in the dense regime, it decreases as the roughness elements block each other. Other researchers have also reported the existence of these two regimes. Jiménez (2004) found that *k*-type roughness falls under the sparse regime while *d*-type roughness belongs to the dense regime. In this thesis, we focus on rough surfaces that are clearly classified as *k*-type, Hence, the following discussions will

also concentrate on studies of k -type flows.

2.3.2 Classical description

The study of turbulent boundary layer flow over rough surfaces involves an additional length scale associated with the roughness (Hama, 1954). The classical analysis of k -type rough-wall flows is similar to that of smooth-wall flows, with the added complexity of surface roughness. Dimensional analysis of the mean flow in the near-wall region reveals an equation that is analogous to Prandtl's law of the wall for smooth-wall flows.

$$U^+ = \frac{U}{U_\tau} = f(y^+, k^+, \dots) = f\left(\frac{(y + \epsilon)U_\tau}{\nu}, \frac{kU_\tau}{\nu}, \dots\right). \quad (2.20)$$

This equation includes the characteristic height of the roughness, other relevant roughness scales, and a term to account for the displacement of the flow by the roughness named the origin offset (ϵ). The viscous length scale is used as the normalising length scale to maintain generality across both smooth and rough walls. The equation 2.5 remains unaltered in the outer region of the flow, however, the ϵ term is added to the wall-normal position:

$$U_\infty^+ - U^+ = \frac{U_\infty - U}{U_\tau} = f(\eta) = f\left(\frac{y + \epsilon}{\delta}\right). \quad (2.21)$$

Using the same approach as described in subsection 2.2.1, the logarithmic law for rough-wall turbulent boundary layers can be derived as follows:

$$U^+ = \frac{1}{\kappa} \ln(y + \epsilon)^+ + C(k^+, \dots). \quad (2.22)$$

However, in this case, the additive constant is influenced by surface roughness parameters. The modified version of the smooth-wall logarithmic law is commonly used to formulate the rough-wall logarithmic law, as follows:

$$U^+ = \frac{1}{\kappa} \ln(y + \epsilon)^+ + A - \Delta U^+. \quad (2.23)$$

The roughness-dependent term ΔU^+ , referred to as the Hama roughness function (Hama, 1954), indicates the increase in rough-wall drag relative to smooth-wall drag. When the surface is smooth, $\Delta U^+ = 0$ and $\epsilon = 0$, and the smooth-wall logarithmic law is recovered. The roughness geometry, typically the roughness height, has a direct effect on ΔU^+ , and various studies have attempted to establish a relationship between them.

The rough-wall layer anatomy is similar to that of the smooth-wall flow, as shown in Figure 2.3. The viscous region is replaced by the roughness sublayer in the vicinity of the roughness elements. The roughness sublayer, which is influenced by the length scales associated with the roughness elements, is typically considered to extend a few roughness heights ($\approx 5k$) above the roughness (Raupach *et al.*, 1991). The extent of the viscous wall effects may be restricted to the roughness sublayer, or it may extend beyond it, depending on the specific roughness being examined. As a result, the boundaries of the various classical layers that make up rough-wall flows are not as well-defined as those for smooth walls. The form of the velocity defect in the overlap region remains unchanged in accordance with the classical rough-wall arguments. Figure 2.6 shows the mean streamwise velocity profile over a rough surface showing the different regions of the profile with the DNS smooth TBL data from Chan *et al.* (2021) at $Re_\tau \approx 2000$.

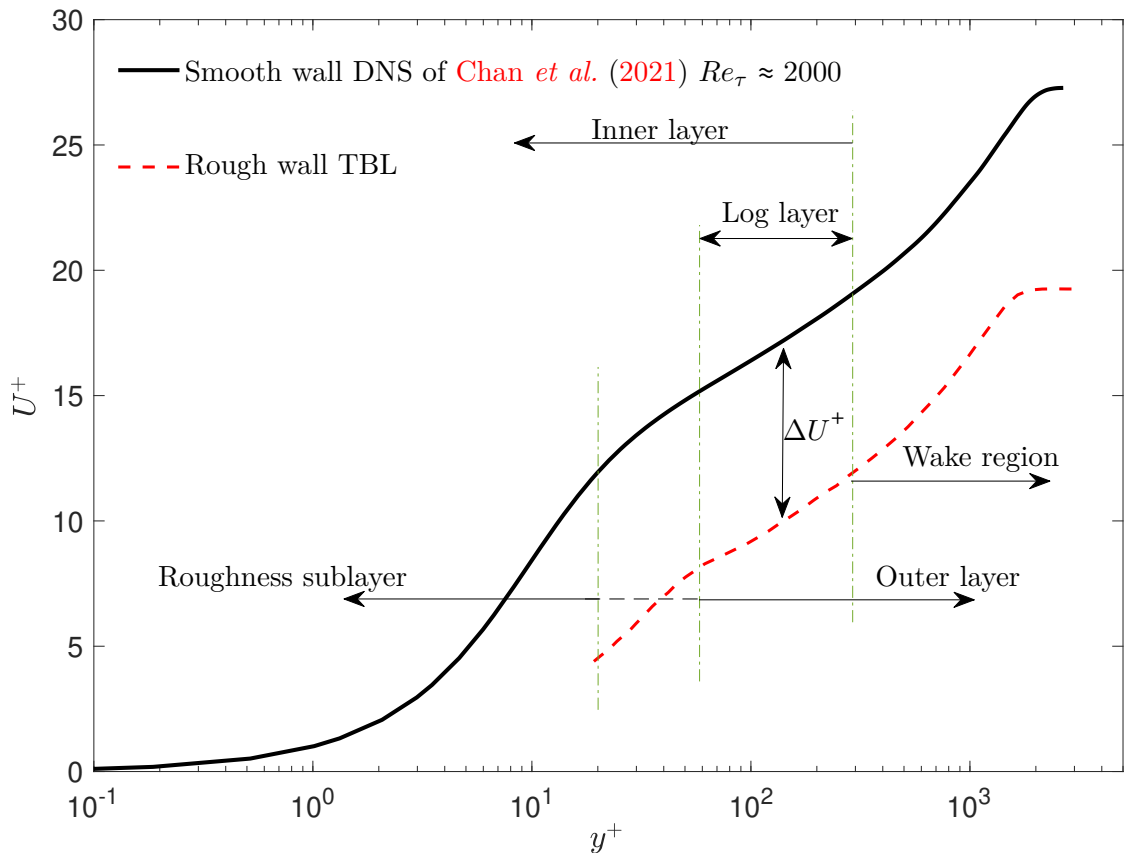


FIGURE 2.6: Mean streamwise velocity profile over rough surface showing the different regions of the profile with the DNS smooth TBL data from Chan *et al.* (2021) at $Re_\tau \approx 2000$.

2.3.3 Outer layer similarity

Regarding turbulence in the presence of a rough wall, Townsend (1980) makes the following statement:

“At distances from the wall large compared with the extent of the flow patterns set up by individual roughness elements, the turbulent flow is unlikely to be affected by the exact nature of the roughness and, as with the smooth wall, it will be determined by the averaged wall stresses, the channel width (or more generally, δ , the layer thickness) and the fluid viscosity.”

The proposition indicates that the effects of modifications near the wall do not have a significant impact on the dynamics of the outer layer and has therefore been extensively studied in rough-wall flows, where it is typically known as the wall similarity hypothesis.

The primary test for wall similarity is comparing the outer region of a rough-wall statistic for different surfaces. Townsend’s hypothesis only applies outside the region where wall perturbations directly affect the flow, i.e., the roughness sublayer. Certain roughness arrangements, such as large wall-parallel length scales or high degrees of anisotropy, can generate significant motions that penetrate deep into the wall layer, even when the roughness height is small (Anderson *et al.*, 2015; Nugroho *et al.*, 2013).

Numerous experimental and numerical studies in the literature have provided evidence for wall similarity in the boundary layer over rough surfaces (e.g. Perry *et al.*, 1969; Ligrani &

Moffat, 1986; Perry *et al.*, 1987; Perry & Li, 1990; Flack *et al.*, 2005; Schultz & Flack, 2005; Kunkel & Marusic, 2006; Flack *et al.*, 2007; Schultz & Flack, 2007; Volino *et al.*, 2007). However, a significant number of studies have also reported a lack of similarity between the outer layers of flows over smooth and rough surfaces (e.g. Furuya *et al.*, 1976; Tani *et al.*, 1987; Krogstad *et al.*, 1992; Krogstad & Antonia, 1994, 1999; Keirsbulck *et al.*, 2002; Lee & Sung, 2007; Castro *et al.*, 2013).

It is suggested by Jiménez (2004) that discrepancies in previous studies concerning Townsend’s hypothesis could be due to the use of large relative roughness heights (k/δ), which can cause the roughness sublayer to occupy a significant portion of the boundary layer. To address this issue, Jiménez (2004) proposes well-controlled experiments in fully-rough flow regimes with ($k_s^+ > 100$) and ($\delta/k > 40$) to clarify the validity of Townsend’s hypothesis. The author suggests that the experiments should be carried out at a minimum friction Reynolds number of 4000 to satisfy both requirements.

In some studies, (i.e. Efros & Krogstad, 2011), it is suggested that $\delta/k > 130$ is necessary for observing wall similarity, which requires a friction Reynolds number of over 10,000. Additionally, Jiménez (2004) has compiled data from previous studies and argues that there is a need for measurements in transitionally rough flows with a low relative roughness height. This thesis aims to address these questions by presenting high-quality data across a broad range of roughness and friction Reynolds numbers, targeting the regimes identified as being sparsely populated by existing data.

2.3.4 Roughness function

A convenient and intuitive way to describe the log-law intercept is through the roughness function ΔU^+ , defined independently by Hama (1954) and given by the shift at matched y^+ of the rough-wall log law (Eq. 2.22) relative to that of the smooth wall (Eq. 2.7):

$$\Delta U^+ = \frac{1}{\kappa} \ln k^+ + B - C, \quad (2.24)$$

where C is constant and equals 8.5 for Nikuradse sand grain roughness in the fully rough regime. In rough-wall flows, the roughness function ΔU^+ quantifies the increase in drag due to surface roughness, and is therefore indicative of the drag penalty relative to a smooth wall. It also represents the difference in coefficient of friction between smooth and rough walls at the same matched Reynolds number Re_τ . This function is particularly useful in scaling up experimental or numerical data obtained at lower outer Reynolds numbers and in specific geometries to predict drag at higher Reynolds numbers and in other geometries. However, it should be noted that at low Re_τ and low δ/k , the distorted log region is not fully formed, leading to some Re_τ dependence in ΔU^+ , as observed by Chan *et al.* (2015) and may overestimate ΔU^+ .

2.3.5 Equivalent sand grain roughness height, k_s

The concept of the equivalent sand grain roughness is a fundamental component of hydraulic engineering and has its roots in the early studies of open channel flow. In the early 19th century, hydraulic engineers sought to understand the relationship between the characteristics of a river or channel and the flow of water within it. One of the key parameters in these studies was the roughness of the channel bed, which was known to influence the rate of flow and the amount of sediment transport. One of the earliest attempts to quantify roughness was made by the American engineer Robert Manning, who developed an empirical formula for computing the flow

rate in an open channel as a function of the channel slope, cross-sectional area, and roughness. Manning *et al.* (1890) introduced a coefficient, known as the Manning roughness coefficient, which was intended to capture the effects of the bed roughness on flow. However, the value of the coefficient was based largely on trial and error, and it was not until later that attempts were made to relate it to physical properties of the bed material.

The French engineer Emile Bazin developed a similar formula to Manning’s, but with a roughness coefficient that was intended to be more physically based. Bazin proposed that the roughness coefficient should be proportional to the size of the bed material, and he developed a series of experiments to determine the relationship between the coefficient and the size of the sand grains in a riverbed. Bazin’s work was later extended by the French engineer Albert Darcy, who developed a formula for the friction factor in a pipe flow that was based on the roughness of the pipe wall. Darcy (1857) relates the pressure or head loss resulting from friction along a specific pipe length to the mean velocity of an incompressible fluid flow.

The concept of the equivalent sand grain roughness was first introduced by German hydraulic engineer, Johann Nikuradse, in the 1930s. Nikuradse was interested in understanding the behavior of turbulent flow in pipes, and he believed that surface roughness played an important role in determining the nature of that flow. He set out to conduct a series of experiments to measure the effect of surface roughness on the frictional resistance of fluid flow in pipes. Nikuradse (1933) used sandpaper to create a range of different surface roughnesses on the interior walls of pipes. He then pumped water through these pipes and measured the frictional resistance of the flow at different Reynolds numbers. Nikuradse (1933) found that the friction factor increased as the surface roughness increased. This observation became known as the Nikuradse experiment.

Nikuradse’s experiments revealed that the relationship between surface roughness and friction factor could be described by a single parameter known as the equivalent sand grain roughness. This parameter represented the height of an imaginary layer of sand grains that would create the same level of surface roughness as the actual rough surface of the pipe. Nikuradse found that the equivalent sand grain roughness varied depending on the type of surface roughness used, but typically ranged from 1 to 5 times the height of the actual roughness. The concept of the equivalent sand grain roughness was later refined and expanded upon by other researchers. In particular, the British mathematician, Lewis Moody, led to the development of a widely used empirical formula for calculating the friction factor in pipes, known as the Moody chart Moody (1944). The Moody chart shown in Figure 2.7 uses the equivalent sand grain roughness as a parameter to account for the effects of surface roughness on frictional resistance.

2.3.6 Rough flow regimes

In the study of fluid dynamics, the presence of roughness on the wall modifies the law of the wall used to describe the viscous sublayer. To describe this phenomenon, the roughness Reynolds number k_s^+ is defined as $k_s^+ = k_s U_\tau / \nu$. Based on the roughness Reynolds number, three distinct roughness regimes are identified, each corresponding to a different region of the wall affected by the turbulent boundary layer. These regimes are hydraulically smooth, transitionally rough, and fully rough regimes. The onsets of the transitionally rough and fully rough regimes are defined as $k_{s-Smooth}^+$ and $k_{s-Rough}^+$, respectively, and their different reported values in the literature can be found in Table 2.1. The hydraulically smooth regime occurs when $k_s^+ < k_{s-Smooth}^+$, in which the roughness elements are entirely embedded in the viscous sublayer, and skin friction and drag coefficient remain unmodified. The transitionally rough regime occurs when $k_{s-Smooth}^+ < k_s^+ < k_{s-Rough}^+$, where the influence of the surface roughness is complex, and both viscous and pressure forces affect the skin friction and drag coefficient. The fully rough regime occurs when

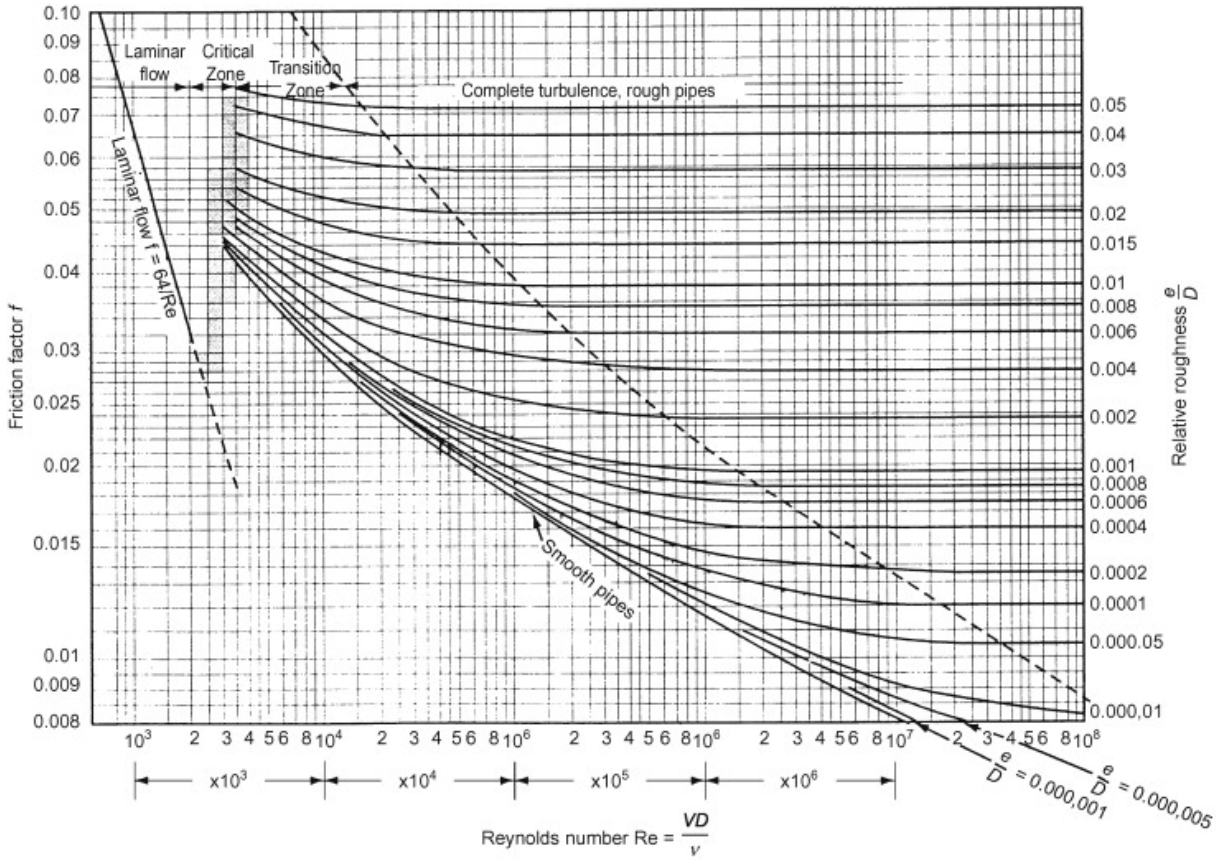


FIGURE 2.7: Moody chart for calculation of the friction factor in pipe flows [Moody \(1944\)](#).

$k_s^+ > k_{s-Rough}^+$, where the rough elements protrude into the fully turbulent region, destroying the viscous sublayer, and shifting the logarithmic profile downwards. In this regime, the friction drag significantly increases due to the pressure force on the roughness, and the pressure loss becomes independent of the molecular viscosity of the fluid and velocity.

Estimating the drag of rough surfaces is a challenging task due to the unique properties exhibited by each rough surface in terms of $\Delta U^+ f(k_s^+)$. The skin friction and drag coefficients of the flow regimes are influenced by both viscous and pressure forces. The transitional rough regime has a complex behaviour that can manifest as either critical (on-or-off) behaviour, similar to the Nikuradse-type roughness function, or gradual behaviour, similar to the Colebrook-type roughness function, as shown in [Figure 2.8](#).

[Bradshaw \(2000\)](#) presented a theoretical explanation for the difference between Nikuradse-type and Colebrook-type behaviours based on the Oseen solution for individual roughness elements ([Oseen, 1910](#)). However, recent research indicates that irregular surfaces with multiple scales of roughness more closely follow Nikuradse-type (critical onset) behaviour than Colebrook-type behaviour. This has been observed in various surfaces, such as honed surfaces, commercial steel pipes, painted and sanded surfaces, grit-blasted surfaces, and even sparsely biofouled surfaces. These surfaces exhibit sudden departure from the hydraulically smooth regime, and many also show inflectional C_f behaviour in the transitionally rough regime ([Shockling et al., 2006](#); [Langelandsvik et al., 2008](#); [Flack et al., 2012, 2016](#); [Monty et al., 2016](#)). When the roughness height, k_s^+ , becomes large, the contribution of the viscous stress to skin friction becomes insignificant compared to the form drag on individual roughness elements. Both Nikuradse-type and Colebrook-type roughness approach the fully-rough asymptote, as demonstrated in [Figure 2.8](#).

Regarding ΔU^+ , the fully rough asymptote is expressed as follows according to [Ligrani & Moffat \(1986\)](#):

$$\Delta U^+ = \frac{1}{\kappa} \log(k_s^+) + B - 8.5. \quad (2.25)$$

2.3.7 k_s Predictive correlations based on roughness parameters

The current impediment to producing comprehensive prognostications of drag is attributed to the absence of a validated technique for assigning k_s based exclusively on topographical characteristics. Consequently, numerous investigations have been focused on establishing a connection between topographical traits and k_s . The primary objective of this research is to develop a universal model or correlation that can effectively capture the behaviour of rough surfaces encountered in different applications. This challenge boils down to the question of which topographical characteristics influence the flow and what minimum set of these features would be necessary to estimate the drag of a surface. In this section, we will concentrate on the earlier studies that have been carried out to tackle the problem of attributing k_s exclusively on the basis of topographical characteristics.

Numerous studies have been conducted in the past few decades to address the issue of identifying the dominant surface parameters that affect friction drag. Various surface parameters have been investigated, including mean roughness height (k_a), root-mean-square roughness

TABLE 2.1: Previous research on the onsets of transitionally rough and fully rough regimes

Authors and year	Roughness type	Range
Nikuradse (1933)	Sand grain	$5 < k_s^+ < 70$
Schlichting & Kestin (1961)	Sand grain	$5 < k_s^+ < 70$
Cebeci & Bradshaw (1977)	Sand grain	$2.25 < k_s^+ < 90$
Lewkowicz & Musker (1978)	Ship hull roughness	$2.25 < k_q^+ < 90$
Ligrani & Moffat (1986)	Sand grain	$2.25 < k_s^+ < 90$
	Uniform spheres	$15 < k_s^+ < 55$
Bandyopadhyay (1987)	k -type roughness	$f(Re_\tau, s_x/k) < k_t^+ < f(Re_\tau, s_x/k)$
Shockling <i>et al.</i> (2006)	Honed pipes	$3.5 < k_s^+ < 30$
Schultz & Flack (2007)	3D roughness similar to the honed pipes of Shockling <i>et al.</i> (2006)	$2.5 < k_s^+ < 25$
Langelandsvik <i>et al.</i> (2008)	Commercial steel pipes	$1.4 \pm 0.2 < k_s^+ < 18 \pm 4$
Flack <i>et al.</i> (2012)	Sandpapers	$5 < k_s^+ < -$
	Ship painted surface	$10 < k_t^+ < -$

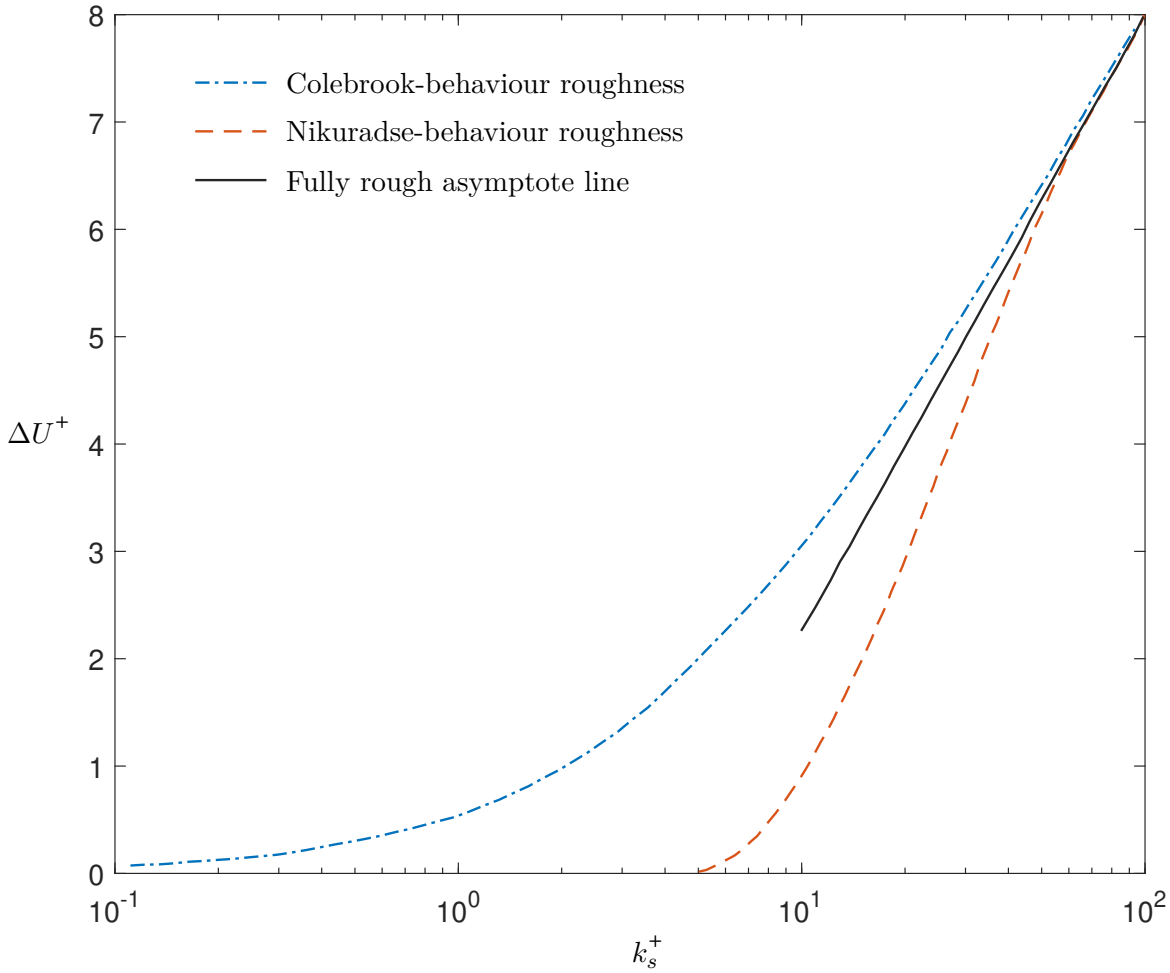


FIGURE 2.8: The roughness function ΔU^+ as a function of the roughness Reynolds number k_s^+ for Nikuradse and Colebrook behaviour roughness.

height (k_q), maximum peak-to-valley roughness height (k_t), average peak-to-valley roughness height (k_z), effective slope (ES), frontal and plan solidity (λ_f and λ_p), roughness skewness (k_{sk}), and roughness flatness or kurtosis (k_{ku}). Despite the extensive exploration of these parameters, none of them has been deemed sufficient to be generalised for all types of roughness. Further discussion on surface roughness parameters will be presented in chapter 3. This section provides an exhaustive survey encompassing early to contemporary research, which consolidates roughness associations primarily derived from roughness parameters.

Forster (1966) investigated the effect of surface finishes on the efficiency of nozzles and blades. The surfaces examined ranged from highly polished specimens to those with deposits and/or pitting resulting from extended periods of operation in the field. **Forster (1966)** found that ratios of $k_s = a.k_t$ can be used to correlate the equivalent sand grain roughness, where a is a constant that depends on the type of surface finish. Specifically, a was found to be 0.625 for spheres, 2 for fences, 1.4 for hemispheres, and 0.4 for machined surfaces.

In their study, **Dvorak (1969)** extended the existing rough surface skin-friction relations and broadened their applicability. However, the correlation was predominantly based on two-dimensional roughness data. They proposed equations for ΔU^+ in this region, which are provided below:

$$\Delta U^+ = \begin{cases} 5.6 \log k^+ + 17.35(1.625 \log \lambda_p - 1), & 1 < \lambda_p < 4.68 \\ 5.6 \log k^+ - 5.95(1.103 \log \lambda_p - 1), & \lambda_p > 4.68 \end{cases} \quad (2.26)$$

In their research, [Simpson \(1973\)](#) discovered that the roughness density correlations proposed by [Dvorak \(1969\)](#) can be generalised to be applicable to various other roughness element geometries. The roughness density parameter λ_f has been found to be more widely applicable than λ_p . A similar correlation for ΔU^+ has been presented by substituting λ_p with λ_f , which is expressed as follows:

$$\Delta U^+ = \begin{cases} 5.6 \log k^+ + 17.35(1.625 \log \lambda_f - 1), & 1 < \lambda_f < 4.68 \\ 5.6 \log k^+ - 5.95(1.103 \log \lambda_f - 1), & \lambda_f > 4.68 \end{cases} \quad (2.27)$$

A correlation was put forth by [Dirling \(1973\)](#) to compute the equivalent sand grain roughness of rough surfaces with arbitrary shape and spacing, which considers both the elements' shape and spacing. The correlation consolidates earlier data for both two-dimensional and three-dimensional roughness elements of arbitrary shape. The correlation is expressed as:

$$\frac{k_s}{k_a} = \begin{cases} 0.0164 \lambda_D^{3.78}, & \lambda_D < 4.93 \\ 139 \lambda_D^{-1.9}, & \lambda_D > 4.93 \end{cases} \quad (2.28)$$

Here, the equivalent roughness element spacing ratio λ_D is defined as $\lambda_D = (D/k)(A_p/A_w)^{-4/3}$, where D/k is a spacing parameter, D is the inverse square root of the number of roughness elements per unit geometric surface area, A_p is the projected area of roughness element in the direction of the free-stream velocity vector, and A_w is the windward surface area of roughness element as seen by the flow. This correlation provides a unified approach to predict the equivalent sand grain roughness of arbitrary rough surfaces, accounting for both the spacing and shape of the roughness elements.

A method was introduced by [Koch & Smith Jr \(1976\)](#) to determine the efficiency potential of a multistage compressor at the design point. The approach employed a loss model constructed using rational fluid-dynamic elements, which included boundary layer theory. [Koch & Smith Jr \(1976\)](#) determined a value of $k_s/k_a = 6.2$ for emery paper, which can be used as a reference value for predicting the equivalent sand grain roughness for this type of surface.

The impact of manufacturing tolerances and surface roughness of blades on turbine performance was examined by [Bammert & Sandstede \(1976\)](#). The study showed that for a milled surface with the flow perpendicular to the milling grooves, the milling roughness equivalent to sand roughness is $k_s/k_t = 0.4$, indicating that the height of the milling roughness, at the same resistance coefficient, is 2.56 times larger than that of sand grains. In comparison to a sand-roughened surface with the same roughness height, a milled surface appears smoother. When the flow is in the direction of the milling grooves, the milling roughness equivalent to sand roughness is $k_s/k_t = 0.2$. For mechanically produced surfaces, it is recommended that the centre-line-average value be converted to the sand roughness height k_s using the relationship $k_s \approx 2.19 k_a^{0.877}$. This conversion will allow for a consistent comparison of different surface roughness types in predicting equivalent sand grain roughness.

[Musker \(1980\)](#) utilised seven air pipelines, consisting of twelve flanged sections that had identical interiors resembling a sample area of ship-hull roughness to study the effect of its roughness on roughness function. [Musker \(1980\)](#) proposed a modified roughness Reynolds

number that accounts for simple geometric statistics of naturally occurring surfaces. This is given by

$$k_s^+ = \frac{\sigma U_\tau}{\nu} (1 + aES) (1 + bk_{sk}k_{ku}), \quad (2.29)$$

where σ is the standard deviation of the surface roughness, and a and b are constants chosen to provide the best fit for roughness functions associated with natural surfaces.

In a similar vein to the work of [Dirling \(1973\)](#), [Sigal & Danberg \(1990\)](#) proposed a new roughness density parameter that considers the inclination of the windward surface of the roughness elements in addition to the total surface-to-total-frontal area ratio. For two-dimensional roughness, the equivalent sand roughness is given by:

$$\frac{k_s}{k} = \begin{cases} 0.003215\Lambda_s^{4.925} & 1.4 \leq \Lambda_s \leq 4.89, \\ 8 & 4.89 < \Lambda_s < 13.25, \\ 139\Lambda_s^{-1.9} & 13.25 \leq \Lambda_s \leq 100, \end{cases} \quad (2.30)$$

which has different formulations for different ranges of Λ_s parameter. Here, $\Lambda_s = \left(\frac{S_t}{S_f}\right)\left(\frac{A_f}{A_w}\right)^{-1.6}$ (A_f is the frontal area of roughness element, and S_t/S_f is a density parameter that represents the reference-area-to-total-frontal area ratio.)

The impact of surface roughness on flow and heat transfer was investigated by [Bogard et al. \(1996\)](#) through the analysis of two rough turbine vanes used in aircraft engines. They concluded that the conventional centerline average (k_a) measurement used to quantify surface roughness was inadequate to predict these effects. Instead, they found that the correlation between the equivalent sand grain roughness (k_s) and the roughness shape/density parameter Λ_s , proposed by [Sigal & Danberg \(1990\)](#), provided a more accurate prediction.

According to [Waigh & Kind \(1998\)](#), the bluntness of an element and its aspect ratio in the spanwise direction are the key parameters that define the roughness function for a regular 3D rough surface. They developed an equation to estimate k_s as follows:

$$C = \begin{cases} 10.56 \log \left[\left(\frac{1}{\lambda_f} \frac{k}{b_m} \right)^{0.87} \left(\frac{A_w}{A_f} \right)^{0.44} \right] - 7.59, & \Lambda < 6 \\ -5.57 \log \left[\left(\frac{1}{\lambda_f} \frac{k}{b_m} \right)^{0.55} \left(\frac{A_w}{A_f} \right)^{1.38} \right] + 5.78, & \Lambda > 6 \end{cases} \quad (2.31)$$

where, C is a roughness constant, $\Lambda = \lambda_f k / s_m$, where s_m represents the streamwise width of roughness element, b_m is its spanwise width of roughness element, $\lambda_f = A_f / A_t$, A_t is the surface area of a repeated unit of the roughness element. $k_s/k = e^{(C+4)/\kappa}$, where $\kappa = 0.41$.

[Van Rij et al. \(2002\)](#) expanded on [Sigal & Danberg \(1990\)](#) work on relating two-dimensional, regular surface roughness to equivalent sand grain roughness (k_s) by incorporating irregular, three-dimensional surface roughness into their analysis. The correlation equation for k_s and roughness shape/density parameter (Λ_s) is given by :

$$\frac{k_s}{k} = \begin{cases} 1.583 \times 10^{-5} \Lambda_s^{5.683} & \Lambda_s \leq 7.842, \\ 1.802 \Lambda_s^{0.03038} & 7.842 < \Lambda_s < 28.12, \\ 255.5 \Lambda_s^{-1.454} & 28.12 \leq \Lambda_s, \end{cases} \quad (2.32)$$

Bons (2002) formulated a novel relationship to determine the equivalent sand grain roughness (k_s) of real turbine roughness, which was dependent on the root-mean-square slope angle (α_{rms}) of the surface. Unlike previous studies that used simulated roughness, roughness panels were created as scaled models of actual turbine surfaces. The new correlation was expressed as:

$$\log\left(\frac{k_{s,adj}}{k}\right) = -0.43 \log \Lambda_s + 0.82, \quad (2.33)$$

where $k_{s,adj} = 0.0138\alpha_{rms}^2 - 0.0261\alpha_{rms}$. $k_{s,adj}$ was then modified by **Bons (2005)**. In the modified version, the equivalent sand grain roughness height was normalised with mean roughness height based on the five largest peak-to-valley (k_z), and it was made a function of the surface slope angle α_{rms} . The modified correlation was given by:

$$\frac{k_{s,adj}}{k_z} = 0.0191\alpha_{rms}^2 + 0.0736\alpha_{rms}. \quad (2.34)$$

In the investigation by **Napoli et al. (2008)**, a novel parameter named the ‘‘effective slope’’ (ES) was introduced. This parameter was defined as the average gradient of the absolute roughness across the surface. Unlike previous roughness parameters, ES can be used to characterise roughness for any surface, including random roughness. To test the effectiveness of ES , the authors conducted a large eddy simulation of a rough wall turbulence channel flow, using corrugated walls with varying ES values. They found that the effective slope played a crucial role in determining the roughness function, and their results revealed that the transitionally rough regime was separated from the fully rough regime at $ES \approx 0.15$. This value also marked the boundary between the linear and nonlinear behaviour of the roughness function $\Delta U^+ = f(ES)$.

The impact of close-packed pyramid roughnesses on flow dynamics was explored in **Schultz & Flack (2009)**. The authors discovered that the change in velocity ΔU^+ was mainly dependent on the height of the roughness. Moreover, they identified a range of effective slopes ES where the roughness function was highly dependent on the ES value, such that if ES was below this range, the surface could be considered wavy, not rough. The authors determined that if $ES < 0.35$, the surface would be classified as wavy.

Boyle & Stripf (2009) presented a novel correlation for determining the equivalent sand grain roughness based on the roughness skewness (k_{sk}) and the root-mean-square roughness (k_q) of turbine vane roughness. The correlation was given by:

$$k_s = 4.3k_q(1 + C_{sk}k_{sk}), \quad (2.35)$$

where C_{sk} is a skewness constant that is slightly less than 1.

Flack & Schultz (2010) investigated the relevant roughness scales for three-dimensional roughness in the fully rough regime and considered a range of commonly used surface statistical parameters. The study indicated that the root-mean-square roughness k_q and roughness skewness k_{sk} of the surface elevation probability density function are the most effective parameters in characterising a surface hydraulically. Based on these parameters, a similar correlation to

that proposed by [Boyle & Stripf \(2009\)](#) is offered, but a power equation instead of a linear one is proposed as follows:

$$k_s = 4.43k_q(1 + k_{sk})^{1.37}. \quad (2.36)$$

In the study conducted by [Yuan & Piomelli \(2014\)](#), large-eddy simulations (LES) in turbulent open channel flows to investigate the roughness function and the equivalent sand-grain roughness height, k_s , over sand-grain roughness and various types of realistic roughness mimicking hydraulic turbine blades. Their results indicated that the beginning of the fully rough regime varies depending on the roughness type, and k_s is highly dependent on the surface topography. Furthermore, they identified that the critical value of ES , which differentiates the waviness and roughness regimes, is higher for realistic surfaces compared to the values obtained for the more uniform roughness types that were examined in [Schultz & Flack \(2009\)](#).

A systematic analysis was conducted by [Chan *et al.* \(2015\)](#) using direct numerical simulation (DNS) to investigate the impact of 3D sinusoidal roughness on turbulent flow through pipes. [Chan *et al.* \(2015\)](#) found that low Reynolds numbers had a minimal effect on ΔU^+ . They then studied the effects of roughness height and wavelength on ΔU^+ in both the transitionally rough and fully rough regimes. Their investigation demonstrated that both k_a and ES had a strong influence on ΔU^+ as follows:

$$\Delta U_{est}^+ = \alpha \log k_a^+ + \beta \log ES + \gamma, \quad (2.37)$$

where $\alpha = 1/\kappa$, $\beta = 1.12$ and $\gamma = 1.47$.

In a study conducted by [Ünal \(2015\)](#), the zero-pressure gradient turbulent boundary layer (ZPG-TBL) was investigated for various rough surfaces, including marine antifouling and other irregularly rough engineering surfaces, in both transitionally and fully rough flow regimes. The objective of the study was to identify a new roughness length scale that can accurately represent the roughness functions for both regimes. The proposed roughness length scale is expressed as follows:

$$k = 15.77k_q^2(1 + k_{sk})^{0.862}/sd_4, \quad (2.38)$$

$$\Delta U^+ = \ln(k^+ + 1)/\kappa,$$

where sd_4 is mean spacing between the zero-crossings.

[Flack *et al.* \(2016\)](#) investigated the effect of roughness on skin friction in fully developed turbulent channel flow using fifteen surfaces generated by grit blasting with various types and sizes of media. [Flack *et al.* \(2016\)](#) found that the equivalent sand-grain roughness height could be predicted using k_q and k_{sk} as follows:

$$\frac{k_s}{k_q} = 3.47(2 + k_{sk})^{-0.405}. \quad (2.39)$$

In the study conducted by [Botros \(2016\)](#), a relationship between the equivalent sand grain roughness height, k_s , and the roughness element rms parameter, k_q , for fully developed turbulent pipe flow in commercial steel pipes was established. The researchers examined eleven steel pipes sourced from different mills and determined k_s using the measured friction factor and the Colebrook or Nikuradse rough functions. The findings revealed that the equation:

$$k_s(\text{Colebrook}) = 0.078k_q^2 + 1.306k_q, \quad (2.40)$$

accurately represents the data when both k_s and k_q are in μm . However, if the Nikuradse-type roughness was used, the equation becomes:

$$k_s(\text{Nikuradse}) = 2.294k_q. \quad (2.41)$$

According to [Goodhand *et al.* \(2016\)](#), the current roughness criteria that rely on a single amplitude parameter, such as k_a , are inadequate for characterising the surface finish because they oversimplify the roughness topography. To explore the effect of roughness on drag, [Goodhand *et al.* \(2016\)](#) varied the roughness on a single, symmetrical aerofoil. They found that a topographical parameter, the roughness amplitude normalised by its wavelength, is a crucial factor that can be correlated with the equivalent sand grain roughness height, k_s .

Large-eddy simulations (LES) were conducted by [De Marchis \(2016\)](#) to estimate energy losses in roughened channel flows. They performed resolved LES over regular triangular rough surfaces and analysed the results in the context of irregular rough surfaces. To describe the results, they proposed a new mathematical logarithmic law that is similar to the one previously proposed using the equivalent sand grain roughness in Eq.(2.25). Their proposed equation is as follows:

$$\Delta U^+ = \frac{1}{\kappa} \ln(ES^2) - B + C, \quad (2.42)$$

where B and C are both equal to 6.5 and 8.5, respectively.

[Stimpson *et al.* \(2017\)](#) investigated the roughness of various channels with different hydraulic length scales produced through direct metal laser sintering (DMLS). [Stimpson *et al.* \(2017\)](#) found a strong correlation between the relative arithmetic mean roughness and the relative equivalent sand grain roughness. The correlation is expressed as:

$$\frac{k_s}{D_h} = 18 \frac{k_a}{D_h} - 0.05, \quad (2.43)$$

where D_h is the hydraulic diameter. However, it should be noted that this correlation is only valid for randomly rough surfaces with $k_a/D_h > 0.028$, as lower values result in negative k_s/D_h .

In a study by [Thakkar *et al.* \(2017\)](#), direct numerical simulations were performed on 17 irregular rough surfaces at the same friction Reynolds number, all of which were scaled to the same physical roughness height under the transitionally rough regime. The study revealed that the roughness function ΔU^+ was significantly influenced by the frontal solidity λ_f , skewness k_{sk} , streamwise correlation length L_x^{cor} , and root-mean-square roughness height k_q . A new parameter, λ_3 , was introduced as a function of λ_f , L_x^{cor} , k_{sk} , and k_q to estimate the roughness function as follows:

$$\lambda_3 = \lambda_f \left[1 + 0.09 \ln \left(\frac{L_x^{cor}}{k_z} \right) \right] \left(\frac{4k_q}{k_z} \right)^{-0.44} e^{-0.074k_{sk}}. \quad (2.44)$$

The resulting equation was:

$$\Delta U^+ = a\lambda_3 + b, \quad (2.45)$$

where a and b were 1.47 and 8, respectively. The fit obtained for ΔU^+ was of high quality, with an R^2 value of 0.9842.

In their study, [Forooghi *et al.* \(2017\)](#) used numerical simulations to investigate the impact of various roughness parameters on the equivalent sand grain roughness (k_s) in the fully rough regime of channel flow at a friction Reynolds number of approximately 500. They generated roughness geometries by systematically altering the moments of the surface height probability density function, the effective slope of the random roughness, and the size distribution of the roughness peaks. The authors correlated k_s based on the roughness parameters k , k_{sk} , and ES . They discovered that these parameters can accurately predict k_s for randomly distributed roughness in the fully rough regime of channel flows. The correlation is expressed as follows:

$$\begin{cases} \frac{k_s}{k} = F(k_{sk}) \cdot G(ES), \\ F(k_{sk}) = 0.67k_{sk}^2 + 0.93k_{sk} + 1.3, \\ G(ES) = 1.07 \cdot (1 - e^{-3.5ES}). \end{cases} \quad (2.46)$$

A novel geometric parameter, referred to as “shelter solidity” (λ_s), was proposed by [Placidi & Ganapathisubramani \(2018\)](#) to address the lack of similarity in surface morphology features. [Placidi & Ganapathisubramani \(2018\)](#) investigated twelve different surface conditions using LEGO bricks with a uniform height. Six cases were tested for a fixed plan solidity (λ_p) with variations in frontal density (λ_f), while the other six cases had varying λ_p for fixed λ_f . The parameter is defined as the ratio of the sheltered plan area of the roughness A_{sh} to the total plan area of a repeating unit A_t , as follows:

$$\lambda_s = \frac{A_t - A_{sh}}{A_t}. \quad (2.47)$$

[Placidi & Ganapathisubramani \(2018\)](#) found that λ_s can also be used to reconcile the variations in surface drag. They observed a linear relationship between the roughness function and λ_s , which was found to be representative of most of the data, with an inverse proportionality.

In their study, [Barros *et al.* \(2018\)](#) created controlled surface roughness by systematically generating roughness parameters. Three surfaces were generated with a fixed amplitude and varying power-law spectral slope of -0.5, -1.0 and -1.5, and they were replicated using high-resolution 3D printing. [Barros *et al.* \(2018\)](#) found that in the wavy flow regime, where the equivalent sand grain roughness height ES is less than 0.35, there exists a correlation between the roughness length scales k_s , k_q , and k_{sk} . Specifically, k_s can be correlated to k_q and k_{sk} as follows:

$$\frac{k_s}{k_q} = 3.41(1 + k_{sk})^{0.61}. \quad (2.48)$$

A Lattice Boltzmann direct numerical simulation was performed by [Kuwata & Kawaguchi \(2019\)](#) to examine the influence of roughness parameters on turbulence in open-channel flows. The simulation involved randomly distributed hemispheres on a solid plane at a friction Reynolds number of approximately 600. The researchers analysed the triple-integrated double-averaged Navier-Stokes equation to examine the impact of root-mean-square roughness and skewness on the skin friction coefficient. They varied the number and diameter of the hemispheres to alter statistical moments of the roughness elevation, such as mean height k_a , standard deviation k_q , skewness k_{sk} , and kurtosis k_{ku} . The authors found that a correlation between k_q and k_{sk} could

accurately predict the roughness function, which was expressed as:

$$\frac{k_s}{k_q} = 4(1 + 0.17k_{sk})^4. \quad (2.49)$$

Large eddy simulations of rough turbulent channel flows were employed by [De Marchis et al. \(2020\)](#) to examine the effect of various geometries on ΔU^+ . The surfaces were generated by superimposing sinusoidal functions with random amplitudes in transitional and fully rough regimes at various friction Reynolds numbers (Re_τ). [De Marchis et al. \(2020\)](#) established a correlation between ES and statistical moments of the roughness elevation such as the mean height (k_a) or the standard deviation (k_q), which could predict the roughness function. The roughness function was expressed as:

$$\Delta U^+ = \frac{1}{\kappa} \ln(ES \cdot k^*) + B, \quad (2.50)$$

where k^* is either k_a^+ or k_q^+ and B was an additive constant to fit the data. The constant B was determined to be 3.5 for the correlation between ΔU^+ and $ES \times k_q^+$, and 4 for the correlation between ΔU^+ and $ES \times k_a^+$.

The impact of roughness height and skewness on the friction coefficient was investigated in a recent study conducted by [Flack et al. \(2020\)](#). They found a relationship between k_s , k_q and k_{sk} , and categorised the friction coefficients into three groups based on roughness skewness values (positive, negative, and zero). Their results indicated that surfaces with negative skewness generate smaller friction coefficients compared to those with positive skewness. The authors also derived a correlation for k_s as follows:

$$k_s = \begin{cases} 2.48k_q(1 + k_{sk})^{2.24} & k_{sk} > 0.00, \\ 2.11k_q & k_{sk} = 0.00, \\ 2.73k_q(2 + k_{sk})^{-0.45} & k_{sk} < 0.00. \end{cases} \quad (2.51)$$

The findings from this study provide valuable insights into the relationship between roughness height, skewness, and friction coefficients.

The investigation conducted by [Ramani et al. \(2020\)](#) aimed to explore the effects of effective slopes on turbulent boundary layer flows in both the streamwise and spanwise directions. Their findings indicated that the streamwise effective slope ES_x had a greater effect on the drag coefficient than the spanwise effective slope ES_z . Nevertheless, the researchers also concluded that ES_z played an essential role in determining the drag coefficient and could not be overlooked.

The influence of surface roughness parameters on the turbulence statistics and drag coefficient of turbulent boundary layer flows over 2D surfaces roughness comprising circular rods and sine-waves with two different heights and two different streamwise spacing to height ratios was investigated in a study conducted by [Abdelaziz et al. \(2020\)](#). They identified k_t , ES , and k_{sk} as the primary parameters affecting the flow. Moreover, they developed an equation to predict k_s based on these parameters, given by:

$$k_s = 0.0013 + 2.0294 \times k_t - 0.1139 \times s_x + 0.013 \times ES \times k_{sk}. \quad (2.52)$$

In a recent investigation, [Jouybari et al. \(2021\)](#) employed machine learning techniques, such as deep neural network (DNN) and gaussian process regression (GPR), to formulate a

sophisticated approach for predicting the Nikuradse equivalent sand-grain roughness k_s in turbulent flows over a wide range of rough surfaces. The authors performed direct numerical simulations (DNS) on 45 rough surfaces with varying roughness characteristics, including moments of roughness height (k_a , k_{sk} , and k_{ku}), ES , average inclination, porosity, and degree of randomness. Out of these 45 surfaces, 30 were identified as being in fully rough flow regimes. The authors used a combination of these 30 DNS results and 15 fully rough experimental data sets from literature to calculate k_s using DNN and GPR. The DNN and GPR models achieved an rms error of less than 10% and a maximum error of less than 30%, which is a more accurate prediction than existing correlations in the literature. However, the authors did not propose any correlation for computing k_s .

The impact of the hierarchy of roughness scales on turbulent boundary layers over multiscale rough surfaces comprising regular cuboid elements was investigated in a research study conducted by [Medjnoun *et al.* \(2021\)](#). The authors considered three iterations, where a first iteration of large-scale cuboids was uniformly supplemented by subsequent smaller cuboids with their size decreasing according to a power-law as the number increased. The study demonstrated that the aerodynamic roughness length scale between subsequent iterations varied linearly, and that this relationship could be described using a geometrical parameter that was proportional to the frontal solidity of the roughness.

[Abdelaziz *et al.* \(2022\)](#) conducted a more comprehensive investigation, in an extension of their previous research on 2D surface roughness reported in [Abdelaziz *et al.* \(2020\)](#), by adding triangular ribs and sine waves as new surface geometries, in addition to circular rods of varying heights and five different streamwise spacing to height ratios. These novel contributions expand the range of roughness scales examined and provide a more complete understanding of the impact of 2D roughness on turbulent boundary layer flows. A new expression for the Nikuradse equivalent sand-grain roughness k_s was derived for 2D uniformly distributed roughness in the fully rough regime. The expression is given by:

$$k_s = a + b \times k + c \times \frac{2k}{ES} + d \times ES \times k_{sk}, \quad (2.53)$$

where the constants a , b , c , and d are equal to 0.001, 1.865, -0.103, and 0.013, respectively. k_s and k units are in mm.

The incorporation of supplementary data, encompassing both 2D and 3D roughness, was carried out, revealing that the intricate nature of roughness topography involving several parameters precludes the existence of a general scaling for all roughness geometries. The findings indicate that each roughness family is likely to possess its own scaling, implying that separate scaling laws for 2D and 3D roughness may be necessary. Nevertheless, an endeavour was undertaken to establish an empirical correlation for both 2D and 3D data, which can be expressed as follows:

$$k_s = a + b \times k + c \times \frac{2k}{ES} + d \times \frac{2k^2}{ES} + e \times e^{f \times ES \times k_{sk}}, \quad (2.54)$$

where, $a = -0.002$, $b = 0.926$, $c = 0.283$, $d = 4.933$, $e = 0.001$, $f = 3.66$. k_s and k units are in mm.

The impact of rough surfaces resembling barnacles on wall-bounded turbulence was investigated by [Sarakinis & Busse \(2022\)](#) using direct numerical simulations of turbulent channel flow. Barnacle-type roughness is a combination of the features of regular rough surfaces, consisting of discrete roughness elements of uniform size and shape, and irregular rough surfaces

that exhibit features with a wide distribution of sizes and shapes, covering the surface with a random areal distribution.

The impact of the orientation of ratchet-type rough surfaces on the roughness function was explored in a study conducted by [Busse & Zhdanov \(2022\)](#), using direct numerical simulations of turbulent channel flow. The study found that the roughness function significantly relies on the orientation of the ratchets. In this regard, [Busse & Zhdanov \(2022\)](#) evaluated two previously developed empirical equations that estimate the roughness function ΔU^+ or the equivalent sand-grain roughness k_s based on surface-slope related parameters like ES or Λ_s . However, these equations failed to predict the differences between ratchet surfaces with high windward slopes and those with high leeward slopes accurately. Therefore, new empirical relationships need to be developed or existing ones need to be modified to account for the orientation-dependency effect.

[Jelly et al. \(2022\)](#) built on the previous work of [Ramani et al. \(2020\)](#) by creating a set of ten irregular surfaces using a surface generation algorithm. The surfaces were designed to have a common mean peak-to-valley height and near-Gaussian roughness profiles to isolate the effect of varying ES_z while holding other roughness parameters constant. Specifically, the authors examined the impact of varying ES_z for three different values of ES_x on the roughness drag penalty. The study showed that changes in ES_z can have a significant effect on roughness drag, particularly for low- ES_x surfaces.

The impact of the streamwise and spanwise spacing to height ratio on the drag coefficient (C_f) of turbulent boundary layer flows was studied by [Abdelaziz et al. \(2023\)](#). The research examined seven different sinewave profiles with the same amplitude and different wavelengths. The aim was to determine the impact of varying s_x and s_z on C_f and the roughness function ΔU^+ . The findings indicate that the streamwise spacing to height ratio s_x/k has a more significant effect on C_f and ΔU^+ when compared to the spanwise spacing to height ratio s_z/k .

 TABLE 2.2: Previous research on k_s correlations

Correlation	Notes	Roughness type	Researchers
$k_s = a.k_t$	$a = 0.625$, Spheres $a = 2$, Fences $a = 1.4$, Hemispheres $a = 0.4$, Machined surfaces	Various grades of emery paper	Forster (1966)
$\Delta U^+ = \begin{cases} a \log k^+ + b(c \log \lambda_p - 1), & 1 < \lambda_p < 4.68 \\ a \log k^+ - d(e \log \lambda_p - 1), & \lambda_p > 4.68 \end{cases}$	$a = 5.6$ $b = 17.35$ $c = 1.625$ $d = 5.95$ $e = 1.103$	2D & 3D roughness	Dvorak (1969)

Continued on next page

TABLE 2.2: Previous research on k_s correlations (continued)

Correlation	Notes	Roughness type	Researchers
$\Delta U^+ = \begin{cases} a \log k^+ + b(c \log \lambda_f - 1), & 1 < \lambda_f < 4.68 \\ a \log k^+ - d(e \log \lambda_f - 1), & \lambda_f > 4.68 \end{cases}$	$\begin{aligned} a &= 5.6 \\ b &= 17.35 \\ c &= 1.625 \\ d &= 5.95 \\ e &= 1.103 \end{aligned}$	2D & 3D roughness	Simpson (1973)
$\frac{k_s}{k_a} = \begin{cases} 0.0164 \lambda_D^{3.78} & \lambda_D < 4.93 \\ 139 \lambda^{-1.9} & \lambda_D > 4.93 \end{cases}$	$\lambda_D = \frac{D}{k} \left(\frac{A_p}{A_w} \right)^{-4/3}$	Arbitrarily rough surfaces	Dirling (1973)
$\frac{k_s}{k_a} = 6.2$	NA	Emery paper	Koch & Smith Jr (1976)
$\frac{k_s}{k_t} = \begin{cases} 0.4 & \text{Flow } \perp \text{ milling grooves} \\ 0.2 & \text{Flow } \parallel \text{ milling grooves} \end{cases}$	NA	Manufacturing tolerances of turbines blades	Bammert & Sandstede (1976)
$k_s^+ = \frac{\sigma U_\tau}{\nu} (1 + aES)(1 + bk_{sk}k_{ku})$	a and b are constants chosen to provide the best fit for roughness functions	Naturally occurring surfaces	Musker (1980)
$\frac{k_s}{k} = \begin{cases} 0.003215 \Lambda_s^{4.925} & 1.4 \leq \Lambda_s \leq 4.89 \\ 8 & 4.89 < \Lambda_s < 13.25 \\ 139 \Lambda^{-1.9} & 13.25 \leq \Lambda_s \leq 100 \end{cases}$	$\Lambda_s = \frac{S_t}{S_f} \left(\frac{A_f}{A_w} \right)^{-1.6}$	2D & 3D roughness	Sigal & Danberg (1990)

Continued on next page

TABLE 2.2: Previous research on k_s correlations (continued)

Correlation	Notes	Roughness type	Researchers
$\frac{k_s}{k} = e^{(C+4)/0.41}$ $C = \begin{cases} a \log \left[\left(\frac{1}{\lambda_f} \frac{k}{b_m} \right)^{0.87} \left(\frac{A_w}{A_f} \right)^{0.44} \right] - b & \Lambda < 6 \\ c \log \left[\left(\frac{1}{\lambda_f} \frac{k}{b_m} \right)^{0.55} \left(\frac{A_w}{A_f} \right)^{1.38} \right] + d & \Lambda > 6 \end{cases}$	$\Lambda = \lambda_f k / s_m$ $\lambda_f = A_f / A_t$ $a = 10.56$ $b = 7.59$ $c = -5.57$ $d = 5.78$	Regular 3D roughness	Waigh & Kind (1998)
$\frac{k_s}{k} = \begin{cases} 1.583 \times 10^{-5} \Lambda_s^{5.683} & \Lambda_s \leq 7.842, \\ 1.802 \Lambda_s^{0.03038} & 7.842 < \Lambda_s < 28.12 \\ 255.5 \Lambda_s^{-1.454} & 28.12 \leq \Lambda_s \end{cases}$	NA	Nonuniform, 3D roughness with irregular geometry	Van Rij <i>et al.</i> (2002)
$\log \left(\frac{k_{s,adj}}{k} \right) = -0.43 \log \Lambda_s + 0.82$ $k_{s,adj} = 0.0138 \alpha_{rms}^2 - 0.0261 \alpha_{rms}$	NA	Real turbine blade roughness	Bons (2002)
$\log \left(\frac{k_{s,adj}}{k} \right) = -0.43 \log \Lambda_s + 0.82$ $\frac{k_{s,adj}}{k_z} = 0.0191 \alpha_{rms}^2 + 0.0736 \alpha_{rms}$	NA	Real turbine blade roughness	Bons (2005)
$\Delta U^+ = f(ES)$	$ES \approx 0.15$ separates the linear and nonlinear behaviour of ΔU^+	2D corrugated walls	Napoli <i>et al.</i> (2008)
$k_s = 4.3 k_q (1 + C_{sk} k_{sk})$	C_{sk} is slightly less than 1	Turbine vane roughness	Boyle & Stripf (2009)

Continued on next page

TABLE 2.2: Previous research on k_s correlations (continued)

Correlation	Notes	Roughness type	Researchers
$k_s = 4.43k_q(1 + k_{sk})^{1.37}$	NA	3D roughness	Flack & Schultz (2010)
$\Delta U_{est}^+ = \alpha \log k_a^+ + \beta \log ES + \gamma$	$\alpha = 1/\kappa$ $\beta = 1.12$ $\gamma = 1.47$	Egg cartoon 3D roughness	Chan <i>et al.</i> (2015)
$k = 15.77k_q^2(1 + k_{sk})^{0.862}/sd_4$ $\Delta U^+ = \ln(k^+ + 1)/\kappa$	sd_4 is mean spacing between the zero-crossings	Marine anti-foulings irregular roughness.	Ünal (2015)
$\frac{k_s}{k_q} = 3.47(2 + k_{sk})^{-0.405}$	NA	Grit blasting with various types and sizes of media.	Flack <i>et al.</i> (2016)
$k_s(\text{Colebrook}) = 0.078k_q^2 + 1.306k_q$ $k_s(\text{Nikuradse}) = 2.294k_q$	NA	Commercial steel pipes	Botros (2016)
$\Delta U^+ = \frac{1}{\kappa} \ln(ES^2) - B + C$	$B = 6.5$ & $C = 8.5$	Regular & irregular rough surfaces	De Marchis (2016)
$\frac{k_s}{D_h} = 18 \frac{k_a}{D_h} - 0.05$	Valid for $\frac{k_a}{D_h} > 0.028$	Additive manufactured random roughness	Stimpson <i>et al.</i> (2017)
$\Delta U^+ = 1.47\lambda_3 + 8$ $\lambda_3 = \lambda_f \left[1 + 0.09 \ln \left(\frac{L_x^{cor}}{k_z} \right) \right]$ $\left(\frac{4k_q}{k_z} \right)^{-0.44} e^{-0.074k_{sk}}$	NA	Irregular roughness	Thakkar <i>et al.</i> (2017)

Continued on next page

TABLE 2.2: Previous research on k_s correlations (continued)

Correlation	Notes	Roughness type	Researchers
$\begin{cases} k_s/k = F(k_{sk}).G(ES), \\ F(k_{sk}) = 0.67k_{sk}^2 + 0.93k_{sk} + 1.3, \\ G(ES) = 1.07.(1 - e^{-3.5ES}). \end{cases}$	NA	Random roughness	Forooghi <i>et al.</i> (2017)
$\Delta U^+ = f(\lambda_s)$	$\lambda_s = \frac{A_t - A_{sh}}{A_t}$	LEGO bricks	Placidi & Ganapathisubramani (2018)
$\frac{k_s}{k_q} = 3.41(1 + k_{sk})^{0.61}$	NA	3D random roughness	Barros <i>et al.</i> (2018)
$\frac{k_s}{k_q} = 4(1 + 0.17k_{sk})^4$	NA	Randomly distributed hemispheres	Kuwata & Kawaguchi (2019)
$\Delta U^+ = \frac{1}{\kappa} \ln(ES.k^*) + B$	If $k^* = k_a^+$ $B = 3.5$, If $k^* = k_q^+$ $B = 4$	Superimposing sinusoidal functions	De Marchis <i>et al.</i> (2020)
$k_s = \begin{cases} 2.48k_q(1 + k_{sk})^{2.24} & k_{sk} > 0.00, \\ 2.11k_q & k_{sk} = 0.00, \\ 2.73k_q(2 + k_{sk})^{-0.45} & k_{sk} < 0.00. \end{cases}$	NA	3D random roughness	Flack <i>et al.</i> (2020)
$k_s = a + b(k_t) + c(s_x) + d(ES)(k_{sk})$	$a = 0.001$ $b = 2.029$ $c = -0.114$ $d = 0.013$	2D regular roughness	Abdelaziz <i>et al.</i> (2020)

Continued on next page

TABLE 2.2: Previous research on k_s correlations (continued)

Correlation	Notes	Roughness type	Researchers
$k_s = a + b(k_t)$ $+ c \left(\frac{2k_t}{ES} \right) + d \left(\frac{2k_t^2}{ES} \right)$ $+ e \left(e^{f(ES)(k_s k)} \right)$	$a = -0.002$ $b = 0.93$ $c = 0.28$ $d = -4.93$ $e = 0.001$ $f = 3.66$	2D & 3D roughness	Abdelaziz et al. (2022)

The estimation of the equivalent sand-grain roughness or roughness functions is a critical aspect in the modelling of turbulent flows over rough surfaces. In the previous extensive literature, several correlations have been proposed to predict the roughness function, but a universal correlation for all roughness geometries has not yet been established. Table 2.2 summarises the existing correlations proposed by different researchers. It is evident that each family of roughness has its unique scaling, and no general scaling exists for all roughness geometries due to the complex nature of the roughness topography involving many parameters.

The prognostic correlation is becoming more intricate through the addition of supplementary roughness parameters. Although an overarching drag correlation, capable of encompassing all scenarios, remains elusive, a limited number of auspicious parameters are emerging from an extensive list of potential candidates. Therefore, the following chapters in this thesis will attempt to add up to the previous literature by exploring the roughness geometries' influence on the drag coefficient in turbulent boundary layer flows, aiming to derive a universal correlation for estimating the roughness function.

Bibliography

- ABDELAZIZ, M., DJENIDI, L., GHAYESH, M., & CHIN, R. 2020 Turbulent boundary layer over various 2d uniform distributed roughness elements. In *22nd Australasian Fluid Mechanics Conference, AFMC 2020*. The University of Queensland.
- ABDELAZIZ, M., DJENIDI, L., GHAYESH, M., & CHIN, R. 2023 On the effect of streamwise and spanwise spacing to height ratios of three-dimensional sinusoidal roughness on turbulent boundary layers. *Physics of Fluids* **35** (2).
- ABDELAZIZ, M., DJENIDI, L., GHAYESH, M. H., & CHIN, R. 2022 A new equivalent sand grain roughness relation for two-dimensional rough wall turbulent boundary layers. *Journal of Fluid Mechanics* **940**, A25.
- ANDERSON, J. D. 2005 Ludwig Prandtl's boundary layer. *Physics Today* **58** (12), 42–48.
- ANDERSON, W., BARROS, J. M., CHRISTENSEN, K. T., & AWASTHI, A. 2015 Numerical and experimental study of mechanisms responsible for turbulent secondary flows in boundary layer flows over spanwise heterogeneous roughness. *Journal of Fluid Mechanics* **768**, 316–347.

- ATKINSON, C., BUCHMANN, N. A., & SORIA, J. 2015 An experimental investigation of turbulent convection velocities in a turbulent boundary layer. *Flow, Turbulence and Combustion* **94**, 79–95.
- BAMMERT, K. & SANDSTEDTE, H. 1976 Influences of manufacturing tolerances and surface roughness of blades on the performance of turbines. *Journal of Engineering for Power* **98** (1), 29–36.
- BANDYOPADHYAY, P. R. 1987 Rough-wall turbulent boundary layers in the transition regime. *Journal of Fluid Mechanics* **180**, 231–266.
- BARROS, J. M., SCHULTZ, M. P., & FLACK, K. A. 2018 Measurements of skin-friction of systematically generated surface roughness. *International Journal of Heat and Fluid Flow* **72**, 1–7.
- BOGARD, D. G., SCHMIDT, D. L., & TABBITA, M. 1996 Characterization and laboratory simulation of turbine airfoil surface roughness and associated heat transfer. In *Turbo Expo: Power for Land, Sea, and Air, Turbo Expo: Power for Land, Sea, and Air*, vol. Volume 4: Heat Transfer; Electric Power; Industrial and Cogeneration. American Society of Mechanical Engineers.
- BONS, J. 2005 A critical assessment of reynolds analogy for turbine flows. *Journal of Heat Transfer* **127** (5), 472–485.
- BONS, J. P. 2002 S_t and C_f augmentation for real turbine roughness with elevated freestream turbulence. *Turbo Expo: Power for Land, Sea, and Air*, vol. Volume 3: Turbo Expo 2002, Parts A and B, pp. 349–363.
- BOTROS, K. 2016 Experimental investigation into the relationship between the roughness height in use with nikuradse or colebrook roughness functions and the internal wall roughness profile for commercial steel pipes. *Journal of Fluids Engineering* **138** (8).
- BOYLE, R. J. & STRIPF, M. 2009 Simplified approach to predicting rough surface transition. *Journal of Turbomachinery* **131** (4).
- BRADSHAW, P. 2000 A note on “critical roughness height” and “transitional roughness”. *Physics of Fluids* **12** (6), 1611–1614.
- BUSSE, A. & ZHDANOV, O. 2022 Direct numerical simulations of turbulent channel flow over ratchet roughness. *Flow, Turbulence and Combustion* **109** (4), 1195–1213.
- CASTRO, I. P., SEGALINI, A., & ALFREDSSON, P. H. 2013 Outer-layer turbulence intensities in smooth-and rough-wall boundary layers. *Journal of Fluid Mechanics* **727**, 119–131.
- CEBECI, T. & BRADSHAW, P. 1977 *Momentum transfer in boundary layers*. Hemisphere Publishing Corporation: New York, NY, USA.
- CENEDESE, A., ROMANO, G., & DI FELICE, F. 1991 Experimental testing of Taylor’s hypothesis by LDA in highly turbulent flow. *Experiments in Fluids* **11** (6), 351–358.
- CHAN, C. I., SCHLATTER, P., & CHIN, R. C. 2021 Interscale transport mechanisms in turbulent boundary layers. *Journal of Fluid Mechanics* **921**, A13.

- CHAN, L., MACDONALD, M., CHUNG, D., HUTCHINS, N., & OOI, A. 2015 A systematic investigation of roughness height and wavelength in turbulent pipe flow in the transitionally rough regime. *Journal of Fluid Mechanics* **771**, 743–777.
- CHAUHAN, K. A., MONKEWITZ, P. A., & NAGIB, H. M. 2009 Criteria for assessing experiments in zero pressure gradient boundary layers. *Fluid Dynamics Research* **41** (2), 021404.
- CHUNG, D., HUTCHINS, N., SCHULTZ, M. P., & FLACK, K. A. 2021 Predicting the drag of rough surfaces. *Annual Review of Fluid Mechanics* **53**, 439–471.
- COLEBROOK, C. F. & WHITE, C. M. 1937 Experiments with fluid friction in roughened pipes. *Proceedings of the Royal Society of London. Series A-Mathematical and Physical Sciences* **161** (906), 367–381.
- COLEMAN, S., NIKORA, V. I., MCLEAN, S., & SCHLICKE, E. 2007 Spatially averaged turbulent flow over square ribs. *Journal of Engineering Mechanics* **133** (2), 194–204.
- COLES, D. 1956 The law of the wake in the turbulent boundary layer. *Journal of Fluid Mechanics* **1** (2), 191–226.
- COLES, D. 1964 The turbulent boundary layer in a compressible fluid. *Physics of Fluids* **7** (9), 1403–1423.
- DARCY, H. 1857 *Recherches expérimentales relatives au mouvement de l'eau dans les tuyaux*. vol. 1., Mallet-Bachelier.
- DE MARCHIS, M. 2016 Large eddy simulations of roughened channel flows: Estimation of the energy losses using the slope of the roughness. *Computers & Fluids* **140**, 148–157.
- DE MARCHIS, M., SACCONI, D., MILICI, B., & NAPOLI, E. 2020 Large eddy simulations of rough turbulent channel flows bounded by irregular roughness: advances toward a universal roughness correlation. *Flow, Turbulence and Combustion* **105**, 627–648.
- DEL ALAMO, J. C. & JIMÉNEZ, J. 2009 Estimation of turbulent convection velocities and corrections to Taylor's approximation. *Journal of Fluid Mechanics* **640**, 5–26.
- DENNIS, D. J. & NICKELS, T. B. 2008 On the limitations of Taylor's hypothesis in constructing long structures in a turbulent boundary layer. *Journal of Fluid Mechanics* **614**, 197–206.
- DIRLING, JR, R. 1973 A method for computing rough wall heat transfer rates on reentry nosetips. In *8th Thermophysics Conference*, p. 763.
- DJENIDI, L., ANTONIA, R., & ANSELMET, F. 1994 LDA measurements in a turbulent boundary layer over a d-type rough wall. *Experiments in Fluids* **16** (5), 323–329.
- DRÓZDŹ, A., NIEGODAJEW, P., ROMAŃCZYK, M., & ELSNER, W. 2023 Convection velocity in turbulent boundary layers under adverse pressure gradient. *Experimental Thermal and Fluid Science* p. 110900.
- DVORAK, F. 1969 Calculation of turbulent boundary layers on rough surfaces in pressure gradient. *AIAA Journal* **7** (9), 1752–1759.
- EFROS, V. & KROGSTAD, P.-Å. 2011 Development of a turbulent boundary layer after a step from smooth to rough surface. *Experiments in Fluids* **51**, 1563–1575.

- FISHER, M. & DAVIES, P. 1964 Correlation measurements in a non-frozen pattern of turbulence. *Journal of Fluid Mechanics* **18** (1), 97–116.
- FLACK, K., SCHULTZ, M., & CONNELLY, J. 2007 Examination of a critical roughness height for outer layer similarity. *Physics of Fluids* **19** (9), 095104.
- FLACK, K. A. & SCHULTZ, M. P. 2010 Review of hydraulic roughness scales in the fully rough regime. *Journal of Fluids Engineering* **132** (4).
- FLACK, K. A., SCHULTZ, M. P., & BARROS, J. M. 2020 Skin friction measurements of systematically-varied roughness: Probing the role of roughness amplitude and skewness. *Flow, Turbulence and Combustion* **104** (2), 317–329.
- FLACK, K. A., SCHULTZ, M. P., BARROS, J. M., & KIM, Y. C. 2016 Skin-friction behavior in the transitionally-rough regime. *International Journal of Heat and Fluid Flow* **61**, 21–30.
- FLACK, K. A., SCHULTZ, M. P., & ROSE, W. B. 2012 The onset of roughness effects in the transitionally rough regime. *International Journal of Heat and Fluid Flow* **35**, 160–167.
- FLACK, K. A., SCHULTZ, M. P., & SHAPIRO, T. A. 2005 Experimental support for Townsend’s Reynolds number similarity hypothesis on rough walls. *Physics of Fluids* **17** (3), 035102.
- FOROOGHI, P., STROH, A., MAGAGNATO, F., JAKIRLIĆ, S., & FROHNAPFEL, B. 2017 Toward a universal roughness correlation. *Journal of Fluids Engineering* **139** (12).
- FORSTER, V. 1966 Performance loss of modern steam-turbine plant due to surface roughness. *Proceedings of the Institution of Mechanical Engineers* **181** (1), 391–422.
- FURUYA, Y., MIYATA, M., & FUJITA, H. 1976 Turbulent boundary layer and flow resistance on plates roughened by wires **98** (4), 635–643.
- GOODHAND, M. N., WALTON, K., BLUNT, L., LUNG, H. W., MILLER, R. J., & MARSDEN, R. 2016 The limitations of using “Ra” to describe surface roughness. *Journal of Turbomachinery* **138** (10), 101003.
- HAGEN, G. H. L. 1854 *Über den einfluss der temperatur auf die bewegung des wassers in röhren*-. Druckerei der Königl. akademie der wissenschaften.
- HAMA, F. R. 1954 Boundary layer characteristics for smooth and rough surfaces. *Trans. Soc. Nav. Arch. Marine Engrs.* **62**, 333–358.
- JELLY, T., RAMANI, A., NUGROHO, B., HUTCHINS, N., & BUSSE, A. 2022 Impact of spanwise effective slope upon rough-wall turbulent channel flow. *Journal of Fluid Mechanics* **951**, A1.
- JIMÉNEZ, J. 2004 Turbulent flows over rough walls. *Annu. Rev. Fluid Mech.* **36**, 173–196.
- JONES, M., NICKELS, T., & MARUSIC, I. 2008 On the asymptotic similarity of the zero-pressure-gradient turbulent boundary layer. *Journal of Fluid Mechanics* **616**, 195.
- JOUYBARI, M. A., YUAN, J., BRERETON, G. J., & MURILLO, M. S. 2021 Data-driven prediction of the equivalent sand-grain height in rough-wall turbulent flows. *Journal of Fluid Mechanics* **912**, A08.
- VON KÁRMÁN, T. v. 1930 Mechanische änlichkeit und turbulenz. *Nachrichten von der Gesellschaft der Wissenschaften zu Göttingen, Mathematisch-Physikalische Klasse* **1930**, 58–76.

- KEIRSBULCK, L., LABRAGA, L., MAZOUZ, A., & TOURNIER, C. 2002 Surface roughness effects on turbulent boundary layer structures. *Journal of Fluids Engineering* **124** (1), 127–135.
- KOCH, C. & SMITH JR, L. 1976 Loss sources and magnitudes in axial-flow compressors. *Journal of Engineering for Power* **98** (3), 411–424.
- KOLMOGOROV, A. N. 1991 The local structure of turbulence in incompressible viscous fluid for very large Reynolds numbers. *Proceedings of the Royal Society of London. Series A: Mathematical and Physical Sciences* **434** (1890), 9–13.
- KROGSTAD, P.-Å. & ANTONIA, R. 1994 Structure of turbulent boundary layers on smooth and rough walls. *Journal of Fluid Mechanics* **277**, 1–21.
- KROGSTAD, P.-Å., ANTONIA, R., & BROWNE, L. 1992 Comparison between rough-and smooth-wall turbulent boundary layers. *Journal of Fluid Mechanics* **245**, 599–617.
- KROGSTAD, P.-Å. & ANTONIA, R. A. 1999 Surface roughness effects in turbulent boundary layers. *Experiments in Fluids* **27** (5), 450–460.
- KUNKEL, G. J. & MARUSIC, I. 2006 Study of the near-wall-turbulent region of the high-reynolds-number boundary layer using an atmospheric flow. *Journal of Fluid Mechanics* **548**, 375–402.
- KUWATA, Y. & KAWAGUCHI, Y. 2019 Direct numerical simulation of turbulence over systematically varied irregular rough surfaces. *Journal of Fluid Mechanics* **862**, 781–815.
- LANGELANDSVIK, L., KUNKEL, G., & SMITS, A. J. 2008 Flow in a commercial steel pipe. *Journal of Fluid Mechanics* **595**, 323–339.
- LEE, S., LELE, S. K., & MOIN, P. 1992 Simulation of spatially evolving turbulence and the applicability of Taylor’s hypothesis in compressible flow. *Physics of Fluids A: Fluid Dynamics* **4** (7), 1521–1530.
- LEE, S.-H. & SUNG, H. J. 2007 Direct numerical simulation of the turbulent boundary layer over a rod-roughened wall. *Journal of Fluid Mechanics* **584**, 125–146.
- LEONARDI, S., ORLANDI, P., DJENIDI, L., & ANTONIA, R. A. 2004 Structure of turbulent channel flow with square bars on one wall. *International Journal of Heat and Fluid Flow* **25** (3), 384–392.
- LEWKOWICZ, A. & MUSKER, A. 1978 The surface roughness on ship hulls: interaction in the viscous sublayer. In *Proceedings of the International Symposium on Ship Viscous Resistance-SSPA*.
- LIGRANI, P. M. & MOFFAT, R. J. 1986 Structure of transitionally rough and fully rough turbulent boundary layers. *Journal of Fluid Mechanics* **162**, 69–98.
- LIN, C. C. 1953 On Taylor’s hypothesis and the acceleration terms in the Navier-Stokes equation. *Quarterly of Applied Mathematics* **10** (4), 295–306.
- LUMLEY, J. 1965 Interpretation of time spectra measured in high-intensity shear flows. *Physics of Fluids* **8** (6), 1056–1062.
- MANNING, R., GRIFFITH, J. P., PIGOT, T., & VERNON-HARCOURT, L. F. 1890 *On the flow of water in open channels and pipes*.

- MARUSIC, I., MCKEON, B. J., MONKEWITZ, P. A., NAGIB, H. M., SMITS, A. J., & SREENIVASAN, K. R. 2010 Wall-bounded turbulent flows at high Reynolds numbers: recent advances and key issues. *Physics of fluids* **22** (6), 065103.
- MARUSIC, I., MONTY, J. P., HULTMARK, M., & SMITS, A. J. 2013 On the logarithmic region in wall turbulence. *Journal of Fluid Mechanics* **716**, R3.
- MEDJNOUN, T., RODRIGUEZ-LOPEZ, E., FERREIRA, M., GRIFFITHS, T., MEYERS, J., & GANAPATHISUBRAMANI, B. 2021 Turbulent boundary-layer flow over regular multiscale roughness. *Journal of Fluid Mechanics* **917**, A1.
- MILLIKAN, C. B. 1939 A critical discussion of turbulent flow in channels and circular tubes. In *Proc. 5th Int. Congress on Applied Mechanics (Cambridge, MA, 1938)*, pp. 386–392. Wiley.
- MONTY, J., DOGAN, E., HANSON, R., SCARDINO, A., GANAPATHISUBRAMANI, B., & HUTCHINS, N. 2016 An assessment of the ship drag penalty arising from light calcareous tubeworm fouling. *Biofouling* **32** (4), 451–464.
- MONTY, J., HUTCHINS, N., NG, H., MARUSIC, I., & CHONG, M. 2009 A comparison of turbulent pipe, channel and boundary layer flows. *Journal of Fluid Mechanics* **632**, 431–442.
- MOODY, L. F. 1944 Friction factors for pipe flow. *Trans. ASME* **66**, 671–684.
- MUSKER, A. J. 1980 Universal roughness functions for naturally-occurring surfaces. *Transactions of the Canadian Society for Mechanical Engineering* **6** (01), 1–6.
- NAPOLI, E., ARMENIO, V., & DE MARCHIS, M. 2008 The effect of the slope of irregularly distributed roughness elements on turbulent wall-bounded flows. *Journal of Fluid Mechanics* **613**, 385–394.
- NIKURADSE, J. 1933 Laws of flow in rough pipes. *Translation from German published 1950 as NACA Tech. Memo. 1292*.
- NUGROHO, B., HUTCHINS, N., & MONTY, J. P. 2013 Large-scale spanwise periodicity in a turbulent boundary layer induced by highly ordered and directional surface roughness. *International Journal of Heat and Fluid Flow* **41**, 90–102.
- OSEEN, C. W. 1910 Uber die stokes' sche formel und uber eine verwandte aufgabe in der hydrodynamik. *Arkiv Mat., Astron. och Fysik* **6**, 1.
- PERRY, A., HENBEST, S., & CHONG, M. 1986 A theoretical and experimental study of wall turbulence. *Journal of Fluid Mechanics* **165**, 163–199.
- PERRY, A., LIM, K., & HENBEST, S. 1987 An experimental study of the turbulence structure in smooth-and rough-wall boundary layers. *Journal of Fluid Mechanics* **177**, 437–466.
- PERRY, A. E. & LI, J. D. 1990 Experimental support for the attached-eddy hypothesis in zero-pressure-gradient turbulent boundary layers. *Journal of Fluid Mechanics* **218**, 405–438.
- PERRY, A. E., SCHOFIELD, W. H., & JOUBERT, P. N. 1969 Rough wall turbulent boundary layers. *Journal of Fluid Mechanics* **37** (2), 383–413.
- PLACIDI, M. & GANAPATHISUBRAMANI, B. 2018 Turbulent flow over large roughness elements: effect of frontal and plan solidity on turbulence statistics and structure. *Boundary-Layer Meteorology* **167** (1), 99–121.

- PRANDTL, L. 1904 On fluid motions with very small friction. *Verhldg* **3**, 484–491.
- PRANDTL, L. 1925 7. Bericht über Untersuchungen zur ausgebildeten Turbulenz. *ZAMM-Journal of Applied Mathematics and Mechanics/Zeitschrift für Angewandte Mathematik und Mechanik* **5** (2), 136–139.
- RAMANI, A., NUGROHO, B., BUSSE, A., MONTY, J. P., HUTCHINS, N., & JELLY, T. O. 2020 The effects of anisotropic surface roughness on turbulent boundary-layer flow. In *22nd Australasian Fluid Mechanics Conference, AFMC 2020*. The University of Queensland.
- RAUPACH, M. R., ANTONIA, R. A., & RAJAGOPALAN, S. 1991 Rough-wall turbulent boundary layers. *Applied Mechanics Reviews* **44** (1), 1–25.
- ROMANO, G. P. 1995 Analysis of two-point velocity measurements in near-wall flows. *Experiments in Fluids* **20** (2), 68–83.
- SARAKINOS, S. & BUSSE, A. 2022 Investigation of rough-wall turbulence over barnacle roughness with increasing solidity using direct numerical simulations. *Physical Review Fluids* **7** (6), 064602.
- SCHLICHTING, H. & KESTIN, J. 1961 *Boundary layer theory*, 9th edn. vol. 121, New York: McGraw-Hill.
- SCHULTZ, M. & FLACK, K. 2005 Outer layer similarity in fully rough turbulent boundary layers. *Experiments in Fluids* **38**, 328–340.
- SCHULTZ, M. & FLACK, K. 2007 The rough-wall turbulent boundary layer from the hydraulically smooth to the fully rough regime. *Journal of Fluid Mechanics* **580**, 381–405.
- SCHULTZ, M. P. & FLACK, K. A. 2009 Turbulent boundary layers on a systematically varied rough wall. *Physics of Fluids* **21**, 015104.
- SHOCKLING, M., ALLEN, J., & SMITS, A. 2006 Roughness effects in turbulent pipe flow. *Journal of Fluid Mechanics* **564**, 267–285.
- SIGAL, A. & DANBERG, J. E. 1990 New correlation of roughness density effect on the turbulent boundary layer. *AIAA Journal* **28** (3), 554–556.
- SIMPSON, R. L. 1973 A generalized correlation of roughness density effects on the turbulent boundary layer. *AIAA Journal* **11** (2), 242–244.
- STIMPSON, C. K., SNYDER, J. C., THOLE, K. A., & MONGILLO, D. 2017 Scaling roughness effects on pressure loss and heat transfer of additively manufactured channels. *Journal of Turbomachinery* **139** (2).
- TANI, I., MEIER, H., & BRADSHAW, P. 1987 Turbulent boundary layer development over rough surfaces. *Perspectives in Turbulence Studies* **3**, 223–249.
- TAYLOR, G. I. 1938 The spectrum of turbulence. *Proceedings of the Royal Society of London. Series A-Mathematical and Physical Sciences* **164** (919), 476–490.
- TENNEKES, H., LUMLEY, J. L., LUMLEY, J. L., ET AL. 1972 *A first course in turbulence*. MIT press.

- THAKKAR, M., BUSSE, A., & SANDHAM, N. 2017 Surface correlations of hydrodynamic drag for transitionally rough engineering surfaces. *Journal of Turbulence* **18** (2), 138–169.
- TOWNSEND, A. 1980 *The structure of turbulent shear flow*. Cambridge university press.
- ÜNAL, U. O. 2015 Correlation of frictional drag and roughness length scale for transitionally and fully rough turbulent boundary layers. *Ocean Engineering* **107**, 283–298.
- VAN RIJ, J. A., BELNAP, B., & LIGRANI, P. 2002 Analysis and experiments on three-dimensional, irregular surface roughness. *Journal of Fluids Engineering* **124** (3), 671–677.
- VOLINO, R., SCHULTZ, M., & FLACK, K. 2007 Disturbance growth in boundary layers subjected to free-stream turbulence. *Journal of Fluid Mechanics* **592**, 263–293.
- WAIGH, D. R. & KIND, R. J. 1998 Improved aerodynamic characterization of regular three-dimensional roughness. *AIAA Journal* **36** (6), 1117–1119.
- YUAN, J. & PIOMELLI, U. 2014 Estimation and prediction of the roughness function on realistic surfaces. *Journal of Turbulence* **15** (6), 350–365.
- ZAMAN, K. & HUSSAIN, A. 1981 Taylor hypothesis and large-scale coherent structures. *Journal of Fluid Mechanics* **112**, 379–396.

Chapter 3

Methodology

3.1 WIND TUNNEL FACILITY

All the experiments were performed in a closed-return wind tunnel at the University of Adelaide. The wind tunnel fan has the capability to spin at a maximum rate of 1500 revolutions per minute (rpm). The air that exits the fan is then directed through a series of turning vanes and into a settling chamber, which contains hexagonal cells, a honeycomb flow straightener, and three screens that help reduce turbulence. The air then undergoes an 8:1 compression before entering the testing section. The testing section is capable of reaching a free-stream velocity of 30 m/s with a turbulence intensity of around 0.5%. The testing section has a rectangular cross-section of 500 mm by 300 mm and a length of 2000 mm. The pressure gradient inside the testing section can be altered by adjusting the sidewalls. After exiting the testing section, the air goes through a diffuser before it is redirected back to the fan. A simple illustration of the wind tunnel is shown in Figure 3.1.

To ensure that the flow was at zero pressure gradient in our experiments, the acceleration parameter $K = (\nu/U_\infty^2)(dU_\infty/dx)$ was maintained less than 3×10^{-8} along the test section from upstream to downstream. The test section's width should be at least six times larger than the boundary layer thickness δ to ensure the boundary layer developed in the test section is 2D (Nickels *et al.*, 2005). In all our measurements, the maximum δ was 70 mm, which is more than seven times smaller than the width of the test section. A 4 mm diameter threaded rod followed by a 100 mm strip of sandpaper with 36 grit No. were used at the inlet of the test section to trip the flow and develop a turbulent boundary layer from the upstream of the test section.

3.2 SURFACE ROUGHNESS

Surface roughness refers to the small, irregular deviations on the surface of a material that causes it to deviate from a perfect plane. Surface roughness can result from various mechanisms, including manufacturing processes and normal wear and tear of products, as well as erosion, corrosion, and deposition processes. These types of roughness can compromise the safety, performance, and efficiency of systems by altering the turbulent structure and momentum and energy transfer. For example, natural degradation and deposition processes in gas turbines have been found to decrease compressor and turbine performance due to surface roughness (Bons, 2010). On the other hand, intentionally manufactured roughness features are used for drag reduction and aerodynamic enhancement. For instance, dimples on golf balls and sharkskin denticles on

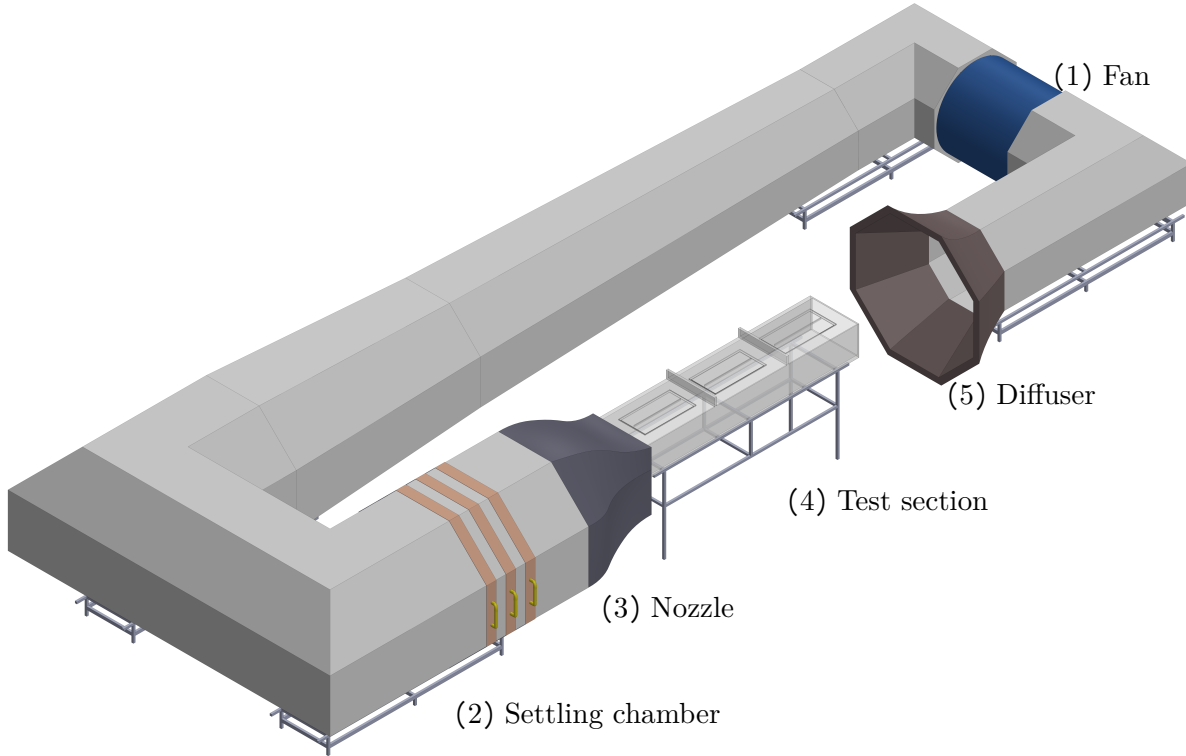


FIGURE 3.1: A schematic of the University of Adelaide wind tunnel. The air is guided from (1) the fan through a series of turning vanes into (2) the settling chamber consists of a honeycomb flow straightener, and three screens, then enter (3) the nozzle and (4) the test section before redirecting back through (5) the diffuser to the fan.

aircraft surfaces provide drag reduction (Soleimani & Eckels, 2021). It is difficult to fully describe roughness using just one physical parameter due to its diverse forms, types and textures. To understand its impact on drag, it is essential to identify the key roughness parameters that have the most influence. Furthermore, a formula for the equivalent sand grain roughness denoted as k_s , should be created by combining these important parameters.

Height is often used as the primary roughness parameter for characterisation. Various heights can be obtained from roughness topography, such as average roughness height (k_a), root-mean-square roughness height (k_q), and the maximum peak to valley roughness height (k_t) (ASME, 2009). However, none of these roughness height parameters is able to fully describe roughness by themselves.

k_a is one of the most commonly used roughness parameters, and it is directly proportional to the drag experienced by an object in a fluid flow. k_a (arithmetic average roughness) is a measure of the overall roughness of a surface. It is the average distance between the roughness profile and the centerline. The roughness profile is a representation of the surface's deviation from a perfect plane, and the centerline is the average height of the surface. The k_a value is calculated by taking the difference between the roughness profile and the centerline at each point along the surface and then averaging these differences over the entire sampling length L_s or area A_s .

$$k_a = \frac{1}{A_s} \int \int_{A_s} |Y(x, z)| dx dz. \quad (3.1)$$

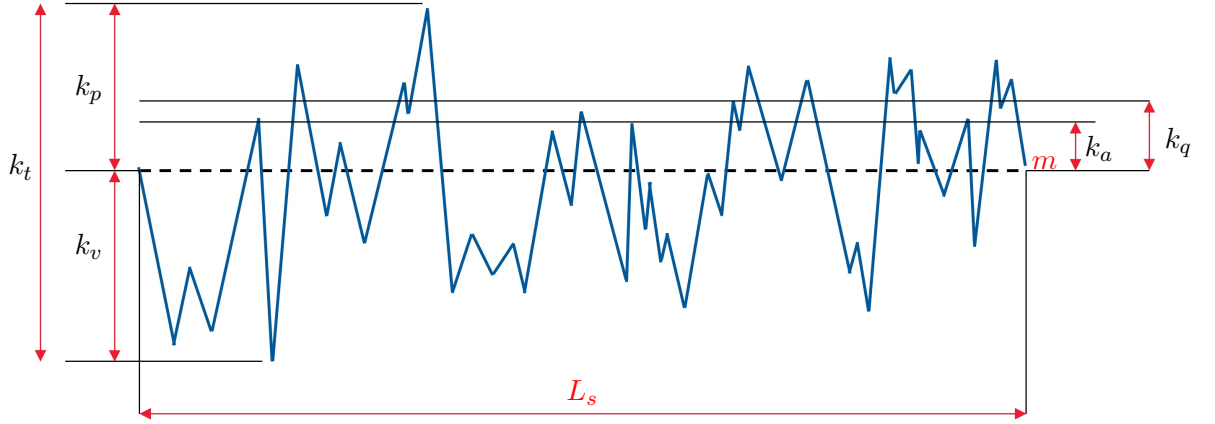


FIGURE 3.2: The main roughness heights parameters on a sampling length L_s . The dashed line represents the mean line m , the reference line about which the profile deviations are measured.

k_q (root-mean-square roughness) is a measure of the roughness of a surface that takes into account the entire roughness profile, not just the average roughness. It is defined as the root-mean-square of the roughness profile's deviation from the centerline. The k_q value is calculated by taking the difference between the roughness profile and the centerline at each point along the surface, squaring these differences, averaging the squares, and then taking the square root of the average. k_q is used to characterise surfaces with a relatively high degree of irregularity. It is also directly proportional to the drag experienced by an object in a fluid flow.

$$k_q = \sqrt{\frac{1}{A_s} \int \int_{A_s} Y(x, z)^2 dx dz}. \quad (3.2)$$

k_t (maximum roughness height) is a measure of the roughness of a surface that is based on the highest peaks and the lowest valleys of the roughness profile. It is defined as the difference between the highest peak and the lowest valley in the roughness profile within the sampling length or area. The k_t value is calculated by measuring the height of the highest peak k_p and the depth of the lowest valley k_v of the roughness profile and subtracting k_v from k_p . k_t is also used to characterise surfaces with a relatively large degree of irregularity. It is also directly proportional to the drag experienced by an object in a fluid flow. Figure 3.2 shows the main roughness heights parameters on a sampling length L_s .

$$k_t = k_p - k_v. \quad (3.3)$$

As mentioned previously, the roughness height is insufficient to characterise the surface roughness solely. Hence, another roughness category must be employed.

Roughness frontal solidity λ_f is a measure of the ratio of A_f to A_t . It is a dimensionless value commonly used to evaluate the effect of surface roughness on fluid flow. A_t is the area of the surface that is occupied by the roughness elements, such as peaks and valleys, while A_f is the area of the surface that is visible to the fluid flow. The roughness frontal solidity is calculated by dividing the frontal projected roughness area by the total area.

$$\lambda_f = \frac{A_f}{A_t}. \quad (3.4)$$

This parameter can be useful in determining the drag force and friction caused by the

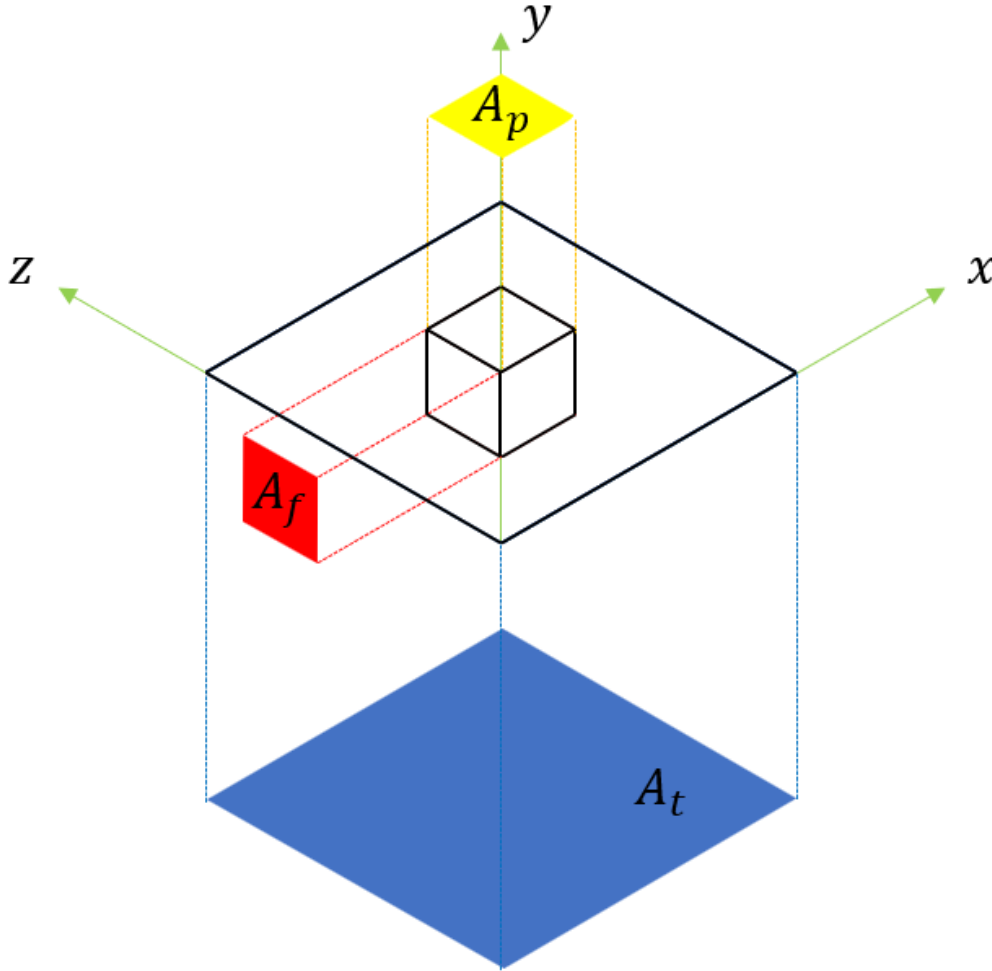


FIGURE 3.3: Sketch of rough surface illustrates how frontal and plan solidity are calculated. The red area is the frontal projection of the rough element. The yellow area represents the plan projection of the rough element. The blue area is the projection of the total area of the surface.

roughness in fluid flow. It is often used in aerodynamics, hydrodynamics, and heat transfer studies. Figure 3.3 shows a simple schematic of how frontal and plan solidity are calculated.

A more general and robust roughness parameter used to characterise the roughness named the effective slope ES introduced by Napoli *et al.* (2008) is a measure of the average slope of the roughness elements on a surface. It is a dimensionless value that is used to evaluate the effect of surface roughness on fluid flow. It is also known as the average slope of the roughness profile or the average inclination angle of the roughness elements. The ES in a specific direction is calculated by measuring the slope of the roughness elements at various points along the surface and then averaging these slopes over the entire sampling length or area.

$$ES_x = \frac{1}{A_s} \iint_{A_s} \left| \frac{dY(x,z)}{dx} \right| dx dz, \quad (3.5)$$

$$ES_z = \frac{1}{A_s} \iint_{A_s} \left| \frac{dY(x,z)}{dz} \right| dx dz. \quad (3.6)$$

Roughness effective slope is an important parameter in understanding the effect of roughness on fluid flow. A high roughness effective slope indicates that the roughness elements are steep and are likely to have a significant effect on the fluid flow. In contrast, a low roughness

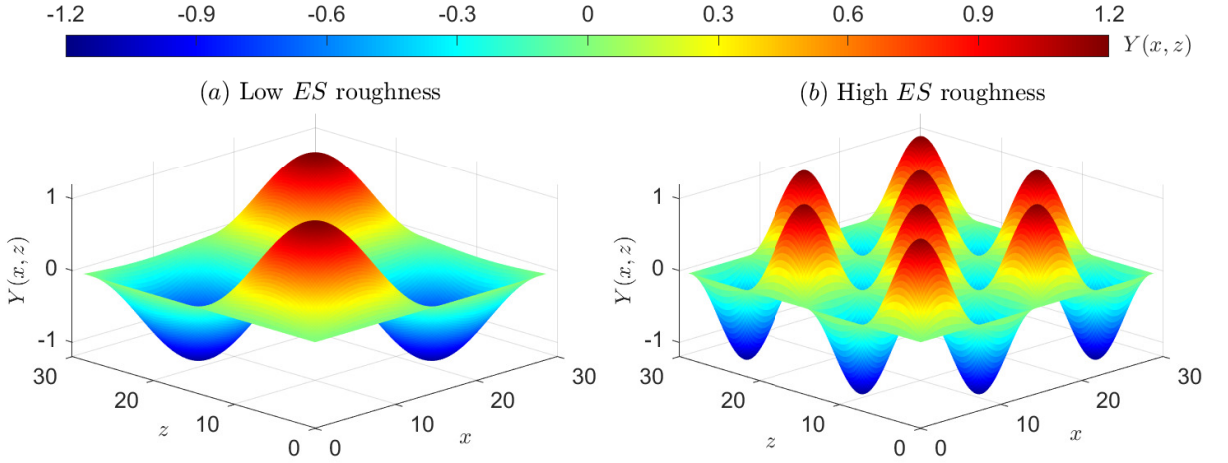


FIGURE 3.4: Sketches of different configurations of 3D isotropic sinusoidal surfaces with equal streamwise and spanwise roughness effective slopes. (a) Low ES value. (b) High ES value. The contours are plotted with the same coordinates for ease of comparison.

effective slope indicates that the roughness elements are gentle and are likely to have a minimal effect on the fluid flow. Figure 3.4 shows a simple schematic of different configurations of 3D isotropic sinusoidal surfaces with low and high ES values.

Even though the roughness height and effective slope are likely to describe the roughness well enough, they do not provide any information about the roughness density or asymmetry in surface-elevation distribution. Hence, a third roughness category should be presented.

The plan solidity λ_p is defined as the ratio between the projected plan area of roughness element A_p to the total area. This parameter measures how dense the roughness (Placidi & Ganapathisubramani, 2015) is.

$$\lambda_p = \frac{A_p}{A_t}. \quad (3.7)$$

The λ_p when combined with λ_f can improve the roughness description. The skewness of the roughness is more usable than the plan solidity and can be used for regular and irregular roughness. Roughness skewness k_{sk} is a measure of the asymmetry of the roughness profile of a surface. It is a dimensionless value commonly used to evaluate the effect of surface roughness on fluid flow. Roughness skewness is calculated by measuring the difference between the roughness profile and the centerline at various points along the surface, cubing these differences, averaging the cubes, and then dividing by the cube of the standard deviation. A positive value of roughness skewness indicates that the roughness profile has more peaks than valleys, while a negative value indicates that the roughness profile has more valleys than peaks.

$$k_{sk} = \frac{1}{k_q^3 A_s} \int \int_{A_s} Y(x, z)^3 dx dz, \quad (3.8)$$

Roughness skewness is an important parameter in understanding the effect of roughness on fluid flow, particularly in turbulent flows. A high positive skewness denotes a surface dominated by peaks, and a high negative skewness denotes a surface dominated by depressions. Figure 3.5 shows a simple schematic of different configurations of 3D isotropic sinusoidal surfaces with negative, zero and positive skewness values.

Roughness kurtosis k_{ku} is a measure of the peakedness or flatness of the roughness profile of a surface. It is a dimensionless value commonly used to evaluate the effect of surface

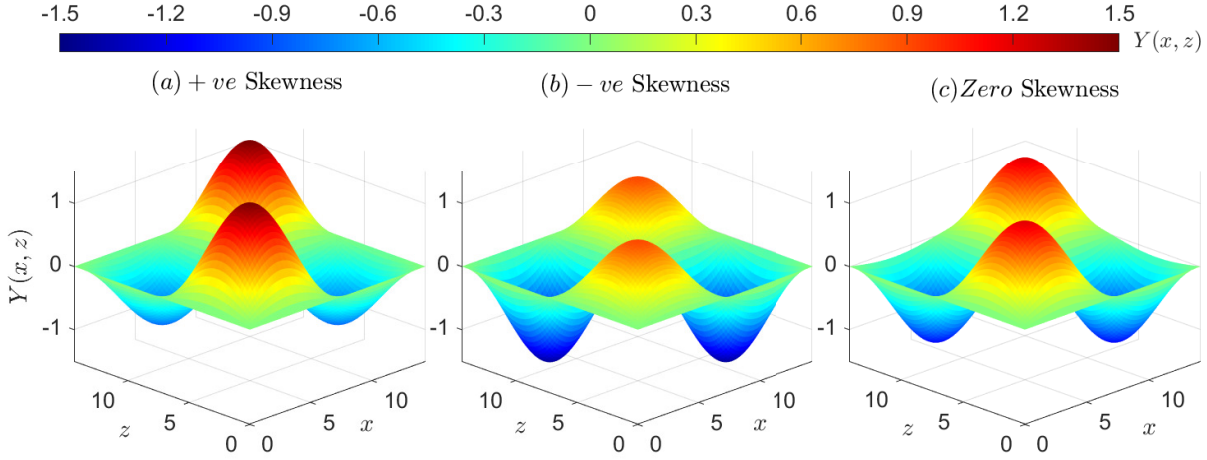


FIGURE 3.5: Sketches of different configurations of 3D isotropic sinusoidal surfaces with equal streamwise and spanwise roughness skewness. (a) Positive skewness value. (b) Negative skewness value. (c) Zero skewness roughness. The contours are plotted with the same coordinates for ease of comparison.

roughness on fluid flow. Roughness kurtosis is calculated by measuring the difference between the roughness profile and the centerline at various points along the surface, raising these differences to the fourth power, averaging the fourth power, and then dividing by the fourth power of the standard deviation. The roughness that exhibits high kurtosis is characterised by a noticeable peak in their distribution around the mean, a rapid decrease in the frequency of observations as we move away from the peak, and a tail that extends far from the mean. On the other hand, the roughness with low kurtosis tends to display a more uniform distribution near the mean, lacking a sharp peak that is commonly observed in high kurtosis datasets. $k_{ku} = 3$ is the normal Gaussian distribution.

$$k_{ku} = \frac{1}{k_q^4 A_s} \int \int_{A_s} Y(x, z)^4 dx dz, \quad (3.9)$$

A combination of that three roughness categories (height, slope and asymmetry) is believed to best characterise the rough surface. To investigate the impact of roughness parameters on a turbulent boundary layer (TBL) and determine which parameters affect turbulence statistics and drag coefficient, various types of specimens are manufactured and tested. The starting point is an aluminium plate serving as a smooth wall reference surface. First, cylindrical rods, triangular ribs, and 2D sinewave surfaces with varying heights and height-to-spacing ratios are used as 2D uniformly distributed roughness and cover a broad range of roughness parameters. Second, 3D sinewave roughness with different streamwise and spanwise wavelengths and different skewness values are used in the systematic investigation of the major roughness parameters over 3D uniformly distributed roughness. A uniformly distributed roughness is the optimal choice for studying the effect of roughness parameters as it is designed to focus on one or two major parameters that impact the drag coefficient while fixing most of the roughness parameters.

For the 2D rough surfaces, where Y is a function of x only, the circular rods are aluminium tungsten inert gas (TIG) rods with 500 mm in length and two different diameters used, $k = 1.6$ and 2.4 mm. The rods are taped on the smooth aluminium sheet with five different streamwise spacing to height ratios s_x/k ranging from 6 to 24. The triangular ribs are 3D printed with a total of 30 plates with height $k = 1.6$ mm and $8k$ wavelength; each plate measures 145 mm \times 153.6 mm. The 3D-printed triangular ribs are printed from acrylonitrile butadiene styrene

(ABS) material using a fused deposition modelling (FDM) 3D printer, Zortrax M200. This model has an accuracy of 200 μm in the x & z directions, and a layer height of 90 μm with a 0.4 mm nozzle diameter. The 2D sinewave surfaces are 6 mm acrylic sheets which, computerized numerical control (CNC) machined with different 2D sinewave profiles that have an amplitude of $k/2 = 0.8$ mm and a wavelength of $8k$; these CNC machined surfaces are machined by a custom carbide engraving cutters (flat-end mill) of a TORMACH PCNC-series 3 machine. The ball nose cutter has a diameter of 12 mm. A periodic function describes the 2D rough surfaces of rods, ribs, and sinewaves, respectively as follows:

$$Y(x) = \begin{cases} \sqrt{kx - x^2} & 0 \leq x \leq k, \\ -\frac{k}{2} & k < x < s_x, \end{cases} \quad (3.10)$$

$$Y(x) = \begin{cases} -\frac{k}{2} + \frac{2kx}{s_x} & 0 \leq x \leq s_x/2, \\ -\frac{k}{2} + \frac{2k(s_x - x)}{s_x} & s_x/2 \leq x \leq s_x, \end{cases} \quad (3.11)$$

$$Y(x) = \frac{k}{2} \sin\left(\frac{2\pi x}{s_x}\right). \quad (3.12)$$

For the 3D rough surfaces, where Y is a function of x & z ; a total of 4 acrylic sheets of 6 mm thickness are CNC machined with 3D sinewave surfaces function that has an amplitude of $k/2 = 1.2$ mm and different wavelengths in the streamwise and spanwise directions ranging from $6k$ to $16k$. Each plate measures around 500 mm \times 500 mm. These surfaces are fabricated by a Multicam M1212 Router machine with custom carbide engraving cutters (flat-end mill) of a TORMACH PCNC-series 3 machine. The 3/8 ball Endmill cutter has a diameter of 9 mm. The absolute values of the profile heights for different rough surfaces are described as follows:

$$Y(x, z) = \frac{k}{2} \sin\left(\frac{2\pi x}{s_x}\right) \sin\left(\frac{2\pi z}{s_z}\right). \quad (3.13)$$

To change the roughness skewness values of the profiles, a different factor is multiplied by either the positive or negative parts of the previous Eq. (3.13) to create different positive and negative skewness values. Figure 3.6 shows a diagram for the systematic variation in roughness parameters for all rough surfaces studied. Statistical parameters used to characterise all the different rough surfaces are tabulated in Table 3.1.

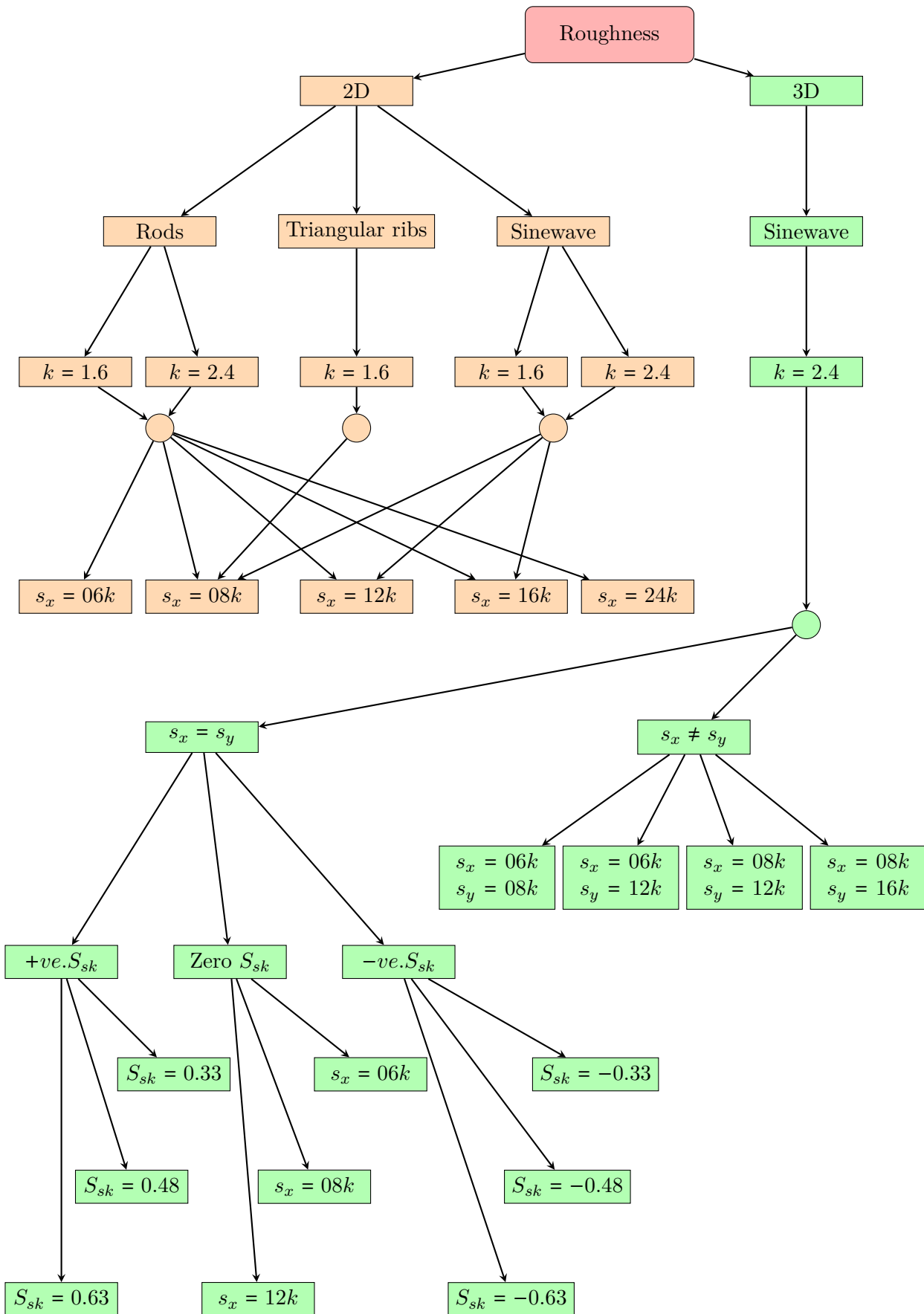


FIGURE 3.6: Roughness chart shows the schematic variation in roughness parameters for all rough surfaces used in the thesis.

TABLE 3.1: Different key surface roughness parameters. The surfaces are defined by the first letter of the geometry: R for rods T for triangular ribs and S for sinewaves, followed by ten times the maximum peak-to-valley height k , then the streamwise spacing to height ratio and the spanwise spacing to height ratio for 3D roughness and followed by the skewness value if it is not equal zero (P for positive and N for negative).

Surface	k_v	k_p	k_t	k_a	k_q	s_x/k	s_z/k	k_{sk}	k_{ku}	ES_x	ES_z
$R16-06$	0.00	1.60	1.60	0.40	0.59	06	-	1.85	4.53	0.33	-
$R16-08$	0.00	1.60	1.60	0.31	0.51	08	-	2.34	6.57	0.25	-
$R16-12$	0.00	1.60	1.60	0.22	0.42	12	-	3.09	10.7	0.18	-
$R16-16$	0.00	1.60	1.60	0.17	0.36	16	-	3.70	14.9	0.13	-
$R16-24$	0.00	1.60	1.60	0.11	0.29	24	-	4.69	23.3	0.08	-
$R24-06$	0.00	2.40	2.40	0.60	0.88	06	-	1.85	4.53	0.33	-
$R24-08$	0.00	2.40	2.40	0.47	0.76	08	-	2.34	6.57	0.25	-
$R24-12$	0.00	2.40	2.40	0.33	0.62	12	-	3.09	10.7	0.18	-
$R24-16$	0.00	2.40	2.40	0.25	0.54	16	-	3.70	14.9	0.13	-
$R24-24$	0.00	2.40	2.40	0.17	0.44	24	-	4.69	23.3	0.08	-
$T16-08$	-0.80	0.80	1.60	0.40	0.92	08	-	0.00	1.80	0.25	-
$S16-08$	-0.80	0.80	1.60	0.51	0.57	08	-	0.00	1.50	0.25	-
$S16-12$	-0.80	0.80	1.60	0.51	0.57	12	-	0.00	1.50	0.17	-
$S16-16$	-0.80	0.80	1.60	0.51	0.57	16	-	0.00	1.50	0.13	-
$S24-08$	-1.20	1.20	2.40	0.76	0.85	08	-	0.00	1.50	0.25	-
$S24-12$	-1.20	1.20	2.40	0.76	0.85	12	-	0.00	1.50	0.17	-
$S24-16$	-1.20	1.20	2.40	0.76	0.85	16	-	0.00	1.50	0.13	-
$S24-07-07P33$	-1.00	1.40	2.40	0.47	0.60	07	07	0.33	2.36	0.18	0.18
$S24-06-06P48$	-0.90	1.50	2.40	0.47	0.60	06	06	0.48	2.43	0.20	0.20
$S24-05-05P63$	-0.80	1.60	2.40	0.47	0.60	05	05	0.63	2.53	0.22	0.22
$S24-06-06$	-1.20	1.20	2.40	0.47	0.60	06	06	0.00	2.30	0.20	0.20
$S24-08-08$	-1.20	1.20	2.40	0.47	0.60	08	08	0.00	2.30	0.15	0.15
$S24-12-12$	-1.20	1.20	2.40	0.47	0.60	12	12	0.00	2.30	0.10	0.10
$S24-07-07N33$	-1.40	1.00	2.40	0.47	0.60	07	07	-0.33	2.36	0.18	0.18
$S24-06-06N48$	-1.50	0.90	2.40	0.47	0.60	06	06	-0.48	2.43	0.20	0.20
$S24-05-05N63$	-1.60	0.80	2.40	0.47	0.60	05	05	-0.63	2.53	0.22	0.22
$S24-06-08$	-1.20	1.20	2.40	0.47	0.60	06	08	0.00	2.30	0.20	0.15
$S24-06-12$	-1.20	1.20	2.40	0.47	0.60	06	12	0.00	2.30	0.20	0.10
$S24-08-06$	-1.20	1.20	2.40	0.47	0.60	08	06	0.00	2.30	0.15	0.20
$S24-08-12$	-1.20	1.20	2.40	0.47	0.60	08	12	0.00	2.30	0.15	0.10
$S24-08-16$	-1.20	1.20	2.40	0.47	0.60	08	16	0.00	2.30	0.15	0.08
$S24-12-06$	-1.20	1.20	2.40	0.47	0.60	12	06	0.00	2.30	0.10	0.20
$S24-12-08$	-1.20	1.20	2.40	0.47	0.60	12	08	0.00	2.30	0.10	0.15
$S24-16-08$	-1.20	1.20	2.40	0.47	0.60	16	08	0.00	2.30	0.08	0.15

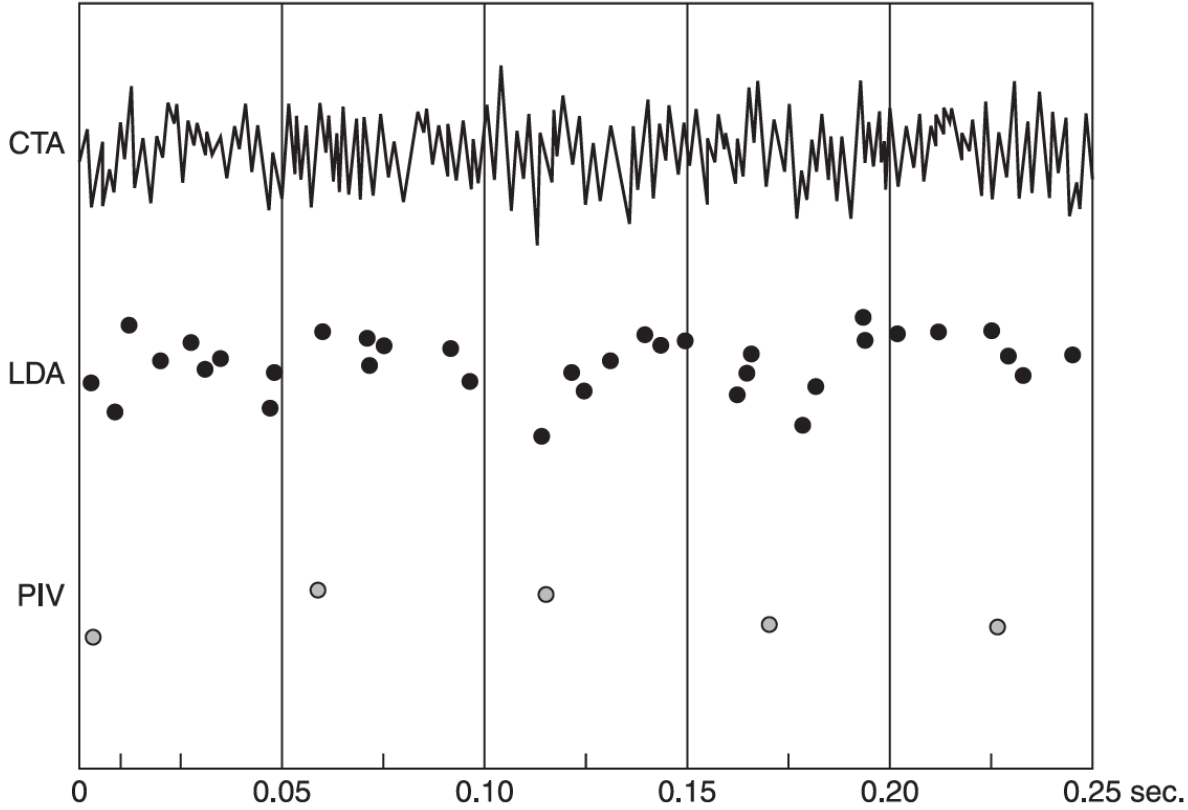


FIGURE 3.7: Output signals from constant temperature anemometry (CTA), laser doppler anemometry (LDA) and particle image velocimetry (PIV) [Chanson \(2013\)](#)

3.3 MEASURING STATION

All the experimental study is conducted using hotwire anemometry (HWA) to assess stream-wise velocity fluctuations, as HWA has a stronger high-frequency response compared to laser doppler anemometry (LDA) and particle image velocimetry (PIV), as shown in Figure 3.7

To minimise the end-conduction effects of the hotwire probe, a hotwire length-to-diameter ratio of 200 is required. The viscous-scaled wire length l^+ should also be kept at 20 or less to reduce the spatial attenuation of the probe, as suggested by ([Ligrani & Bradshaw, 1987](#); [Hutchins *et al.*, 2009](#)). Therefore, a single hotwire boundary layer probe is constructed by soldering a 1.5 mm Wollaston wire with a Platinum core onto the prongs, and then etching a 0.5 mm length to reveal a 2.5 μm diameter Platinum wire for measurements. A constant temperature anemometer (CTA), in-house manufactured, is attached to the probe and an overheat ratio (OHR) of 1.8 is utilised. The impact of varying the OHR on the response of hotwire anemometers was studied experimentally by [Ardekani & Farhani \(2009\)](#), who found that increasing OHR reduced the error in the constant temperature anemometer response. The offset and gain are adjusted to make use of the full range of voltages acquired with the best resolutions. Dynamic calibration of the hotwire, known as a square wave test (SQT), is performed to determine the hotwire's cut-off frequency. The system bandwidth f_c , where the frequency response drops 3 dB, is calculated using the equation $f_c = 1/1.3\tau$, where τ is the time when the response signal drops to 97% of its peak response. The cut-off frequency is defined as f_c . It is considered optimal for the frequency response of a constant temperature anemometer to have an undershoot of 15% of the peak response.

An in-situ static calibration of the hotwire using a Pitot-static tube in the freestream

is conducted before and after each experiment, to account for any drift. The measurement is repeated if the pre- and post-calibrations do not match within a 1% error margin. The hotwire output voltage is mapped to the actual velocity measured by the Pitot-static tube using a sixth-degree polynomial. The pressure analogue voltage signal is obtained with Baratron differential pressure transducer connected to the Pitot-static tube. The mean temperature during experiments is recorded using a T-type thermocouple, and the temperature variation was monitored within $\pm 0.5^\circ\text{C}$ for each measurement. A National Instruments data acquisition board NI-9234 model is connected to the PC computer to convert the velocity, pressure, and temperature analogue voltage signals to digital voltage signals. The DAQ has four analog input channels with a dynamic range of 102 dB. Each input channel can sample at rates as fast as 51.2 kHz with 24-bit resolution. The NI-9234 DAQ has signal ranges from -5 to 5 Volts. Figure 3.8 shows a diagram of the measuring station of the streamwise velocity.

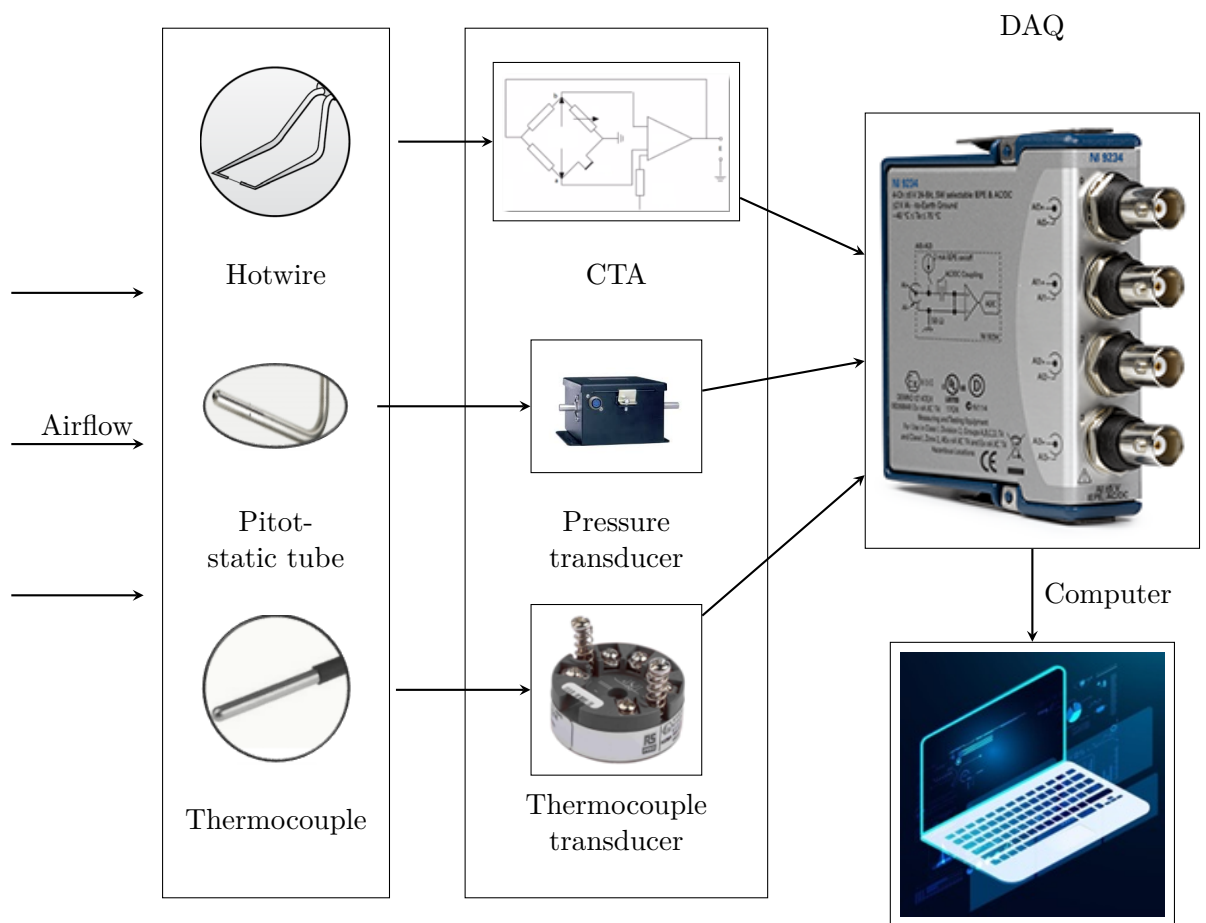


FIGURE 3.8: A schematic of the streamwise velocity measurement procedures.

The hotwire probe is attached to a 2D traverse that can move 300 mm with a step of 50 μm and 5 μm in z and y directions, respectively. Closed feedback from two linear glass encoders with 10 μm and 1 μm resolution in z and y axis, respectively, attached to the 2D traverse, is used to minimise the movement error of the 2D traverse.

Bibliography

- ARDEKANI, M. & FARHANI, F. 2009 Experimental study on response of hot wire and cylindrical hot film anemometers operating under varying fluid temperatures. *Flow Measurement and Instrumentation* **20** (4-5), 174–179.
- ASME 2009 Surface Texture (Surface Roughness, Waviness, and Lay). *Revision of ANSI/ASME B46.1-1995. Standard. ASME.* .
- BONS, J. P. 2010 A review of surface roughness effects in gas turbines. *Journal of Turbomachinery* **132** (2).
- CHANSON, H. 2013 Book review: Aerodynamic measurements: From physical principles to turnkey instrumentation.
- HUTCHINS, N., NICKELS, T. B., MARUSIC, I., & CHONG, M. S. 2009 Hot-wire spatial resolution issues in wall-bounded turbulence. *Journal of Fluid Mechanics* **635**, 103–136.
- LIGRANI, P. M. & BRADSHAW, P. 1987 Spatial resolution and measurement of turbulence in the viscous sublayer using subminiature hot-wire probes. *Experiments in Fluids* **5** (6), 407–417.
- NAPOLI, E., ARMENIO, V., & DE MARCHIS, M. 2008 The effect of the slope of irregularly distributed roughness elements on turbulent wall-bounded flows. *Journal of Fluid Mechanics* **613**, 385–394.
- NICKELS, T. B., MARUSIC, I., HAFEZ, S., & CHONG, M. S. 2005 Evidence of the k_1^{-1} law in a high-Reynolds-number turbulent boundary layer. *Physical Review Letters* **95**, 074501.
- PLACIDI, M. & GANAPATHISUBRAMANI, B. 2015 Effects of frontal and plan solidities on aerodynamic parameters and the roughness sublayer in turbulent boundary layers. *Journal of Fluid Mechanics* **782**, 541–566.
- SOLEIMANI, S. & ECKELS, S. 2021 A review of drag reduction and heat transfer enhancement by riblet surfaces in closed and open channel flow. *International Journal of Thermofluids* **9**, 100053.

Chapter 4

Outer Turbulent Boundary Layer Similarities

4.1 CHAPTER OVERVIEW

The similarity of the outer layer in boundary layers that develop over different 2D roughness elements in zero pressure gradient conditions is being evaluated in this chapter. Turbulent boundary layer measurements were performed with single hotwire anemometry on various rough surfaces with a δ/k ratio ranging from 21 to 45 in a zero pressure gradient flow. The study examined how turbulence statistics and the drag coefficient are affected by altering the roughness parameters. The study employed two types of 2D roughness geometries: circular rods and sinewave surfaces with varying heights ($k = 1.6$ mm and 2.4 mm) and streamwise spacings ($8k$, $12k$, and $16k$).

The roughness causes the inner-normalised mean profile to shift downward. The shift is called the roughness function. The circular rods cause a greater shift than the sinewave surfaces, resulting in a fully rough regime at lower Re_τ . The greatest shift is observed when the spacing between roughness elements is around $8k$. Varying the roughness height while keeping the same spacing has a minor impact on the drag coefficient in the fully rough regime.

The results of the study showed that the velocity defect profile, when normalized by the friction velocity, exhibits a good collapse between smooth and rough walls, which indicates the universality and similarity of velocity profiles in turbulent boundary layer flows. It further supports the applicability of Townsend's similarity hypothesis, even for small values of δ/k and Re_τ , regardless of the surface or flow conditions.

The mean streamwise turbulence intensity profiles in the fully rough regime have only one peak located at around $y/\delta = 0.06$, which is independent of the roughness geometry. The roughness suppresses the inner peak that is present on smooth walls. The autocorrelation analysis indicates that the coherent motions (on average) have a similar length scale, regardless of the roughness geometry, in the regions above $y/\delta = 0.5$.

4.2 OUTER TURBULENT BOUNDARY LAYER SIMILARITIES FOR DIFFERENT 2D SURFACE ROUGHNESSES AT MATCHED REYNOLDS NUMBER

This section consists of the following published journal article:

Cite as: International Journal of Heat and Fluid Flow **94**, 108940 (2022);

<https://doi.org/10.1016/j.ijheatfluidflow.2022.108940>

Received 2 August 2021 • Revised 20 January 2022 • Accepted 24 January 2022

• Available online 6 February 2022

Misarah Abdelaziz, L. Djenidi, Mergen H. Ghayesh, and Rey Chin.

The article is identical to its submitted format with the following exceptions:

- The numbering of figures, tables and equations has been altered to include the chapter number.
- The position of some figures and tables has been changed to improve the article's legibility.

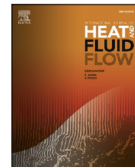
International Journal of Heat and Fluid Flow 94 (2022) 108940



Contents lists available at [ScienceDirect](#)

International Journal of Heat and Fluid Flow

journal homepage: www.elsevier.com/locate/ijhff



Outer turbulent boundary layer similarities for different 2D surface roughnesses at matched Reynolds number

Misarah Abdelaziz ^{a,*}, L. Djenidi ^b, Mergen H. Ghayesh ^a, Rey Chin ^a

^a School of Mechanical Engineering, University of Adelaide, Adelaide 5005, South Australia, Australia

^b Mechanical Engineering Discipline, The University of Newcastle, Callaghan 2308, NSW, Australia

Statement of Authorship

Title of paper	Outer turbulent boundary layer similarities for different 2D surface roughnesses at matched Reynolds number
Publication status	Published
Publication details	Misarah Abdelaziz, L. Djenidi, Mergen H. Ghayesh, and Rey Chin. Outer turbulent boundary layer similarities for different 2D surface roughnesses at matched Reynolds number. <i>International Journal of Heat and Fluid Flow</i> , 94 , 108940 (2022); https://doi.org/10.1016/j.ijheatfluidflow.2022.108940

Principal Author

Name of principal author (candidate)	Misarah Abdelaziz
Contribution to the paper	Conception, acquiring data, knowledge, analysis and drafting
Certification	This paper reports on original research I conducted during the period of my Higher Degree by Research candidature and is not subject to any obligations or contractual agreements with a third party that would constrain its inclusion in this thesis. I am the primary author of this paper.
Signature:	Date: 05/07/2023

Co-author contributions

By signing the Statement of Authorship, each author certifies that:

- i.* the candidate's stated contribution to the publication is accurate (as detailed above)
- ii.* permission is granted for the candidate to include the publication in the thesis; and
- iii.* the sum of all co-author contributions is equal to 100% less the candidate's stated contribution.

Name of co-author	Lyazid Djenidi
Contribution to the paper	Conception, knowledge, analysis and drafting
Signature:	Date: 27/06/2023

Name of co-author	Mergen H. Ghayesh
Contribution to the paper	Conception, knowledge and drafting
Signature:	Date: 04/07/2023

Name of co-author	Rey Chin
Contribution to the paper	Conception, knowledge, analysis and drafting
Signature:	Date: 04/07/2023

Outer turbulent boundary layer similarities for different 2D surface roughnesses at matched Reynolds number

Misarah Abdelaziz^{a,*}, L. Djenidi^b, Mergen H. Ghayesh^a, Rey Chin^a

^a*School of Mechanical Engineering, University of Adelaide, Adelaide, 5005, South Australia, Australia*

^b*Mechanical Engineering Discipline, The University of Newcastle, Callaghan, 2308, NSW, Australia*

Received 2 August 2021; Received in revised form 20 January 2022; Accepted 24 January 2022

Available online 6 February 2022

ABSTRACT

The outer layer similarity in zero pressure gradient (ZPG) boundary layers developing over different geometries of 2D roughness elements is assessed, using single hotwire anemometry. Two types of 2D roughness are used: circular rods and sinewave surfaces with two different heights, $k = 1.6$, and 2.4 mm, and three different streamwise spacings, i.e. $s_x = 8k$, $12k$, and $16k$. These roughnesses cover a range of ratios of the boundary layer thickness (δ) to the roughness height (k) from $\delta/k = 21$ to 45 . As expected, all roughnesses caused a downward shift on the wall-unit normalised streamwise mean velocity profiles compared with smooth wall profiles, with a maximum shift observed for rods with a spacing of $s_x = 8k$, while the minimum shift is noticed for a sinewave surface with a spacing of $s_x = 16k$. The defect velocity profiles collapse entirely for all smooth and rough wall flows when normalised by the friction velocity. It was found that the shape factor, H is a suitable scaling parameter for improving the collapse of the data when using the diagnostic plot. The inner peak of the turbulence intensity profiles for the sinewave roughness is reduced gradually with increasing Reynolds number while the turbulent boundary layer (TBL) develops from a transitionally to a fully rough regime. Meanwhile, this inner peak disappears completely for all rod roughnesses, as the TBL is always in a fully rough regime, and the profiles exhibit only an outer peak, located at a wall-normal location $y/\delta \approx 0.06$. The results suggest that Townsends similarity hypothesis for 2D surface roughness is relatively well approximated in the outer region of the flow as reflected by the collapse of the distributions of velocity defect, turbulence intensity, skewness, and flatness when scaled with δ .

Keywords: Turbulent Boundary Layers, Roughness

*Corresponding author. *E-mail address:* misarah.abdelaziz@adelaide.edu.au (M. Abdelaziz)

<https://doi.org/10.1016/j.ijheatfluidflow.2022.108940>

0142-727X/© 2022 Elsevier Inc. All rights reserved.

4.3 INTRODUCTION

Turbulent boundary layers (TBLs) are present in many fluid dynamics applications, such as aeroplanes and ships. Almost all wall-bounded flow engineering applications have a rough surface. This roughness is a significant design parameter, as it affects the turbulence statistics

and drag coefficient by producing a higher coefficient of friction than smooth surfaces. Therefore, a better understanding of the effect of surface roughness on TBL is the first step towards controlling these flows. Although many researchers have studied the effects of surface roughness on a TBL, roughness remains an active area of research.

Turbulent flows over rough surfaces have been investigated since the early work of [Darcy \(1857\)](#), who was concerned with the pressure losses in water ducts. The literature before the 21st century focused on the flow itself over the rough surfaces. However, in the last twenty years, researchers have been more concerned with the different types of roughness. Roughness has a wide range of geometries and sizes. It is, therefore, crucial to have an approach for comparing different roughnesses. The k -type roughness is the most common type (see [Perry and Joubert, 1963](#)). This type is usually characterised by the equivalent sand grain roughness k_s introduced by [Nikuradse \(1933\)](#), who performed extensive experiments in which pipe surfaces were roughened by coating their internal surfaces with a layer of sand. Roughness height was thus defined as the average diameter of a sand grain.

Rough wall flows have a higher wall drag than flows over smooth surfaces. The coefficient of friction is defined as the wall shear stress over the dynamic pressure, $C_f = 2\tau_w/\rho U_\infty^2$, where U_∞ is the free-stream velocity, τ_w is the wall shear stress, and ρ is the density of the fluid. The rise in C_f is revealed in the streamwise mean velocity profile, as it causes a downward shift of the logarithmic region. This shift is known as the roughness function defined as $\Delta U^+ = \Delta U/U_\tau$, where U is the mean streamwise velocity, and U_τ is the friction velocity; $U_\tau = \sqrt{\tau_w/\rho}$ ([Hama, 1954](#)). Furthermore, (⁺) means normalisation by viscous velocity scale U_τ or length scale ν/U_τ , where ν is the kinematic viscosity. x , y & z are the streamwise, wall-normal and spanwise directions, respectively.

For a fully rough flow regime, there is a log-linear relationship between k_s^+ and ΔU^+ . Conversely, the wall roughness does not affect the viscous sublayer for a dynamically smooth flow regime, and almost all velocity profiles at different Reynolds numbers collapse in the log region. However, for a transitionally rough flow regime, the near-wall flow is affected by both pressure and viscous drag (see [Nikuradse, 1933](#)). There is no clear evidence for the start of these regimes. However, it is commonly considered that the hydraulically smooth regime is at $k_s^+ < 4$, and the fully rough regime is above $k_s^+ > 70$ ([Jiménez, 2004](#); [Ligrani and Moffat, 1986](#)).

Most of the experimental and numerical studies confirm Townsend’s claims about wall similarity theory ([Townsend, 1956](#)) that, “At distances from the wall large compared with the extent of the flow patterns set up by individual roughness elements, the turbulent flow is unlikely to be affected by the exact nature of the roughness and, as with the smooth wall, it will be determined by the averaged wall stresses, the channel width, the boundary layer thickness and the fluid viscosity”. [Raupach et al. \(1991\)](#) and [Jiménez \(2004\)](#) performed an extensive literature review on the roughness effect on TBL. These reviews support Townsend’s claims for wall similarity. ([Flack et al., 2005](#); [Connelly et al., 2006](#); [Kunkel and Marusic, 2006](#), among others) performed experiments over different types of roughness at different Reynolds numbers. Their findings support the similarity hypothesis. Others have noticed an effect of the roughness surface in the outer boundary layer region and have demonstrated that there is a considerable difference between smooth and rough-wall mean velocity profiles while optimising the friction velocity to fit the modified log law ([Krogstad et al., 1992](#); [Bergstrom et al., 2002](#); [Akinlade et al., 2004](#)).

[Jiménez \(2004\)](#) proposed a criterion to satisfy the wall similarity: the ratio between δ and k should be larger than 40. [Flack et al. \(2005\)](#) suggested that k_s is a better representative length scale than k for comparing the roughness effects of different roughness geometrical characteristics.

They proposed an alternative criterion to satisfy the wall similarity with k_s : that δ/k_s should be larger than 40, and the extent of the roughness sublayer is $5k_s$ rather than $5k$.

In this work, turbulent boundary layer measurements over various 2D rough surfaces are exploited to validate the outer layer similarity with a wide range of height ratios δ/k ranging from 21 to 45 at the matched friction Reynolds number, $Re_\tau = \delta U_\tau / \nu$.

4.4 EXPERIMENTAL DETAILS

4.4.1 Wind tunnel facility

The present experiments were undertaken in a closed-circuit wind tunnel facility at the University of Adelaide. The tunnel has a settling section with a honeycomb straightener and three screens, followed by an 8:1 contraction and a test section of 2 m in length, with a 0.5 m by 0.3 m cross-section. Then it has a diffuser and a fan. The wind tunnel can run with a maximum velocity of 30 m/s and free-stream turbulence intensity of around 0.5 %. According to [Nickels et al. \(2005\)](#) recommendations, the width of the test section should be at least six times larger than the boundary layer thickness to assume the boundary layer developed is two-dimensional. This assumption is valid in our present experiments, as w/δ ranges from 6.3 to 13, where w is the width of the test section. A 4 mm diameter rod and a 100 mm strip of sandpaper with 40 grit No. are used to trip the flow upstream of the test section.

4.4.2 Surface roughness

The roughness details of this study are: circular rods of 500 mm length with two different diameters, $k = 1.6$ and 2.4 mm, and three different streamwise spacings, $s_x = 8k$, $12k$, and $16k$, and CNC machined plates with 2D sinewave surfaces function with amplitudes of $k/2 = 0.8$ and 1.2 mm and wavelengths of $8k$, $12k$, and $16k$. A Multicam M1212 Router machine was used to fabricate these surfaces, with a 0.6 mm stepover and 12 mm ball nose cutter. The periodic function that describes the rough surface of the circular rods, and the sinewave surfaces, respectively, are as follows:

$$Z(x) = \begin{cases} \sqrt{kx - x^2}, & 0 \leq x \leq k \\ -\frac{k}{2}, & k < x < s_x \end{cases} \quad (4.1)$$

$$Z(x) = \frac{k}{2} \sin\left(\frac{2\pi x}{s_x}\right). \quad (4.2)$$

The equation of the sinewave surface is a straightforward sinewave equation that allows us to control either the amplitude or the wavelength of the roughness while keeping the other parameters constant. The surfaces are defined by the first letter of the geometry: R for rods and S for sinewaves, followed by ten times the maximum peak to valley height k and finally, the spacing between two consecutive roughness peaks. For example, $S24-12$ represents a sinewave surface with a maximum peak to valley height of 2.4 mm and a wavelength of $12k$. All the different roughnesses and the sandpaper strip are secured onto an aluminium sheet using double-sided tape. The statistical parameters used to characterise the different rough surfaces are tabulated in [Table 4.1](#).

TABLE 4.1: Different key surface roughness parameters. The surfaces are defined by the first letter of the geometry: R for rods and S for sinewaves, followed by ten times the maximum peak to valley height k and finally, the spacing between two consecutive roughness peaks.

Surface	Symbol	k (mm)	s_x (mm)	k_a (mm)	k_{rms} (mm)	k_{sk}	k_{ku}	ES
$R16-16$	◆	1.6	25.6	0.17	0.36	3.70	14.9	0.125
$R24-16$	◆	2.4	38.4	0.25	0.54	3.70	14.9	0.125
$R16-12$	■	1.6	19.2	0.22	0.42	3.09	10.7	0.167
$R24-12$	■	2.4	28.8	0.33	0.62	3.09	10.7	0.167
$R16-08$	●	1.6	12.8	0.31	0.51	2.34	6.57	0.250
$R24-08$	●	2.4	19.2	0.47	0.76	2.34	6.57	0.250
$S16-16$	◇	1.6	25.6	0.51	0.57	0.00	1.50	0.125
$S24-16$	◇	2.4	38.4	0.76	0.85	0.00	1.50	0.125
$S16-12$	□	1.6	19.2	0.51	0.57	0.00	1.50	0.167
$S24-12$	□	2.4	28.8	0.76	0.85	0.00	1.50	0.167
$S16-08$	○	1.6	12.8	0.51	0.57	0.00	1.50	0.250
$S24-08$	○	2.4	19.2	0.76	0.85	0.00	1.50	0.250

The arithmetical average of the absolute values of the roughness profile ordinates is called k_a (see [ASME, 2009](#)). The equation used for calculating k_a , defined on the sampling length L_s , is as follows:

$$k_a = \frac{1}{L_s} \int_0^{L_s} |Z(x) - m| dx, \quad (4.3)$$

where m is the mean line of the roughness heights.

The root-mean-square height k_{rms} , one of the dispersion parameters for characterising the surface roughness, is obtained by squaring each height value on the sampling length L_s , then taking the square root of the mean (see [ASME, 2009](#)). k_{rms} is defined as:

$$k_{rms} = \sqrt{\frac{1}{L_s} \int_0^{L_s} (Z(x) - m)^2 dx}. \quad (4.4)$$

The roughness skewness k_{sk} (the normalised third-order moment) measures the asymmetry of the surface deviation about the mean plane, defined on the sampling length. This parameter provides a morphology of the surface texture. $k_{sk} > 0$ corresponds to a higher number of peaks than valleys, while $k_{sk} < 0$ corresponds to surfaces with pores and scratches. For a Gaussian surface that has a symmetrical shape of surface height distribution, $k_{sk} = 0$. k_{sk} is defined as:

$$k_{sk} = \frac{1}{\sigma^3 L_s} \int_0^{L_s} (Z(x) - m)^3 dx. \quad (4.5)$$

The roughness kurtosis k_{ku} is a measure of the sharpness of the surface height distribution. k_{ku} for a Gaussian surface is equal to 3. k_{ku} is defined on the sampling length as:

$$k_{ku} = \frac{1}{\sigma^4 L_s} \int_0^{L_s} (Z(x) - m)^4 dx. \quad (4.6)$$

The mean absolute gradient of a rough surface is called the effective slope ES and is defined by Napoli et al. (2008) for the streamwise direction as follows:

$$ES = \frac{1}{L_s} \int_0^{L_s} \left| \frac{dZ(x)}{dx} \right| dx. \quad (4.7)$$

The higher the value of ES , the denser the roughness becomes. ES is also equivalent to twice the solidity of λ_f , which is the ratio of the total projected frontal area of the roughness element A_f to the unit wall parallel area A_p (see Napoli et al., 2008).

4.4.3 Measurement rig

A single hotwire probe with 2.5 μm diameter Wollaston (pure Platinum core wire) and $l = 0.5$ mm is used in measurements over smooth and rough wall measurements to give a length to diameter ratio of around 200, as recommended by (Ligrani and Bradshaw, 1987; Hutchins et al., 2009). An overheat ratio of 1.8 is applied using an in-house constant temperature anemometer for all measurements. A T-type thermocouple is used to record the mean temperature during the experiments. Twenty-six different velocities, ranging from zero to 20 m/s, are used for static calibration of the hotwire in situ before and after each experiment. If the pre-and post-calibrations do not collapse well, the measurement is repeated. A fourth-order polynomial of voltage (E) is used to map the hotwire's voltage to the velocity. Linear interpolation between pre-and post-calibrations is used to account for drifting of the hotwire throughout the experiment.

The first point offset from the wall is measured using a high magnification digital microscope mounted on a 3D printed plate and placed on top of the rough surfaces. Measurements are recorded at one streamwise location at the midpoint of two consecutive roughness peaks at $x \approx 1.5$ m downstream, measured from the first roughness element after the tripping sandpaper. A linear glass encoder with 1 μm resolution attached to a Mitutoyo height gauge is used to move the probe vertically to reduce the uncertainty of the wall-normal location. Streamwise velocity fluctuations are acquired at 48 logarithmically spaced points from 0 to around 1.5δ along the wall-normal position for each surface, with sufficient sampling frequency and time to capture the smallest turbulence scales and obtain the energy in the very large scale structure. Figure 4.1 shows a schematic of the different rough surfaces setups and the measurement location.

4.4.4 Experiments

A smooth wall TBL measurement was conducted at $U_\infty = 20$ m/s. Two sets of rough TBL experiments were conducted. The first set free-stream velocity was $U_\infty = 10$ m/s over 2D circular rods of two different heights, $k = 1.6$, and 2.4 mm diameter and three different spacings, $8k$, $12k$, and $16k$. For the second set of experiments, the free-stream velocity is set to 13 and 18 m/s over 2D sinewave surfaces of the same heights and spacings as rods to match the $Re_\tau = 2800 \pm 300$. A single hotwire probe with l^+ around 23 ± 3 was used for all measurements. The details of the three sets of experiments are indicated in Table 4.2. The sets are used to assess Townsend's outer layer similarity with a wide range of δ/k ranges from 21 to 45 and to investigate the effect of changing roughness parameters on turbulence statistics and the drag coefficient at the same Re_τ .

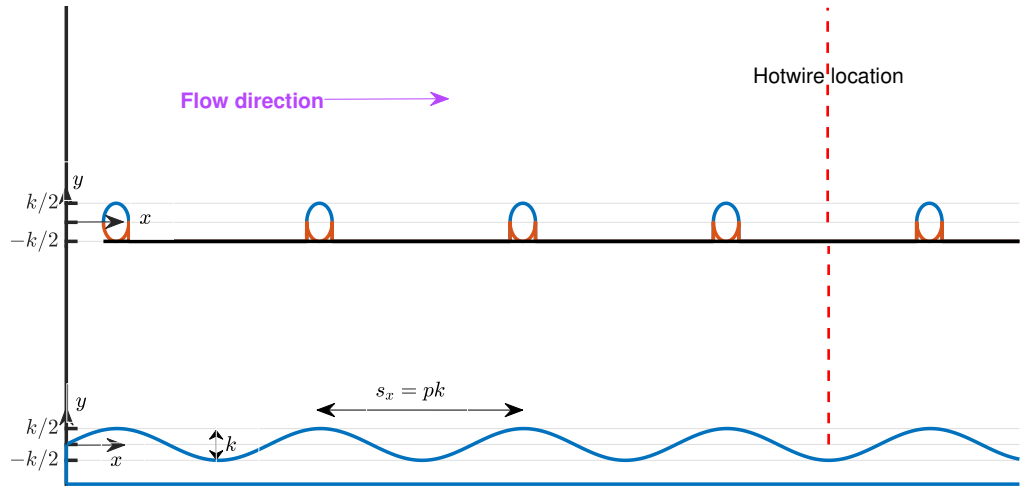


FIGURE 4.1: Schematic of different surfaces setups where $p = 8, 12, \text{ or } 16$. The red dotted line shows the measurement location at $x \approx 1.5$ m downstream. The coordinate system used in experiments and $y = 0$ as a reference point are indicated in the schematic.

TABLE 4.2: Details of the experimental data sets.

Surface	U_∞ (m/s)	ν/U_τ (μm)	Re_τ	l^+	H	C_f	δ/k	k_s^+	ΔU^+	$5k_s$ (mm)
Smooth	20	20	1930	25	1.34	0.0028	-	-	-	-
R16-16	10	25	2610	20	1.65	0.0069	41	265	10.3	33
R24-16	10	25	2830	20	1.67	0.0069	30	275	10.7	34
R16-12	10	25	2670	20	1.69	0.0069	42	275	10.4	34
R24-12	10	25	2990	20	1.69	0.0070	31	322	10.9	40
R16-08	10	25	2930	20	1.71	0.0073	45	363	11.1	45
R24-08	10	25	3160	20	1.70	0.0072	33	386	11.1	48
S16-16	18	19	2550	26	1.48	0.0039	30	-	4.6	-
S24-16	18	19	2730	26	1.47	0.0040	21	-	5.0	-
S16-12	14	22	2490	23	1.53	0.0048	34	65	7.0	7
S24-12	14	22	3070	23	1.53	0.0048	28	82	7.4	9
S16-08	13	22	2590	22	1.56	0.0053	36	95	8.0	10
S24-08	13	22	2740	22	1.58	0.0054	25	113	8.3	12

4.5 FRICTION VELOCITY

It is common, especially for rough-wall flows, to calculate U_τ indirectly using some modification to the [Clauser \(1956\)](#) approach. This method involves forcing the log region of the mean velocity to adhere to a predefined logarithmic law as,

$$U^+ = \frac{1}{\kappa} \ln y^+ + B, \quad (4.8)$$

where κ is the von Karman constant, and B is an additive constant. A limitation of this method is that it requires knowledge of the lower and upper limits of the overlap region as well as the

values of κ and B . The lower and upper limits of the log region may vary the friction velocity value slightly; also, as shown in Eq. 4.8 the friction velocity is dependant on κ and B . [Perry and Joubert \(1963\)](#) introduced the modified Clauser method used for rough surface TBLs, by adding two more variables to the previous equation, as follows:

$$U^+ = \frac{1}{\kappa} \ln \frac{(y + \epsilon) U_\tau}{\nu} + B - \Delta U^+, \quad (4.9)$$

where ϵ is an origin offset, The origin offset adds further uncertainties in calculating U_τ . The lower and higher limits of the log region used in the current study are $y^+ > 3\sqrt{Re_\tau}$ and $y/\delta = 0.15$, respectively. Those limits are recommended by [Marusic et al. \(2013\)](#) based on high Reynolds numbers smooth wall TBLs investigation, as these limits also best fit with the log region of the velocity profiles over rough surfaces. The outer layer similarity between the smooth and rough flows and the collapse of the velocity defect distributions were utilised by [Djenidi et al. \(2019\)](#) recently to estimate U_τ . In the current investigation, both the modified Clauser chart of [Perry and Li \(1990\)](#) and the velocity defect chart of [Djenidi et al. \(2019\)](#) methods are used to calculate U_τ . Since the main goal of the present study is to compare various roughness geometries and focus on the outer layer similarity, we assume ϵ to be fixed and equal to $k/2$ for all the rough surfaces following previous studies ([Djenidi et al., 2018](#); [Squire et al., 2016](#)). κ is optimised from 0.395 to 0.405, and $B = 5$ are used to maximise the goodness of fit of the linear regression through the points in the log region. Since the values obtained from both methods show good agreement, with less than 1 % difference for all the different surfaces considered, the U_τ obtained from the velocity defect chart is used in the presented results for all rough wall flows.

4.6 RESULTS

4.6.1 Mean velocity profile

Figure 4.2 shows the distributions U^+ versus y^+ for all the different rough surfaces used in this study. The data of the smooth TBL of [Marusic et al. \(2015\)](#) at $Re_\tau \approx 2800$ are also plotted to allow comparison with the rough TBL data at matched Re_τ . Also, the DNS smooth wall velocity distribution data of [Chan et al. \(2021\)](#) at $Re_\tau \approx 2000$ are shown in the figure as a further reference and to validate our smooth wall measurements.

All sinewave roughnesses have lower roughness functions ΔU^+ than the rods at the same Re_τ . The main reason for this is the capability of the rods to produce a fully rough regime at a relatively low Reynolds number. This was confirmed by ([Kamruzzaman et al., 2015](#); [Djenidi et al., 2018](#)). They investigated the turbulent boundary layer developed over a rod-roughened wall with a spacing between two consecutive rods of $8k$. They reported that the C_f is constant and independent of the Reynolds number $Re_\tau > 4000$ in a fully rough regime.

Fixing the spacing ratio s_x/k while changing k has a small effect on shifting the mean velocity profile downward, as shown in Figure 4.2 when comparing the same symbols with a different colour. Keeping k constant while decreasing s_x/k for both rods and sinewaves causes a noticeable downward shift, reflecting an increase of C_f . If one compares for examples the profiles $R16-16$ and $R16-08$ shown in Figure 4.2 and Table 4.2, increasing s_x/k from 8 and above reduces the drag. The initial increase from $s_x/k = 0$ to 8, drag increases. Eventually, if s_x increases to $s_x \gg k$, C_f decreases until it reaches the smooth wall case. These observations are more obvious in the sinewave roughness cases as the roughness function ΔU^+ is halved as seen in the comparison of the profile of $S16-08$ to $S16-16$. The present results agree well with the study of [Napoli et al. \(2008\)](#), who performed a numerical analysis of turbulent flows over rough walls

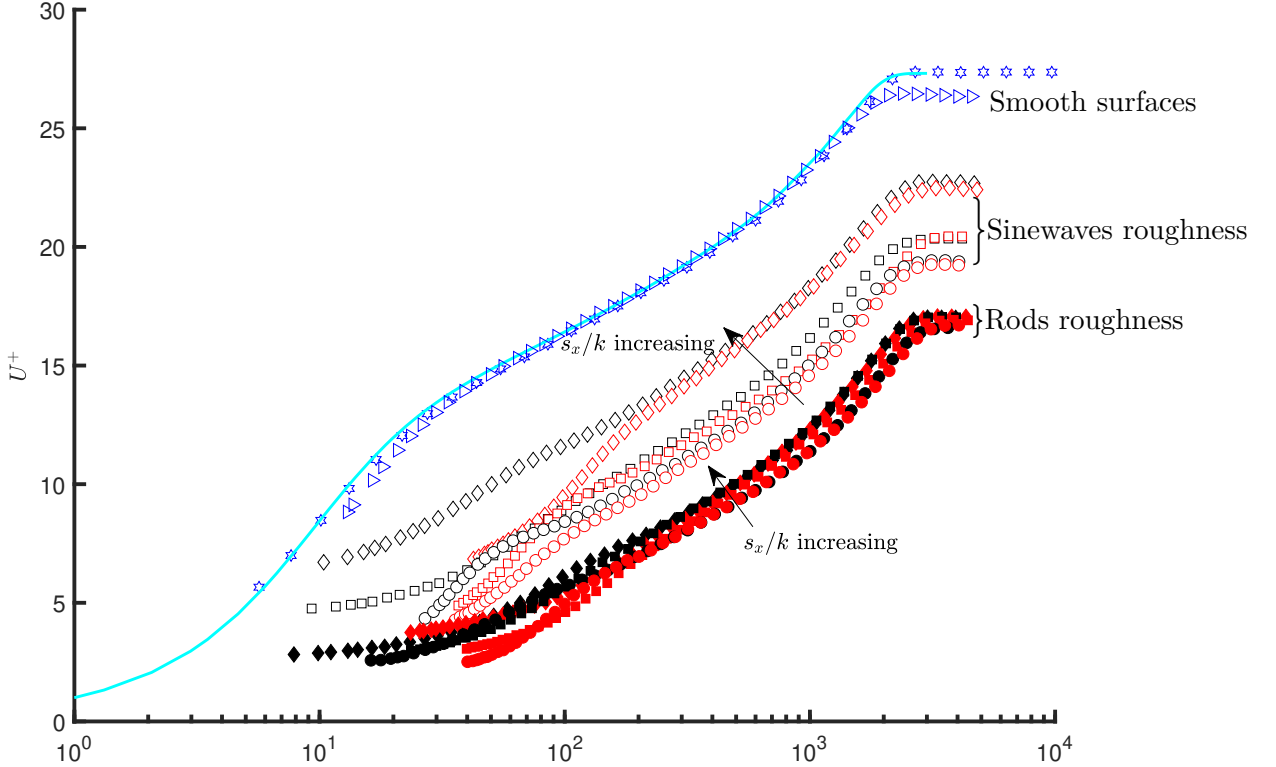


FIGURE 4.2: Streamwise mean velocity y^+ profiles over different rough surfaces at matched Reynolds number $Re_\tau = 2800 \pm 300$ for each surface are normalised by the friction velocity U_τ . Our smooth wall measurements are represented in blue triangle symbols. The symbols of our rough wall measurements are detailed in Table 4.1. The blue hexagram symbols are smooth TBL data from [Marusic et al. \(2015\)](#) at $Re_\tau = 2800$. The cyan line is DNS smooth TBL data from [Chan et al. \(2021\)](#) at $Re_\tau \approx 2000$. The inner length scale ν/U_τ normalises the wall-normal position y .

with irregular two-dimensional shapes. They revealed the importance of ES , which is a function of s_x/k in characterising the geometry of irregular rough walls. They varied the ES from 0.04 to 0.75 and observed that the ES of 0.15 separates the transitionally rough regime from the fully rough regime. We observe the same trend for the wavy sinewave surface. However, for the rod roughness, all the values of ES , including values smaller than 0.15, are in a fully rough regime. This is believed to be due to the high roughness skewness values of rods. One expects to observe differences in the region $y < k$ between different geometries, heights and spacings. These differences, though, diminish as we move far from the rough wall. For example, all the profiles exhibit almost the same shape at $y^+ \geq 200$.

[Townsend \(1956\)](#) proposes that self-preservation distributions of mean velocity can be expressed in the following deficit form

$$\frac{U_\infty - U}{u_a} = f\left(\frac{y}{y_b}\right), \quad (4.10)$$

where u_a and y_b are the appropriate velocity and length scales, respectively. [Townsend \(1956\)](#) showed that under self-preservation $u_a/U_\infty = \text{constant}$. It should be stated that [Townsend \(1956\)](#) acknowledges that a turbulent boundary layer evolving on a smooth wall cannot be in a complete self-preservation state across the entire layer due to the presence of the inner viscous layer; if self-preservation exists, it can only be in the outer the region where the effects of viscosity are negligible. A lot of work ([Rotta, 1962](#); [Townsend, 1956](#); [George and Castillo, 1997](#); [Jones et al., 2008](#); [Talluru et al., 2016](#)) has been carried out to determine appropriate scales.

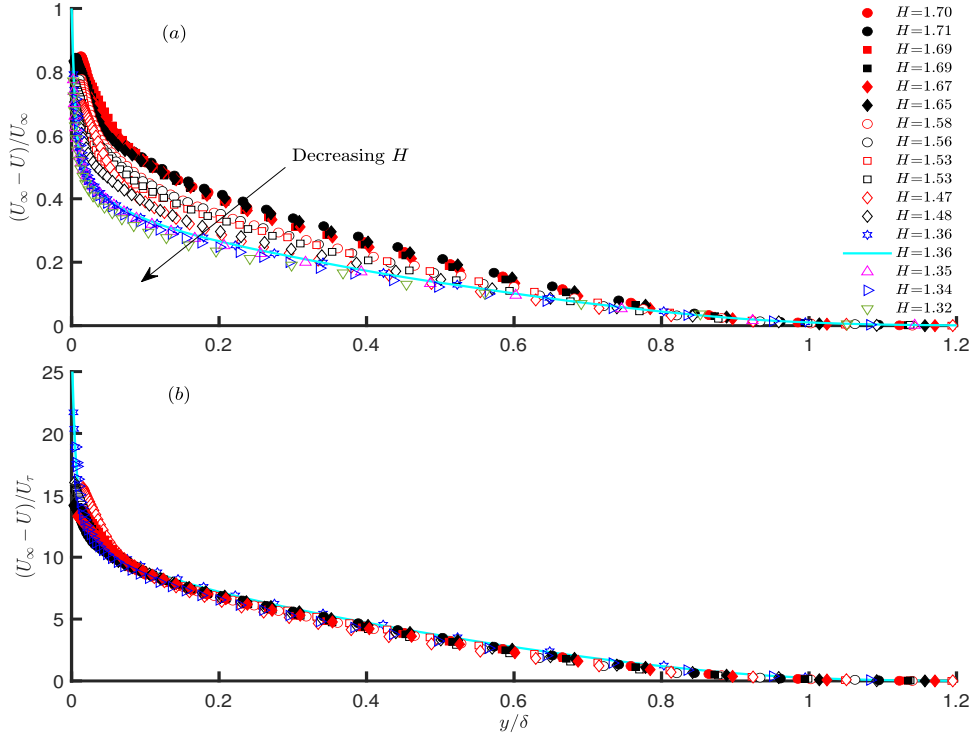


FIGURE 4.3: Comparison of streamwise mean velocity deficit profiles over a smooth wall and different rough wall surfaces at $Re_\tau = 2800 \pm 300$ for each rough surface. The symbols are the same as in Figure 4.2. The magenta and green triangle symbols are smooth TBL from (Marusic et al., 2015) at $Re_\tau \approx 3600$ with different tripping conditions. The cyan line is DNS smooth TBL data from Chan et al. (2021) at $Re_\tau \approx 2000$. (a) The deficit profiles are normalised by U_∞ . (b) The deficit profiles are normalised by U_τ .

Figure 4.3 shows the mean velocity profiles of Figure 4.2 expressed in the deficit form (4.10), where u_a is represented by U_∞ (plot 4.3(a)) and U_τ (plot 4.3(b)), respectively. When $u_a = U_\infty$, there is clearly no collapse between all the profiles shown. However, when one considers individual surface conditions several, observations can be made. Let us first consider the smooth wall TBL case. The perfect collapse of the smooth TBL data of Marusic et al. (2015) at $Re_\tau = 2800$ (represented by blue hexagram symbols) with the DNS smooth TBL data from Chan et al. (2021) at $Re_\tau \approx 2000$ (illustrated by the cyan line) is expected, as both TBLs have the same C_f and H . However, two smooth wall velocity profiles of Marusic et al. (2015) at $Re_\tau \approx 3600$ with different tripping conditions are also plotted in Figure 4.3(a) to ascertain the effect of C_f and H . The data for the smooth TBL tripped by sandpaper (TBL_s, magenta triangle symbols) correspond to C_f and H equal to 0.0026 and 1.35, respectively. While data for the smooth TBL tripped by a 6 mm threaded rod (TBL_r, green inverted triangle symbols) are for C_f and H equal 0.0028 and 1.32, respectively. The TBL_r deficit velocity profile lies below the TBL_s, illustrating the importance of C_f and H when comparing TBLs, even on smooth walls. The lack of collapse due to variation of C_f can be explained as follows: expression (4.10) can be expressed as,

$$1 - U^+ \sqrt{\frac{C_f}{2}} = f\left(\frac{y}{y_b}\right), \quad (4.11)$$

when $u_a = U_\infty$. Expression (4.11) shows that if the wall-normalised mean velocity profiles, U^+ , between two surfaces are similar, and if the surfaces have the same C_f , then the mean velocity deficit profiles should collapse when normalised by either U_∞ or U_τ . The lack of collapse seen

in Figure 4.3(a) is consistent with the variation of C_f . In contrast to the case where $u_a = U_\infty$, all velocity deficit profiles collapse regardless of the surface condition when $u_a = U_\tau$ across the boundary layer thickness outside the very near-wall region.

This excellent collapse suggests a universal velocity profile in the outer region of the turbulent boundary layer. This universality has been exploited by Djenidi et al. (2019) to develop a velocity defect chart for determining U_τ . The authors also argued that the collapse of the U_τ -normalised velocity defect profiles illustrates the similarity in the U_τ -normalised mean velocity profiles (see Figure 4.2) even though these profiles exhibit a downward shift whose magnitude is dependent on the surface condition. In that respect, one can argue that Townsend's similarity hypothesis is valid for the mean velocity profiles. The results of Figure 4.3 further indicate that this similarity holds even for values of δ/k and Re_τ smaller than the values reported by Jiménez (2004), regardless of the surface or flow conditions.

4.6.2 Turbulence intensities

For this section, the mean turbulence intensity in the streamwise direction, u' , is analysed. Figure 4.4 shows the distributions of u' for all roughness surfaces. Also shown are our smooth wall data, the smooth wall data of Marusic et al. (2015) and Chan et al. (2021). The smooth wall TBL distributions exhibit a maximum of u'^+ at $y^+ \approx 15$, often referred as inner-peak. This inner peak is affected by roughness. For example, it is shifted toward higher y^+ and reduced gradually with decreasing s_x/k for the sinewave roughness. While it vanishes for the rod roughnesses in the fully rough regime. Others have already observed this behaviour of the inner peak. For instance, Ligrani and Moffat (1986) show a gradual reduction in the inner peak of u'^+ profiles with increasing k_s^+ in a transitionally rough regime. The vanishing of the inner peak is a characteristic feature of fully rough wall TBLs, which reflects a different mechanism of energy production in the near-wall region than in a smooth wall TBL.

Note that while the rough wall profiles show an outer peak located in the region around $y^+ \approx 200$ to 300 or $0.06 \leq y/\delta \leq 0.09$, they do not collapse. This lack of collapse is also seen in Figure 4.4(b), which shows the same data as Figure 4.4(a) but as a function of y/δ . However, a close examination of Figures 4.4(c), (d), (e), and (f) shows that the data for the rod roughened surfaces exhibit significantly less variation than the data for the sinewave rough surfaces. This is likely to be associated with the fact that the boundary layers evolving on the former rough surfaces are in a fully rough regime, while they are in a transitionally rough regime over the latter rough surfaces. The transitionally rough regime is well illustrated by an existing small inner peak in the u'^+ profiles.

This lack of overall collapse between all u'^+ profiles indicates a lack of similarity between TBL over different rough surfaces. However, it does not exclude a possible Reynolds number similarity for a given roughness geometry in a fully rough regime, as the data for the rod roughened surfaces suggest. This slight lack of collapse between all u'^+ profiles in the outer layer is due to the uncertainty in calculating the friction velocity U_τ and the origin offset ϵ , and may also be due to relatively low Reynolds number (see Lee and Sung, 2007; Volino et al., 2009; Krogstad and Efros, 2012).

Despite this general lack of collapse, if one uses a diagnostic plot (Alfredsson et al., 2011; Castro et al., 2013) (i.e. the plot reports the turbulence intensity (u'/U) as a function of (U/U_∞)) one can produce a collapse of the data. The interesting feature of the diagnostic plot is that it avoids any uncertainties in both the wall-normal position y , and the friction velocity U_τ . If the flow is fully developed, then the profiles should collapse in the outer region of the TBL, regardless of the Reynolds number and the roughness morphology. Castro et al. (2013)

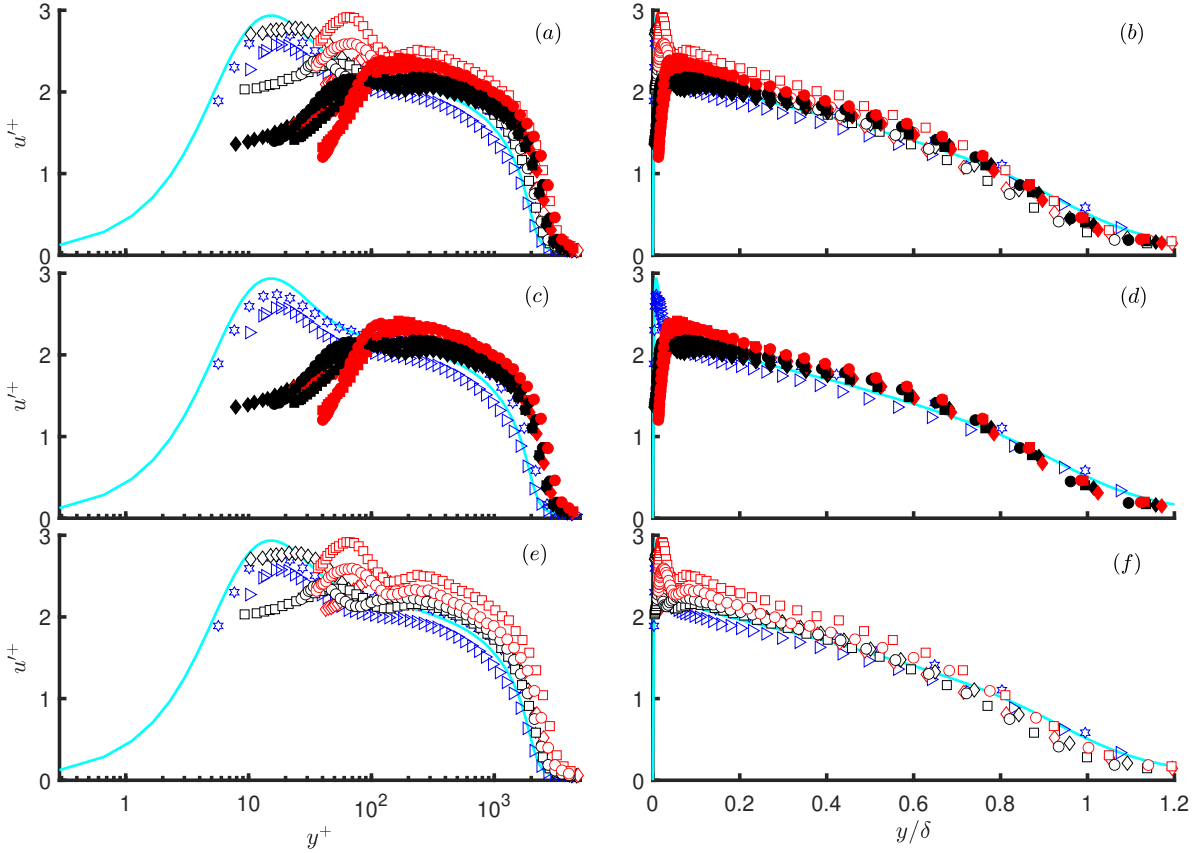


FIGURE 4.4: The mean streamwise turbulence intensities profiles at $Re_\tau = 2800 \pm 300$ for each surface are normalised by U_τ . (a), (c), & (e): y is normalised by the inner length scale ν/U_τ . (b), (d), & (f): y is normalised by the outer length scale δ . The symbols of our measurements are detailed in Table 4.1. (a), & (b): shows all the profiles, while, (c), & (d): are the rods roughness compared to the smooth wall, and (e), & (f): compare the smooth wall with the sinewave roughness. The blue triangle symbols represent our smooth TBL at $Re_\tau = 2000$, while the blue hexagram symbols represent the smooth TBL from Marusic et al. (2015) at $Re_\tau = 2800$. The cyan line is DNS smooth TBL data from Chan et al. (2021) at $Re_\tau \approx 2000$.

showed that the diagnostic plot emphasises differences between smooth wall and fully rough-wall boundary layer and help ascertain whether a TBL is in a transitionally rough regime or not. Further, Djenidi et al. (2018) noticed differences between 2D bars and sand grain roughness in the TBL outer region when they used diagnostic plots to compare the data.

Table 4.2 and Figures 4.3(a) & 4.5(a) suggest that the shape factor can also play a role in the diagnostic plot, as the higher the shape factor, the higher the curve from a reference point (smooth wall). This is illustrated in Figure 4.5, which shows both data in the original diagnostic plot (Figure 4.5(a) and the same plot where $1/\sqrt{H}$ weights the turbulence intensity u'/U . There is a clear difference between the smooth wall data and the rough wall data in the original plot, as already noted by Castro et al. (2013). Introducing the factor $1/\sqrt{H}$ for the rough wall data dramatically improves the collapse between all smooth and rough wall data. The physical explanation why this factor improves collapse needs to be investigated further. It should be noted that such collapse does reveal a possible similarity. It can be used though, as a convenient way to present the u' -distributions for different surface conditions.

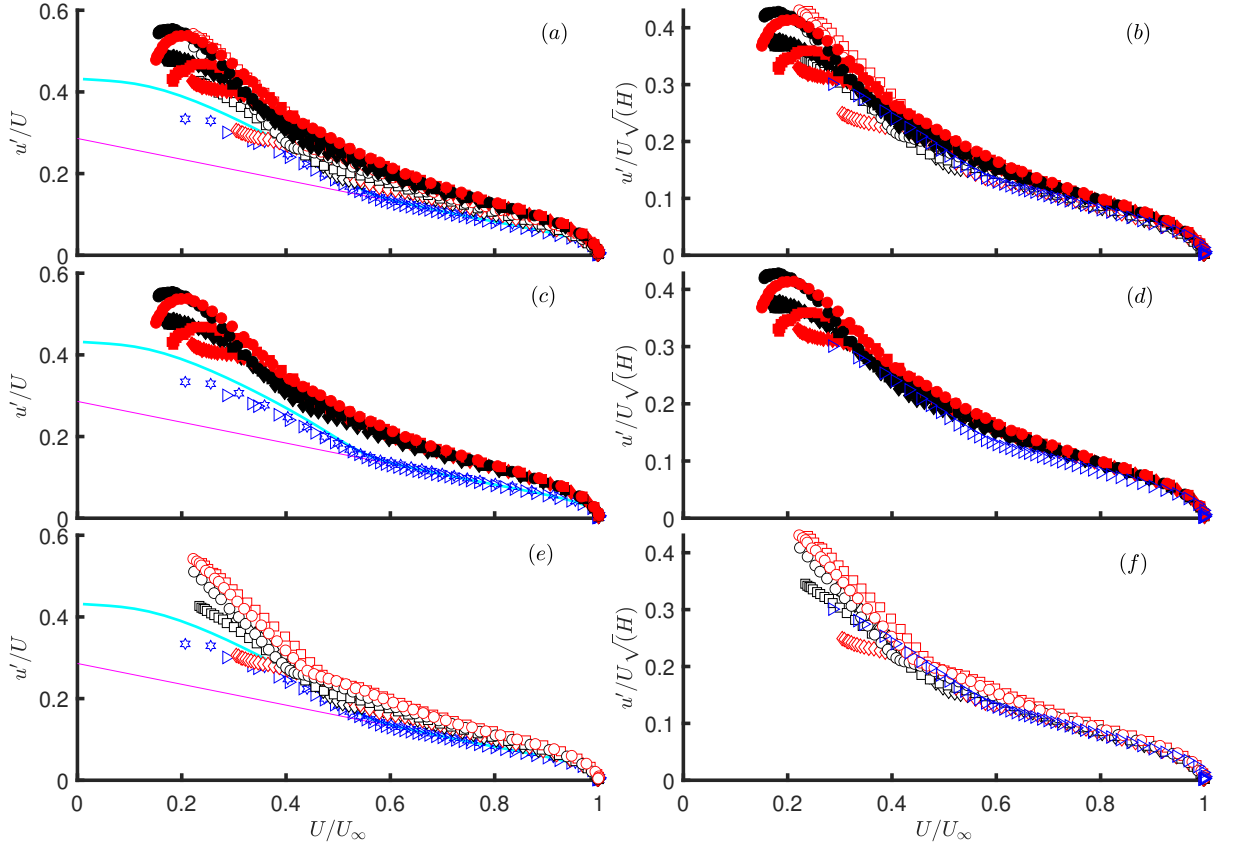


FIGURE 4.5: (a), (c), & (e): u' is normalised by U and plotted against U normalised by U_∞ . (b), (d), & (f): u' is normalised by $U\sqrt{H}$ and plotted against U normalised by U_∞ . The symbols of our measurements are detailed in Table 4.1. (a), & (b): shows all the profiles, while, (c), & (d): are the rods roughness compared to the smooth wall, and (e), & (f): compare the smooth wall with the sinewave roughness. The solid straight magenta line corresponds to the linear relationship $u'/U = 0.286 - 0.255 U/U_\infty$ (see Alfredsson et al., 2012).

4.6.3 Velocity skewness and flatness factor

Figure 4.6 indicates the distribution of the streamwise velocity skewness, S_u , and flatness factor (or kurtosis), K_u , for the rough wall TBL. Our smooth wall data, the smooth experimental data from Marusic et al. (2015) and the smooth DNS TBL data from Chan et al. (2021) at Re_τ of 1930, 2800 and 2000, respectively, are also shown.

The S_u distributions (Figure 4.6(a)) vary between the different surfaces in the region $0 \leq y/\delta \leq 0.1$. Beyond this region, the distributions collapse relatively well. A comment should be made regarding the difference between smooth wall measurements of Marusic et al. (2015) and the DNS smooth wall data of Chan et al. (2021) in the region $0 \leq y/\delta \leq 0.1$; the latter exhibit negative values of S_u , not visible in the experimental data. The difference can be due to an attenuation effect associated with the spatial resolution in the hotwire measurements. However, that impact is likely to be minimal since the experimental results do show an inner peak in the u' distribution; had the spatial resolution been severe, that inner peak would be either of a smaller magnitude or absent (Samie, 2018).

Interestingly, Ghanadi and Djenidi (2021) investigated the effect of the hotwire l^+ ranging from 24 to 168 in TBL measurements over a rough wall made of 2D rods. In contrast to results observed in smooth wall TBL measurements, they found that there is no effect of hotwire length on the measurements. This gives further confidence in the present rough wall measurements

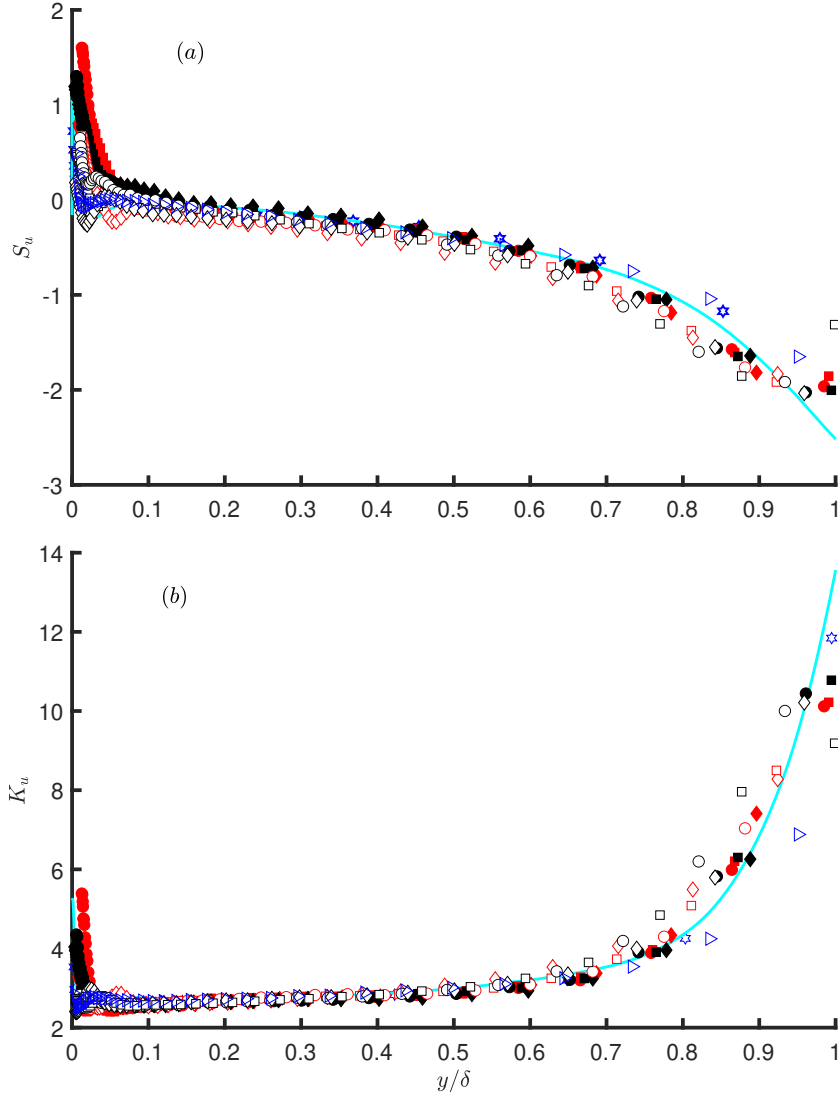


FIGURE 4.6: (a) The smooth and rough wall streamwise velocity skewness comparisons. (b) The smooth and rough wall streamwise velocity kurtosis comparisons. The wall-normal position y is normalised by the outer length scale δ . The blue triangle symbols represent our smooth TBL at $Re_\tau = 2000$. The blue hexagram symbols represent the smooth TBL from Marusic et al. (2015) at $Re_\tau = 2800$. The cyan line is DNS smooth TBL data from Chan et al. (2021) at $Re_\tau \approx 2000$.

where l^+ values are around 23. In contrast to the distributions of S_u , the K_u -distributions show a better collapse from $y/\delta > 0.03$ (Figure 4.6(b)), suggesting that K_u is less sensitive to the surface morphology than S_u .

4.6.4 Autocorrelations

Figure 4.7 shows the outer-scaled autocorrelation of streamwise velocity fluctuations R_{uu} as a function of $\Delta x/\delta$ at different wall-normal locations in the logarithmic and outer regions for each rough surface and the smooth wall TBL; this quantity provides a statistical characterisation of the average half-length of the turbulence structure. For each rough surface, the streamwise length of the positively correlated regions increases first as δ increases in the logarithmic region then reduces in the outer region. This is well illustrated in Table 4.3, which reports the values $\Delta x/\delta$ at which at R_{uu} of 0.05.

Table 4.3 shows that for all the rod roughness cases, the average length of the turbulence structures is significantly smaller than the wavy sinewave surfaces and the smooth wall. This indicates that the rods tend to break the turbulence structure and shorten its length in the near-wall region. On the other hand, the turbulence structure of the wavy sinewave surfaces are similar to the smooth wall, and the slight differences between them are due to noise and uncertainties in sampling the signal.

Note the good collapse between all surface data at $y/\delta=0.5$. This collapse also provides further evidence in support of Townsend’s outer layer similarity hypothesis between smooth and rough turbulent boundary layer flows.

TABLE 4.3: Streamwise length of the correlated regions normalised by outer length scale $\Delta x/\delta$ at $R_{uu} = 0.05$ at different wall-normal locations in the log and outer region.

Surface	Location			
	$y/\delta = 0.06$	$y/\delta = 0.1$	$y/\delta = 0.2$	$y/\delta = 0.5$
Smooth	4.2	4.5	5.0	3.6
R16 – 16	2.6	3.1	4.2	3.0
R24 – 16	2.0	2.6	4.0	2.9
R16 – 12	2.6	2.9	4.4	3.0
R24 – 12	2.2	2.7	4.0	2.8
R16 – 08	2.6	3.1	3.8	2.9
R24 – 08	2.4	2.8	3.6	2.8
S16 – 16	4.9	5.9	6.4	3.4
S24 – 16	4.9	5.6	6.4	3.4
S16 – 12	4.0	4.9	5.8	3.2
S24 – 12	4.0	5.0	6.2	3.2
S16 – 08	3.9	4.8	5.8	3.3
S24 – 08	3.8	5.0	6.2	3.1

4.6.5 Pre-multiplied energy spectra

This section presents the streamwise velocity fluctuations power spectral density, ϕ_{uu} multiplied by its associated streamwise wavelength k_x and normalised by U_τ^2 . To transform frequency into wavenumber, we used Taylor’s hypothesis of frozen turbulence, using the approximation $U_c = U$. All the spectra are plotted against wavelength, $\lambda_x = 2\pi/k_x$ normalised by δ in Figure 4.8 at locations $y/\delta = 0.06, 0.1, 0.2,$ and 0.5 . The coloured line and symbols matched the colours of the symbols in Table 4.1.

Overall, the figure indicates a lack of collapse among the distributions, although the figure shows a trend toward a collapse, as the plots for y/δ from 0.2 would imply. This may suggest that the surface condition impacts the energy distribution among scales of motion in the TBL and that the closer to the wall, the larger the impact. One can also notice that the distributions for the same type of roughness (e.g. 2D rod and 2D sinewaves) are closer to each other. This is particularly evident for $\lambda_x/\delta \geq 1$. On the other hand, the distinction is less

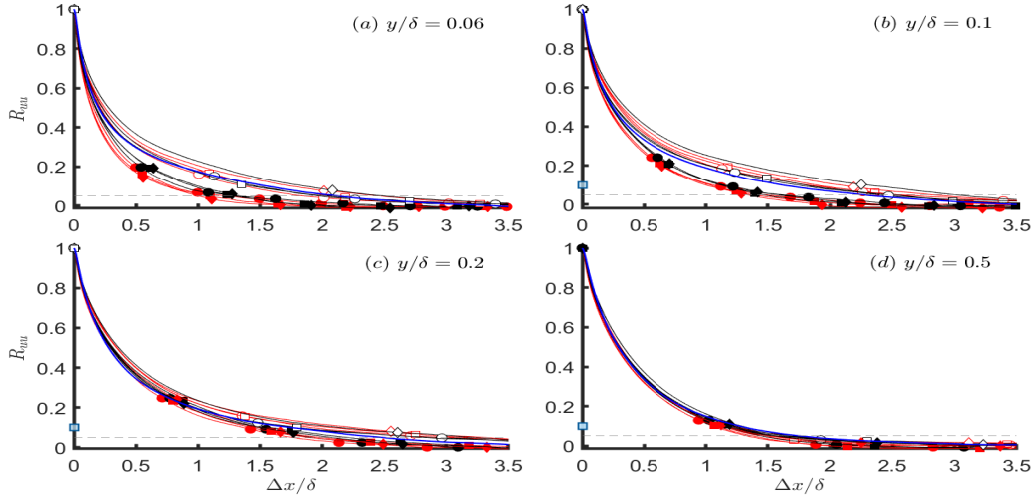


FIGURE 4.7: Autocorrelation R_{uu} of streamwise velocity fluctuations at different wall-normal locations for each rough surface as well as the smooth wall surface. The smooth wall surface is plotted in a blue line. The symbols of our rough wall measurements are detailed in Table 4.1. Marks are only for surface differentiation and does not indicate any specific data. (a) $y/\delta = 0.06$, (b) $y/\delta = 0.1$, (c) $y/\delta = 0.2$, (d) $y/\delta = 0.5$. The dashed grey line represents R_{uu} of 0.05.

when $\lambda_x/\delta \leq 1$. This distinction may be used to separate the distributions into two wavelength domains: large wavelength motions, $\lambda_x > \delta$, and small and medium wavelength motions, $\lambda_x < \delta$.

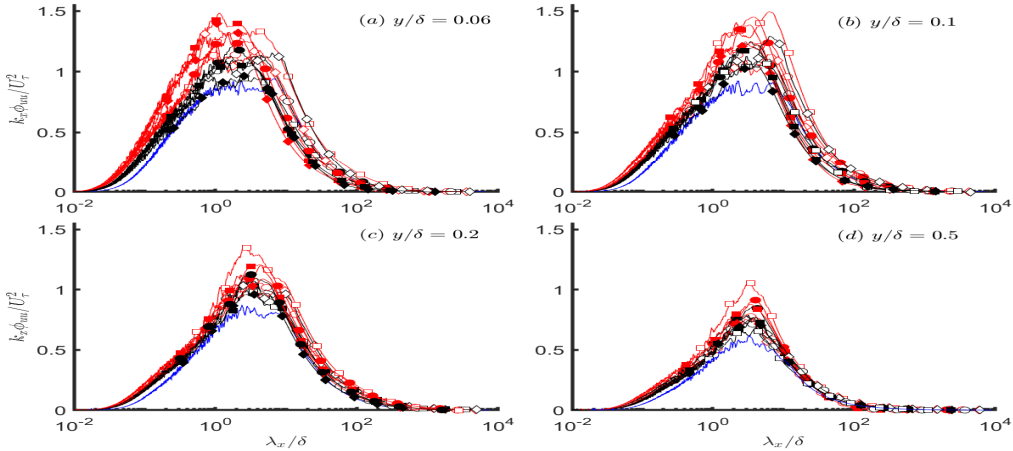


FIGURE 4.8: Pre-multiplied energy spectra of different rough and smooth surfaces at four different wall-normal locations. The wavelength λ_x is normalised by the outer length scale δ . (a) $y/\delta = 0.06$. (b) $y/\delta = 0.1$. (c) $y/\delta = 0.2$. (d) $y/\delta = 0.5$. The coloured lines and symbols represent the different rough surfaces, as indicated in Table 4.1. The blue line is our smooth wall measurement at $Re_\tau = 1930$.

4.7 CONCLUSIONS

Measurements were performed for a zero pressure gradient rough wall turbulent boundary layer to assess Townsend's outer layer similarity on different rough surfaces with a wide range of δ/k ranges from 21 to 45. The effect of changing the roughness parameters on turbulence statistics and the drag coefficient at the same Re_τ was investigated. Single hotwire probes were used to measure the streamwise velocity for two different 2D roughness geometries, using circular rods and sinewaves with two different heights, $k = 1.6$ and 2.4 mm, and three different streamwise spacings, $8k$, $12k$, and $16k$.

The roughness causes a downward shift of the wall-unit normalised mean velocity profile, known as the roughness function. The rods cause a more significant shift than the sinewave, producing a fully rough regime at relatively small Re_τ . The maximum downward shift is achieved when the spacing between two roughness elements is about $8k$. Changing the roughness height while maintaining the same spacing slightly affect the drag coefficient in the fully rough regime. Also, no effect of the ratio δ/k is observed as this ratio varies from 21 to 45. Further study with larger δ/k should be carried out to assess conclusively the effect of this ratio.

The excellent collapse between the smooth and different rough walls using a velocity defect profile, when normalised by the friction velocity, suggests the universality and similarity of the velocity profiles in turbulent boundary layer flows. It further suggests that Townsend's similarity hypothesis, even for smaller values of δ/k and Re_τ , regardless of surface or flow conditions, can be applied to the mean velocity distributions.

Plots of $u'/(U\sqrt{H})$ vs U/U_∞ (a slightly modified diagnostic plot) shows a reasonable collapse of all the rough wall profiles in the outer layer of the turbulent boundary layer; interestingly, the collapse align with the linear relation $u'/U = 0.286 - 0.255 U/U_\infty$ introduced by [Alfredsson et al. \(2012\)](#).

The mean streamwise turbulence intensity profiles have only an outer peak in the fully rough regime. It occurs almost at the same location, at around $y/\delta = 0.06$. The effect of the roughness is to suppress the inner peak that appears on the smooth wall. This observation is in agreement with the results from [Ligrani and Moffat \(1986\)](#). Their results showed a gradual reduction in the inner peak in u'^{+2} with increasing k_s^+ in the transitionally rough regime. Attenuation of the inner peak is observed when the fully-rough regime is reached. A significant variation in the streamwise turbulence intensity in the inner region of the flow is observed; however, for $y/\delta > 0.5$, there was a relative collapse in the outer region between the smooth and diverse rough wall flows.

In the outer region, from wall-normal location $y \approx 0.2\delta$, there is a collapse between smooth and different rough wall streamwise velocity skewness profiles. Streamwise velocity kurtosis is independent of surface morphology in any fully rough regime from the buffer layer, as all kurtosis profiles of different surface roughnesses collapse from $y/\delta > 0.02$ with the smooth wall.

The autocorrelation analysis shows that the coherent motions (in an average sense) have a similar length scale independent of the surface roughness at wall-normal locations above $y/\delta = 0.5$.

There are no significant differences between smooth and rough wall pre-multiplied energy spectra contours in the logarithmic and outer regions, at moderate Re_τ considered in this study. Both flows have an outer peak, which occurs near the same location at around $y/\delta \approx 0.06$ and $\lambda_x \approx 3\delta$ and decays with increasing distance from the wall.

CRediT authorship contribution statement

Misarah Abdelaziz: Conceptualization, Methodology, Software, Writing - original draft. **L. Djenidi:** Conceptualization, Writing - review & editing, Supervision. **Mergen H. Ghayesh:** Writing - review & editing, Supervision. **Rey Chin:** Conceptualization, Methodology, Resources, Writing - review & editing, Supervision.

Declaration of Competing Interest

The authors declare that they have no known competing financial interests or personal relationships that could have appeared to influence the work reported in this paper.

Acknowledgement

The authors acknowledge the financial support of the Australian Research Council.

Bibliography

- Akinlade, O. G., Bergstrom, D. J., Tachie, M. F. & Castillo, L. 2004 Outer flow scaling of smooth and rough wall turbulent boundary layers. *Experiments in Fluids*. **37** (04), 604–612.
- Alfredsson, P. H., Örlü, R. & Segalini, A. 2012 A new formulation for the streamwise turbulence intensity distribution in wall-bounded turbulent flows. *European Journal of Mechanics-B/Fluids*. **36**, 167–175.
- Alfredsson, P. H., Segalini, A. & Örlü, R. 2011 A new scaling for the streamwise turbulence intensity in wall-bounded turbulent flows and what it tells us about the “outer” peak. *Physics of Fluids*. **23**, 041702.
- ASME 2009 Surface Texture (Surface Roughness, Waviness, and Lay). *Revision of ANSI/ASME B46.1-1995. Standard. ASME*.
- Bergstrom, D. J., Kotey, N. A. & Tachie, M. F. 2002 The effects of surface roughness on the mean velocity profile in a turbulent boundary layer *Journal of Fluids Engineering*, **124** (03), 664–670.
- Castro, I. P., Segalini, A., & Alfredsson, H. 2013 Outer layer turbulence intensities in smooth-and rough-wall boundary layers. *Journal of Fluid Mechanics*. **727**, 119–131.
- Chan, C. I., Schlatter, P. & Chin, R. C. 2021 Interscale transport mechanisms in turbulent boundary layers. *Journal of Fluid Mechanics*. **921**.
- Clauser, F. H. 1956 The turbulent boundary layer. *Advances in Applied Mechanics*. **4**, 1–51.
- Connelly, J. S., Schultz, M. P. & Flack, K. A. 2006 Velocity-defect scaling for turbulent boundary layers with a range of relative roughness. *Experiments in Fluids*. **40** (02), 188.
- Darcy, H. 1857 Recherches expérimentales relatives au mouvement de l’eau dans les tuyaux. *Paris: Mallet-Bachelier*. **268**.
- Djenidi, L., Talluru, K. M. & Antonia, R. A. 2018 Can a turbulent boundary layer become independent of the Reynolds number? *Journal of Fluid Mechanics*. **851**, 1–22.
- Djenidi, L., Talluru, K. M. & Antonia, R. A. 2019 A velocity defect chart method for estimating the friction velocity in turbulent boundary layers. *Fluid Dynamics Research*. **51**, 045502.
- Flack, K. A., Schultz, M. P. & Shapiro, T. A. 2005 Experimental support for Townsend’s Reynolds number similarity hypothesis on rough walls. *Physics of Fluids*. **17**, 035102.

- George, W. K. & Castillo, L. 1997 Zero-pressure-gradient turbulent boundary layer. *Applied Mechanics Reviews* **50** (12), 689–729.
- Ghanadi, F. & Djenidi L., 2021 Spatial resolution effects on measurements in a rough wall turbulent boundary layer. *Experiments in Fluids* **62** 1–6.
- Hama, F. R. 1954 Boundary layer characteristics for smooth and rough surfaces. *Trans. Soc. Nav. Arch. Marine Engrs.* **62**, 333–358.
- Hutchins, N., Nickels, T. B., Marusic, I. & Chong, M. S. 2009 hotwire spatial resolution issues in wall-bounded turbulence. *Journal of Fluid Mechanics.* **635**, 103–136.
- Jiménez, J. 2004 Turbulent flows over rough walls. *Annual Review of Fluid Mechanics* **36**, 173–196.
- Jones, M. B., Nickels, T. B. & Marusic, I. 2008 On the asymptotic similarity of the zero-pressure-gradient turbulent boundary layer. *Journal of Fluid Mechanics.* **616**, 195–203.
- Kamruzzaman, M. D., Djenidi, L., Antonia, R. A. & Talluru, K. M. 2015 Drag of a turbulent boundary layer with transverse 2D circular rods on the wall. *Experiments in Fluids.* **56** (06), 121(1-8).
- Krogstad, P.-Å., Antonia, R. A. & Browne, L. W. B. 1992 Comparison between rough-and smooth-wall turbulent boundary layers. *Journal of Fluid Mechanics.* **245**, 599–617.
- Krogstad, P.-Å. & Efron, V. 2012 About turbulence statistics in the outer part of a boundary layer developing over two-dimensional surface roughness. *Physics of Fluids.* **24**, 7, 075112.
- Kunkel, G. J. & Marusic, I. 2006 Study of the near-wall-turbulent region of the high-Reynolds-number boundary layer using an atmospheric flow. *Journal of Fluid Mechanics.* **548**, 375–402.
- Lee, S. H. & Sung, H. J. 2007 Direct numerical simulation of the turbulent boundary layer over a rod-roughened wall. *Journal of Fluid Mechanics,* **584**, 125–146.
- Ligrani, P. M. & Bradshaw, P. 1987 Spatial resolution and measurement of turbulence in the viscous sublayer using subminiature hotwire probes. *Experiments in Fluids.* **5** (06), 407–417.
- Ligrani, P. M. & Moffat, R. J. 1986 Structure of transitionally rough and fully rough turbulent boundary layers. *Journal of Fluid Mechanics.* **162**, 69–98.
- Marusic, I., Chauhan, K. A., Kulandaivelu, V. & Hutchins, N. 2015 Evolution of zero-pressure-gradient boundary layers from different tripping conditions. *Journal of Fluid Mechanics.* **783**, 379–411.
- Marusic, I., Monty, J. P., Hultmark, M., & Smits, A. J. 2013 On the logarithmic region in wall turbulence. *Journal of Fluid Mechanics.* **716**, R3.
- Napoli, E., Armenio, V. & De Marchis, M. 2008 The effect of the slope of irregularly distributed roughness elements on turbulent wall-bounded flows. *Journal of Fluid Mechanics.* **613**, 385–394.
- Nickels, T. B., Marusic, I., Hafez, S. & Chong, M. S. 2005 Evidence of the k_1^{-1} law in a high-Reynolds-number turbulent boundary layer. *Physical Review Letters.* **95**, 074501.

- Nikuradse, J. 1933 Laws of flow in rough pipes. *Translation from German published 1950 as NACA Tech. Memo.* 1292.
- Perry, A. E. & Joubert, P. N. 1963 Rough-wall boundary layers in adverse pressure gradients. *Journal of Fluid Mechanics.* **17** (02), 193–211.
- Perry, A. E. & Li, J. D. 1990 Experimental support for the attached-eddy hypothesis in zero-pressure-gradient turbulent boundary layers. *Journal of Fluid Mechanics.* **218**, 405–438.
- Raupach, M. R., Antonia, R. A. & Rajagopalan, S. 1991 Rough-wall turbulent boundary layers. *Applied Mechanics Reviews* **44** (01), 1-25.
- Rotta, J. C. 1962 Turbulent boundary layers in incompressible flow. *Progress in Aerospace Sciences.* **2** (01), 1–95
- Samie, M., Marusic, I., Hutchins, N., Fu, M. K., Fan, Y., Hultmark, M., & Smits, A. J., Fully resolved measurements of turbulent boundary layer flows up to $Re_\tau = 20000$, *Journal of Fluid Mechanics*, **851**, 391–415.
- Squire, D. T., Morrill-Winter, C., Hutchins, N., Schultz, M. P., Klewicki, J. C., & Marusic, I. 2016 Comparison of turbulent boundary layers over smooth and rough surfaces up to high Reynolds numbers *Journal of Fluid Mechanics.* **795**, 210-240.
- Talamelli, A., Segalini, A., Örlü, R., Schlatter, P., & Alfredsson, P. H. 2013 Correcting hotwire spatial resolution effects in third-and fourth-order velocity moments in wall-bounded turbulence. *Experiments in Fluids.* **54** (04), 1496.
- Talluru, K. M., Djenidi, L., Kamruzzaman, M. D. & Antonia, R. A. 2016 Self-preservation in a zero pressure gradient rough-wall turbulent boundary layer. *Journal of Fluid Mechanics.* **788**, 57–69.
- Townsend, A. A. 1956 The structure of turbulent shear flow. *Cambridge university press.*
- Volino, R. J., Schultz, M. P., & Flack, K. A. 2009 Turbulence structure in a boundary layer with two-dimensional roughness. *Journal of Fluid Mechanics.* **635**, 75–101.

Chapter 5

A New Equivalent Sand Grain Roughness Relation For 2-D Rough Surfaces

5.1 CHAPTER OVERVIEW

A new expression for k_s , which is used to quantify the roughness of a surface, has been developed for 2D uniformly distributed roughness in the fully rough regime. This expression is based on three major roughness parameters: k , ES and k_{sk} .

A ZPG - TBL measurements were conducted over different rough walls to study how changes in roughness parameters affect the roughness function. Single hot-wire probes were utilised to measure the streamwise velocity at different Reynolds numbers for various 2D roughness geometries. These geometries include: circular rods with heights of 1.6 mm and 2.4 mm, five different streamwise spacing-to-height ratio ranges from 6 to 24, 3D printed triangular ribs with a height of 1.6 mm and a spacing-to-height ratio of 8, and CNC machined sinewave surfaces with heights of 1.6 mm and 2.4 mm, and a spacing to height ratio of 8. The roughness of a surface causes a downward shift in the wall-unit normalised mean velocity profile, known as the roughness function. The greatest shift occurs when the spacing ratio between two roughness elements is around 8. However, changing the roughness height while keeping the same spacing ratio has no effect on the drag coefficient in the fully rough regime. Additionally, varying the ratio of δ/k does not affect the mean streamwise velocity profile, as long as δ/k is above 23 in this study. This suggests that roughness height is not sufficient for characterising roughness.

A new expression for k_s , involving the physical roughness parameters k , ES , and k_{sk} , is proposed as a promising practical means to calculate the roughness function directly from the roughness topography in 2D uniformly distributed rough surfaces.

It is important to keep in mind that the new expression for k_s is only applicable to 2D rough surfaces that are fully rough, and further research is necessary to determine the impact of k , ES , and k_{sk} on turbulence statistics and drag coefficient. This includes studying 2D and 3D rough surfaces and random roughness. Such studies will assist in creating a more general relation for k_s if one can be developed.

5.2 A NEW EQUIVALENT SAND GRAIN ROUGHNESS RELATION FOR TWO-DIMENSIONAL ROUGH SURFACES

This section consists of the following published journal article:

Cite as: Journal of Fluid Mechanics **940**, A25 (2022);

<https://doi.org/10.1017/jfm.2022.242>

Received 18 April 2021 • Revised 8 February 2022 • Accepted 13 March 2022

• Published online by Cambridge University Press: 8 April 2022

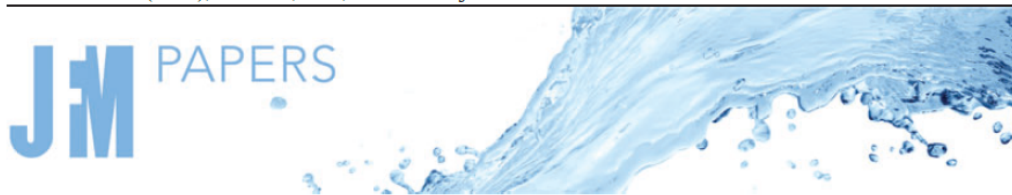
Misarah Abdelaziz, L. Djenidi, Mergen H. Ghayesh, and Rey Chin.

The article is identical to its submitted format with the following exceptions:

- The numbering of figures, tables and equations has been altered to include the chapter number.
- The position of some figures and tables has been changed to improve the article's legibility.



J. Fluid Mech. (2022), vol. 940, A25, doi:10.1017/jfm.2022.242



A new equivalent sand grain roughness relation for two-dimensional rough wall turbulent boundary layers

Misarah Abdelaziz^{1,†}, L. Djenidi², Mergen H. Ghayesh¹ and Rey Chin¹

¹School of Mechanical Engineering, University of Adelaide, Adelaide, South Australia 5005, Australia

²Mechanical Engineering Discipline, The University of Newcastle, Callaghan, NSW 2308, Australia

(Received 18 April 2021; revised 8 February 2022; accepted 13 March 2022)

Statement of Authorship

Title of paper	A new equivalent sand grain roughness relation for two-dimensional rough wall turbulent boundary layers
Publication status	Published
Publication details	Misarah Abdelaziz, L. Djenidi, Mergen H. Ghayesh, and Rey Chin. A new equivalent sand grain roughness relation for two-dimensional rough wall turbulent boundary layers <i>Journal of Fluid Mechanics</i> , 940 , A25 (2022); https://doi.org/10.1017/jfm.2022.242

Principal Author

Name of principal author (candidate)	Misarah Abdelaziz
Contribution to the paper	Conception, acquiring data, knowledge, analysis and drafting
Certification	This paper reports on original research I conducted during the period of my Higher Degree by Research candidature and is not subject to any obligations or contractual agreements with a third party that would constrain its inclusion in this thesis. I am the primary author of this paper.
Signature:	_____ Date: 05/07/2023

Co-author contributions

By signing the Statement of Authorship, each author certifies that:

- i.* the candidate's stated contribution to the publication is accurate (as detailed above)
- ii.* permission is granted for the candidate to include the publication in the thesis; and
- iii.* the sum of all co-author contributions is equal to 100% less the candidate's stated contribution.

Name of co-author	Lyazid Djenidi
Contribution to the paper	Conception, knowledge, analysis and drafting
Signature:	_____ Date: 27/06/2023

Name of co-author	Mergen H. Ghayesh
Contribution to the paper	Conception, knowledge, and drafting
Signature:	_____ Date: 04/07/2023

Name of co-author	Rey Chin
Contribution to the paper	Conception, knowledge, analysis and drafting
Signature:	_____ Date: 04/07/2023

A new equivalent sand grain roughness relation for two-dimensional rough wall turbulent boundary layers

Misarah Abdelaziz^{1,†}, L. Djenidi², Mergen H. Ghayesh¹ and Rey Chin¹

¹School of Mechanical Engineering, University of Adelaide, Adelaide, 5005, South Australia, Australia

²Mechanical Engineering Discipline, The University of Newcastle, Callaghan, 2308, NSW, Australia

(Received 18 April 2021; revised 8 February 2022; accepted 13 March 2022)

ABSTRACT

The effects of different geometries of two-dimensional (2-D) roughness elements in a zero pressure gradient (ZPG) turbulent boundary layer (TBL) on turbulence statistics and drag coefficient are assessed using single hot-wire anemometry. Three kinds of 2-D roughness are used: (i) circular rods with two different heights, $k = 1.6$ and 2.4 mm, and five different streamwise spacing of $s_x = 6k$ to $24k$, (ii) three-dimensional (3-D) printed triangular ribs with heights of $k = 1.6$ mm and spacing of $s_x = 8k$ and (iii) computerized numerical control (CNC) machined sinewave surfaces with two different heights, $k = 1.6$ and 2.4 mm, and spacing of $s_x = 8k$. Those roughness cover a wide range of ratios of the boundary layer thickness to the roughness height ($23 < \delta/k < 41$), where δ is the boundary layer thickness. All roughnesses cause a downward shift on the wall-unit normalised streamwise mean velocity profile when compared with the smooth wall profiles agreeing with the literature, with a maximum downward shift observed for $s_x = 8k$. In the fully rough regime, the drag coefficient becomes independent of the Reynolds number. Changing the roughness height while maintaining the same spacing ratio s_x/k exhibit little influence on the drag coefficient in the fully rough regime. On the other hand, the effective slope (ES) and the height skewness (k_{sk}) appear to be major surface roughness parameters that affects the drag coefficient. These parameters are used in a new expression for k_s , the equivalent sand grain roughness, developed for 2-D uniformly distributed roughness in the fully rough regime.

Key words: turbulent boundary layers

† Email address for correspondence: misarah.abdelaziz@adelaide.edu.au

<https://doi.org/10.1017/jfm.2022.242> Published online by Cambridge University Press

5.3 INTRODUCTION

Turbulence is arguably one of the most difficult subjects in nonlinear physics due to its complex and challenging mathematical descriptions, its inherent instabilities and chaotic nature (Sun 2019). The presence of a wall compounds further the challenge to investigate turbulence, such as in turbulent boundary layers. In addition, complications arise when the wall is rough.

Rough wall flows tend to produce a higher coefficient of friction ($C_f = 2\tau_w/\rho U_\infty^2$, where U_∞ is the free-stream velocity, τ_w is the wall shear stress and ρ is the density of the fluid),

than flows over smooth surfaces. The increase of C_f is manifested in the downward shift of wall–unit normalised mean velocity profile when compared with the smooth wall profile (Hama 1954). The shift, known as the roughness function, is defined as $\Delta U^+ = \Delta U/U_\tau$, where U is the mean streamwise velocity and U_τ is the friction velocity $U_\tau = \sqrt{\tau_w/\rho}$; the superscript, $(^+)$ means normalisation by the wall units U_τ or ν/U_τ , where ν is the kinematic viscosity. The roughness function is a function of the equivalent sand grain roughness k_s (Schlichting & Kestin 1961). Ideally, one would like to determine ΔU^+ based solely on the roughness topology. This would provide a way of predicting C_f without the need to perform lengthy measurements. Unfortunately, k_s is not a physical roughness parameter and its determination relies on an empirical method based on the mean velocity profile (Nikuradse 1933).

When k_s^+ is large enough the flow is considered to be in the ‘fully rough’ regime and the drag is mainly composed of the pressure (or form) drag (Squire *et al.* 2016). This regime is characterised by a log–linear relationship between ΔU^+ and k_s^+ . On the other hand, when k_s^+ is too small, the roughness does not have a noticeable effect on the viscous sublayer of the flow. This flow regime is called ‘dynamically smooth’ and can be treated as a smooth wall flow. At moderate values of k_s^+ , both the pressure drag and the viscous drag contribute to the total drag. This flow regime is called ‘transitionally rough’ (Nikuradse 1933). So far there are no clear thresholds that delimit these flow regimes. However, it is commonly agreed that the flow is hydraulically smooth when $k_s^+ < 4$, and fully rough when $k_s^+ > 70$ (Jiménez 2004).

The roughness function ΔU^+ is determined by ‘measuring’ the vertical shift between the log regions of the rough wall and smooth wall wall-unit normalised velocity profiles. This requires that experiments be conducted for each rough surface to obtain the velocity profile and friction velocity. A more practical way to proceed, but one that also presents a big challenge, is to predict ΔU^+ directly from surface topology or by other means, correlating k_s to one or more parameters characterising the roughness. So far, there has been no definite consensus on which length scale or roughness parameter best characterises a surface that can correlate with the friction drag. Over the last decade, a large body of work has been undertaken to address this issue (Musker 1980; Napoli, Armenio & De Marchis 2008; Schultz & Flack 2009; Foroughi *et al.* 2017; Flack, Schultz & Barros 2020, among many others). A wide range of different surface parameters has been studied to predict which of these parameters dominantly affects the friction drag. Some of these parameters are the mean roughness height k_a , root-mean-square height k_{rms} , maximum peak to valley height k , average peak to valley height k_z , effective slope ES , solidarity λ_f , skewness k_{sk} , and flatness k_{ku} . However, none of these parameters is sufficient to be generalised for all kinds of roughness.

Musker (1980) developed a modified roughness Reynolds number as a function of simple geometric statistics (average absolute slope, standard deviation, skewness, and flatness) for naturally occurring surfaces as follows:

$$k_s^+ = \frac{\sigma U_\tau}{\nu} (1 + aES)(1 + bk_{sk}k_{ku}), \quad (5.1)$$

where a and b are constants to give the best fit of roughness functions related to naturally occurring surfaces, and σ is the standard deviation of the surface roughness.

Waigh & Kind (1998) studied a regular three-dimensional (3-D) roughness and found that the element bluntness and spanwise aspect ratio are the main parameters characterising

the roughness function as follows:

$$\Delta U^+ = \begin{cases} 10.56 \log \left[\left(\frac{1}{\lambda_f} \frac{k}{b_m} \right)^{0.87} \left(\frac{A_w}{A_f} \right)^{0.44} \right] - 7.59 & \Lambda < 6, \\ -5.57 \log \left[\left(\frac{1}{\lambda_f} \frac{k}{b_m} \right)^{0.55} \left(\frac{A_w}{A_f} \right)^{1.38} \right] + 5.78 & \Lambda > 6, \end{cases} \quad (5.2)$$

where $\Lambda = \lambda_f k / s_m$, s_m is the streamwise width of the roughness element, b_m is the spanwise width of the roughness element, $\lambda_f = A_f / A_s$, A_s is the surface area, A_f is the projected frontal area, and A_w is the wetted area.

Bons (2002) derived a new k_s correlation, based on the surface slope angle for real turbine roughness; the roughness panels were scaled models of actual turbine surfaces instead of using the traditional simulated roughness

$$k_s = -0.0261ES + 0.0138ES^2. \quad (5.3)$$

Schultz & Flack (2009) studied close-packed pyramid roughnesses to study the effect of the height and slope of roughness on the flow. They found that ΔU^+ mainly depends on the roughness height. They also found a range of ES such that, below this level, the surface is considered to be wavy, not rough, and the roughness function strongly depends on the ES . If $ES < 0.35$, the surface is considered to be wavy.

Forooghi et al. (2017) investigated numerically the effect of various roughness parameters on k_s in the fully rough regime of channel flow at friction Reynolds number $Re_\tau \approx 500$. Their roughness geometries were generated by systematically changing the moments of the surface height probability density function, the effective slope of the random roughness and the size distribution of the roughness peaks. **Forooghi et al. (2017)** correlate k_s based on k , k_{sk} and ES . They found that these roughness parameters can predict k_s accurately for randomly distributed roughness in the fully rough regime of channel flows

$$\left. \begin{aligned} k_s/k &= F(k_{sk}) \cdot G(ES), \\ F(k_{sk}) &= 0.67k_{sk}^2 + 0.93k_{sk} + 1.3, \\ G(ES) &= 1.07 \cdot (1 - e^{-3.5ES}). \end{aligned} \right\} \quad (5.4)$$

Flack et al. (2020) investigated the importance of roughness height and skewness on the coefficient of friction. A k_s correlation was derived as:

$$k_s = A_1 k_{rms} (1 + k_{sk})^{B_1}, \quad (5.5)$$

with $A_1 = 4.43$, and $B_1 = 1.37$.

While many roughness function formulations in terms of one or more roughness parameters have been proposed recently, they are limited to the particular roughness investigated. In other words, they lack universality. This is certainly associated with the fact that, so far, a ‘universal’ critical parameter for all roughnesses is yet to be determined. Whether such a ‘universal’ parameter exists or not is still an open issue. It is nevertheless conceivable that such a parameter can be identified for families of rough surfaces, such as 2-D roughness, and 3-D roughness, in the fully rough regime. The present work is an attempt to determine such a parameter with the view

to develop an expression for k_s . The roughness family considered here is that of 2-D roughness. One reason to focus on this roughness family is that it was shown to produce a fully rough regime at relatively low Reynolds number, which can be easily achieved in wind tunnels. For example the use of 2-D rods attached to a smooth wall where the spacing between two consecutive rods, s_x , is approximately $8k$ leads to a fully rough regime (Djenidi, Talluru & Antonia 2018). In their direct numerical simulations of a turbulent rough wall channel flow, Leonardi *et al.* (2003) used transverse square bars as a roughness, with s_x varying from $2k$ to $32k$. They showed that the form drag was the main contributor to the total drag when $8k \leq s_x \leq 16k$. Later, Leonardi *et al.* (2015) used circular rods and investigated friction and pressure drags numerically, confirming their previous observations. Kamruzzaman *et al.* (2015) investigated the turbulent boundary layer developed over a rod roughened wall that has a spacing between two consecutive rods of $8k$. They calculated the pressure drag directly from the distribution of static pressure around one rod. They revealed that the C_f is constant and independent of the Reynolds number in the fully rough regime. This was further confirmed by Djenidi *et al.* (2018).

In this present work, we carry out turbulent boundary layer measurements over various 2-D rough surfaces with a height ratio δ/k ranging from 23 to 41. Two sets of experiments are conducted. The first one is to validate our rough wall measurements and estimation of U_τ . Also, the experiments are used to validate the Reynolds number independence when the flow is fully rough. The second set of experiments is exploited to determine the most critical dominant roughness parameters impacting C_f with the view to developing an expression for k_s^+ valid for the 2-D rough wall family.

5.4 EXPERIMENTAL DETAILS

5.4.1 Wind tunnel facility

The experiments are performed in a closed-return-type wind tunnel located at the University of Adelaide. It can achieve a maximum velocity of 30 m s^{-1} with a low-level turbulence intensity of approximately 0.53 %. The test section is rectangular and has a cross-section of $500 \text{ mm} \times 300 \text{ mm}$ and a 2000 mm in length. A 125 mm long circulation flap is also installed downstream of the test section to reduce the circulations generated over the flat plates as much as possible and to make sure that the stagnation point is on the measurement side of the plate. This flap can be regulated to keep the flow with a zero pressure gradient (ZPG) along with adjusted sidewalls. The tunnel should be wider than six times the boundary layer thickness to ensure the boundary layer developed in the test section is two-dimensional, as reported by Nickels *et al.* (2005). In our measurements, the 500 mm width is more than 7δ of the largest boundary layer thickness developed. The inlet flow is tripped by a 4 mm diameter rod and a 100 mm strip of sandpaper with a 40 grit number.

5.4.2 Surface roughness

The roughness details of this study are: circular rods of 500 mm length with two different diameters, $k = 1.6$ and 2.4 mm , and five different streamwise spacing ratios s_x/k ranges from 6 to 24. A total of 30 plates, 3-D printed triangular ribs, of $k = 1.6 \text{ mm}$ and $8k$ spacing; each plate measures $145 \text{ mm} \times 153.6 \text{ mm}$. The 3D printed triangular ribs were printed from acrylonitrile butadiene styrene (ABS) plastic material using a fused deposition modelling 3D printer, Zortrax M200. This model has an accuracy of $200 \text{ }\mu\text{m}$ in the x and z directions, and a layer height of $90 \text{ }\mu\text{m}$ with a 0.4 mm nozzle diameter, where x and z are the streamwise and spanwise directions,

respectively. A total of 8 CNC machined plates are employed, each of which has a 2-D sinewave surface function, an amplitude of $k/2 = 0.8$ mm and a wavelength of $8k$; each plate measures 435 mm \times 192 mm. These CNC machined surfaces were machined by a custom carbide engraving cutter of a TORMACH PCNC-series 3 machine. Two CNC machined plates have a 2-D sinewave surface function, an amplitude of $k/2 = 1.2$ mm and a wavelength of $8k$; each plate measures 480 mm \times 768 mm. This surface was fabricated by a Multicam M1212 Router machine, with a 0.6 mm stepover and 12 mm ball nose cutter. The absolute values of the profile heights for different rough surfaces are described as follows: a periodic function describes the rough surface of the circular rods, triangular ribs and sinewaves, respectively, as follows:

$$Z(x) = \begin{cases} \sqrt{kx - x^2} & 0 \leq x \leq k, \\ -\frac{k}{2} & k < x < s_x, \end{cases} \quad (5.6)$$

$$Z(x) = \begin{cases} -\frac{k}{2} + \frac{2kx}{s_x} & 0 \leq x \leq s_x/2, \\ -\frac{k}{2} + \frac{2k(s_x - x)}{s_x} & s_x/2 \leq x \leq s_x, \end{cases} \quad (5.7)$$

$$Z(x) = \frac{k}{2} \sin\left(\frac{2\pi x}{s_x}\right), \quad (5.8)$$

where $k = 1.6$ mm, and $s_x = 8k$. The surfaces are defined by the first letter of the shape name: R for rods, T for triangular ribs and S for sinewaves followed by $10k$ and finally the spacing ratio between two consecutive roughness peaks. For example $R16 - 08$ means a surface with cylindrical rods with a height of 1.6 mm and spacing ratio between two consecutive roughness rods of 8 . All different roughnesses, as well as the strip of sandpaper are taped using double-sided tape on an aluminium sheet of dimensions 500 mm \times 1600 mm. Statistical parameters used to characterise the different rough surfaces are tabulated in Table 5.1.

The roughness average height k_a , is defined by ASME (2009) as the arithmetic average of the absolute values of the profile height deviations from the mean m line, defined on the sampling length L_s as

$$k_a = \frac{1}{L_s} \int_0^{L_s} |Z(x) - m| dx. \quad (5.9)$$

The root-mean-square height k_{rms} corresponds to the standard deviation σ of the height distribution, defined on the sampling length as

$$k_{rms} = \sqrt{\frac{1}{L_s} \int_0^{L_s} Z(x)^2 dx}. \quad (5.10)$$

The roughness skewness k_{sk} (normalised third-order moment), is the asymmetry of the height distribution, defined on the sampling length. This parameter is crucial, as it indicates a morphology of the surface texture (see Flack *et al.* 2016). Positive values correspond to high peaks spread on a regular surface, while negative values correspond to surfaces with pores and scratches. However, this parameter does not give any information about the absolute height of the profile, contrary to k_a

$$k_{sk} = \frac{1}{\sigma^3 L_s} \int_0^{L_s} (Z(x) - m)^3 dx. \quad (5.11)$$

TABLE 5.1: Different key surface roughness parameters.

No.	Surface	k (mm)	s_x (mm)	k_a (mm)	k_{rms} (mm)	k_{sk}	k_{ku}	ES	λ_f
01	<i>R16 – 06</i>	1.6	9.60	0.40	0.59	1.85	4.53	0.333	0.1670
02	<i>R16 – 08</i>	1.6	12.8	0.31	0.51	2.34	6.57	0.250	0.1250
03	<i>R16 – 12</i>	1.6	19.2	0.22	0.42	3.09	10.7	0.167	0.0830
04	<i>R16 – 16</i>	1.6	25.6	0.17	0.36	3.70	14.9	0.125	0.0625
05	<i>R16 – 24</i>	1.6	38.4	0.11	0.29	4.69	23.3	0.083	0.0417
06	<i>R24 – 06</i>	2.4	14.4	0.60	0.88	1.85	4.53	0.333	0.1670
07	<i>R24 – 08</i>	2.4	19.2	0.47	0.76	2.34	6.57	0.250	0.1250
08	<i>R24 – 12</i>	2.4	28.8	0.33	0.62	3.09	10.7	0.167	0.0830
09	<i>R24 – 16</i>	2.4	38.4	0.25	0.54	3.70	14.9	0.125	0.0625
10	<i>R24 – 24</i>	2.4	57.6	0.17	0.44	4.69	23.3	0.083	0.0417
11	<i>T16 – 08</i>	1.6	12.8	0.40	0.92	0.00	1.80	0.250	0.1250
12	<i>S16 – 08</i>	1.6	12.8	0.51	0.57	0.00	1.50	0.250	0.1250
13	<i>S24 – 08</i>	2.4	19.2	0.76	0.85	0.00	1.50	0.250	0.1250

The roughness kurtosis k_{ku} (normalised fourth-order moment), is the sharpness of the height distribution, defined on the sampling length as

$$k_{ku} = \frac{1}{\sigma^4 L_s} \int_0^{L_s} (Z(x) - m)^4 dx. \quad (5.12)$$

The equation for the effective slope ES , which is the mean absolute streamwise gradient of the surface, as defined by [Napoli *et al.* \(2008\)](#) for 2-D rough surfaces is as follows:

$$ES = \frac{1}{L_s} \int_0^{L_s} \left| \frac{dZ(x)}{dx} \right| dx, \quad (5.13)$$

this parameter is also related to solidity λ_f , which is defined as the total projected frontal area of the roughness element A_f per unit wall parallel area A_p , by the relationship $ES = 2\lambda_f$ (see [Napoli *et al.* 2008](#))

$$\lambda_f = \frac{A_f}{A_p}. \quad (5.14)$$

5.4.3 Measurement rig

Single hot-wire probes with 5 μm diameter tungsten wire, and 1 mm sensing length (l) are used in measurements to give a length to diameter ratio of approximately 200, as recommended by [Ligrani & Bradshaw \(1987\)](#) and [Hutchins *et al.* \(2009\)](#). An overheat ratio of 1.6 is applied using an IFA300 constant temperature anemometer. A T-type thermocouple integrated with the IFA300 is used to record the mean temperature in the free stream throughout the experiment. Dynamic calibration of the hot-wire is performed with a square wave test also integrated into the IFA300 to determine the cutoff frequency of the hot-wire. A -3 dB drop off at approximately 10 kHz is recorded. Static calibration of the hot-wire is performed before and after each experiment. Calibrations are performed *in situ* against the Pitot-static tube positioned in the free-stream

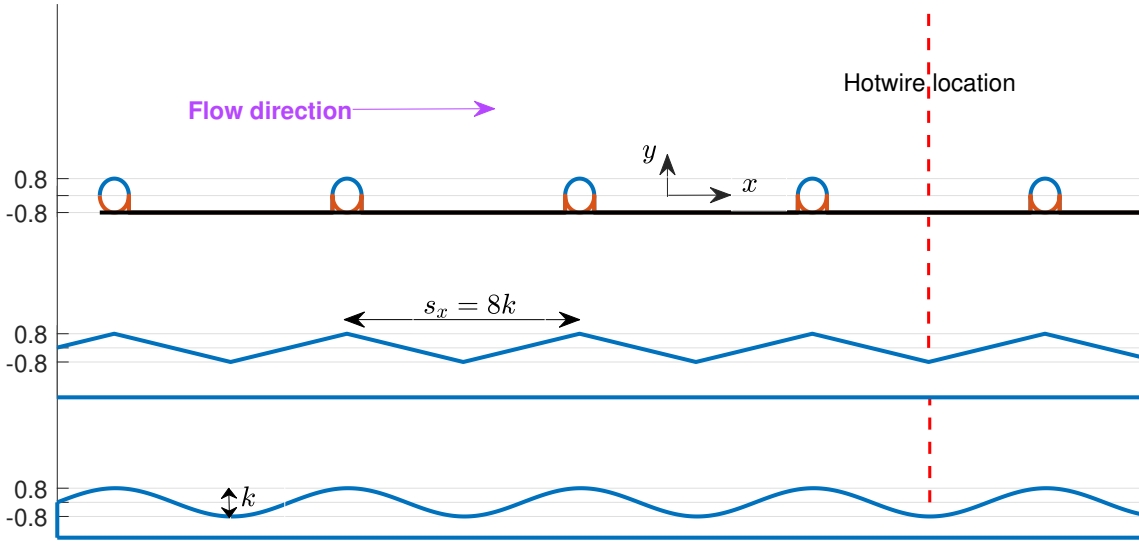


FIGURE 5.1: Schematic of different surface geometry set-ups with the same $k = 1.6$ mm and $s_x = 8k$. The red dotted line shows the measurement location. The coordinate system used in the experiments and $y = 0$ as a reference point are indicated in the schematic.

flow. More than 20 different velocities ranging between zero and 1.2 of the free-stream velocity of the experiment, are used for the calibration. If the pre-and post-calibrations do not collapse well, with a maximum 2 % error, the measurement is repeated. A polynomial of order six is used for fitting the voltage of the hot-wire and the measured velocity from the Pitot-static tube. Linear interpolation between pre-and post-calibrations are used to account for the hot-wire voltage drifting during the whole experiment.

A high magnification digital microscope is used to determine the offset from the wall at the first measurement point. The microscope is mounted on a 3D printed plate and placed on the rough surfaces to determine the wall offset. The probe is moved down to a distance of $100 \mu\text{m}$ over the plate before removing the plate. Then, the probe is moved down by a specific distance. This distance is equal to the thickness of the plate, plus the $100 \mu\text{m}$ offset, plus half of the roughness height ($20 + 0.1 + k/2$) mm. Thus $y = 0$ is located at the midpoint of the roughness element height. The criterion for choosing this location is detailed in section 5.5. Measurements are taken at the midpoint of two consecutive roughness peaks at $x \approx 1.5$ m downstream, measured after the tripping sandpaper. A total of 48 logarithmically spaced measurement points along the wall-normal position are taken by a Mitutoyo height gauge with a linear glass encoder attached to it, with $1 \mu\text{m}$ resolution, to determine the distance travelled away from the wall accurately. Measurements are taken with a sampling rate of 35 kHz for each wall-normal location. Figure 5.1 shows a schematic of the different rough surfaces set-ups and the measurement location.

5.4.4 Experiments

Two sets of experiments are conducted. In the first set the free-stream velocity U_∞ is varied from 5 to 20 m s^{-1} over 2-D circular rods of $k = 1.6$ mm diameter and $8k$ spacing. The results are validated with data from Djenidi *et al.* (2018) with almost the same roughness, and the same Re_τ range from 1300 to 5220. The boundary layer thicknesses are different because of the variation of the measurement location. The details of the first set of experiments are

TABLE 5.2: Details of the first set of rough wall experimental data. *R16 – 08L* refer to [Djenidi et al. \(2018\)](#) data.

Surface	$x(\text{m})$	U_∞ (m s^{-1})	U_τ (m s^{-1})	ν/U_τ (μm)	δ (mm)	Re_τ	Re_θ	l^+	H	C_f	δ/k	k_s^+	ΔU^+
<i>R16 – 08</i>	1.5	5.0	0.32	47	60	1295	3080	21	1.73	0.0082	38	210	9.8
		7.0	0.45	34	60	1779	4278	30	1.72	0.0081	38	288	10.5
		10.0	0.63	24	61	2583	6189	42	1.72	0.0079	38	406	11.4
		15.0	0.93	16	63	3916	9385	62	1.72	0.0077	39	647	12.5
		19.7	1.22	12	64	5223	12435	81	1.73	0.0077	40	903	13.4
<i>R16 – 08L</i>	2.54	4.2	0.24	65	98	1516	3922	8	1.73	0.0065	61	220	9.6
		6.4	0.38	41	96	2340	6045	12	1.73	0.0070	62	299	10.4
		10.4	0.62	25	99	3945	9925	20	1.73	0.0072	62	450	11.5
		15.0	0.90	17	100	5766	14305	29	1.67	0.0072	63	625	12.3

indicated in Table 5.2. The first set aims to validate our measurements and calculation of the friction velocity U_τ , as well as validate the fully rough Reynolds number independence and the consistency of the coefficient of friction C_f in the fully rough regime.

For the second set of experiments, measurements over different rough surfaces such as rods, triangular ribs and sinewaves, are carried out. All measurements in the second set are in the fully rough regime where $k_s^+ > 100$, with three different free-stream velocities ranging from 10 to 23 m s^{-1} for each surface. The boundary layer thickness varied from 48 to 70 mm ($23 < \delta/k < 41$). All information and details of the second set of data are presented in Table 5.3. This set is used to investigate the dominant roughness parameter that affects the turbulence statistics as well as the drag coefficient and correlate it directly to the roughness function.

5.5 FRICTION VELOCITY

One of the challenges of turbulent boundary layer (TBL) measurements over a rough surface is the calculation of the friction velocity U_τ . [Clauser \(1956\)](#) introduced a method, the Clauser chart method, widely used for smooth wall TBL. The method consists of fitting the measured velocity profile data to the so-called law of the wall

$$U^+ = \frac{1}{\kappa} \ln y^+ + B, \quad (5.15)$$

where κ is the von Kármán constant, and B is an additive constant. Unfortunately, the method has some uncertainties, such as the values of κ , B , and the lower and upper limits of the overlap region. For rough surface TBLs, the method requires two more variables, adding further uncertainties ([Perry & Joubert 1963](#)) since the law of the wall becomes

$$U^+ = \frac{1}{\kappa} \ln \frac{(y + \epsilon)U_\tau}{\nu} + B - \Delta U^+, \quad (5.16)$$

where ϵ is an origin offset.

[Marusic et al. \(2013\)](#) carried out measurements on high Reynolds number smooth wall TBLs. They found that the boundaries of the log region that best fits the velocity profiles are $y^+ > 3\sqrt{Re_\tau}$ and $y/\delta = 0.15$, which will be adapted in the present study as they best fit the log region of the velocity profiles over rough surfaces as well. Recently, [Djenidi, Talluru &](#)

TABLE 5.3: Details of the second set of rough wall experimental data.

Surface	Symbol	U_∞ (m s ⁻¹)	U_τ (m s ⁻¹)	ν/U_τ (μm)	δ (mm)	Re_τ	Re_θ	l^+	H	C_f	δ/k	k_s^+	ΔU^+
Smooth	+	09.9	0.40	37	38	990	2930	15	1.35	0.0031	NA	NA	NA
	×	19.9	0.76	20	33	1640	4850	29	1.31	0.0028	NA	NA	NA
R16 – 06	■	10.0	0.62	24	59	2443	5954	42	1.69	0.0078	37	358	11.0
	■	15.0	0.92	16	60	3655	8961	61	1.69	0.0076	37	562	12.1
	■	19.5	1.19	12	61	4861	11806	79	1.70	0.0075	38	785	13.0
R16 – 08	●	10.1	0.63	24	61	2583	6189	42	1.72	0.0079	38	406	11.4
	●	15.0	0.93	16	63	3916	9385	62	1.72	0.0077	39	647	12.5
	●	19.7	1.22	12	64	5223	12435	81	1.73	0.0076	40	903	13.4
R16 – 12	◆	10.0	0.60	25	58	2353	5835	40	1.66	0.0074	37	290	10.5
	◆	14.9	0.89	16	64	3791	9273	60	1.70	0.0072	40	478	11.8
	◆	19.3	1.15	13	65	4972	12013	77	1.74	0.0071	41	708	12.9
R16 – 16	▶	10.1	0.60	25	60	2412	5866	40	1.61	0.0071	38	240	10.3
	▶	15.0	0.89	17	62	3689	9379	59	1.63	0.0070	39	450	11.5
	▶	19.8	1.17	13	62	4804	12427	78	1.65	0.0070	38	679	12.3
R16 – 24	◀	10.0	0.58	26	55	2112	5412	38	1.60	0.0066	34	181	09.3
	◀	15.0	0.85	18	57	3256	8231	57	1.60	0.0065	36	270	10.5
	◀	19.4	1.10	14	54	3999	10406	74	1.61	0.0065	34	379	11.1
R24 – 06	■	10.0	0.63	24	69	2873	6804	42	1.72	0.0079	29	445	11.7
	■	14.9	0.93	16	70	4330	10380	62	1.70	0.0077	29	740	12.9
	■	20.0	1.24	12	69	5702	13696	83	1.70	0.0076	29	1039	13.7
R24 – 08	●	09.9	0.63	24	65	2754	6524	42	1.78	0.0082	27	510	11.9
	●	14.9	0.92	16	66	4049	9967	61	1.76	0.0077	27	678	12.7
	●	19.7	1.22	12	66	5321	12702	81	1.77	0.0077	27	1026	13.7
R24 – 12	◆	09.6	0.60	25	61	2435	5939	40	1.74	0.0078	25	373	11.0
	◆	14.7	0.89	17	62	3699	9044	60	1.73	0.0074	26	548	12.0
	◆	19.3	1.15	13	63	4858	11944	77	1.73	0.0071	26	697	12.7
R24 – 16	▶	10.0	0.60	25	65	2592	6254	40	1.66	0.0072	27	286	10.7
	▶	14.9	0.89	17	66	3897	9592	59	1.65	0.0071	27	482	11.9
	▶	20.1	1.17	13	65	5070	12434	78	1.64	0.0068	27	547	12.4
R24 – 24	◀	09.9	0.57	26	55	2090	5371	38	1.57	0.0066	23	168	09.2
	◀	15.0	0.84	18	60	3361	8554	56	1.57	0.0063	25	255	10.3
	◀	19.9	1.12	13	58	4307	11087	75	1.57	0.0063	24	351	11.1
T16 – 08	▲	12.0	0.67	22	53	2374	6102	45	1.60	0.0062	33	164	09.1
	▲	14.9	0.82	18	54	2977	7777	55	1.59	0.0061	34	199	09.6
	▲	19.6	1.06	14	53	3738	9681	71	1.59	0.0059	33	234	10.1
S16 – 08	▼	14.9	0.81	19	48	2596	6652	54	1.59	0.0058	30	139	08.8
	▼	19.9	1.06	14	50	3542	9182	70	1.59	0.0057	31	181	09.6
	▼	22.7	1.20	12	52	4141	10515	80	1.61	0.0057	32	218	10.2
S24 – 08	▼	10.1	0.54	28	59	2139	5511	25	1.52	0.0057	25	95	08.0
	▼	15.0	0.80	19	63	3347	8495	37	1.52	0.0057	26	159	09.4
	▼	20.0	1.07	14	65	4683	11722	50	1.51	0.0057	27	237	10.8

[Antonia \(2019\)](#) proposed a method for estimating U_τ for both smooth and rough wall TBLs. The method assumes an outer layer similarity between the smooth and rough flow and uses the velocity defect distribution, which is shown to exhibit a universal form for these two TBLs. A practical advantage of this latter method is that it involves empirical constants, thus eliminating the uncertainties of the modified Clauser chart method.

In the present work both the modified Clauser chart ([Perry & Li 1990](#)) and the velocity defect chart ([Djenidi *et al.* 2019](#)) methods will be used. Regarding the modified Clauser chart method, we performed a detailed study of the effect of κ and ϵ on the estimate of U_τ , in an attempt to understand how these parameters affect the results. Estimates based on both methods are compared. Figure 5.2(a) shows the values U_τ , based on the modified Clauser chart, for different values of ϵ and κ over the $R24 - 06$ surface at $U_\infty = 20 \text{ m s}^{-1}$; ϵ varies from 0 to k while κ ranges from 0.38 to 0.42. The least squares error of the fitting equation in the log region is shown in Figure 5.2(b). Results for different free-stream velocities and different surface roughnesses follow the same pattern of contours and are not shown here. These contours also show an infinite number of solutions that can be fitted with the same least squares error, illustrating the strong reliance on ϵ and κ of the modified Clauser chart method, and thus somehow its weakness. Figure 5.2(a) indicates that the maximum deviation for U_τ when using the modified Clauser chart is approximately 10 %. Figure 5.2(b) shows that $\kappa \approx 0.4$ gives the smallest error, regardless of the value of ϵ . Also, using $k/2 < \epsilon < 3k/4$ yields the same minimum error from fitting the mean velocity profile by the modified Clauser method regardless of the value of κ . The roughness function ΔU^+ is determined by averaging the vertical shift between the log region ($y^+ > 3\sqrt{Re_\tau}$ to $y/\delta = 0.15$) of the rough wall and smooth wall wall-unit normalised velocity profiles.

Since the main goal of the present study is to compare various roughness geometries and the focus of the results is on the outer layer similarity, we fix $\epsilon = k/2$ for all rough walls under investigation with $\kappa \approx 0.405$ and $B = 5$. Fixing these values, we found that U_τ obtained from the modified Clauser chart method matches that obtained from the velocity defect chart with an error of less than 3 % for all Reynolds numbers considered. The value of U_τ obtained from the velocity defect chart is used in the presented results for all rough wall flows, since the values obtained from both methods show good agreement.

5.6 RESULTS

5.6.1 Validation

Streamwise mean velocity profiles of the TBL over the $R16 - 08$ surface, normalised by inner scaling parameters at different Re_τ , are plotted with filled symbols in Figure 5.3. For comparison with our measurements, the data of [Djenidi *et al.* \(2018\)](#) at comparable Re_τ are represented with unfilled symbols. Also, our smooth wall data measurements are compared with the smooth TBL direct numerical simulation (DNS) data of [Schlatter & Örlü \(2010\)](#) and [Sillero, Jiménez & Moser \(2014\)](#) for $Re_\tau = 1040$ and $Re_\tau = 2000$, respectively. Two sets of smooth wall TBL experimental data ([Marusic *et al.* 2015](#)) are also reported on the figure for comparison. As expected, all smooth wall data collapse very well in the buffer and log regions. The friction velocity for smooth wall measurements is calculated by the Clauser method with $\kappa = 0.405$ and $B = 5$.

Using 2-D cylindrical rods for roughening a surface leads to a fully rough regime at a relatively low Re_τ . All rough data in Figure 5.3 are in a fully rough regime, as indicated in

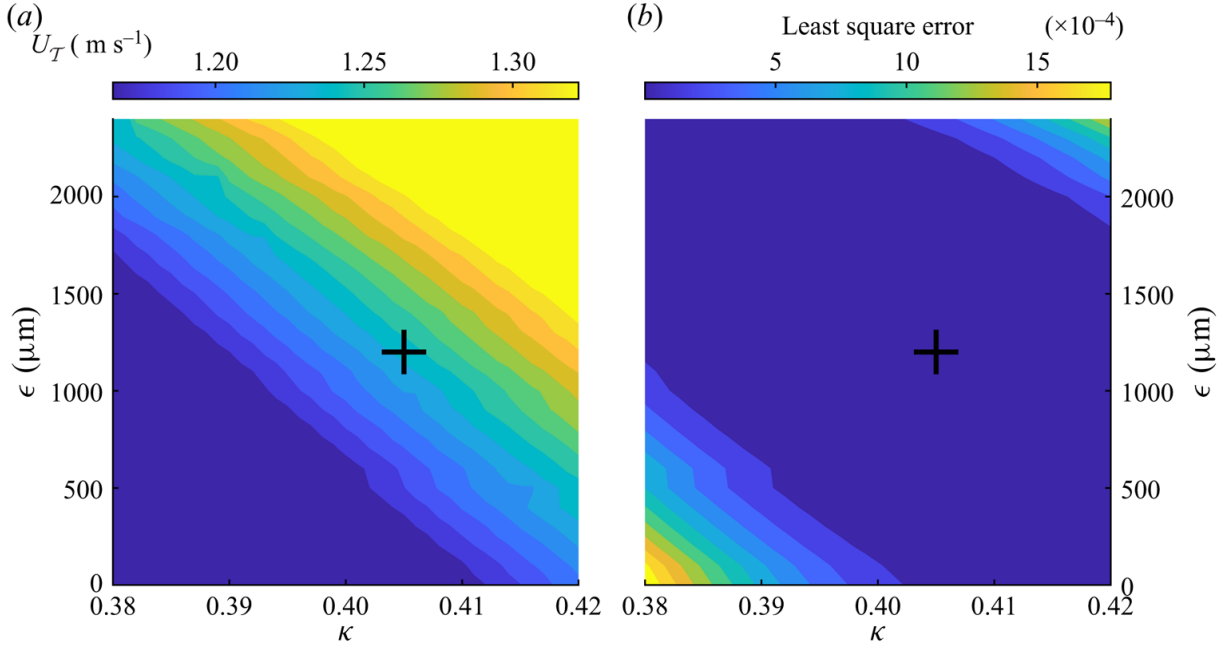


FIGURE 5.2: Friction velocity and least square error of TBL measurement over the R24-06 surface at $Re_\tau = 5700$ (a) Contours of U_τ calculated from the modified Clauser chart. (b) Contours of least square error from fitting data to the modified Clauser chart. The plus mark (+) refers to $\kappa = 0.405$ and $\epsilon = k/2 = 1200 \mu\text{m}$.

Table 5.2. Increasing Re_τ , or equivalently U_∞ , once the fully rough regime is achieved causes a rightwards shift towards larger y^+ , while $U^+ = U/U_\tau$ (or $C_f \sim (U_\tau/U)^2$) remains constant. The present data are in good agreement with the data of Djenidi *et al.* (2018), especially at Re_τ higher than 4000. The rightwards shift towards larger y^+ while maintaining the same C_f suggests that the inner length scale ν/U_τ is not an adequate scaling length for rough wall mean streamwise velocity profiles.

Profiles of streamwise root-mean-square (r.m.s.) velocity fluctuating u^{l+} for the R16-08 surface are reported in Figures 5.4(a) and 5.4(b) as functions of y/δ and $y/U_\tau/\nu$, respectively. Figure 5.4(a) shows an excellent collapse in the outer layer $y/\delta > 0.6$, regardless of the Reynolds number or the roughness of the surface. The present rough and smooth wall data exhibit lower magnitudes than those of Djenidi *et al.* (2018) and Marusic *et al.* (2015) in the near-wall region. This is believed to be due to larger values of our l^+ , which may attenuate the actual values of u^{l+} . Nevertheless, this has a negligible effect on the scope of the work as our focus is on comparing different kinds of roughnesses in terms of their effects on the mean velocity profiles. Chin *et al.* (2009) investigated spatial resolution issues in hot-wire measurements of wall-bounded turbulent flows. They applied different spanwise filter lengths to channel flow DNS data streamwise velocity components to simulate different spatial resolutions of single hot-wire probes. They found that the most severe attenuation occurs in the near-wall region due to the dominance of the small turbulence scales in this region. These attenuations are less severe in the outer region and are practically negligible for $y/\delta > 0.6$.

Figure 5.4(b) shows a noticeable systematic shift of the u^{l+} profiles when plotted as a function of y^+ . The rightward shift is similar to that observed in U^+ as Re_τ increases, further confirming that the inner length scale ν/U_τ is not an appropriate scaling length. For the rough wall data, one can observe a local inner peak at low Reynolds which tends to vanish as the Reynolds number increases. This behaviour is consistent with that observed in Schultz & Flack 2007, Krogstad & Efros 2012, Squire *et al.* 2016 and Djenidi *et al.* 2018, further indicating that

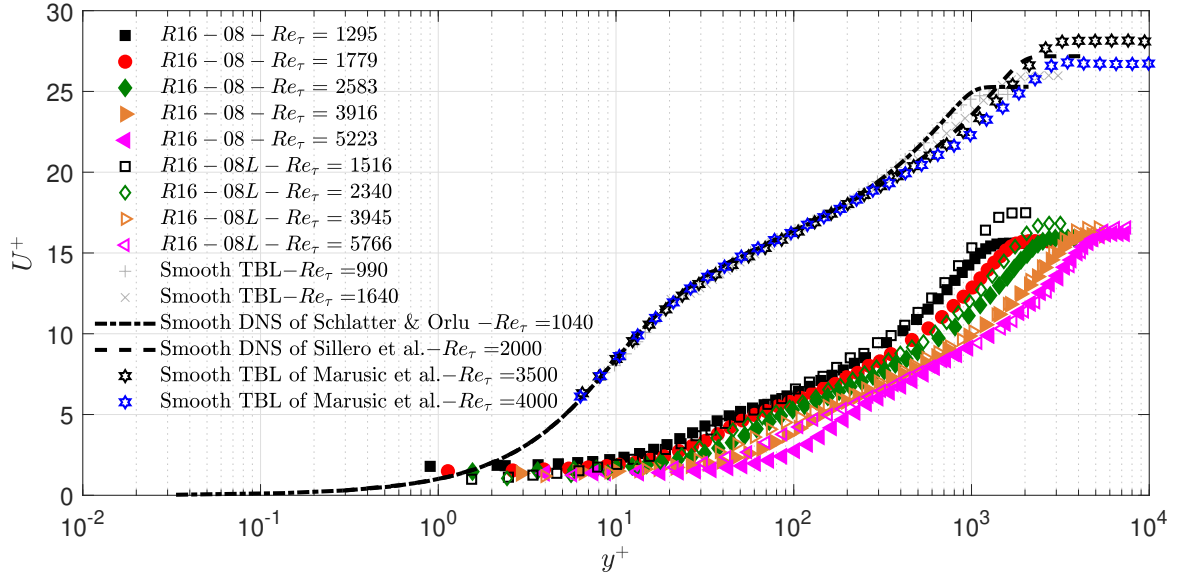


FIGURE 5.3: The streamwise mean velocity profiles over the $R16 - 08$ surface at different free-stream velocities normalised by the friction velocity U_τ . The unfilled symbols represent data from [Djenidi et al. \(2018\)](#) at the closest Re_τ . Our smooth wall TBL measurements are plotted in grey symbols and are detailed in Table 5.3. The dot-dashed line shows the smooth DNS data from [Schlatter & Örlü \(2010\)](#) at $Re_\tau = 1040$. The dashed line shows the smooth DNS data from [Sillero et al. \(2014\)](#) at $Re_\tau = 2000$. The black and blue hexagram symbols are smooth TBL data from [Marusic et al. \(2015\)](#) at $Re_\tau = 3500$ and 4000 , respectively. The wall-normal position y is normalised by the inner length scale ν/U_τ .

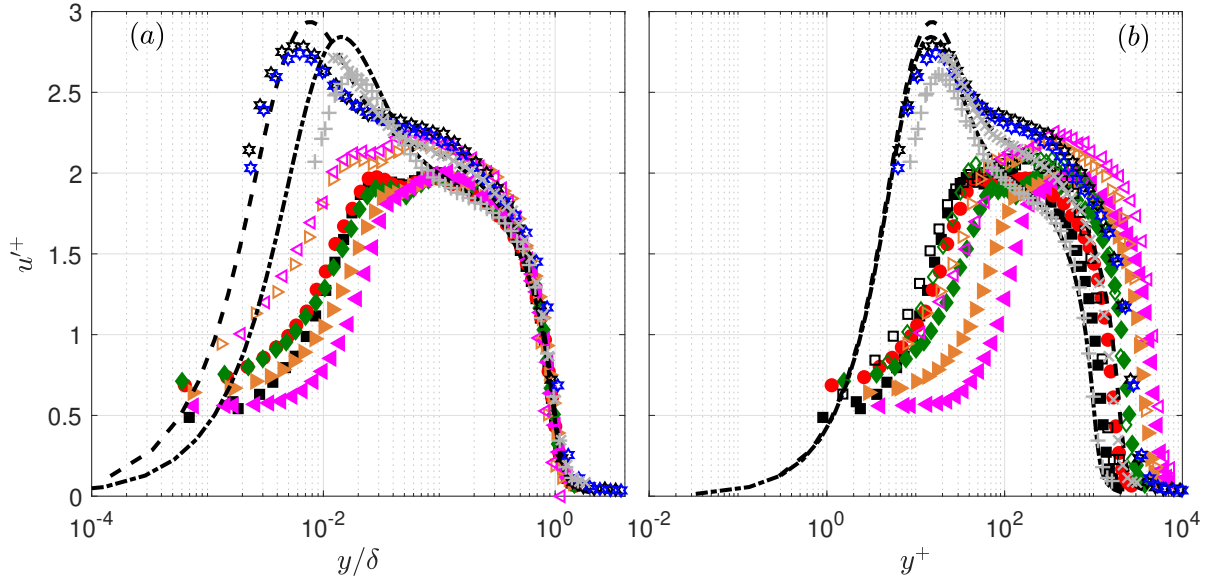


FIGURE 5.4: Profiles of u^i over the $R16 - 08$ surface at different free-stream velocities normalised by the friction velocity U_τ . The symbols are the same as indicated in Figure 5.3. (a) The wall-normal position y is normalised by the outer length scale δ . (b) The wall-normal position y is normalised by the inner length scale ν/U_τ .

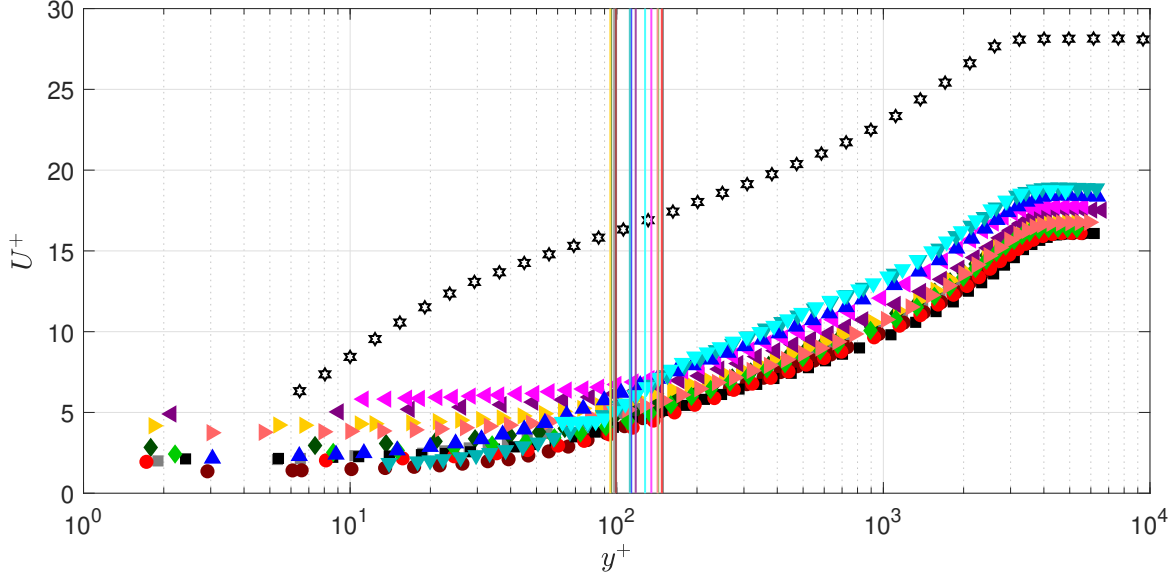


FIGURE 5.5: Streamwise mean velocity profiles over different rough surfaces at matched Reynolds number $3300 < Re_\tau < 4300$ where each surface is normalised by the friction velocity U_τ . The symbols of our measurements are detailed in Table 5.3. The black hexagram symbols are smooth TBL data from Marusic *et al.* (2015) at $Re_\tau = 3500$. The wall-normal position y is normalised by the inner length scale ν/U_τ . The vertical lines indicate the roughness heights in terms of viscous length scale units k^+ .

the possible attenuation associated with the relatively large values of l^+ does not critically affect the data, at least qualitatively in the inner region, giving us confidence in our measurements.

5.6.2 Second set of experiments

5.6.2.1 Mean velocity profile

Figure 5.5 shows the distributions U^+ vs y^+ for all the different rough surfaces used in this study; the vertical lines correspond to $y = k$ and their colours match those of the profiles they are associated with. For each rough wall, only one velocity distribution corresponding to a fully rough regime is reported; Re_τ ranges from 3300 to 4300. Also, the smooth wall velocity distribution data of Marusic *et al.* (2015) at $Re_\tau = 3500$ are shown in the figure as reference.

As we mentioned earlier, in a fully rough regime and at high Reynolds numbers, increasing the Reynolds number simply shifts the mean velocity profile to the right, to larger y^+ , while C_f remains constant. Roughnesses with the same spacing ratio s_x/k are represented by the same symbol, while the colours indicate different roughness heights, as indicated in Table 5.3. If we consider the rod and sinewave roughnesses and consult Table 5.1, we note that keeping s_x constant while changing k does not change k_{sk} , k_{ku} , ES and λ_f . Thus, the excellent collapse we observe between the distribution s_x for the rod and sinewave rough wall suggests that, in the fully rough regime, changing k or δ/k does not affect the mean streamwise velocity profile if δ/k is large enough ($\delta/k > 23$ in the present case). Changing of the spacing ratio between rods from 6 to 24 while maintaining the same roughness height causes a downward shift as a result of an increase of C_f . Decreasing the s_x/k ratio, which results in an increase of the effective slope ES and a decrease of the skewness k_{sk} for the same geometry, leads to a larger C_f with a resulting downward shift. More details about the effect of roughness parameters on the coefficient of friction will be discussed later, in section 5.6.2.2.

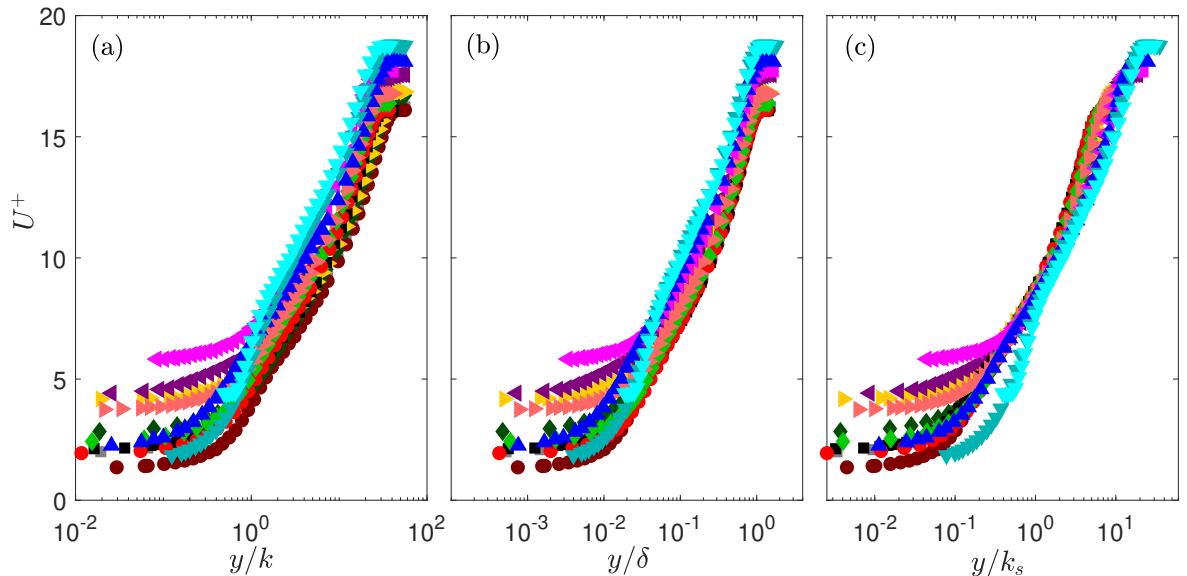


FIGURE 5.6: The streamwise mean velocity profiles over different rough surfaces at matched Reynolds number $3300 < Re_\tau < 4300$ where each surface is normalised by the friction velocity U_τ . The wall-normal position y is normalised by different outer length scales. The symbols of the different rough surfaces are detailed in Table 5.3. (a) The wall-normal position y is normalised by the outer roughness length scale k . (b) The wall-normal position y is normalised by the outer length scale δ . (c) The wall-normal position y is normalised by the outer roughness length scale k_s .

The velocity profiles for the rods with spacing ratios of 6 and 8 collapse relatively well, indicating that the boundary layer is only marginally affected by the small change of s_x , which is illustrated by the fact that C_f values for both spacing ratios are practically the same (see Table 5.3). This is consistent with DNS data of [Leonardi *et al.* \(2003\)](#) which show that the drag in a rod roughened turbulent channel flow is practically unchanged for $6 \leq s_x/k \leq 8$. Similar results are also observed in the data for a TBL over a rod roughened wall in [Furuya, Miyata & Fujita \(1976\)](#). Although sinewaves and triangular rib geometries have comparable sizes to the rods, ($k = 1.6$ or 2.4 mm and $s_x = 8k$), they exhibit the lowest C_f and ΔU^+ (see Table 5.3), resulting in a reduced downward shift for the corresponding velocity profiles in comparison with those for the rods.

The above observation applies to the region $y > k$. Since the distributions are only local ones (taken midway between two roughness elements), one expects to observe differences in the region $y < k$. These differences, however, disappear quite rapidly as y increases above k . For example, all the profiles exhibit almost the same shape when $y^+ \geq 200$. It is interesting to note that all the present rough surfaces have a similar wall-unit roughness height $100 < k^+ < 150$, while C_f varies from 0.0057 to 0.0077. This would confirm that roughness height alone is not a suitable roughness parameter to characterise the roughness function or the roughness geometry. This appears to be confirmed by the data of [Krogstad & Efron \(2012\)](#) and the data of [Djenidi *et al.* \(2018\)](#). Other parameters, such as ES and k_{sk} , may be more appropriate. This will be discussed in section 5.6.2.2. below.

Figure 5.6 shows the mean streamwise velocity profiles normalised by different outer length scales for all the different rough surfaces used in this study. While for a given roughness geometry the corresponding profiles collapse regardless of the length scale used, the situation is different when we consider all roughness geometries together. Indeed, a lack of a general collapse is observed when the length scales k and δ are used, as shown in Figure 5.6(a) and Figure

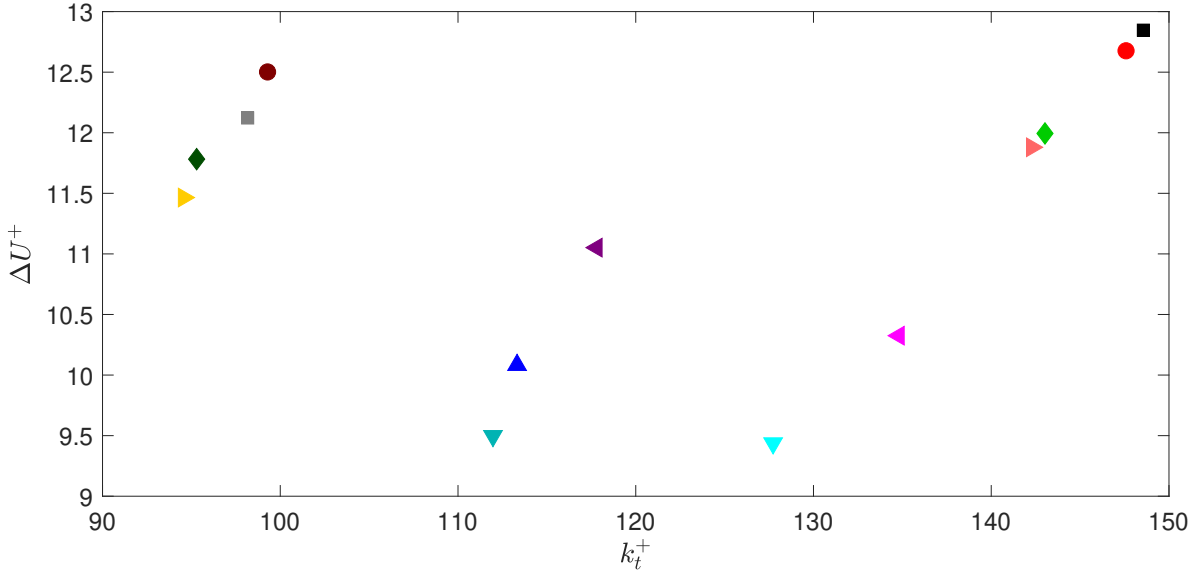


FIGURE 5.7: Roughness function ΔU^+ as a function of maximum peak-to-valley roughness height, k normalised by the inner length scale ν/U_τ . The filled symbols are the different surfaces roughness symbols indicated in Table 5.3.

5.6(b), respectively. This clearly indicates that the roughness height alone is not sufficient parameter to characterise the surface roughness. A similar remark has been made by [Squire *et al.* \(2016\)](#) and [Djenidi *et al.* \(2018\)](#) who argued that an outer length scale cannot be used to collapse velocity profiles normalised by the inner velocity scale when considering different kinds of roughnesses. However, when the equivalent sand grain roughness k_s is used the profiles appear to collapse better, as seen in Figure 5.6(c). This suggests that, even though k_s has no real physical meaning, it is nevertheless commonly used to characterise roughness. In that aspect, it is, from an engineering point of view, a very useful roughness length scale. Unfortunately, its lack of physical meaning makes it impossible to measure it directly from the topology of the surface. Nevertheless, there are attempts to correlate this parameter with the actual roughness parameters ([Schultz & Flack 2009](#); [Flack *et al.* 2020](#)). Unfortunately, none of these attempts provides a universal k_s that can be used for all kinds of roughness geometries. This, however, does not preclude the possibility of proposing a k_s that can be valid for a given family of a roughness geometries. In the next section we attempt to develop an expression for k_s for 2-D roughness.

5.6.2.2 Roughness function

Roughness has a wide range of shapes, types and textures that makes it almost impossible to characterise it by a single physical roughness parameter. Firstly, we need to define, if possible, the major roughness parameters that mostly affect the drag. Then, develop an equation for the equivalent sand grain roughness k_s that combines these parameters. The most common roughness parameter used to characterise the roughness is its height. There are various heights that can be measured from the roughness topography such as the average roughness height k_a , the root-mean-square roughness height k_{rms} , the maximum peak to valley roughness height k and the average of the highest 5 roughness peaks to the maximum lowest valleys k_z ([ASME 2009](#)). However, none of these roughness height parameters are alone capable of describing the roughness completely.

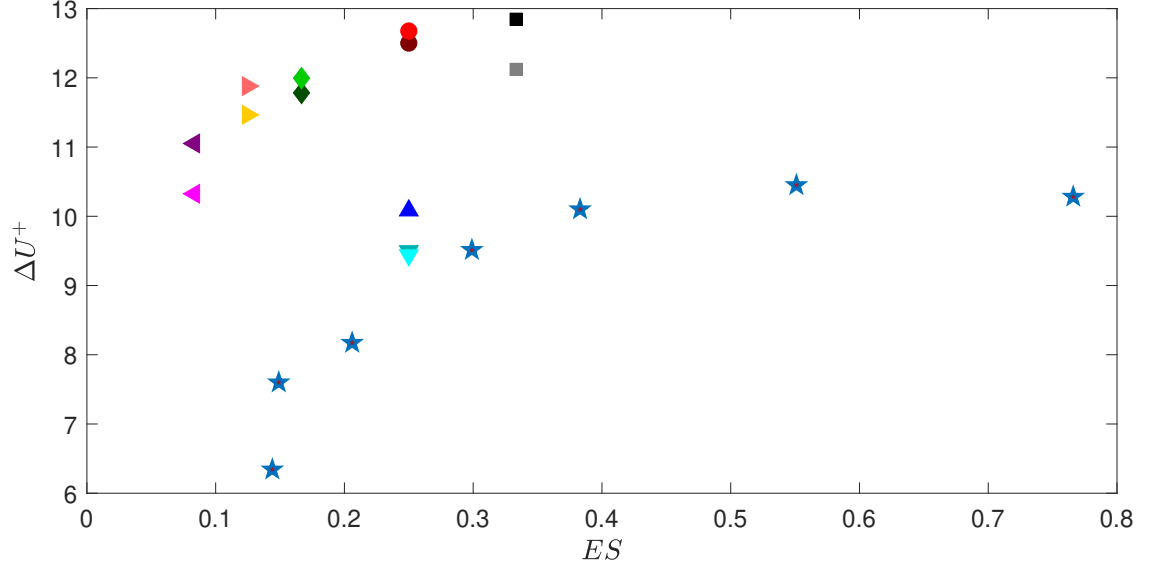


FIGURE 5.8: Roughness function ΔU^+ as a function of effective slope, ES . The filled symbols are the different surfaces roughness symbols indicated in Table 5.3. The blue pentagram symbols are channel flow data over various irregularly distributed sinusoidal roughness from Napoli *et al.* (2008).

Figure 5.7 shows ΔU^+ as a function of maximum peak-to-valley roughness height, k , for all the different surfaces used in this study. Each rough surface has different ΔU^+ in the fully rough regime, and there is no corresponding map function between the roughness height and the roughness function. All the surfaces used in this study only have two maximum peak to valley heights, even though the wall drag changes from one surface to another. Hence, another family of roughness parameters must be employed.

The frontal solidity λ_f is defined as the ratio of the total projected frontal area to the total plan area. This parameter indicates how big the area exposed to the flow is, which can be directly related to the pressure drag (MacDonald *et al.* 2016). Napoli *et al.* (2008) introduced the effective slope ES , defined as the mean absolute gradient of a roughness surface $ES = 2\lambda_f$. The advantage of using ES over λ_f is that the gradient can be calculated for any surface, even for random roughnesses, which makes it more general and robust in characterising the roughness.

Figure 5.8 shows ΔU^+ as a function of ES . It can be seen that, for the rods, ΔU^+ increases with ES . Note that the roughness function for triangular rib and sinewave surfaces is much lower than rods that have the same ES . This may be due to the fact that $k_{sk} = 0$ for the former roughnesses. The data of Napoli *et al.* (2008), who carried out a large eddy simulation of a rough wall turbulence channel flow, are reported in Figure 5.8. Their roughness consisted of corrugated walls covering a wide range of ES . We observe that our sinewave roughness functions match very well with their data. This validates the argument concerning the importance of the effective slope in determining the roughness function as well as in validating our measurements. The message of Figure 5.8 is that, for a fixed ES , highly skewed surfaces, such as rods, have higher roughness functions than corrugated-like surfaces. Further information one can infer from the figure is that it is challenging to describe a surface with only one roughness parameter. This reinforces the idea that a combination of two or more roughness parameters is likely to be needed to adequately characterise roughnesses. Although roughness height and slope reveal most of the roughness characteristics, they are not sufficient to completely describe the roughness.

Figure 5.9 shows the streamwise mean velocity profiles over $R16 - 08$, $S16 - 08$ and

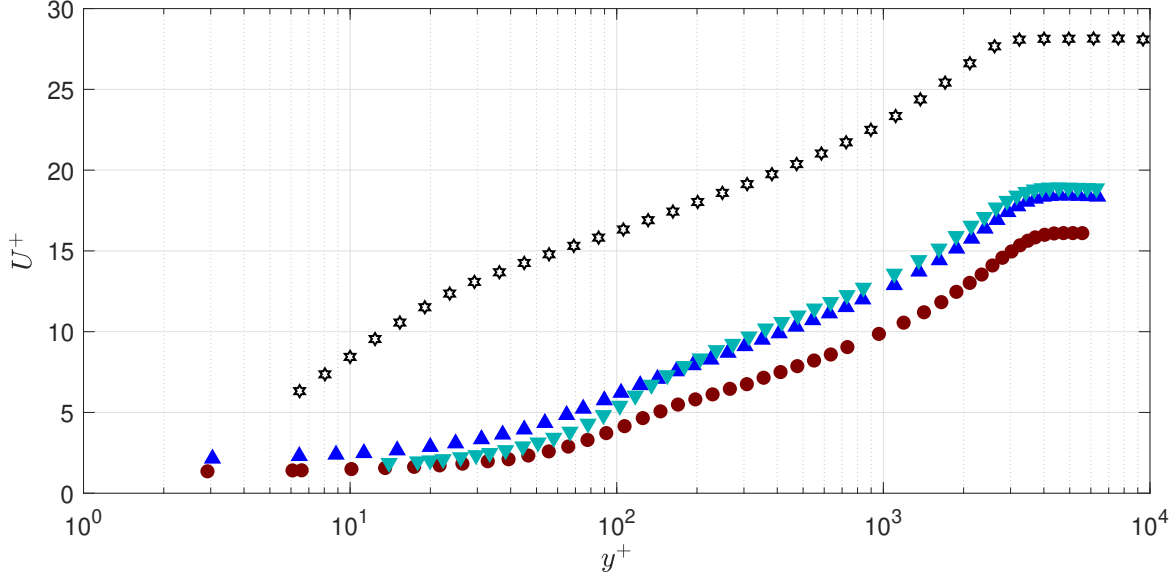


FIGURE 5.9: The streamwise mean velocity profiles over three different roughnesses with the same height, k , and effective slope, ES , but different geometries normalised by the friction velocity U_τ . Cases $R16 - 08$, $S16 - 08$ and $T16 - 08$ are compared with The smooth TBL data from [Marusic *et al.* \(2015\)](#). The symbols of our different surfaces are indicated in [Table 5.3](#).

$T16 - 08$ surfaces. These three surfaces have the same roughness height, k , and the same effective slope, ES , but different geometries. The roughness function, ΔU^+ , for $S16 - 08$ and $T16 - 08$ are almost the same, however, they have lower ΔU^+ than $R16 - 08$.

If we consider these roughnesses and consult [Table 5.1](#) we note that the skewness, k_{sk} , of the sinewave and the triangular ribs is the same, but different from the rods. Hence, a third group of roughness parameters should be introduced to adequately describe the roughness.

The plan solidity, λ_p , is defined as the ratio of the total projected plan area to the total plan area. This parameter measures how dense the roughness is ([Placidi & Ganapathisubramani 2015](#)). As mentioned above, ES is more usable than λ_f and can be used even for random roughness, the skewness of the roughness is more usable than the plan solidity and can be used for regular and irregular roughnesses. The skewness measures the symmetry of a profile about the mean line. It indicates a morphology of the surface texture; $k_{sk} > 0$ corresponds to high peaks, while $k_{sk} < 0$ corresponds to pitted surfaces.

[Figure 5.10](#) shows ΔU^+ as a function of k_{sk} in the fully rough regime. It can be noticed that, for the rods only, the roughness function decreases with increasing roughness skewness. The roughness functions for triangular rib and sinewave surfaces have lower values than rods, as they have zero roughness skewness value.

Attempts to correlate the k_s with roughness parameters like k_{sk} , and k_{rms} have been carried out (see [Flack *et al.* 2016](#)). Others proposed to relate ΔU^+ to ES instead of k_s ([Napoli *et al.* 2008](#)). However, a review of these different proposals shows that they apply to particular roughness geometries. This raises an interesting practical issue concerning whether these roughness parameters can be related to k_s , which controls the roughness function ΔU^+ as follows ([Nikuradse 1933](#)):

$$\Delta U^+ = \frac{1}{\kappa} \log(k_s^+) + B - 8.5. \quad (5.17)$$

In the following analysis we use $\kappa = 0.405$ and $B = 5$ and only data for which $\Delta U^+ > 8.5$

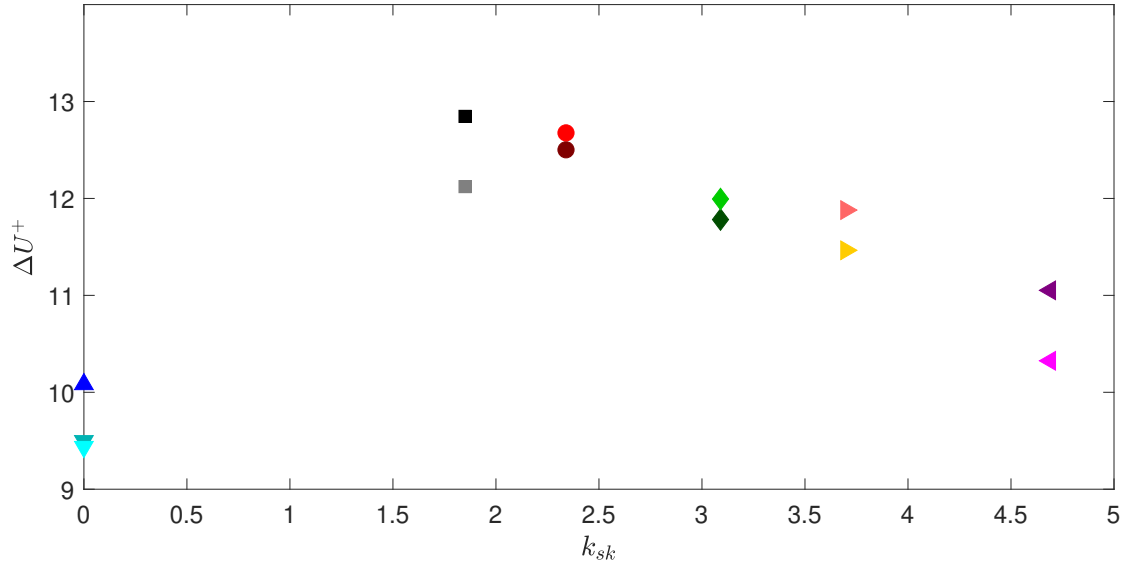


FIGURE 5.10: Roughness function ΔU^+ as a function of roughness skewness, k_{sk} . The filled symbols are the different surfaces roughness symbols indicated in Table 5.3.

are used to compute k_s^+ . It would seem that a combination of the three roughness parameters (k , ES and k_{sk}) would provide a better correlation function for k_s .

Figure 5.11 suggests that the expression (5.18) provides a suitable empirical relation for k_s for 2-D roughness. It is thus of interest to assess how this relation compares with previous experimental and numerical results for k_s . This comparison is reported in Figure 5.12, which shows the present predicted values of k_s with those of Krogstad & Efros (2012), Djenidi *et al.* (2018) and Leonardi *et al.* (2003). In this figure, a perfect agreement between the present predictions and measurement is represented by a straight line. While there is some scatter in the data, the figure shows a clear trend: the data align relatively well with the straight line, providing support for (5.18).

$$k_s = a + b \times k + c \times \frac{2k}{ES} + d \times ES \times k_{sk}, \quad (5.18)$$

where, $a = 0.001$, $b = 1.865$, $c = -0.103$, $d = 0.013$, with $R^2 = 0.93$. Here, R^2 is a statistical measure of how close the data are to the fitted regression line. It can be noticed that $2k/ES = s_x$ for uniform distributed roughness. It can be observed that, when $k_{sk} = 0$, as for sinewaves or triangular ribs, k_s will depend only on the roughness height k and the spacing between two consecutive roughness peaks s_x for distributed 2-D roughness or the effective slope for random roughness. However, for highly positive skewed roughness like 2-D cylindrical rods, both k_{sk} and ES affect k_s and are accounted for by the last term of (5.18). All data in the fully rough regime are on Nikuradse's asymptote line. These data support the proposal that k_s correlates very well with the drag coefficient ΔU^+ in the fully rough regime. Remarkably, a very good agreement is observed between ΔU^+ obtained using the measured and predicted values of k_s^+ , indicating that (5.18) provides a suitable equation for predicting k_s for a family of 2-D rough surfaces, i.e., 2-D cylindrical rod roughnesses and 2-D sinewaves or triangular ribs. This linear equation is developed for uniform 2-D roughnesses with ES varying from 0.08 to 0.33 and positive skewness roughness $0 \leq k_{sk} \leq 4.7$.

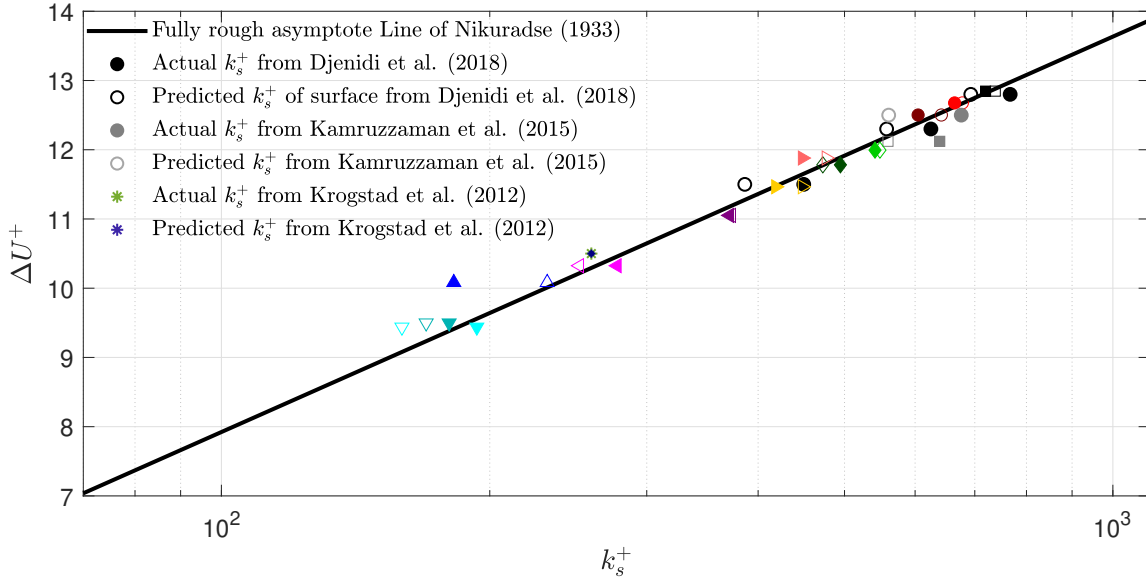


FIGURE 5.11: The roughness function for 2-D roughness as a function of equivalent sand grain roughness height k_s , normalised by the inner length scale ν/U_τ . The filled symbols are the different surface roughness symbols indicated in Table 5.3. The unfilled symbols are the predicted k_s^+ from (5.18) for the same rough surface. The black solid line is the fully rough asymptote of Nikuradse (1933). The values of k_s of Krogstad & Antonia (1999), Kamruzzaman *et al.* (2015) and Djenidi *et al.* (2018) are reported in the figure for comparison and validation.

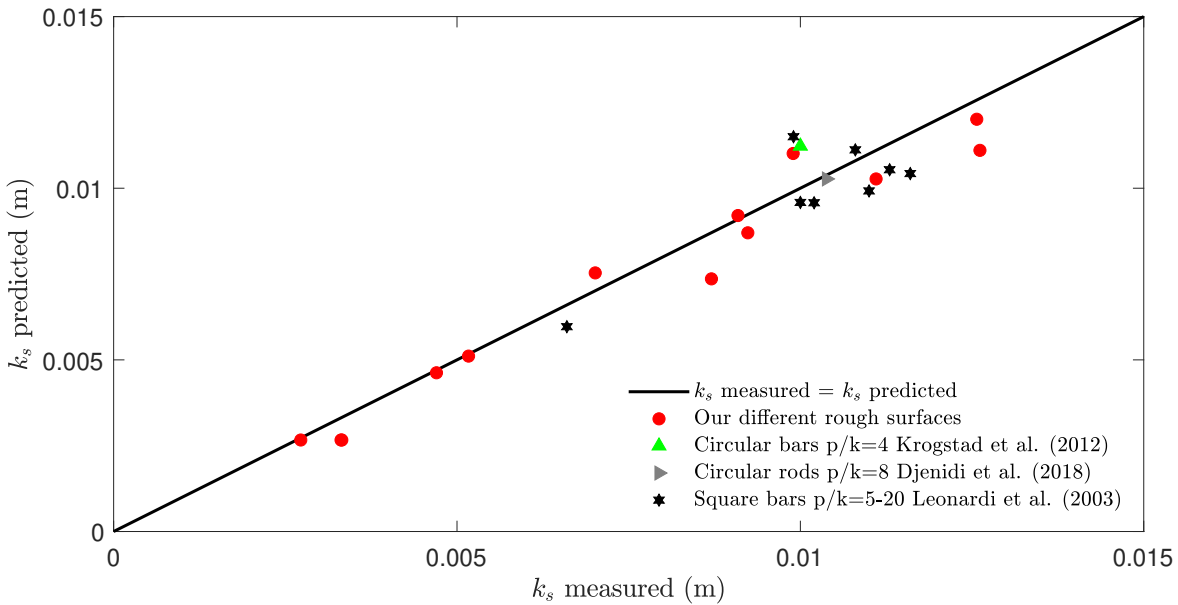


FIGURE 5.12: Comparison between actual k_s measured from mean velocity profiles and the calculated k_s from (5.18) for our surfaces along with previous experimental and numerical results of 2-D roughness only.

Since this empirical relation (5.18) has been developed for 2-D roughness, it was observed that it was not valid for 3-D roughness. Instead, a new empirical relation was developed for the 3-D roughness. Using the data of Flack *et al.* (2020), Barros, Schultz & Flack (2018), Busse, Thakkar & Sandham (2017), Forooghi *et al.* (2017) and Squire *et al.* (2016) and the same physical roughness parameters used for 2-D roughness (k , k_{sk} and ES), we obtained the following empirical relation:

$$k_s = a + b \times k + c \times k_{sk} + d \times \frac{2k}{ES} + e \times ES \times k_{sk}, \quad (5.19)$$

where, $a = -0.000025$, $b = 1.654$, $c = 0.004$, $d = -0.2$, $e = -0.0009$ with $R^2 = 0.79$. Notice the addition of a fifth term. Figure 5.13 compares the prediction of k_s using (5.19) with the values of k_s for the same data used to develop (5.19). While the data tend to exhibit an alignment with the straight line, there is a stronger scatter than in Figure 5.12, as quantified by a lower value of R^2 . The fact that two separate relations are required for the 2-D and 3-D roughnesses suggests that it is unlikely that one can develop a truly universal relation for k_s . We nevertheless attempted to obtain an empirical relation for both the 2-D and 3-D data. The result was the following relation:

$$k_s = a + b \times k + c \times \frac{2k}{ES} + d \times \frac{2k^2}{ES} + e \times e^{f \times ES \times k_{sk}}, \quad (5.20)$$

where, $a = -0.002$, $b = 0.926$, $c = 0.283$, $d = 4.933$, $e = 0.001$, $f = 3.66$, with $R^2 = 0.87$, k_s and k units are in mm.

Notice that, conversely to the two previous relations, (5.20) is non-linear; it was not possible to obtain a linear function that yields a reasonable fit to the data. Figure 5.14 shows the comparison between the predicted values of k_s with the measured ones. The data exhibit a large scatter around the straight line, even though the data show a tendency to align with that line, particularly the 2-D rough wall data.

It is important to stress that, like k_s itself, empirical relations like (5.18), (5.19), and (5.20) bear no physical meaning. However, their relevance and usefulness, from an engineering viewpoint, lie in the fact that they relate physical quantities for characterising the roughness geometry. Thus, the ability to predict k_s , which can be related to the drag, using simply the roughness parameters has an obvious practical interest.

More experiments for various kinds of roughnesses (2-D roughness such as grooves instead of rods to include negative skewness roughness as well as 3-D sinusoidal and random roughnesses) are needed to either validate and/or improve the previous expressions and to determine whether a universal formula for k_s can be developed for all kinds of roughness geometries.

5.7 CONCLUSIONS

Measurements are performed in a ZPG rough wall TBL to investigate the effect of different roughness parameters. Single hot-wire probes are used to measure the streamwise velocity at various Reynolds numbers and for 2-D roughness geometries. Circular rods with two different heights, $k = 1.6$ and 2.4 mm, and five different streamwise spacing ratios ranging from 6 to 24, 3D printed triangular ribs with heights of $k = 1.6$ mm and a spacing of $8k$ and CNC machined sinewave surfaces with two different heights, $k = 1.6$ and 2.4 mm, and a spacing ratio of 8 were investigated. These surface roughnesses covered a wide range of δ/k ranging from 23 to 41 in the fully rough regime.

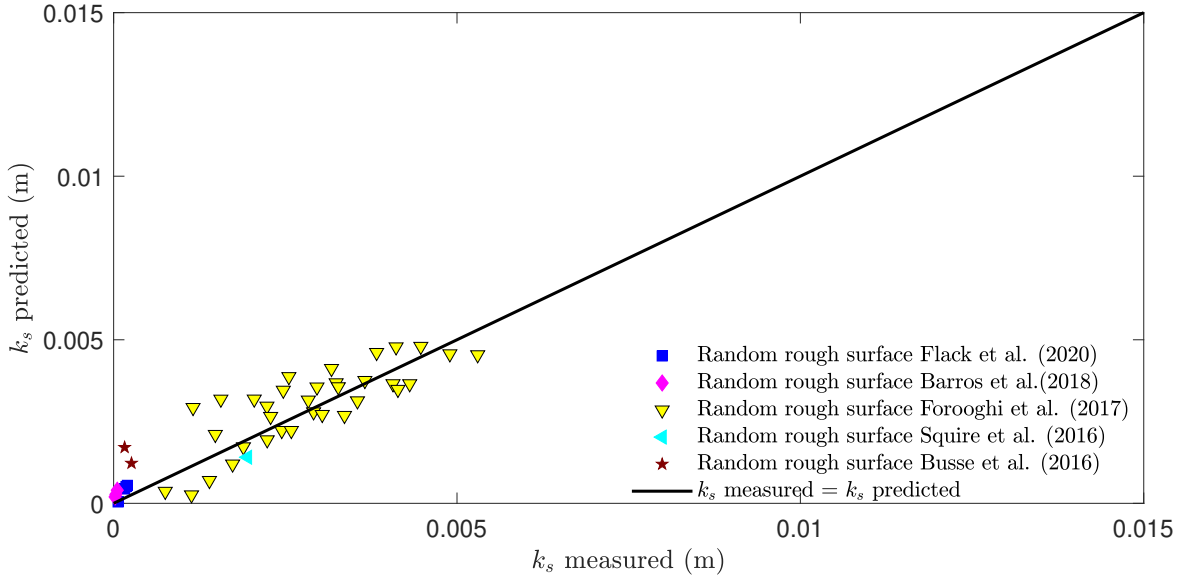


FIGURE 5.13: Comparison between actual k_s from literature and the calculated k_s from (5.19) for 3-D roughness only.

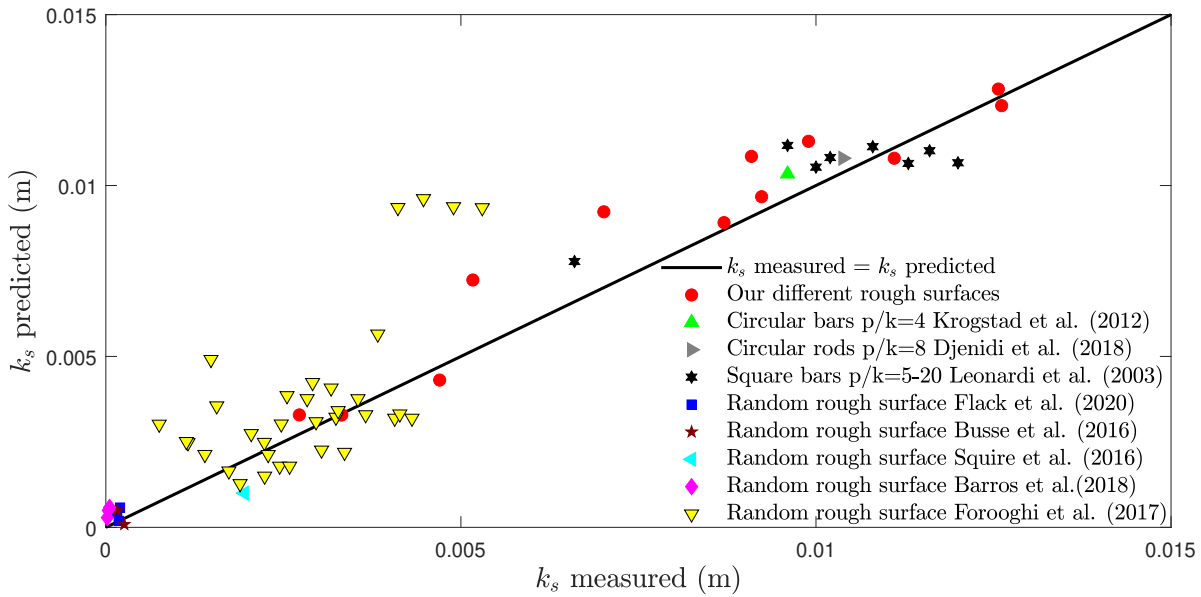


FIGURE 5.14: Comparison between actual k_s and the calculated k_s from (5.20) for 2-D and 3-D roughnesses

The roughness causes a downward shift of the wall-unit normalised mean velocity profile, known as the roughness function. The maximum downward shift is reached when the spacing ratio between two roughness elements is approximately 8. Changing the roughness height, while maintaining the same spacing ratio, does not affect the drag coefficient in the fully rough regime. Varying δ/k does not affect the mean streamwise velocity profile, if δ/k is large enough; $\delta/k > 23$ in this study. This reveals that roughness height is not an appropriate parameter to characterise the roughness.

An excellent collapse of the log region in the mean velocity profiles is observed when the equivalent roughness length scale k_s is used as a length scale to normalise the mean velocity profiles. Further, while k_s is not an actual physical roughness parameter that can be measured

directly from the topology of the surface, a new expression for k_s involving the physical roughness parameters k , ES and k_{sk} is proposed. It is shown that this new empirical relation provides a promising practical means to calculate the roughness function directly from the roughness topography in 2-D uniformly distributed rough surfaces. The relation shows that k , ES and k_{sk} are major surface roughness parameters affecting the turbulence statistics and drag coefficient.

Our results indicate that such general scaling cannot exist because of the complexity of the roughness geometries which involve too the many parameters. Further, the results suggest it is likely each family of roughnesses (for example 2-D roughness, 3-D roughness) would have its own scaling.

It should be noted that this new relation for k_s is limited to 2-D uniformly distributed roughness in a fully rough regime and more experiments on 2-D and 3-D rough surfaces, as well as random roughness, are needed to assess the importance of k , ES and k_{sk} in the turbulence statistics and drag coefficient. Such studies will help develop a more generalised relation for k_s , if such a generalisation can be made.

Funding.

The authors acknowledge the financial support of the Australian Research Council.

Declaration of interests.

The authors report no conflict of interest.

Author ORCIDs

Misarah Abdelaziz <https://orcid.org/0000-0003-2417-1755>;

L. Djenidi <https://orcid.org/0000-0001-8614-3595>;

Rey Chin <https://orcid.org/0000-0002-2709-4321>.

Bibliography

- ASME 2009 Surface texture (surface roughness, waviness, and lay). *Rrevision of ANSI/ASME B46.1-1995. Standard. ASME* .
- BARROS, J. M., SCHULTZ, M. P., & FLACK, K. A. 2018 Measurements of skin-friction of systematically generated surface roughness. *International Journal of Heat and Fluid Flow* **72**, 1–7.
- BONS, J. P. 2002 S_t and C_f augmentation for real turbine roughness with elevated freestream turbulence. *Journal of Turbomachinery* **124** (4), 632–644.
- BUSSE, A., THAKKAR, M., & SANDHAM, N. D. 2017 Reynolds-number dependence of the near-wall flow over irregular rough surfaces. *Journal of Fluid Mechanics* **810**, 196–224.
- CHIN, C. C., HUTCHINS, N., OOI, A. S. H., & MARUSIC, I. 2009 Use of direct numerical simulation (DNS) data to investigate spatial resolution issues in measurements of wall-bounded turbulence. *Measurement Science and Technology* **20**, 115401.

- CLAUSER, F. H. 1956 The turbulent boundary layer. *Advances in Applied Mechanics* **4**, 1–51.
- DJENIDI, L., TALLURU, K. M., & ANTONIA, R. A. 2018 Can a turbulent boundary layer become independent of the Reynolds number? *Journal of Fluid Mechanics* **851**, 1–22.
- DJENIDI, L., TALLURU, K. M., & ANTONIA, R. A. 2019 A velocity defect chart method for estimating the friction velocity in turbulent boundary layers. *Fluid Dynamics Research* **51**, 045502.
- FLACK, K. A., SCHULTZ, M. P., & BARROS, J. M. 2020 Skin friction measurements of systematically-varied roughness: Probing the role of roughness amplitude and skewness. *Flow, Turbulence and Combustion* **104** (2), 317–329.
- FLACK, K. A., SCHULTZ, M. P., BARROS, J. M., & KIM, Y. C. 2016 Skin-friction behavior in the transitionally-rough regime. *International Journal of Heat and Fluid Flow* **61**, 21–30.
- FOROOGHI, P., STROH, A., MAGAGNATO, F., JAKIRLIĆ, S., & FROHNAPFEL, B. 2017 Toward a universal roughness correlation. *Journal of Fluids Engineering* **139** (12).
- FURUYA, Y., MIYATA, M., & FUJITA, H. 1976 Turbulent boundary layer and flow resistance on plates roughened by wires. *Journal of Fluids Engineering* **98** (4), 635–643.
- HAMA, F. R. 1954 Boundary layer characteristics for smooth and rough surfaces. *Trans. Soc. Nav. Arch. Marine Engrs.* **62**, 333–358.
- HUTCHINS, N., NICKELS, T. B., MARUSIC, I., & CHONG, M. S. 2009 Hot-wire spatial resolution issues in wall-bounded turbulence. *Journal of Fluid Mechanics* **635**, 103–136.
- JIMÉNEZ, J. 2004 Turbulent flows over rough walls. *Annual Review of Fluid Mechanics* **36**, 173–196.
- KAMRUZZAMAN, M. D., DJENIDI, L., ANTONIA, R. A., & TALLURU, K. M. 2015 Drag of a turbulent boundary layer with transverse 2d circular rods on the wall. *Experiments in Fluids* **56** (6), 121(1–8).
- KROGSTAD, P.-Å. & ANTONIA, R. A. 1999 Surface roughness effects in turbulent boundary layers. *Experiments in Fluids* **27** (5), 450–460.
- KROGSTAD, P.-Å. & EFROS, V. 2012 About turbulence statistics in the outer part of a boundary layer developing over two-dimensional surface roughness. *Physics of Fluids* **24**, 075112.
- LEONARDI, S., ORLANDI, P., DJENIDI, L., & ANTONIA, R. A. 2015 Heat transfer in a turbulent channel flow with square bars or circular rods on one wall. *Journal of Fluid Mechanics* **776**, 512–530.
- LEONARDI, S., ORLANDI, P., SMALLEY, R. J., DJENIDI, L., & ANTONIA, R. A. 2003 Direct numerical simulations of turbulent channel flow with transverse square bars on one wall. *Journal of Fluid Mechanics* **491**, 229–238.
- LIGRANI, P. M. & BRADSHAW, P. 1987 Spatial resolution and measurement of turbulence in the viscous sublayer using subminiature hot-wire probes. *Experiments in Fluids* **5** (6), 407–417.
- MACDONALD, M., CHAN, L., CHUNG, D., HUTCHINS, N., & OOI, A. 2016 Turbulent flow over transitionally rough surfaces with varying roughness densities. *Journal of Fluid Mechanics* **804**, 130–161.

- MARUSIC, I., CHAUHAN, K. A., KULANDAIVELU, V., & HUTCHINS, N. 2015 Evolution of zero-pressure-gradient boundary layers from different tripping conditions. *Journal of Fluid Mechanics* **783**, 379–411.
- MARUSIC, I., MONTY, J. P., HULTMARK, M., & SMITS, A. J. 2013 On the logarithmic region in wall turbulence. *Journal of Fluid Mechanics* **716**, R3.
- MUSKER, A. J. 1980 Universal roughness functions for naturally-occurring surfaces. *Transactions of the Canadian Society for Mechanical Engineering* **6** (01), 1–6.
- NAPOLI, E., ARMENIO, V., & DE MARCHIS, M. 2008 The effect of the slope of irregularly distributed roughness elements on turbulent wall-bounded flows. *Journal of Fluid Mechanics* **613**, 385–394.
- NICKELS, T. B., MARUSIC, I., HAFEZ, S., & CHONG, M. S. 2005 Evidence of the k_1^{-1} law in a high-Reynolds-number turbulent boundary layer. *Physical Review Letters* **95**, 074501.
- NIKURADSE, J. 1933 Laws of flow in rough pipes. *Translation from German published 1950 as NACA Tech. Memo. 1292* .
- PERRY, A. E. & JOUBERT, P. N. 1963 Rough-wall boundary layers in adverse pressure gradients. *Journal of Fluid Mechanics* **17** (02), 193–211.
- PERRY, A. E. & LI, J. D. 1990 Experimental support for the attached-eddy hypothesis in zero-pressure-gradient turbulent boundary layers. *Journal of Fluid Mechanics* **218**, 405–438.
- PLACIDI, M. & GANAPATHISUBRAMANI, B. 2015 Effects of frontal and plan solidities on aerodynamic parameters and the roughness sublayer in turbulent boundary layers. *Journal of Fluid Mechanics* **782**, 541–566.
- SCHLATTER, P. & ÖRLÜ, R. 2010 Assessment of direct numerical simulation data of turbulent boundary layers. *Journal of Fluid Mechanics* **659**, 116–126.
- SCHLICHTING, H. & KESTIN, J. 1961 *Boundary layer theory*. vol. 121, New York: McGraw-Hill.
- SCHULTZ, M. P. & FLACK, K. A. 2007 The rough-wall turbulent boundary layer from the hydraulically smooth to the fully rough regime. *Journal of Fluid Mechanics* **580**, 381–405.
- SCHULTZ, M. P. & FLACK, K. A. 2009 Turbulent boundary layers on a systematically varied rough wall. *Physics of Fluids* **21**, 015104.
- SILLERO, J. A., JIMÉNEZ, J., & MOSER, R. D. 2014 Two-point statistics for turbulent boundary layers and channels at Reynolds numbers up to $\delta^+ = 2000$. *Physics of Fluids* **26**, 105109.
- SQUIRE, D. T., MORRILL-WINTER, C., HUTCHINS, N., SCHULTZ, M. P., KLEWICKI, J. C., & MARUSIC, I. 2016 Comparison of turbulent boundary layers over smooth and rough surfaces up to high Reynolds numbers. *Journal of Fluid Mechanics* **795**, 210–240.
- SUN, B. 2019 Thirty years of turbulence study in China. *Applied Mathematics and Mechanics* **40** (2), 193–214.
- WAIGH, D. R. & KIND, R. J. 1998 Improved aerodynamic characterization of regular three-dimensional roughness. *AIAA Journal* **36** (6), 1117–1119.

Chapter 6

Streamwise And Spanwise Effective Slopes Effect on Turbulent Boundary Layers

6.1 CHAPTER OVERVIEW

The previous chapter 5 introduced a new expression for k_s for 2D uniformly distributed roughness in the fully rough regime. It was discovered that ES and k_{sk} have a significant impact on the drag coefficient and turbulence statistics. This chapter examines the effect of varying the streamwise and spanwise effective slopes (ES_x and ES_z) on turbulence statistics. It's important to note that the results from chapter 5 were limited to 2D uniformly distributed roughness and expanding the study to 3D uniformly distributed roughness is a step towards more realistic representations of roughness.

Experimentally, single hot-wire anemometry was used to conduct ZPG-TBL measurements over 3D sinusoidal rough walls with the same amplitude but different streamwise and spanwise spacing-to-height ratios. The systematic variation of the roughness was divided into two groups. The first group had a constant s_x/k , while s_z/k was varied from 6 to 16. The surfaces in this group were then rotated 90 degrees in the (x, z) plane to form the second group, which had a constant s_z/k while s_x/k was varied from 6 to 16.

A comparison was made between two 3D sinewave roughnesses and two 2D sinewave roughnesses with similar roughness parameters. The results showed that the 3D sinewave surfaces produced less drag and had a lower roughness function and turbulence intensity than the 2D counterparts. As anticipated, the wall-normalised mean velocity profiles were shifted downward for all roughnesses compared to the smooth wall profile. The streamwise effective slope (ES_x) had a bigger impact on the roughness function (ΔU^+) and skin friction coefficient (C_f) compared to the spanwise effective slope (ES_z). However, ES_z had a greater effect on the streamwise turbulence intensities in the log and outer layer. For isotropic 3D sinusoidal roughness, the premultiplied streamwise turbulence energy spectrograms showed an increase in energy content in the outer layer with an increase in s_x/k . For anisotropic 3D sinusoidal roughness, the energy content increased in the outer layer with an increase in s_z/s_x from half to two.

6.2 ON THE EFFECT OF STREAMWISE AND SPANWISE SPACING TO HEIGHT RATIOS OF THREE-DIMENSIONAL SINUSOIDAL ROUGHNESS ON TURBULENT BOUNDARY LAYERS

This section consists of the following published journal article:

Cite as: Phys. Fluids **35**, 025130 (2023); <https://doi.org/10.1063/5.0136072>

Submitted: 23 November 2022 • Accepted: 01 February 2023 • Accepted Manuscript Online: 01 February 2023 • Published Online: 21 February 2023

Misarah Abdelaziz, L. Djenidi, Mergen H. Ghayesh, and Rey Chin.


The article is identical to its submitted format with the following exceptions:

- The numbering of figures, tables and equations has been altered to include the chapter number.
- The position of some figures and tables has been changed to improve the article's legibility.
- References style has been changed to be consistent with the thesis style.

On the effect of streamwise and spanwise spacing to height ratios of three-dimensional sinusoidal roughness on turbulent boundary layers

Cite as: Phys. Fluids **35**, 025130 (2023); <https://doi.org/10.1063/5.0136072>

Submitted: 23 November 2022 • Accepted: 01 February 2023 • Accepted Manuscript Online: 01 February 2023 • Published Online: 21 February 2023

 Misarah Abdelaziz,  L. Djenidi, Mergen H. Ghayesh, et al.



View Online



Export Citation



CrossMark

Statement of Authorship

Title of paper	On the effect of streamwise and spanwise spacing to height ratios of three-dimensional sinusoidal roughness on turbulent boundary layers
Publication status	Published
Publication details	Misarah Abdelaziz, L. Djenidi, Mergen H. Ghayesh, and Rey Chin. On the effect of streamwise and spanwise spacing to height ratios of three-dimensional sinusoidal roughness on turbulent boundary layers <i>Physics of Fluids</i> , 35 , 025130 (2023); https://doi.org/10.1063/5.0136072

Principal Author

Name of principal author (candidate)	Misarah Abdelaziz
Contribution to the paper	Conception, acquiring data, knowledge, analysis and drafting
Certification	This paper reports on original research I conducted during the period of my Higher Degree by Research candidature and is not subject to any obligations or contractual agreements with a third party that would constrain its inclusion in this thesis. I am the primary author of this paper.
Signature:	Date: 05/07/2023

Co-author contributions

By signing the Statement of Authorship, each author certifies that:

- i.* the candidate's stated contribution to the publication is accurate (as detailed above)
- ii.* permission is granted for the candidate to include the publication in the thesis; and
- iii.* the sum of all co-author contributions is equal to 100% less the candidate's stated contribution.

Name of co-author	Lyazid Djenidi
Contribution to the paper	Conception, knowledge, analysis and drafting
Signature:	Date: 27/06/2023

Name of co-author	Mergen H. Ghayesh
Contribution to the paper	Conception, knowledge, and drafting
Signature:	Date: 04/07/2023

Name of co-author	Rey Chin
Contribution to the paper	Conception, knowledge, analysis and drafting
Signature:	Date: 04/07/2023

On the effect of streamwise and spanwise spacing to height ratios of three-dimensional sinusoidal roughness on turbulent boundary layers

Cite as: Phys. Fluids **35**, 025130 (2023); <https://doi.org/10.1063/5.0136072>

Submitted: 23 November 2022. Accepted: 1 February 2023.

Published Online: 21 February 2023

Misarah Abdelaziz,^{1,a)} L. Djenidi,² Mergen H. Ghayesh,¹ and Rey Chin¹

AFFILIATIONS

¹School of Electrical & Mechanical Engineering, University of Adelaide, Adelaide, South Australia, 5005, Australia

²Department of Mechanical Engineering, Indian Institute of Technology - Bombay, Powai, Mumbai 400076, India

^{a)} Author to whom correspondence should be addressed: misarah.abdelaziz@adelaide.edu.au

ABSTRACT

A developing zero pressure gradient (ZPG) turbulent boundary layer (TBL) over different three-dimensional (3D) sinewave roughnesses is investigated experimentally using single hot-wire anemometry. Seven different sinewave profiles are fabricated with the same amplitude and with different wavelengths in the streamwise (s_x) and spanwise (s_z) directions. The effects of varying s_x and s_z on turbulence statistics and the drag coefficient (C_f) are assessed. The wall-unit normalized streamwise mean velocity profile is shifted downward compared with the smooth wall profile for all roughnesses. The streamwise spacing to height ratio s_x/k has a more significant effect on the roughness function ΔU^+ and C_f compared with the spanwise spacing to height ratio s_z/k . However, s_z/k has a large impact on the streamwise turbulence intensities in the log and outer layer. An excellent collapse is observed among the mean streamwise velocity profiles plotted in defect form in the outer region. However, a lack of similarity between TBLs over different rough surfaces is observed in the outer region for the turbulence intensities profiles. For isotropic 3D sinusoidal roughness (equal streamwise and spanwise spacing to height ratios), the contours of premultiplied streamwise turbulent energy spectrograms show an increase in energy in the outer layer with increasing spacing to height ratios. For anisotropic 3D sinusoidal roughness (unequal streamwise and spanwise spacing to height ratios), the contours of premultiplied streamwise turbulent energy spectrograms show an increase in energy in the outer layer with increasing s_z/s_x from half to two in this study.

Published under an exclusive license by AIP Publishing. <https://doi.org/10.1063/5.0136072>

6.3 INTRODUCTION

A large container ship can emit pollutants equivalent to 50×10^6 cars in one year. Even a recently cleaned ship-hull has a noticeable drag increase compared with a smooth wall resulting from some imperfection and bio-fouling. (Nugroho *et al.* 2017; Utama *et al.* 2017) All surfaces are hydro-dynamically rough at sufficiently high Reynolds numbers, such as those on container

ships or very large crude carriers. A long-lasting goal in fluid dynamics research is to calculate the drag penalty over surfaces solely from the topographical parameters of the surface.

About 50 % of the total drag of a commercial aircraft in flight is due to the skin-friction drag. This number can reach 80 % - 90 % for a large carrier ship; thus, characterizing different roughness parameters and their effect on the drag coefficient is imperative. (Marec 2001) The drag coefficient of a rough surface is larger than that of a smooth wall ($C_f = 2U_\tau^2/U_\infty^2$, where U_τ is the friction velocity, and U_∞ is the free-stream velocity, $U_\tau = \sqrt{\tau_w/\rho}$, where τ_w is the wall shear stress, and ρ is the fluid density). The increase in C_f is reflected by the downward shift of the mean velocity profile normalized by the wall units compared with a smooth wall profile. (Hama 1954) This shift is known as the Hama roughness function and is defined as $\Delta U^+ = \Delta U/U_\tau$, where U is the mean streamwise velocity; the superscript, $(^+)$ represents normalization in the wall-units U_τ or ν/U_τ , where ν is the kinematic viscosity. The roughness function ΔU^+ is a function of the equivalent sand grain roughness k_s . (Schlichting & Kestin 1961)

Most engineers use the Moody chart to predict the skin friction drag of pipe flows over rough walls. (Moody 1944) The roughness length scale k_s must be known before the Moody diagram is used. k_s is defined as the sand grain size from Nikuradse experiments that produce the same friction factor as the surface of interest in the fully rough regime. (Nikuradse 1933) However, k_s is not a physical roughness parameter; its determination relies either on an empirical method based on the mean velocity profile or it could be obtained straightforwardly by performing a hydraulic experiment for the surface of interest. Ideally, one would prefer to determine the frictional drag based on the roughness topology. This would provide perhaps a more adequate and objective way of predicting C_f without the need to perform lengthy measurements.

When $k_s^+ = k_s \times U_\tau/\nu$ is small, $k_s^+ < 5$, the wall roughness does not affect the viscous sublayer. This flow regime is called “dynamically smooth” and can be treated as a smooth wall flow. On the other hand, when k_s^+ is large, $k_s^+ > 70$, the viscous effects are negligible, and the drag is mainly composed of the form drag due to the roughness elements. This regime is called “fully rough” and is characterized by a log-linear relationship between ΔU^+ and k_s^+ . When k_s^+ has moderate values, $5 < k_s^+ < 70$, the flow regime is called “transitionally rough”, and both the pressure drag and the viscous drag influence the near-wall flow. (Nikuradse 1933; Jiménez 2004)

To date, there has been no definite consensus on which length scale or roughness parameter best characterizes a surface that can correlate with friction drag. Mainly because of the disparity of rough surfaces and their irregular nature. Whether such a universal parameter exists is still an open issue. Artificial intelligence and machine learning may soon be used to develop a high-fidelity prediction approach of k_s for turbulent flows over a wide variety of rough surfaces. (Jouybari *et al.* 2021) However, enlarging the roughness database and identifying the main roughness parameters that affect the drag coefficient for families of rough surfaces, such as two-dimensional (2D) roughness and 3D roughness, would accelerate this process.

The roughness family considered here is 3D sinusoidal roughness. There are many reasons to focus on this roughness family. One reason is that it adds more complexity to the 2D roughness and makes it more realistic and closer to real roughness. Second, it is effortless to systematically change one or two roughness parameters while keeping other parameters fixed. This enables us to study the effect of these parameters independently on the drag coefficient. Over the last decade, a large body of work has been undertaken to address the issues of the effect of surface morphology on turbulent boundary layers and correlating one or more roughness parameters to the equivalent sand grain roughness k_s . Researchers investigated a wide range of surface roughnesses, i.e., 2D roughness, 3D regular, and random roughness. (Bai *et al.* 2018; Hamed *et al.* 2019; De Marchis *et al.* 2020; Forooghi *et al.* 2020; Medjnoun *et al.* 2021; Brereton *et al.* 2021; Abdelaziz *et al.*

2022a; Gul & Ganapathisubramani 2022) A wide range of different surface parameters have been studied to determine which of these parameters dominantly affect the friction drag. The roughness parameters considered are the mean roughness height k_a , root-mean-square height k_q , maximum peak to valley height k_t , average peak to valley height k_z , effective slope ES , solidarity λ_f , skewness k_{sk} , and flatness k_{ku} .

Napoli *et al.* (2008) introduced the effective slope ES , defined as the mean absolute roughness gradient. This parameter can be used for any surface, even random roughness, making it more general and robust to characterize the roughness. Napoli *et al.* (2008) carried out a large eddy simulation of a rough wall turbulence channel flow. They used corrugated walls for their roughness to cover a wide range of ES . They revealed the importance of the effective slope in determining the roughness function. Their results showed that $ES \approx 0.15$ separates the transitionally rough regime from the fully rough regime. This value also separates the region where the roughness function $\Delta U^+ = f(ES)$ is linear from that where a smooth nonlinear behavior is observed.

Chan *et al.* (2015) carried out a DNS for turbulent flow through pipes with 3D sinusoidal roughnesses. ΔU^+ is found to be marginally affected by low Reynolds numbers. They systematically studied the effects of roughness height and wavelength in a turbulent pipe flow in both transitionally rough and fully rough regimes. Their investigation showed a strong dependence of ΔU^+ on both k_a and ES . Using large eddy simulations, De Marchis *et al.* (2020) looked at the effects of different geometrical surfaces generated by the superimposition of sinusoidal functions with random amplitudes in transitional and fully rough regimes on ΔU^+ at various friction Reynolds number, $Re_\tau (= \delta U_\tau / \nu$, where δ is the half channel height or the boundary layer thickness). They showed a correlation between ES and k_q could predict the roughness function. Forooghi *et al.* (2017) revealed the importance of k_t , k_{sk} , and ES on roughness function on their DNS simulations of a fully rough turbulent channel flow at $Re_\tau \approx 500$. They generated their roughness by varying the moments of surface height probability density function, the effective slope, and the size distribution of the random roughness. They showed that these roughness parameters could accurately predict k_s in the fully rough regime of channel flows.

Although the numerical investigation of different roughness parameters' effects on the roughness function is more convenient than experimental investigations in systematically changing roughness parameters, they are limited to low and moderate Reynolds numbers. For higher Reynolds numbers, many researchers have addressed these issues experimentally (among many others, Schultz & Flack 2009; Flack *et al.* 2020; Ramani *et al.* 2020). To investigate the effect of roughness slope and height on ΔU^+ , Schultz & Flack (2009) conducted water tunnel experiments on close-packed pyramid roughnesses. They found that ΔU^+ mainly depends on the roughness height. They also determined that an ES of 0.35 separates the roughness from the wavy regimes. If ES is less than 0.35, the surface is wavy, and the roughness function strongly depends on ES . Flack *et al.* (2020) investigated the importance of roughness height and skewness on the drag coefficient. Their random roughness has a Gaussian power spectral density distribution of surface elevations. Their results showed that negative skewness had a smaller C_f than positive skewness. Ramani *et al.* (2020) investigated the effects of both the streamwise and spanwise effective slopes of surface roughness on turbulent boundary layer flows. Their results suggested that even though the streamwise effective slope ES_x have a more significant impact on the drag coefficient than the spanwise effective slope ES_z , ES_z plays a vital role in the drag coefficient and cannot be neglected. Abdelaziz *et al.* (2022a) found that k_t , ES and k_{sk} are the major surface roughness parameters affecting the turbulence statistics and drag coefficient of turbulent boundary layer flows over 2D surfaces roughness. Their results reveal that a general

scaling for 2D and 3D roughness is unlikely to exist, and each family of roughnesses would likely have its own scaling.

While a large body of work has been undertaken to correlate k_s with real roughness parameters, these correlations still lack universality and are only limited to specific surface roughnesses. So far, universal critical parameters for all roughnesses are yet to be determined. However, some parameters can likely be identified for families of rough surfaces, such as 2D roughness and 3D roughness, in the fully rough regime. While different roughness parameters are needed in predictive drag correlations, it is crucial to study the effect of each parameter individually.

The present work attempts to study the effect of the streamwise and spanwise effective slope parameters on the turbulent boundary layer flow while keeping all other roughness parameters unchanged. To the best of our knowledge, no one isolates the effect of ES_x and ES_z only on turbulence statistics and the drag coefficient. These 3D sinusoidal roughnesses can be compared with 2D ones and can be used to understand more deeply the difference between 2D and 3D roughnesses with very close or similar parameters. In this present work, we carry out turbulent boundary layer measurements over various 3D sinusoidal rough surfaces with a fixed boundary layer to roughness height ratio δ/k . The experiments determine how the streamwise and spanwise effective slopes impact C_f for this 3D rough wall family.

6.4 EXPERIMENTAL DETAILS

6.4.1 Wind tunnel facility

The experiments are performed at the University of Adelaide in a closed-return wind tunnel. The wind tunnel can achieve 30 m/s with a low-level turbulence intensity of about 0.53 %. The test section is rectangular with a cross-section of $500 \times 300 \text{ mm}^2$ and 2000 mm in length. The sidewalls of the test section can be adjusted to maintain the flow at ZPG. The acceleration parameter $K = \frac{\nu}{U_\infty^2} \frac{dU_\infty}{dx}$ was lower than 3×10^{-8} along the test section from upstream to downstream. According to [Nickels *et al.* \(2005\)](#), to ensure the boundary layer developed in the test section is 2D, the test section's width should be at least six times larger than the boundary layer thickness δ . In our measurements, the largest δ is less than 60 mm, which is more than eight times smaller than the width of the test section. A 4 mm diameter threaded rod followed by a 100 mm strip of sandpaper with 36 grit No. are used at the inlet to trip the flow and develop a turbulent boundary layer from the upstream of the test section.

6.4.2 Surface roughness

The roughness details of this study are as follows: a total of four acrylic sheets of 6 mm thickness are computerized numerical control (CNC) machined with 3D sinewave surfaces function that has an amplitude of $k/2 = 1.2 \text{ mm}$. Different wavelengths in the streamwise and spanwise directions ranging from $6k$ to $16k$ are used in this study. Each plate measures around $500 \times 500 \text{ mm}^2$. These surfaces are fabricated by a Multicam M1212 Router machine, with a 0.6 mm stepover and 12 mm ball nose cutter. The absolute values of the profile heights for different rough surfaces are described as follows:

$$Y(x, z) = \frac{k}{2} \sin\left(\frac{2\pi x}{s_x}\right) \sin\left(\frac{2\pi z}{s_z}\right), \quad (6.1)$$

where $k = 2.4$ mm, and s_x and s_z are the streamwise and spanwise wavelengths, respectively.

The surfaces are defined by the first letter of the shape name: S for a sinewave, followed by $10k$, then the streamwise and spanwise spacing to height ratios between two consecutive roughness peaks, respectively. For example, $S24-08-16$ represents a 3D sinusoidal surface with a height of 2.4 mm, streamwise spacing between two consecutive roughness peaks of $8k$ and a spanwise spacing of $16k$. All different roughnesses and the strip of sandpaper are taped using double-sided tape on an aluminum sheet of dimensions 500×2400 mm². Statistical parameters used to characterize the different rough surfaces are tabulated in Table 6.1.

The roughness arithmetical mean height k_a is defined in ASME (2009) as the arithmetic mean of the absolute values of the height deviations from the mean plane of the surface, defined on the sampling area A_s as follows:

$$k_a = \frac{1}{A_s} \int \int_{A_s} |Y(x, z)| dx dz, \quad (6.2)$$

where $k_a = 0.47$ mm in all our 3D sinusoidal roughness.

The root- mean- square height within the definition area k_q corresponds to the standard deviation σ of the height distribution, (ASME 2009) defined on the sampling area as follows:

$$k_q = \sqrt{\frac{1}{A_s} \int \int_{A_s} Y(x, z)^2 dx dz}, \quad (6.3)$$

where $k_q = 0.59$ mm in all our 3D sinusoidal roughness.

The roughness skewness k_{sk} (normalized third-order moment) is the asymmetry of the height distribution, defined on the sampling area.(Aver'Yanova *et al.* 2017) This parameter is crucial, as it indicates the morphology of the surface texture.(Flack *et al.* 2016) Positive values correspond to the height distribution being skewed above the mean plane, while negative values are skewed below the mean plane. $k_{sk} = 0$ means peaks and valleys are symmetrical around the mean plane. However, this parameter does not give any information about the absolute height of the surface, contrary to k_a .

$$k_{sk} = \frac{1}{k_q^3 A_s} \int \int_{A_s} Y(x, z)^3 dx dz, \quad (6.4)$$

where all our 3D sinusoidal roughnesses are zero skewness.

The roughness kurtosis k_{ku} (normalized fourth-order moment) is the sharpness of the height distribution, defined in Aver'Yanova *et al.* (2017) on the sampling area as follows:

$$k_{ku} = \frac{1}{k_q^4 A_s} \int \int_{A_s} Y(x, z)^4 dx dz, \quad (6.5)$$

where $k_{ku} = 2.3$ in all our 3D sinusoidal roughness.

If $k_{ku} < 3$, the height distribution is skewed above the mean plane, while $k_{ku} > 3$ corresponds to the spike height distribution, and $k_{ku} = 3$ is the normal distribution.

The equation for the effective slope ES , in both streamwise and spanwise directions, which is the mean absolute gradient of the surface, as defined by Jouybari *et al.* (2021) for 3D rough surfaces is as follows:

$$ES_x = \frac{1}{A_s} \int \int_{A_s} \left| \frac{dY(x, z)}{dx} \right| dx dz, \quad (6.6)$$

TABLE 6.1: Different key surface roughness parameters.

No.	Surface	s_x/k	s_z/k	ES_x	ES_z
01	S24-06-06	$6k$	$6k$	0.20	0.20
02	S24-06-08		$8k$		0.15
03	S24-06-12		$12k$		0.10
04	S24-08-06	$8k$	$6k$	0.15	0.20
05	S24-08-08		$8k$		0.15
06	S24-08-12		$12k$		0.10
07	S24-08-16		$16k$		0.08
08	S24-12-06	$12k$	$6k$	0.10	0.20
09	S24-12-08		$8k$		0.15
10	S24-12-12		$12k$		0.10
11	S24-16-08	$16k$	$8k$	0.08	0.15

$$ES_z = \frac{1}{A_s} \int \int_{A_s} \left| \frac{dY(x, z)}{dz} \right| dx dz. \quad (6.7)$$

The effective slope parameter is also related to solidity λ_f , which is defined as the total projected frontal area of the roughness element A_f per unit wall parallel area A_p , by the relationship $ES_x = 2\lambda_f$. (Napoli *et al.* 2008) Several studies examined the effect of surface topology on C_f , and attempted to find correlations between ΔU^+ and λ_f (among others, Zheng & Anderson 2021; Placidi & Ganapathisubramani 2018). These studies have mainly classified the rough surfaces into two regimes: sparse regime ($\lambda_f < 0.15$, or $ES_x < 0.3$) in which ΔU^+ increases with solidity or effective slope, and dense regime ($\lambda_f > 0.15$, or $ES_x > 0.3$), in which ΔU^+ decreases.

6.4.3 Measurement rig

Figure 6.1 shows the test section of the wind tunnel with the experimental setup of the hot-wire probe and the 3D sinewave rough surface. The sensing material of the single hot-wire probe is a 2.5 μm diameter Wollaston wire (pure Platinum core) with an active length (l) of 500 μm to satisfy a length-to-diameter ratio of around 200, as recommended in (Ligrani & Bradshaw 1987; Hutchins *et al.* 2009). An overheat ratio of 1.8 is applied using an in-house constant temperature anemometer (CTA). A T-type thermocouple is used to record the mean temperature in the free-stream throughout the experiment. Dynamic calibration of the hot-wire is performed with a square wave test integrated into the CTA to determine the cutoff frequency of the hot-wire. A - 3 dB drop-off at around 20 kHz is recorded. Static calibration of the hot-wire is performed before and after each experiment. The sensor is calibrated *in situ*; the probe is traversed to the free-stream location along with the Pitot-static tube, and the wind tunnel speed is varied over the range of velocities ranging between zero and 22 m/s. If the pre- and post-calibrations do not collapse well, within a maximum of 2% error, the measurement is

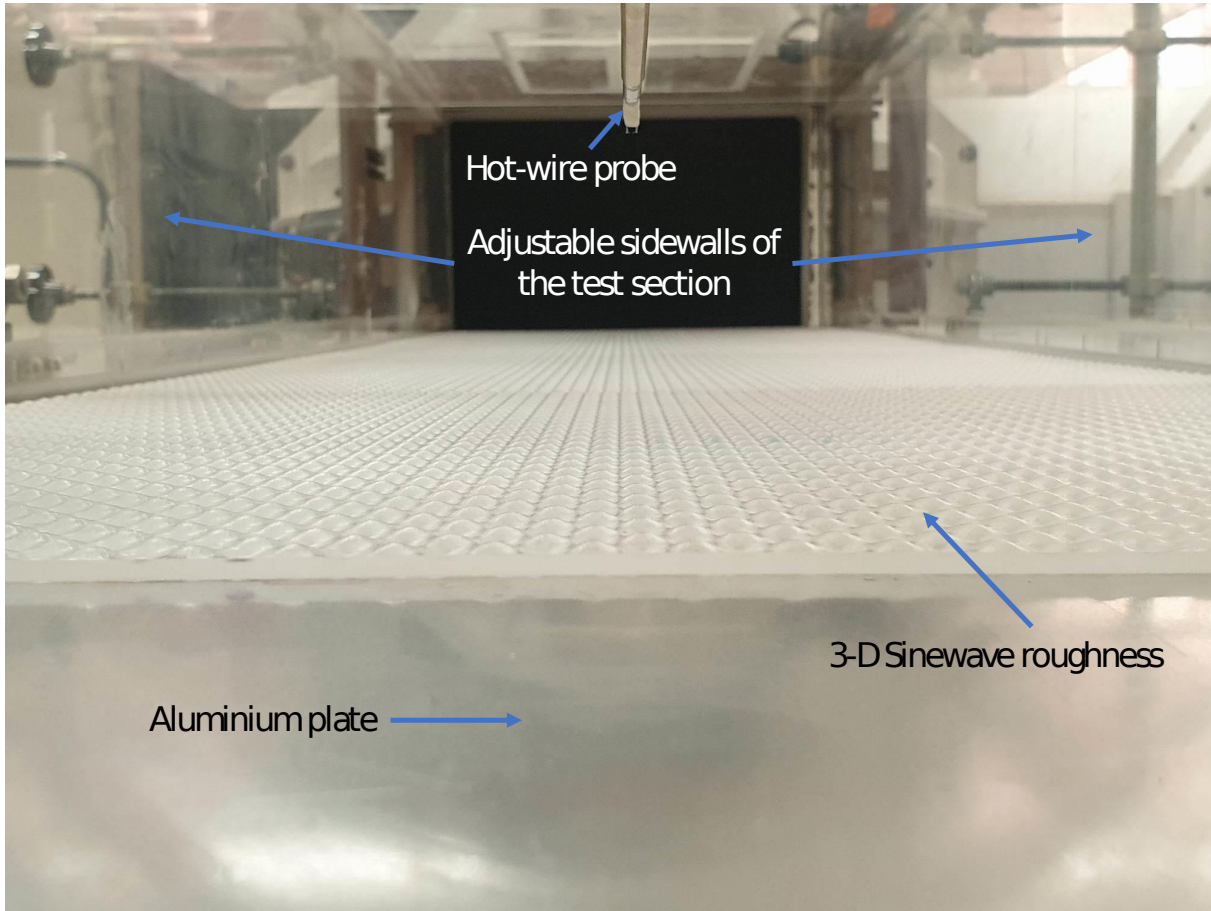


FIGURE 6.1: The experimental setup of the adjustable sidewalls test section of the wind tunnel with the hot-wire probe and the 3D sinewave rough surface.

repeated. A voltage vs speed curve is generated from such data. A polynomial of order six-degree function fits the data as it provides a better fit over the velocity range than the King's Law fitting function. (Perry & Chong 1982) Each measurement takes less than 2 h, which has a neglected effect on hot-wire voltage drifting. However, for more accurate results, a linear interpolation between pre- and post-calibrations with time accounts for the hot-wire voltage drifting throughout the experiment. (Talluru *et al.* 2014) An intermediate calibration curve is generated using a different proportional drift R , obtained using interpolation with time,

$$R_i = \frac{t_i - t_{pre}}{t_{post} - t_{pre}}, \quad (6.8)$$

where t_{pre} is the time at which the pre-calibration was conducted, t_{post} is the time at which the post-calibration was conducted and t_i is the time of each point within the experiment. Then, we used the value of R_i in the following equation to generate an intermediate calibration curve for the measurement:

$$E_{int} = R_i \times (E_{post} - E_{pre}) + E_{pre}, \quad (6.9)$$

where E_{pre} and E_{post} are calculated from the pre- and post-calibration curves using a polynomial of order six-degree fit at the free stream velocity corresponding to the i -th calibration point, in which the pre-calibration was conducted.

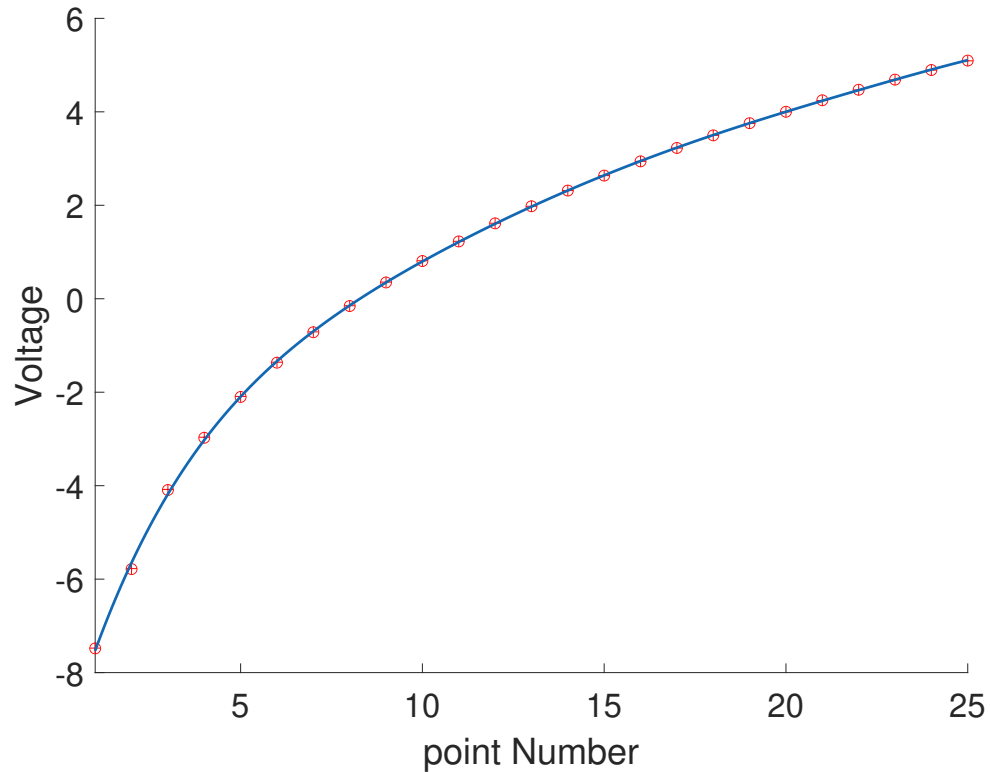


FIGURE 6.2: Pre- and post-calibration of hot-wire example with an intermediate calibration curve. Circle symbols are pre-calibration, while plus symbols are post-calibration points. The blue line represents the intermediate calibration curve.

Figure 6.2 shows one of the pre- and post-calibration measurements done during the experiments and the polynomial of order six-degree fitting equation. Clearly, the hot-wire drifting is neglected, as shown by the collapse of the pre- and post-calibration data.

One of the TBL measurement challenges is accurately determining the offset from the rough wall at the first measurement point. A high-magnification digital microscope is used to determine the offset. The microscope is mounted on a 20 mm thickness flat plate and placed on top of the rough surface. The probe is moved down to the location where the probe is in the focus of the microscope. This distance is then adjusted to be 23 mm from the bottom of the microscope plate, which equals the distance from the peaks of the sinusoidal rough surface to the probe location. Next, after removing the microscope, the probe is moved down by 23 mm to be exactly at the same height as the peaks. The wire is now located on top of a valley between two consecutive roughness peaks. Measurements are taken at the midpoint of two consecutive roughness peaks (the lowest possible valley) at one location where $x \approx 1.5$ m downstream is measured after the tripping sandpaper. This streamwise location is equivalent to about 35δ in the smooth wall and from 26δ to 35δ in the rough wall. A Mitutoyo height gauge takes a total of 48 logarithmically spaced measurement points along with the wall-normal position with a 1 μm resolution linear glass encoder attached to it. Measurements are taken with a sampling rate of 51.2 kHz for each wall-normal location for 120 s. A schematic of the 3D surface roughness and the measurement location is shown in Figure 6.3.

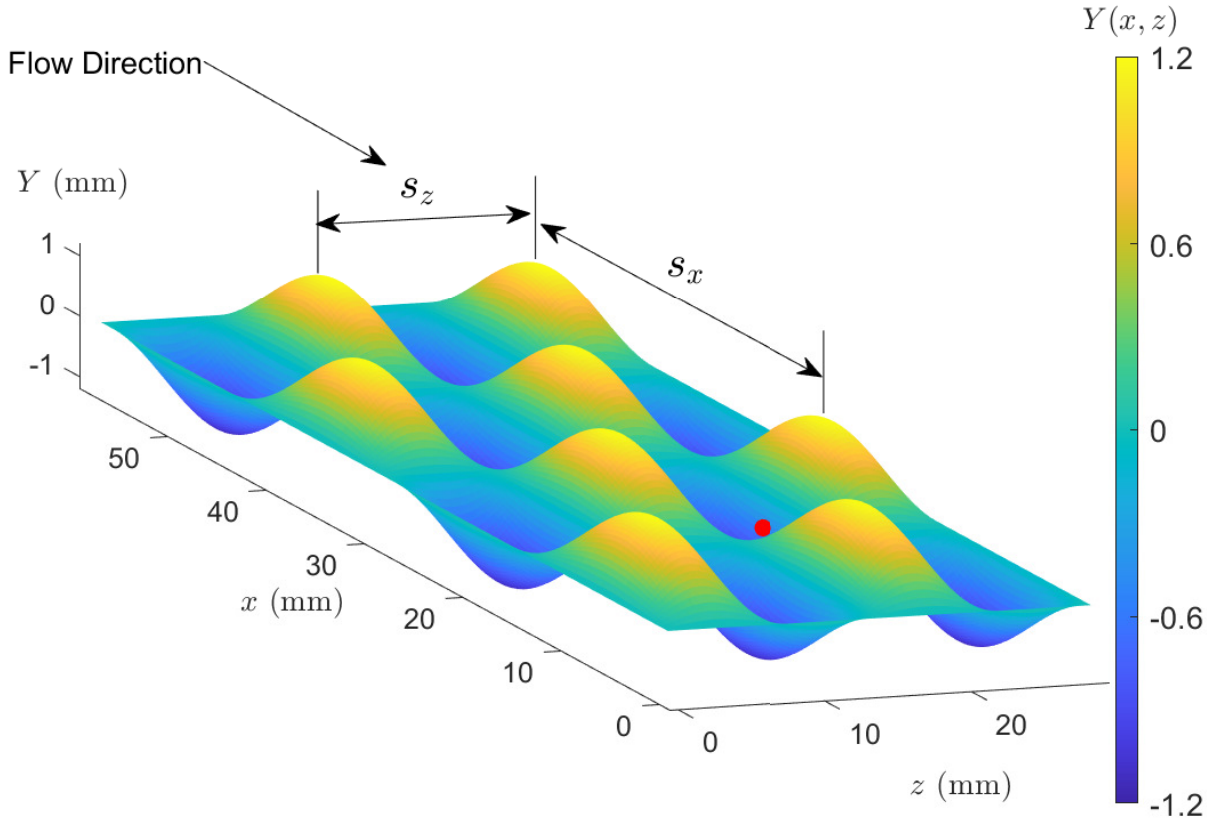


FIGURE 6.3: A schematic of a 3D sinewave roughness. *S24-12-06*, represented in this figure, is a 3D sinusoidal surface with a roughness height of 2.4 mm and a streamwise spacing between two consecutive roughness peaks of $12k$ and a spanwise spacing of $6k$. The red mark shows the hot-wire measurement location.

6.4.4 Experiments

Four sets of experiments and a smooth wall set used as a reference are conducted. Each set has a fixed streamwise spacing to height ratio s_x/k and a variable spanwise spacing to height ratio s_z/k . In the first set we fix $s_x/k = 6$, and vary s_z/k from 6 to 12. In the second set, $s_x/k = 8$, and s_z/k varies from 6 to 16. For the third set, $s_x/k = 12$, and s_z/k varies from 6 to 12. Finally, in the last set, $s_x/k = 16$ and $s_z/k = 8$. The free-stream velocities U_∞ for each case are varied from 7 to 20 m/s. For the anisotropic surfaces, the surfaces shown in Figure 6.3 are rotated 90° around the Y axis to change the surface from a spanwise elongated to a streamwise elongated surface. Hence, we investigated the effect of varying the streamwise and spanwise spacing to height ratios on the roughness function and the drag coefficient. The details of the sets of experiments are reported in Table 6.2.

6.5 FRICTION VELOCITY

The most challenging part in TBL measurements is the determination of the friction velocity U_τ . The most widely indirect method used for smooth TBL flows is the Clauser chart method. (Clauser 1956) This method is based on fitting the logarithmic region of the measured velocity profile data to the law of the wall, as shown in the following equation:

$$U^+ = \frac{1}{\kappa} \ln y^+ + B, \quad (6.10)$$

TABLE 6.2: Details of the experimental datasets. U_∞ , U_τ , and δ units are in m/s, m/s, and mm, respectively.

Surface	Sym.	U_∞	U_τ	δ	Re_τ	l^+	H	C_f	δ/k	s_z/δ	k_s^+	ΔU^+
Smooth	•	07	0.30	43	850	10	1.39	0.0035	NA	NA	NA	NA
	•	10	0.40	42	1120	13	1.37	0.0031	NA	NA	NA	NA
	•	15	0.57	46	1740	19	1.35	0.0028	NA	NA	NA	NA
	•	20	0.72	45	2190	24	1.33	0.0026	NA	NA	NA	NA
S24-16-08	◀	07	0.30	47	940	10	1.46	0.0036	20	0.41	06	1.0
	◀	10	0.43	47	1360	15	1.46	0.0036	20	0.41	10	2.2
	◀	15	0.64	44	1860	21	1.46	0.0036	18	0.44	13	2.9
	◀	20	0.85	46	2580	28	1.46	0.0036	19	0.42	19	3.9
S24-12-12	×	07	0.32	46	990	10	1.46	0.0040	19	0.63	11	2.6
	×	10	0.45	44	1320	13	1.47	0.0039	18	0.67	14	3.1
	×	15	0.68	42	1920	22	1.47	0.0039	18	0.67	20	4.0
	×	20	0.93	42	2610	31	1.47	0.0039	18	0.67	28	4.6
S24-12-08	▶	07	0.32	48	1020	11	1.47	0.0041	20	0.40	13	2.9
	▶	10	0.45	48	1450	15	1.47	0.0040	20	0.40	17	3.7
	▶	15	0.67	48	2140	22	1.47	0.0040	20	0.40	26	4.8
	▶	20	0.88	49	2890	29	1.47	0.0040	21	0.38	35	5.4
S24-12-06	◊	07	0.33	46	1000	11	1.48	0.0043	19	0.32	14	3.0
	◊	10	0.45	46	1400	15	1.48	0.0043	19	0.32	18	3.8
	◊	15	0.68	45	2030	23	1.48	0.0043	19	0.32	27	4.9
	◊	20	0.89	46	2750	30	1.48	0.0043	19	0.32	39	5.7
S24-08-16	★	07	0.33	54	1180	11	1.48	0.0043	22	0.72	18	3.8
	★	10	0.47	52	1620	16	1.48	0.0043	22	0.72	25	4.4
	★	15	0.69	56	2570	23	1.48	0.0043	23	0.70	41	5.8
	★	20	0.92	58	3560	31	1.48	0.0043	24	0.67	64	6.7
S24-08-12	●	07	0.33	47	1050	11	1.49	0.0045	20	0.60	19	3.9
	●	10	0.48	47	1520	16	1.49	0.0045	20	0.60	28	4.9
	●	15	0.73	44	2150	24	1.49	0.0045	18	0.67	44	5.9
	●	20	0.94	46	2880	31	1.49	0.0045	19	0.63	59	6.8
S24-08-08	+	07	0.35	44	1040	12	1.51	0.0047	19	0.42	23	4.1
	+	10	0.49	43	1410	16	1.51	0.0047	18	0.44	32	5.0
	+	15	0.75	44	2180	25	1.51	0.0047	18	0.44	54	6.4
	+	20	0.96	44	2810	32	1.51	0.0047	18	0.44	71	6.8
S24-08-06	▼	07	0.35	46	1070	12	1.52	0.0049	19	0.32	27	4.5
	▼	10	0.50	45	1470	17	1.52	0.0049	19	0.32	38	5.5
	▼	15	0.74	44	2180	25	1.52	0.0049	18	0.33	60	6.6
	▼	20	1.00	43	2870	33	1.52	0.0049	18	0.33	82	7.5
S24-06-12	▲	07	0.36	54	1280	12	1.52	0.0052	22	0.55	44	5.9
	▲	10	0.51	56	1900	17	1.52	0.0052	23	0.52	63	6.9
	▲	15	0.77	57	2920	26	1.52	0.0052	24	0.50	109	8.2
	▲	20	1.00	58	3890	33	1.52	0.0052	24	0.50	159	9.0
S24-06-08	■	07	0.37	48	1180	12	1.56	0.0054	20	0.40	46	5.9
	■	10	0.52	48	1680	17	1.56	0.0054	20	0.40	65	6.9
	■	16	0.81	47	2570	27	1.56	0.0054	20	0.40	112	8.2
	■	20	1.04	48	3300	35	1.56	0.0054	20	0.40	155	9.0
S24-06-06	*	07	0.38	45	1160	13	1.60	0.0057	19	0.32	55	5.9
	*	10	0.55	46	1670	18	1.60	0.0057	19	0.32	81	7.3
	*	15	0.80	47	2500	27	1.60	0.0057	20	0.30	127	8.4
	*	20	1.05	49	3410	35	1.60	0.0057	20	0.30	186	9.3

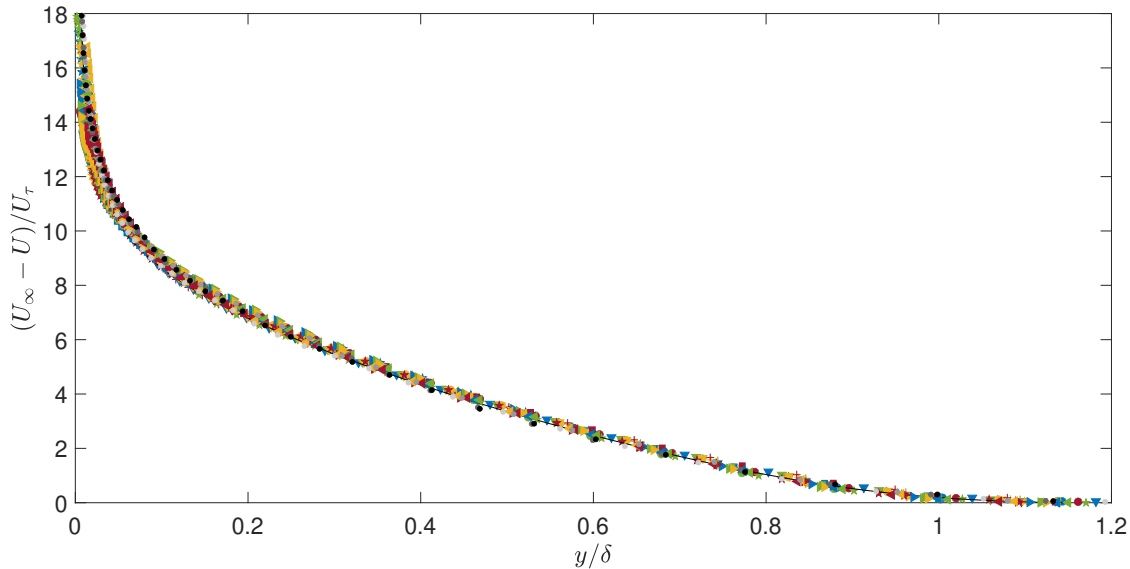


FIGURE 6.4: Streamwise mean velocity deficit profiles over different rough wall surfaces at four different Reynolds numbers for each surface. The symbols of our measurements are detailed in Table 6.2. Solid black line: DNS smooth TBL data from Chan *et al.* (2021) at $Re_\tau \approx 2000$.

where κ is the von Karman constant, and B is an additive constant. From Eq. (6.10), this method has some uncertainties, such as the values of κ , B , and the lower and upper limits of the overlap region. For rough surfaces, Perry & Joubert (1963) introduced a modified method to consider the roughness function. Unfortunately, this method requires two more variables, the origin offset (ϵ) and the roughness function ΔU^+ , adding further uncertainties since the law of the wall becomes

$$U^+ = \frac{1}{\kappa} \ln \frac{(y + \epsilon)U_\tau}{\nu} + B - \Delta U^+. \quad (6.11)$$

Marusic *et al.* (2013) suggest that the start and the end of the log region that best fit the velocity profiles are $y^+ > 3\sqrt{Re_\tau}$ and $y/\delta = 0.15$. These boundaries are within the log region for all our rough surfaces at different values of Re_τ . Hence, it is adopted in the present study.

Utilizing the outer layer similarity between the smooth and rough flow and the collapse of the velocity profiles in defect form, Djenidi *et al.* (2019) proposed a more straightforward method for estimating U_τ . This method uses fewer empirical constants, reducing the uncertainties of the estimated U_τ , which provides a practical advantage over the modified Clauser chart method.

In the present work, we used the velocity defect chart (Djenidi *et al.* 2019) method to calculate the friction velocity. We also used the modified Clauser chart (Perry & Li 1990). By comparing both the modified Clauser chart (Perry & Li 1990) and the velocity defect chart (Djenidi *et al.* 2019) methods to calculate the friction velocity, we found that the U_τ obtained from the modified Clauser chart method matches that obtained from the velocity defect chart within an error less than 3 % for all Reynolds numbers considered. We thus show the results in tables and figures of the velocity defect method only. This method is well justified by the collapse of the streamwise mean velocity profiles plotted in deficit form for various 3D sinewave roughnesses at four different Reynolds numbers for each surface, as seen in Figure 6.4.

We used the universal profile equation in Djenidi *et al.* (2019) as our reference.

$$f(x) = \frac{p_1x^5 + p_2x^4 + p_3x^3 + p_4x^2 + p_5x + p_6}{x^5 + q_1x^4 + q_2x^3 + q_3x^2 + q_4x + q_5}, \quad (6.12)$$

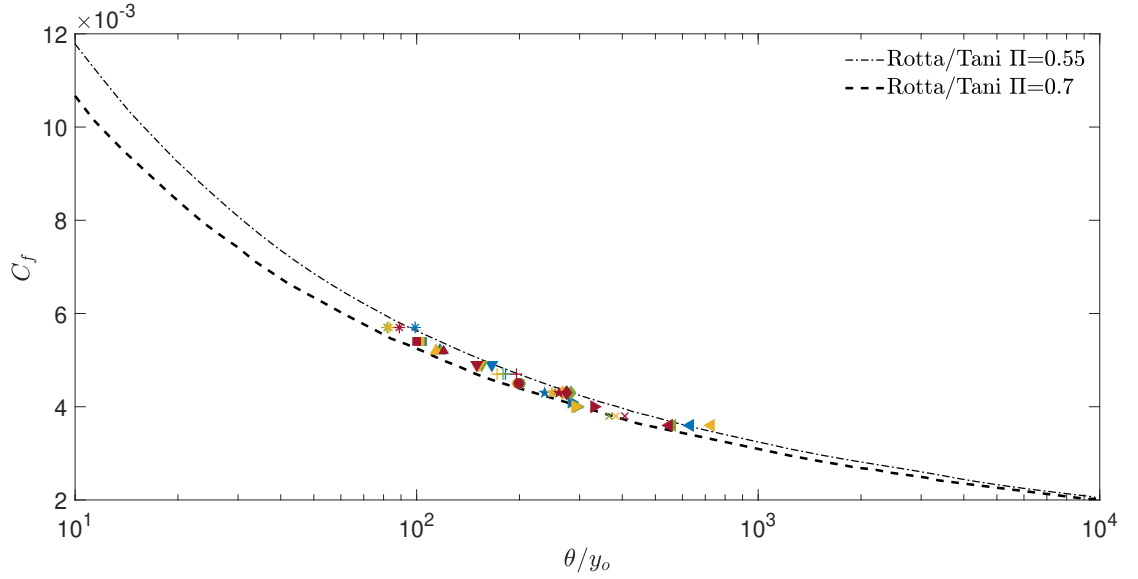


FIGURE 6.5: Variation of C_f as a function of θ/y_o . The dashed and dashed-dotted curves represent the standard two-parameter family results with wake strengths of $\Pi = 0.7$ and $\Pi = 0.55$, respectively.

where the coefficients are $p_1 = 110.50$, $p_2 = -230.50$, $p_3 = 114.50$, $p_4 = 7.24$, $p_5 = -0.00638$, $p_6 = -0.0000460$; $q_1 = -10.07$, $q_2 = 15.56$, $q_3 = 0.4466$, $q_4 = -0.000820$, and $q_5 = -0.000001789$.

We fit the different velocity profiles from $y/\delta=0.1$ to $y/\delta=1$ and use the least squares error technique to calculate the friction velocity that best fits the universal profile.

The validity of the two methods used to calculate U_τ is done by plotting the C_f values with the normalized momentum thickness, θ/y_o , where y_o is the roughness length. The roughness length, y_o , is calculated via a least-square-fit procedure between $y^+ > 3\sqrt{Re_\tau}$ and $y/\delta = 0.15$. This is another way of expressing the TBL profile over rough surfaces in a fully rough regime,

$$U^+ = \frac{1}{\kappa} \ln \frac{(y - \epsilon)}{y_o}. \quad (6.13)$$

Figure 6.5 shows the results using the defect method for calculating C_f and the corresponding θ/y_o values. It can be seen that our data using the defect method are consistent with previous results in the literature. This type of plot was first proposed in [Castro \(2007\)](#) and allows us to validate whether the current C_f calculated by the defect method agrees with previous findings. All our results at different Re_τ values for different rough surfaces have been found to scatter around the two curves (for different values of the wake parameter Π) shown in Figure 6.5.

6.6 RESULTS

6.6.1 2D roughness vs 3D roughness

[Abdelaziz et al. \(2022b\)](#) studied the outer layer similarity for different 2D sinewave surface roughnesses with two different heights and three different streamwise spacing to height ratios. The 2D sinewave surface roughness with $k = 2.4$ mm has a ratio of the boundary layer thickness to the roughness height, $\delta/k \approx 25$. The first degree of complexity that can be added to this family of roughness is transforming it from 2D to 3D sinewave roughness, with the same roughness height and equal spacing in the streamwise and spanwise directions.

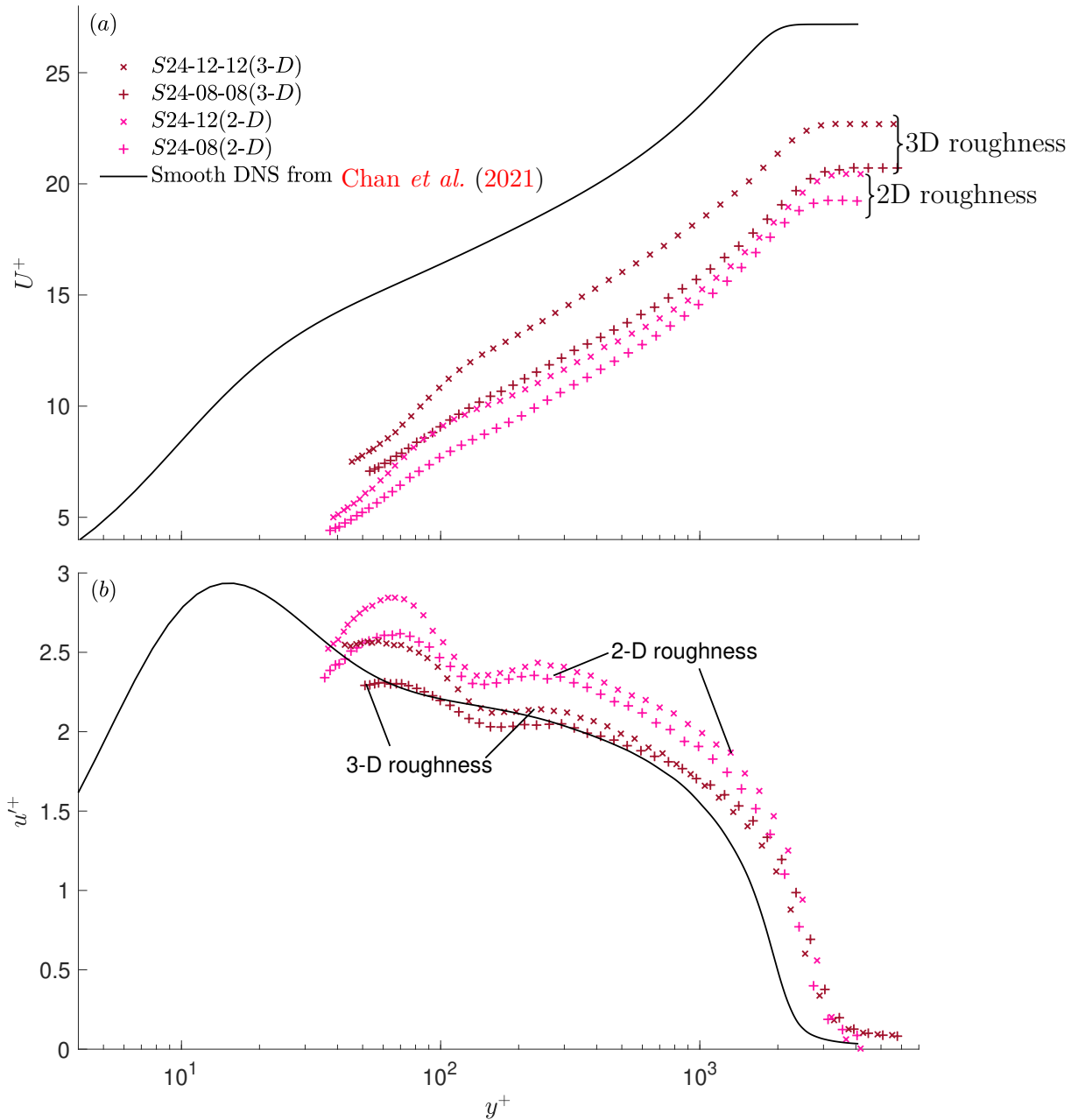


FIGURE 6.6: (a) Mean streamwise velocity profiles over 2D and 3D sinewave roughness. (b) Mean streamwise turbulence intensity profiles over 2D and 3D sinewave roughness. The symbols of the 3D roughness are indicated in Table 6.2, and the same symbols are used for the 2D sinewave roughness with a magenta color. Solid black line: DNS smooth TBL data from Chan *et al.* (2021) at $Re_\tau \approx 2000$.

Figure 6.6 shows profiles of the mean U and rms u' of the streamwise velocity over 2D and 3D sinewave roughness with the same amplitude $k = 2.4$ mm, where u denotes the streamwise velocity fluctuation and the superscript, ($'$), represents the rms. The 2D sinewave surfaces have streamwise wavelengths of $8k$ and $12k$ (see Abdelaziz *et al.* 2022b) while the 3D sinewave surfaces have streamwise and spanwise wavelengths of $8k$ and $12k$. The symbols of the 3D roughness are indicated in Table 6.2, and the same symbols are used for the 2D sinewave roughness with a magenta color. The 2D roughness has higher drag coefficients C_f and roughness functions ΔU^+ than the 3D roughness. This increase is caused by the higher blockage area imposed by 2D roughness, which forces the fluid to flow over the roughness elements. For the 3D sinewave roughness, the fluid can flow around and above the roughness elements. Also, the 2D sinewave roughness produces higher turbulence intensities than the 3D sinewave roughness. These findings are consistent with the previous findings of Hamed *et al.* (2015). They investigate experimentally channel flow over 2D and 3D sinusoidal wavy walls at low and very high Reynolds numbers. They found that the 3D sinewave surface has lower turbulent stresses and average drag than the 2D wavy surface due to reduction in the dynamics of turbulent structures in the spanwise direction.

6.6.2 Streamwise spacing vs spanwise spacing in 3D sinusoidal roughness

Section 6.6.1 motivates us to investigate further the effect of streamwise and spanwise spacing on turbulence statistics and drag coefficients. By consulting Table 6.1, the systematic variation of s_x/k and s_z/k enables us to isolate these parameters and keep all other roughness parameters constant. Hence, two sets of experiments are conducted. The first set is turbulent boundary layers flow over surfaces with constant s_x/k while changing s_z/k from 6 to 16. The second set is turbulent boundary layers flow over surfaces with constant s_z/k while changing s_x/k from 6 to 16. The surfaces are rotated by 90° in the (x, z) plane so that the s_x/k and s_z/k are reversed, as shown in Table 6.1.

Figure 6.7 shows the streamwise mean velocity profiles normalized by U_τ for different rough surfaces. The inner length scale ν/U_τ normalizes the wall-normal position y . Figure 6.7(a) shows the data for the surfaces ($S24-06-06$, $S24-06-08$, and $S24-06-12$). These three surfaces have the same s_x/k of 6, while s_z/k varies from 6 to 12. Figure 6.7(c) shows the data for the surfaces ($S24-08-06$, $S24-08-08$, $S24-08-12$, and $S24-08-16$). Those four surfaces have the same s_x/k of 8, while s_z/k varies from 6 to 16. Figure 6.7(e) shows the data for the surfaces ($S24-12-06$, $S24-12-08$, and $S24-12-12$). These three surfaces have the same s_x/k of 12, while s_z/k varies from 6 to 12. Figures 6.7(b), 6.7(d) and 6.7(f) show the data for the same 3D sinewave rough surfaces after rotating them by 90° in the (x, z) plane. The mean streamwise velocity profiles of smooth wall data at different free-stream velocities are shown as a reference in Figure 6.7(b). The symbols of the measurements are detailed in Table 6.2. The solid black line is DNS smooth TBL data from Chan *et al.* (2021) at $Re_\tau \approx 2000$.

For smooth wall mean streamwise velocity profiles, increasing Re_τ reduces the drag coefficient C_f and elongates the mean streamwise velocity profile more and shifts the constant U^+ part of the velocity profile upward as shown in Figure 6.7(b). To study the effect of Re_τ , the streamwise mean velocity profiles at various values of U_∞ are plotted for $S24-06-06$ surface in Figures 6.7(b). All other profiles have the same trend, so we removed the profiles for the simplicity of the figures. Also, to investigate the effect of streamwise and spanwise spacing to height ratios, the streamwise mean velocity profiles at $U_\infty = 20$ m/s over the different rough surfaces in the group are plotted in Figures 6.7(a)-6.7(f).

By consulting Figure 6.7(b) and Table 6.2, the results show that increasing Re_τ by increasing U_∞ for the same surface roughness increases ΔU^+ , while keeping the C_f constant.

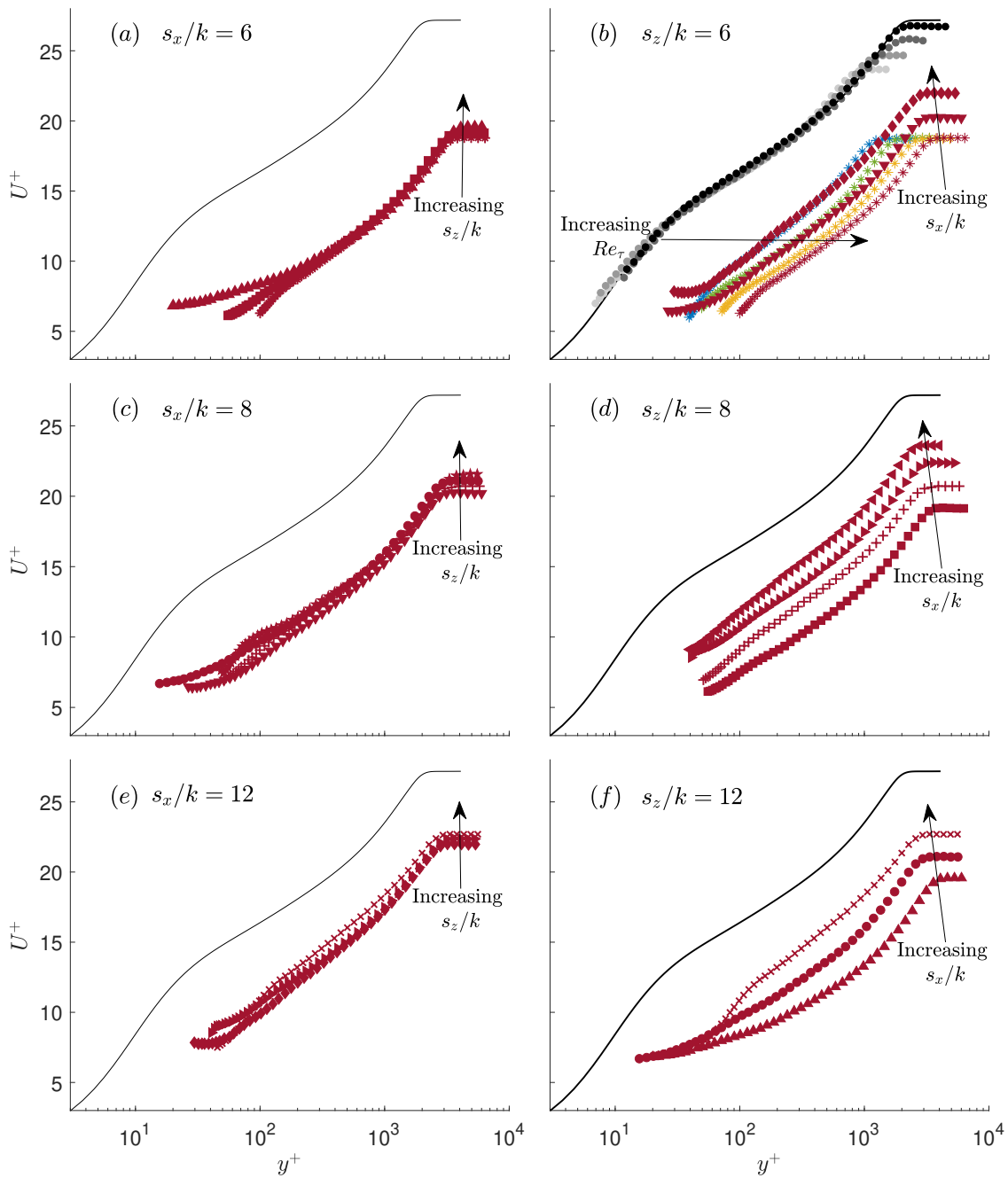


FIGURE 6.7: Mean streamwise velocity profiles over different rough surfaces at a free-stream velocity of $U_\infty = 20$ m/s. The symbols of our measurements are detailed in Table 6.2. Solid black line: DNS smooth TBL data from Chan *et al.* (2021) at $Re_\tau \approx 2000$. The profiles over rough surfaces with constant $s_x/k = 6, 8$, and 12 are shown in (a), (c) and (e), respectively. The profiles over rough surfaces with constant $s_z/k = 6, 8$, and 12 are shown in (b), (d) and (f), respectively. The profiles over smooth and rough surfaces at four different free-stream velocities U_∞ are shown for one surface in panel (b), the same symbol with different colors, as the other profiles have the same trend.

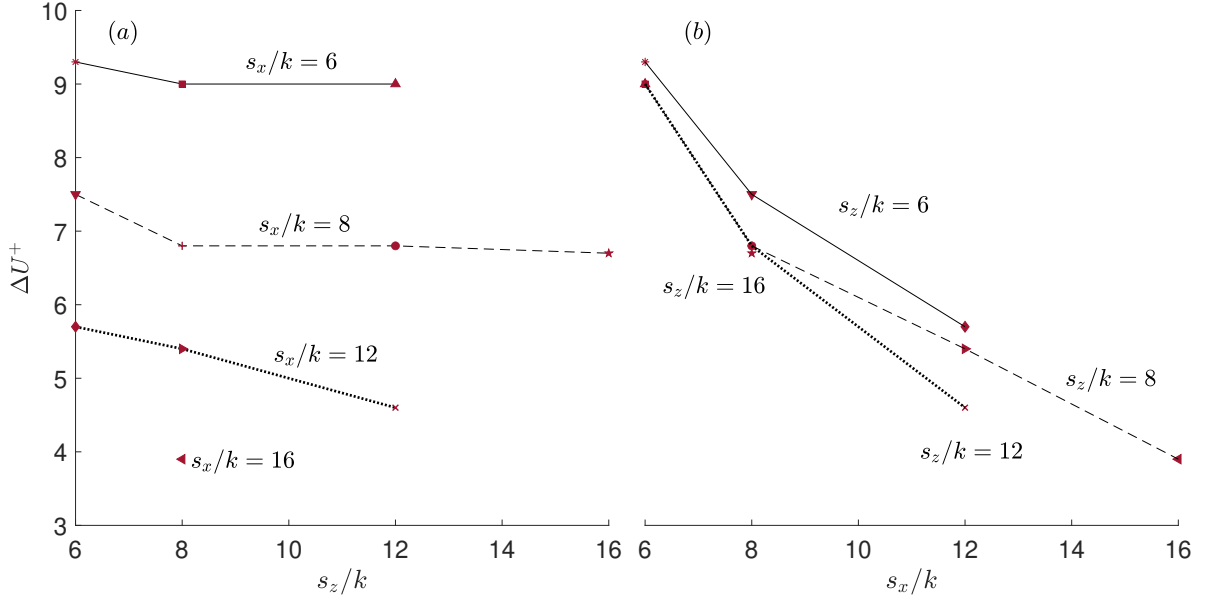


FIGURE 6.8: (a) ΔU^+ as a function of the spanwise spacing to height ratio s_z/k for different values of s_x/k . (b) ΔU^+ as a function of the streamwise spacing to height ratio s_x/k for different values of s_z/k . The symbols of each roughness are indicated in Table 6.2.

This is manifested in the shifting of the mean streamwise velocity profiles to the right only with increasing U_∞ , as shown in Figure 6.7(b). The constant C_f values with increasing Re_τ values indicates that the flow is at a fully rough regime and the viscous effects are negligible. The drag is mainly composed of the form drag due to the roughness elements.

For fixed s_x/k , increasing s_z/k has a little effect on ΔU^+ . It slightly reduces C_f and ΔU^+ , as shown in Figures 6.7(a), 6.7(c), and 6.7(e). On the other hand, fixing s_z/k and increasing s_x/k has a significant effect, reducing both C_f and ΔU^+ dramatically, as shown in Figures 6.7(b), 6.7(d), and 6.7(f).

It is obvious from Figure 6.7 that s_x/k represented in ES_x has a major effect on ΔU^+ and C_f . However, the effect of s_z/k represented in ES_z on ΔU^+ and C_f cannot be neglected. It should be considered for any accurate prediction of the equivalent sand grain roughness k_s based on the roughness topography. The minor effect s_z/k on ΔU^+ shown here in our cases is due to the fully rough regime flow. ES_z has a larger effect on ΔU^+ in a transitionally rough regime due to the larger contribution of the viscous component on the total wall drag. In other words, at larger values of ES_x , ES_z can be totally neglected as shown from the solid line slope in Figure 6.8(a), ΔU^+ is almost constant. However, when ES_x decreases, the ES_z effect starts to be more pronounced, as shown in Figure 6.8(a) from the dotted line slope. More experiments with wider ranges of s_x/k and s_z/k are needed for a deep understanding of their effects on ΔU^+ and C_f .

To better understand the effect of the effective slopes in both the streamwise and the spanwise directions on C_f and H , the relationship between C_f and H as a function of s_x/k and s_z/k are plotted in Figure 6.9(a). The gentle slopes for C_f of the linear approximation in Figure 6.9(a) indicates that for a fixed value of ES_x , ES_z is a roughness parameter that should be considered in describing a roughness topology and cannot be neglected. However, the steep slope in Figure 6.9 (b) emphasizes the significant role ES_x plays in determining C_f . Also, the steeper slope of the dotted black line in Figure 6.9(a) compared with the solid black one is another indication of the effect of s_z/k on C_f and H at smaller values of s_x/k . The shape factor H behavior has a very similar trend to C_f , except for s_x/k and $s_z/k = 6$, the slopes of H have

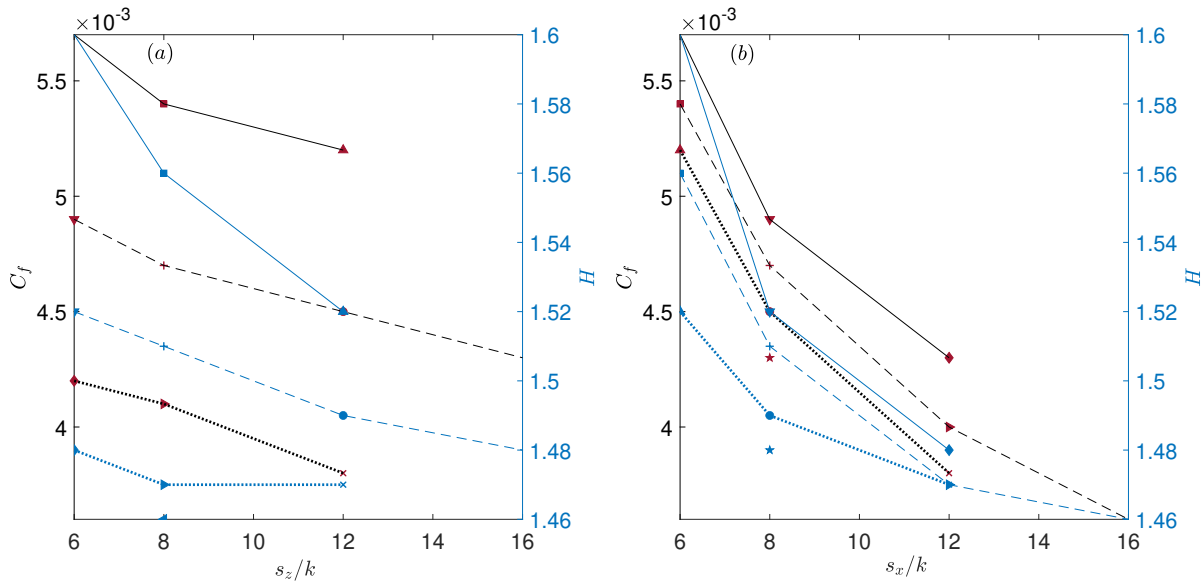


FIGURE 6.9: (a) C_f and H as a function of the spanwise spacing to height ratio s_z/k for different values of s_x/k . (b) C_f and H as a function of the streamwise spacing to height ratio s_x/k for different values of s_z/k . The symbols of each roughness are indicated in Table 6.2. Black lines represent the linear approximation of C_f , while blue lines represent the linear approximation of H . The solid lines are for s_x/k , and $s_z/k = 6$ in (a) and (b), respectively. The dashed lines are for s_x/k , and $s_z/k = 8$ in (a) and (b), respectively. The dotted lines are for s_x/k , and $s_z/k = 12$ in (a) and (b), respectively.

a little steeper slope than C_f . This emphasizes the strong relationship between C_f and H in smooth and rough turbulent boundary layer flows.

Figure 6.10 shows the profiles of U^+ vs y/k . Recall that all the roughness elements have the same height k . For each rough surface, the profiles with different U_∞ exhibit a collapse, as shown in Figure 6.10, (same symbol and different colors), thereby indicating the Reynolds number independence on these plots and shows that a fully rough regime is reached as the profiles of different Reynolds number values of the same surface collapse very well. Increasing s_x/k shifts the profiles up, as explained previously in Figure 6.7.

Figures 6.10(a), 6.10(c), and 6.10(e) show the streamwise mean velocity profiles over the same rough surfaces used in Figures 6.7(a), 6.7(c), and 6.7(e), respectively, for constant s_x/k . Figures 6.10(b), 6.10(d), and 6.10(f) show the streamwise mean velocity profiles over the same rough surfaces used in Figures 6.7(b), 6.7(d), and 6.7(f), respectively, for constant s_z/k . Four different free-stream velocities U_∞ are plotted (same symbols with different colors from blue to red) for all the surfaces of each group. The left column of Figure 6.10 shows that s_z/k has very little effect on the roughness function as all the profiles with constant s_x/k values are collapsing in the log region. However, the right column of Figure 6.10 shows that s_x/k has an effect on mean velocity profiles as all the profiles with constant s_z/k values exhibiting an upward shift in the log and outer regions with increasing s_x/k .

Figure 6.11 shows the mean streamwise turbulence intensity profiles normalized by U_τ as a function of y/δ over the same rough surfaces mentioned in Figure 6.7 for four different Reynolds numbers. Figures 6.11(a), 6.11(c), and 6.11(e) are for different rough surfaces with constant $s_x/k = 6, 8,$ and 12 , respectively, while s_z/k is varied from 6 to 12 in (a) and (e), and from 6 to 16 in (c). Figures 6.11(b), 6.11(d), and 6.11(f) are for different rough surfaces with constant $s_z/k = 6, 8,$ and 12 , respectively, while s_x/k is varied from 6 to 12 in panels (b) and (f), and from 6 to 16 in panel (d). Profiles for four values of U_∞ are shown (same symbol with different

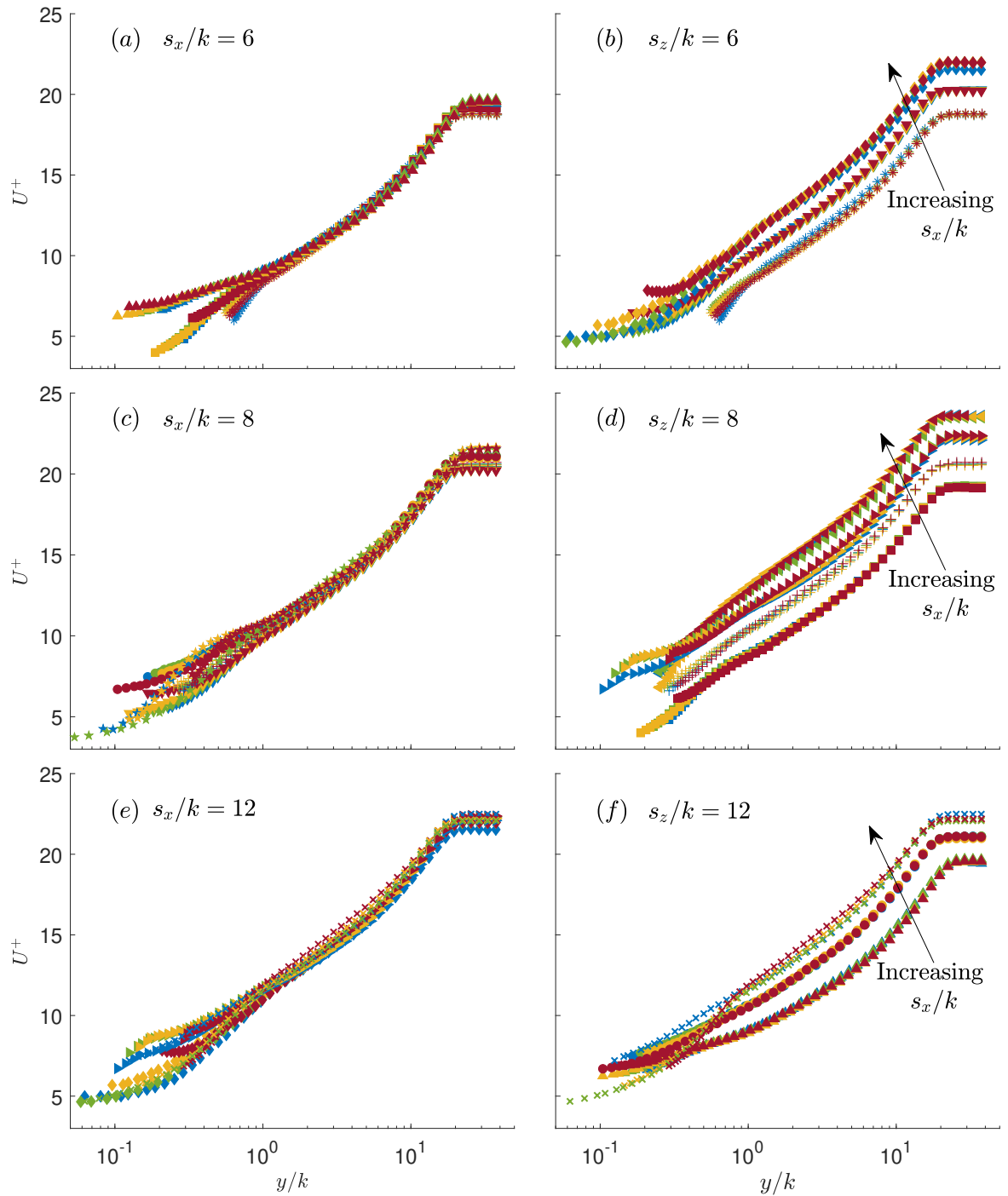


FIGURE 6.10: Mean streamwise velocity profiles over different rough surfaces at different Reynolds numbers for each surface. The wall-normal location y is normalized by k . The symbols of the different rough surfaces are detailed in Table 6.2. The profiles over rough surfaces with constant $s_x/k = 6, 8,$ and 12 are shown in (a), (c), and (e), respectively. The profiles over rough surfaces with constant $s_z/k = 6, 8$ and 12 are shown in (b), (d), and (f), respectively.

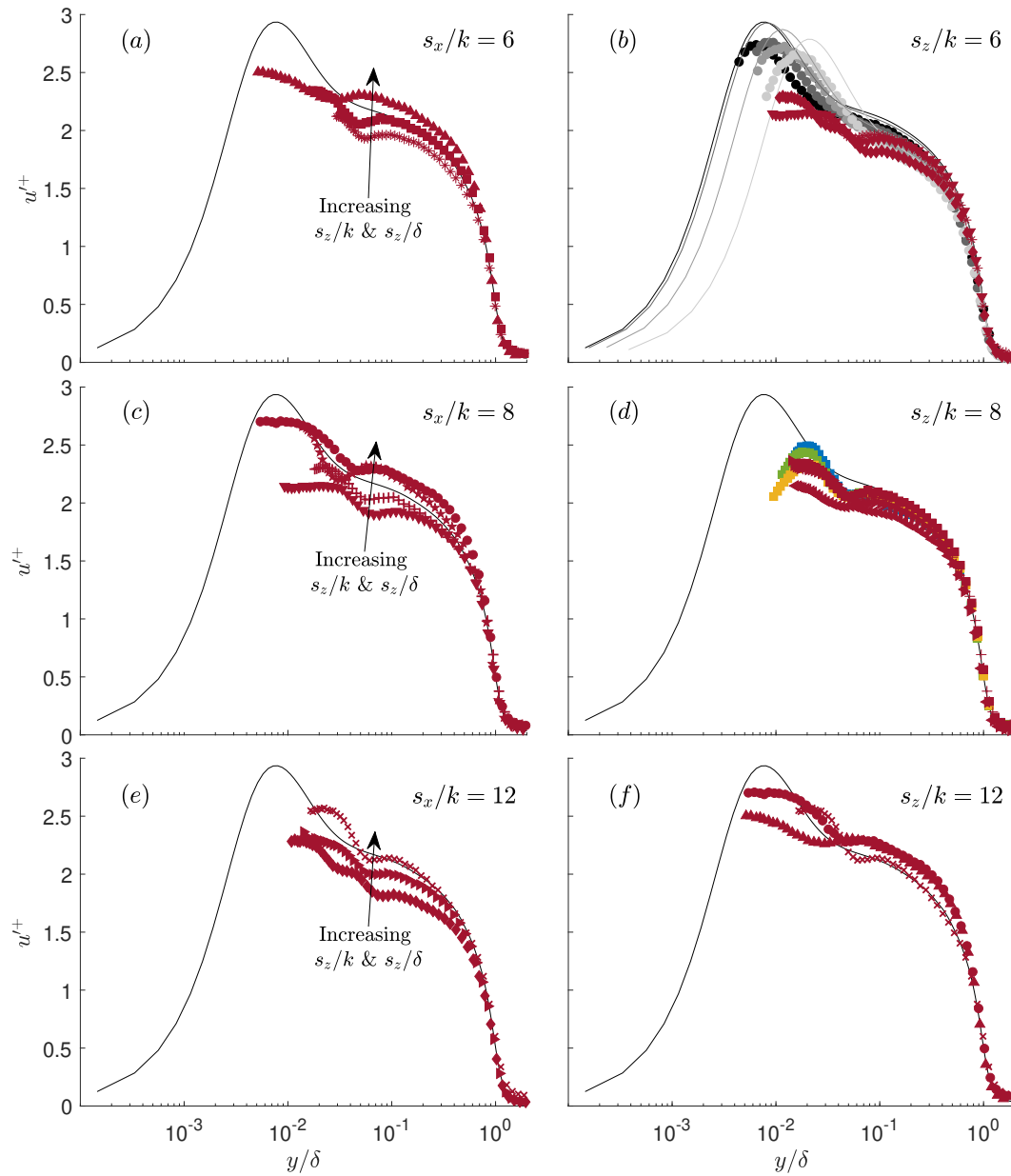


FIGURE 6.11: Mean streamwise turbulence intensity profiles over different rough surfaces at a free-stream velocity of $U_\infty = 20$ m/s. The symbols of our measurements are detailed in Table 6.2. The profiles over the smooth wall at different Reynolds numbers and the DNS smooth TBL data from Sillero *et al.* (2014) at approximately matched Reynolds numbers are also shown in (b). The profiles over the rough surface S24-06-08 at four different free-stream velocities U_∞ , the same symbol with different colors, are shown in (d) only, as the other profiles have the same trend. The profiles over rough surfaces with constant $s_x/k = 6, 8,$ and 12 are shown in (a), (c), and (e), respectively. The profiles over rough surfaces with constant $s_z/k = 6, 8,$ and 12 are shown in (b), (d), and (f), respectively.

colors) for the surface S24-06-08 in Figure 6.11(d). u^+ profiles over different rough surfaces are plotted at $U_\infty = 20$ m/s with different symbol in red. The mean streamwise turbulence intensity profiles of smooth wall data at different free-stream velocities are shown in Figure 6.11(b) along with DNS smooth TBL data from Sillero *et al.* (2014) at the closest Reynolds number value, as a reference.

Contrary to the mean velocity profiles, the s_z/k variation of roughness has a larger effect on u^+ than s_x/k . This is manifested in the upward shift of the profiles with increasing s_z/k [red symbols in Figure 6.11(a), 6.11(c), and 6.11(e)]. However, in Figures 6.11(b), 6.11(d), and 6.11(f) the shift is less pronounced, and s_x/k has little effect. By consulting Table 6.2 and Figure 6.11, we notice that when the ratio $s_z/\delta < 0.5$, the profiles of u^+ in the log region and the outer region is lower than on the smooth wall as shown in Figures 6.11(b) and 6.11(d). However, when s_z becomes larger than 0.5δ , the profiles of u^+ in the log region and the outer region are higher than on the smooth wall, as shown in Figure 6.11(f). This shift is due to the large perturbations to the structure of the mean velocity field due to the presence of large secondary flows that increase with the roughness's spanwise spacing. These findings are consistent with the literature from Vanderwel & Ganapathisubramani (2015). They determined the critical value of s_z/δ of about 0.5 for developing the secondary vortex structures. The secondary flows are made up of huge counter-rotating re-circulation zones and are associated with low- and high-momentum momentum pathways.

The small differences appear in the right column of Figure 6.11, when they have almost the same s_z/δ values because of the ratio s_z/s_x . The higher the value of s_z/s_x , the higher the magnitude of u^+ in the log region and up to 0.3δ . The effect of s_z/s_x will be investigated in more detail in section 6.6.4.

The inner peak of the smooth wall's mean streamwise turbulence intensity profiles is shifting to the left with increasing the Reynolds number when the wall's normal position is normalized by the outer length scale δ . The value of the inner peak is slightly increasing with increasing the Reynolds number. The small differences between the experimental and DNS smooth wall data profiles are due to the spatial resolutions of single hot-wire probes'. Chin *et al.* (2009) applied various spanwise filter lengths to streamwise velocity components DNS data of a channel flow. They investigated different spatial resolutions of single hot-wire probes' effects on hot-wire measurements. They found that the attenuation is most severe in the near-wall region, and this attenuation decreases gradually as we move to the outer region and can be neglected from $y/\delta > 0.6$.

For the rough wall cases, increasing the Reynolds number for the same roughness reduces only the inner peak value while having a negligible effect on the outer layer. This reduction of the inner peak may be due to an attenuation effect associated with the spatial resolution in the hot-wire measurements as the l^+ values are almost tripled from the lowest to the highest Reynolds number, or a transition from the transitionally rough regime to the fully rough regime TBLs. Ligriani & Moffat (1986) showed a gradual reduction of the inner peak with increasing k_s^+ in a transitionally rough regime. This inner peak is completely destroyed in the fully rough wall TBLs. This vanishing of the inner peak reflects a different energy production mechanism in the near-wall region than in a smooth wall TBL. Ghanadi & Djenidi (2021) observed that there is no effect of hot-wire length on TBL measurements over 2D rods' rough walls. They investigated the effect of the hot-wire length l^+ ranging from 24 to 168. This observation gives further confidence in our present rough wall measurements, where l^+ values vary from 10 to 35.

Figure 6.11 also shows an inner peak shift away from the wall compared with a smooth

wall. The roughness is believed to redistribute the near-wall turbulence intensity due to counter-rotating vortices very close to the surface roughness. [Nugroho *et al.* \(2013\)](#) observed that shift when they studied the effect of converging-diverging riblets on ZPG TBL flows. They showed that the inner peak of turbulence intensity profiles was shifted closer to the surface over the diverging part of the riblets and shifted further away from the wall over the converging part of the riblets. They suggested that over the converging region, the common-flow-up tendency will increase the turbulence intensity, and the inner peak will shift further from the rough surface. However, over the diverging region, the turbulence intensity decreases near the wall due to the damping of the turbulent fluctuations closer to the wall from the common-flow-down region and the inner peak will shift closer to the wall.

Another way to investigate the similarity of the turbulence intensities of TBL is using the diagnostic plot introduced in [Alfredsson *et al.* \(2012\)](#). Using the diagnostic plot avoids uncertainties in measuring the accurate wall-normal position y and in calculating U_τ . For each rough surface, if the flow is fully developed, then the profiles should collapse in the outer region of the TBL, regardless of the Reynolds number. This is confirmed in Figure 6.12 when comparing the profiles with the same symbols but different colors. The symbols of our measurements are detailed in Table 6.2. The solid black line is DNS smooth TBL data from [Chan *et al.* \(2021\)](#) at $Re_\tau \approx 2000$. The solid straight magenta line corresponds to the linear relationship $u'/U = 0.286 - 0.255 U/U_\infty$ ([Alfredsson *et al.* \(2012\)](#)). Figures 6.12(a), 6.12(c), and 6.12(e) are for different rough surfaces with constant $s_x/k = 6, 8$ and 12 , respectively, while s_z/k is varied from 6 to 12 in panels (a) and (e), and from 6 to 16 in panel(c). Figures 6.12(b), 6.12(d), and 6.12(f) are for different rough surfaces with constant $s_z/k = 6, 8$ and 12 , respectively, while s_x/k is varied from 6 to 12 in panels (a) and (e), and from 6 to 16 in panel (c). Our smooth wall data at different free-stream velocities are shown as a reference in Figure 6.12(a).

Figures 6.12(a), 6.12(c), and 6.12(e) show a very slight variation between profiles with the same s_x/k and different s_z/k . However, these differences are more apparent in Figures 6.12(b), 6.12(d), and 6.12(f) representing the same s_z/k and different s_x/k . These differences are due to the variation of the ratio s_z/s_x as mentioned before. [Djenidi *et al.* \(2018\)](#) also noticed differences in the diagnostic plots between 2D bars and sand grain roughness, indicating a lack of similarity between TBL over different rough surfaces.

6.6.3 TBL over different rough surfaces at matched friction Reynolds number

In Subsection 6.6.2, we discussed the effect of changing s_x/k and s_z/k on ΔU^+ and C_f . However, the Reynolds number at the same free-stream velocity is reduced for a large streamwise spacing ratio (i.e., $s_x/k = 12$ and 16). So, it is better to plot the streamwise mean velocity and turbulence intensity profiles at matched Reynolds number Re_τ . This is shown in Figure 6.13 for $Re_\tau = 2500 \pm 400$ over the eleven different rough surfaces presented in Table 6.2. These profiles are plotted against the DNS smooth TBL data from [Chan *et al.* \(2021\)](#) at $Re_\tau \approx 2000$, for comparison. Figure 6.13(a) shows the large discrepancy between the velocity profiles at matched Reynolds numbers. From consulting Table 6.2, it can be found that ΔU^+ varies from 3.9 to 8.4 between the different rough surfaces. Also, k_s^+ varied from 19 to 127, which emphasizes the role of ES in determining the roughness function ΔU^+ . Also, the large discrepancy between the streamwise turbulence intensity profiles, as plotted in Figure 6.13(b), is evidence of a lack of similarity between TBL over different rough surfaces.

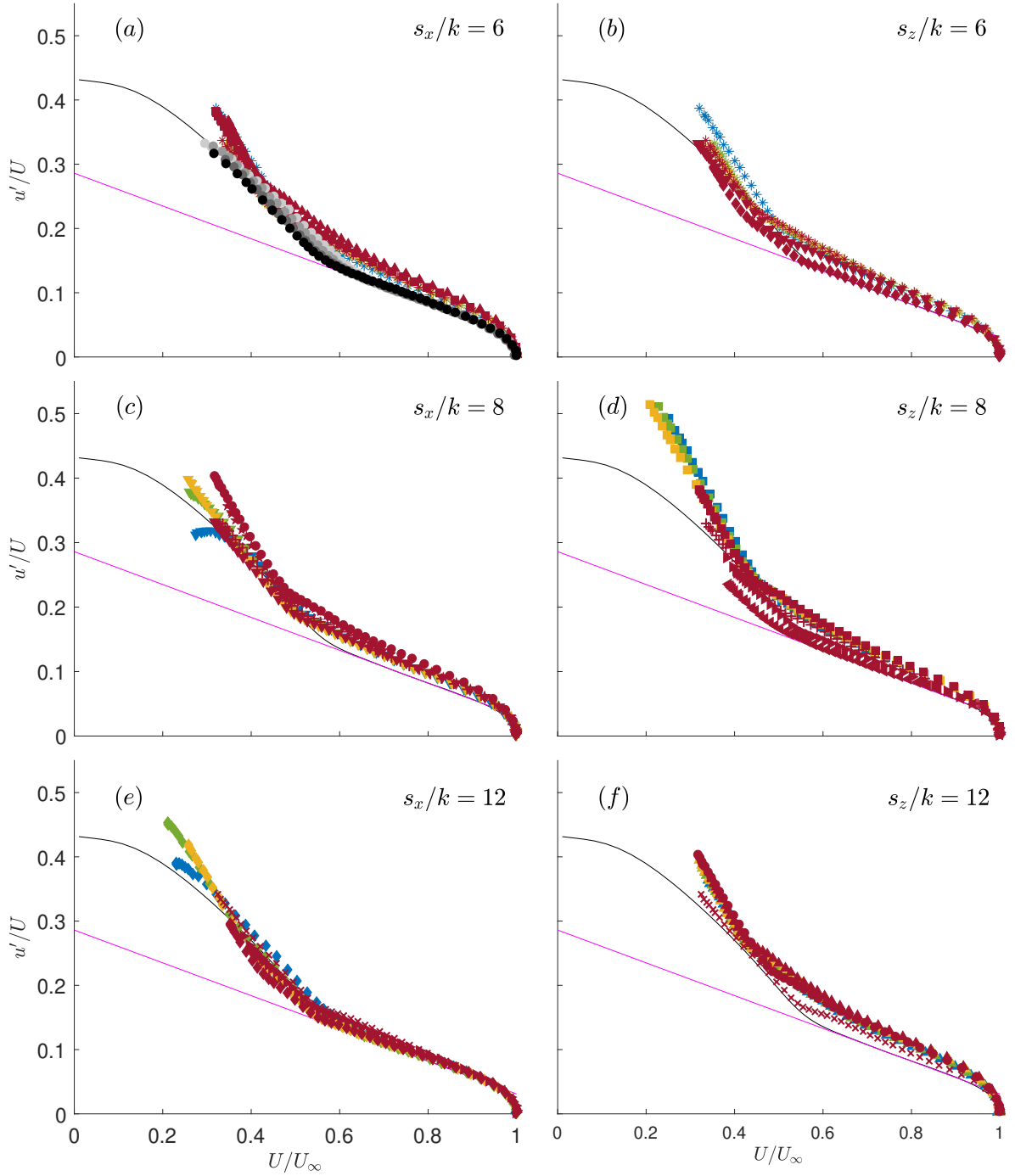


FIGURE 6.12: Mean streamwise turbulence intensity profiles over smooth and rough surfaces are compared using the diagnostic plot. The symbols of our measurements are detailed in Table 6.2. Solid black line: DNS smooth TBL data from Chan *et al.* (2021) at $Re_\tau \approx 2000$. The solid straight magenta line corresponds to the linear relationship $u'/U = 0.286 - 0.255 U/U_\infty$ (Alfredsson *et al.* 2012). The profiles over rough surfaces with constant $s_x/k = 6, 8,$ and 12 are shown in (a), (c), and (e), respectively. The profiles over rough surfaces with constant $s_z/k = 6, 8,$ and 12 are shown in (b), (d), and (f), respectively.

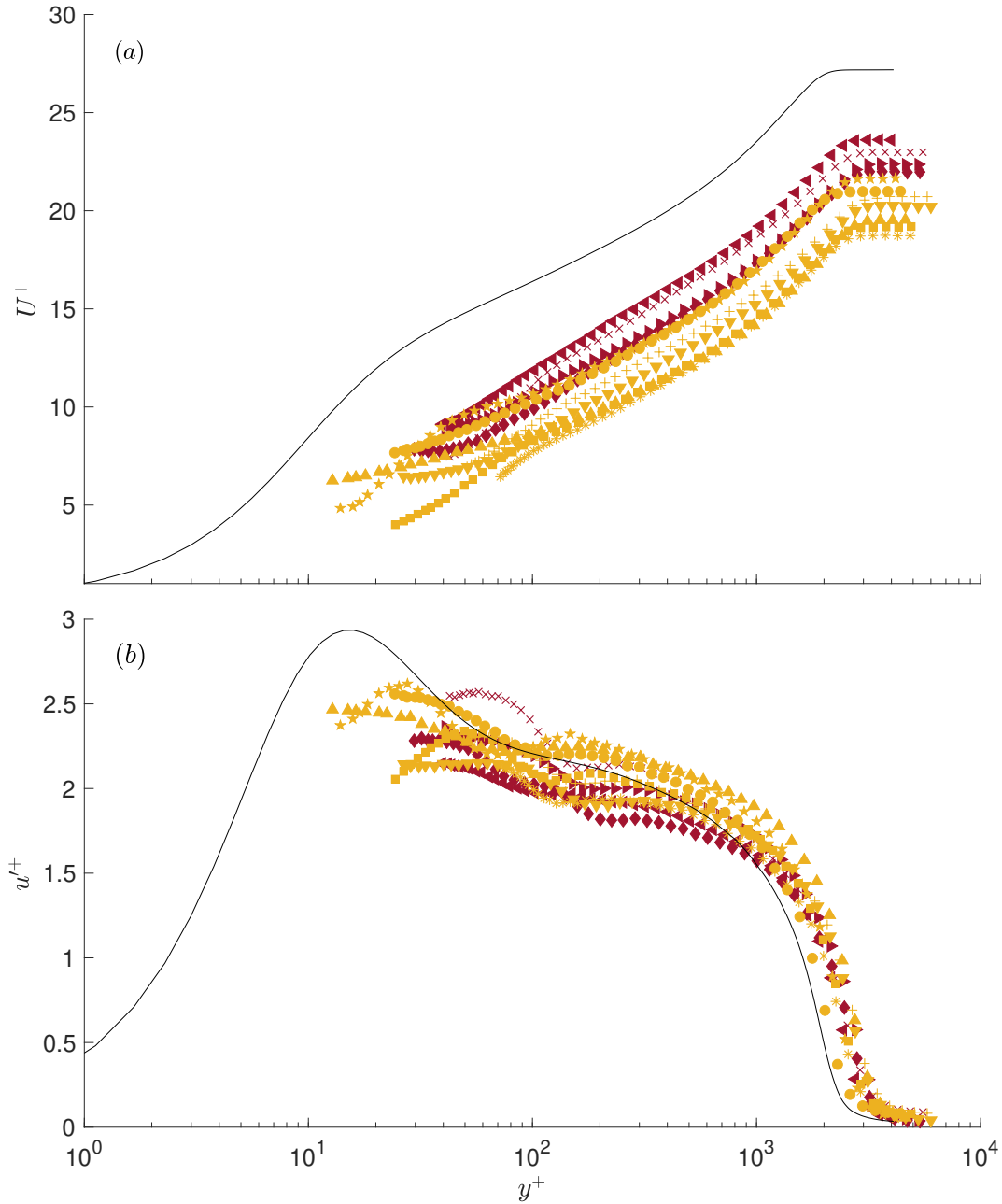


FIGURE 6.13: (a) Mean streamwise velocity profiles for the different rough surfaces presented in Table 6.2 at matched Reynolds number $Re_\tau = 2500 \pm 400$. (b) Mean streamwise turbulence intensity profiles of the different rough surfaces at matched Reynolds number $Re_\tau = 2500 \pm 400$. The symbols of our measurements are detailed in Table 6.2. Solid black line: DNS smooth TBL data from Chan *et al.* (2021) at $Re_\tau \approx 2000$.

6.6.4 Energy spectra

A spectral analysis enables us to understand the effect of changing s_x/k , and s_z/k on the various length scales of the turbulent boundary layer. Inner normalized premultiplied streamwise turbulent energy spectrograms ($k_x \phi_{uu}/U_\tau^2$) of smooth and 3D sinewave surfaces are shown in Figures 6.14 and 6.15. The spectrogram contours are plotted with fixed levels from 0.2 to 1.8 with 0.1 steps. Here, $k_x = 2\pi/\lambda_x$ is the streamwise wavenumber, λ_x is the streamwise wavelength, and ϕ_{xx} is the spectral density of u' . Taylor's frozen field hypothesis converts the measured frequency spectra to the spatial domain (Taylor 1938). The local mean velocity is used as a convection velocity. Measurements are taken with a sampling rate of 51.2 kHz for each of the 48 wall-normal locations for 120 s. A fast Fourier transform (FFT) algorithm was used to evaluate the streamwise velocity signal's power spectral density, employing 24 windows with 75 % overlap.

Squire *et al.* (2017) studied the applicability of using Taylor's frozen field hypothesis for TBL over smooth and rough wall flows. The results showed that Taylor's hypothesis is applicable to the streamwise velocity component for $y/\delta > 0.02$. Ghanadi & Djenidi (2021) investigated the Reynolds number effect on TBL over rod roughness surface with local wall suction. Their results showed that beyond the region $y/k < 1$, Taylor's hypothesis is appropriate to plot 2D contour maps velocity spectra. Our main focus here will be on the region $y/k > 1$, bounded by a thick black line shown in the following spectra contour maps.

Three different sinewave surfaces with $s_x/k = s_z/k$ equal to 6, 8 and 12, respectively, are compared with our smooth TBL data at relatively matched $Re_\tau \approx 2000$ in Figure 6.14. The high level of energy content, which reflects the inner peak of energy, is observed in a smooth wall at $y^+ = 15$, and $\lambda_x^+ = 1000$. This highly energetic peak is due to the near-wall cycle. This location which corresponds to the maximum of u' , is consistent with Ligrani & Bradshaw (1987). Figure 6.14 shows again that the inner peak shifts away from the wall compared with the smooth wall due to the redistribution of the near-wall turbulence intensity caused by roughness. Then this inner peak is gradually reduced when the surface becomes rougher until it is completely destroyed in the fully rough wall TBLs. Squire *et al.* (2016) also made a comparison between smooth and sand-grain rough wall premultiplied streamwise energy spectrogram at different values of matched Re_τ . Their results showed that at $Re_\tau = 2900$ (very close to our case), the spectrogram of both smooth and rough walls are similar, but the magnitude of the rough wall energy at all scales is lower than the smooth wall. The outer layer of the smooth wall has higher energy content than the isotropic sinewave rough surfaces. The energy content for these latter surfaces decreases with decreasing s_x/k . The maximum contour level in the outer region of S24-06-06 is around 0.8 [Figure 6.14(a)]. The magnitude of the contours in the outer layer increased to 0.9 for the S24-08-08 surface [Figure 6.14(b)]. The magnitude of the contours shown in Figure 6.14(c) increases more in the outer region of S24-12-12, and the maximum contour level that appears in S24-12-12 is almost 1.0. For the smooth wall, the maximum contour level in the outer region is higher than the 3D isotropic sinewave surfaces and reaches more than 1.1 [Figure 6.14(d)].

To further investigate the effect of s_x/k and s_z/k , $k_x \phi_{uu}/U_\tau^2$ contours for the different anisotropic surfaces are plotted in Figure 6.15. The left-hand side of the figure shows the four surfaces which have $s_z/k > s_x/k$, and they are arranged from the highest s_z/k to the lowest s_z/k from top to bottom. The right-hand side is the same surfaces after rotating them by 90° in the (x, z) plane to have $s_x/k > s_z/k$.

The interesting findings from Figure 6.15 are that the magnitudes of contours of $k_x \phi_{uu}/U_\tau^2$ are much higher when s_z/k is higher than s_x/k (the left column of Figure 6.15 compared with the right column). The highest kinetic energy contour values appear when the ratio of s_z/s_x equals

two, as shown in Figures 6.15(a) and 6.15(c). The values of the contours decrease gradually when the ratio decreases. The lowest values occur when $s_z/s_x = 0.5$ as shown in Figures 6.15(b) and 6.15(d). The highly energetic outer peak over the surfaces $S24-08-16$, $S24-06-12$ and $S24-08-12$ in Figures 6.15(a), 6.15(b), and 6.15(c) can indicate that the formation of quasi-streamwise vortices in the outer layer that can indeed be associated with the secondary flow. Those surfaces have $s_z > 0.5\delta$, which is the critical value for the development of the secondary vortex structures, as mentioned in section 6.6.2.

6.7 CONCLUSION

Hot-wire anemometry is used to investigate a turbulent boundary layer over 3D sinewave surface roughnesses. Most roughness parameters are constant such as the average, rms, maximum heights, skewness and kurtosis. We only varied the streamwise and spanwise spacing to height ratios (s_x/k and s_z/k) to investigate the effect of these roughness parameters on the drag coefficient C_f and the roughness function ΔU^+ . The results are categorized into two groups of rough surfaces. The first group has a constant s_x/k while, s_z/k is varied from 6 to 16. Those surfaces are rotated by 90° in the (x, z) plan to form the second group, which has a constant s_z/k while, s_x/k is varied from 6 to 16.

Two isotropic 3D sinewave roughnesses are compared with 2D sinewave roughnesses with almost similar roughness parameters in Abdelaziz *et al.* (2022b). The results show that the 3D sinewave surface produces less drag than the 2D ones and has a lower roughness function and turbulence intensity. This is due to the higher blockage area imposed by 2D roughness, which forces the fluid to flow over the roughness elements.

As expected, the wall-unit normalized streamwise mean velocity profiles are shifted downward relative to the smooth wall profile for all roughnesses. For the first group with constant s_x/k , changing ES_z has a slight effect on C_f and ΔU^+ . C_f and ΔU^+ are slightly reduced by decreasing ES_z from 0.2 to 0.1. On the other hand, for the second group with constant s_z/k , changing ES_x has a drastic effect on C_f and ΔU^+ . C_f and ΔU^+ are more significantly reduced by decreasing ES_x from 0.2 to 0.1. Contrary to the mean velocity profiles, the first group shows a larger discrepancy in the u^{I+} profiles than the second group. This is due to the large perturbations to the structure of the mean velocity field associated with the presence of large secondary flow motion.

A lack of similarity between TBL over different rough surfaces at matched $Re_\tau = 2500 \pm 400$ is observed between the different streamwise turbulence intensity profiles. However, the defect form of mean velocity profiles shows an excellent collapse between the velocity profiles of different rough surfaces. The spanwise spacing to height ratio s_z/k of the 3D sinewave roughness has little effect on the mean streamwise velocity profiles. However, it greatly impacts the u^{I+} profiles in the log and outer layer. This explains why we observe similar log-law shifts in ΔU^+ but a lack of similarity of streamwise turbulence intensity profiles among different roughnesses.

Also, plotting the mean streamwise velocity profiles for the same surface at different values of free-stream velocities U_∞ shows a Reynolds number independence, as the C_f is constant for four different values of the Reynolds numbers. This is manifested in the shifting of the mean streamwise velocity profiles to the right only with increasing U_∞ .

For isotropic 3D sinusoidal roughness, the premultiplied streamwise turbulent energy spectrograms show that the energy content increases in the outer layer with increasing s_x/k . For anisotropic 3D sinusoidal roughness, the energy content increases in the outer layer with the increase of s_z/s_x from half to two.

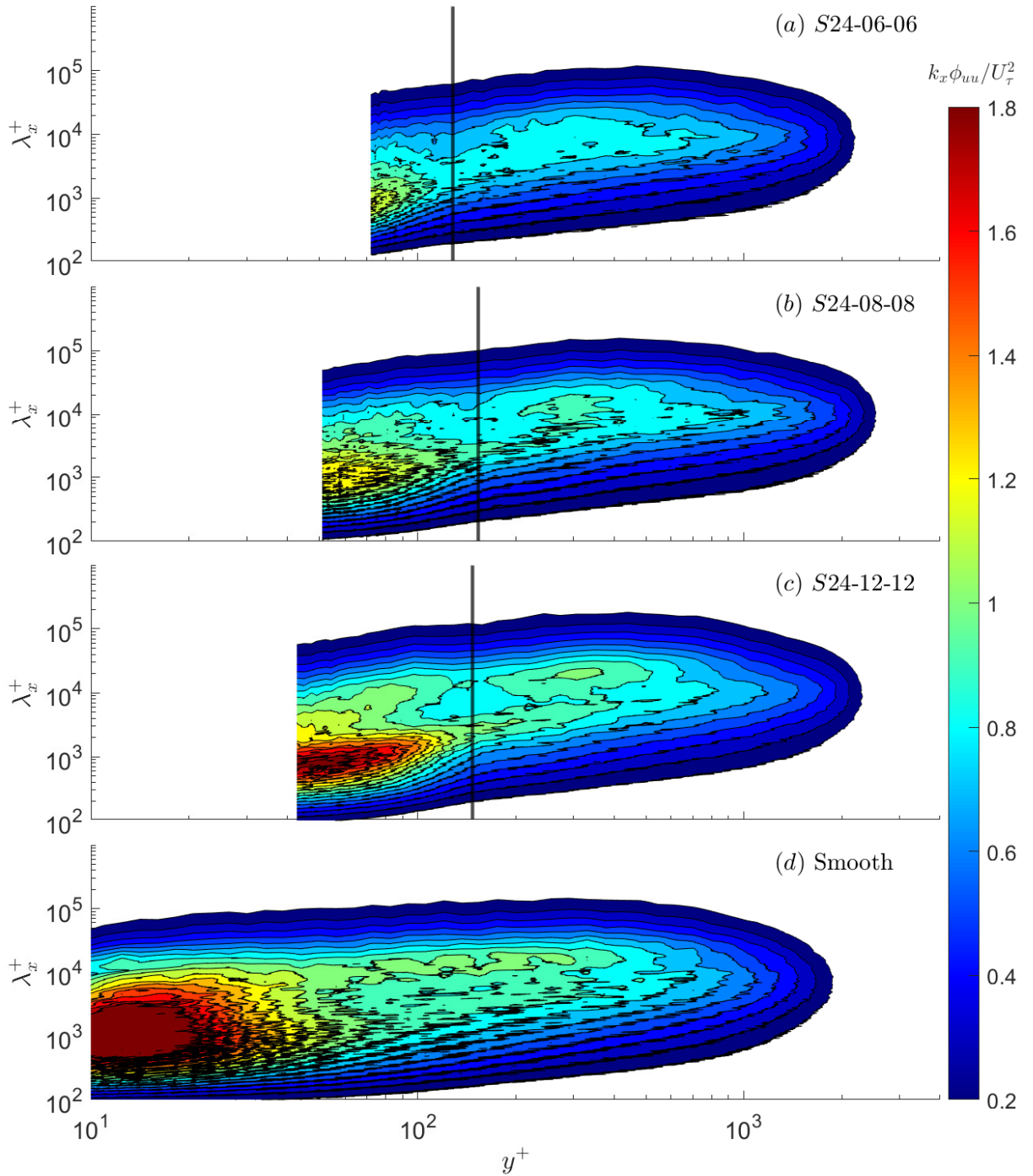


FIGURE 6.14: The premultiplied streamwise energy spectrograms at approximately matched Re_τ , for the isotropic surfaces with equal streamwise and spanwise effective slopes, and compared with our smooth wall data as a reference in (d). The vertical solid line in (a)-(C) corresponds to $y = k$ in S24-06-06, S24-08-08 and S24-12-12, respectively.

This work is a step toward investigating the major roughness parameters affecting the roughness function over 3D sinusoidal roughness. More systematic approaches for varying the roughness skewness from negative to positive values on a 3D sinusoidal roughness are required for a more accurate prediction of the equivalent sand grain roughness k_s^+ .

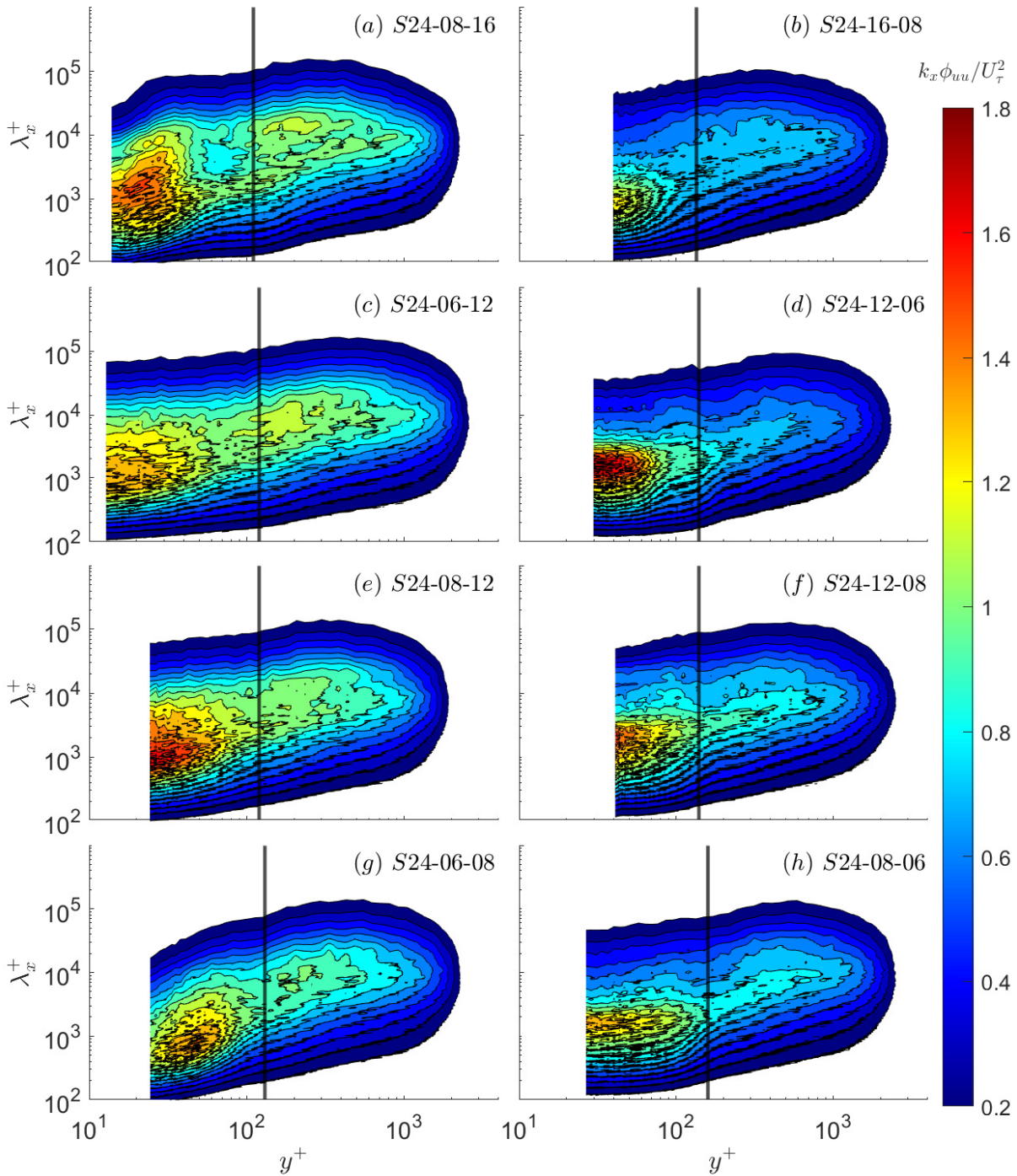


FIGURE 6.15: The premultiplied streamwise energy spectrograms at approximately matched Re_τ for the anisotropic surfaces. The left column represents spectrograms of surfaces with a higher spanwise spacing to height ratios than the streamwise spacing to height ratios [(a): S24-08-16, (c): S24-06-12, (e): S24-08-12, (g): S24-06-08]. The right column represents spectrograms of the same surfaces after rotating them by 90° in the (x, z) plane, a higher streamwise spacing to height ratios than the spanwise spacing to height ratios, [(b): S24-16-08, (d): S24-12-06, (f): S24-12-08, (h): S24-08-06]. The vertical solid line corresponds to $y = k$.

ACKNOWLEDGMENTS

The authors acknowledge the financial support of the Australian Research Council.

AUTHOR DECLARATIONS

Conflict of Interest

The authors have no conflicts to disclose.

Author Contributions

Misarah Abdelaziz: Conceptualization (equal). **Lyazid Djenidi:** Conceptualization (equal). **Mergen Ghayesh:** Conceptualization (equal). **Rey Chin:** Conceptualization (equal).

DATA AVAILABILITY

The data that support the findings of this study are available from the corresponding author upon reasonable request.

Bibliography

- ABDELAZIZ, M., DJENIDI, L., GHAYESH, M. H., & CHIN, R. 2022a A new equivalent sand grain roughness relation for two-dimensional rough wall turbulent boundary layers. *Journal of Fluid Mechanics* **940**, A25.
- ABDELAZIZ, M., DJENIDI, L., GHAYESH, M. H., & CHIN, R. 2022b Outer turbulent boundary layer similarities for different 2D surface roughnesses at matched Reynolds number. *International Journal of Heat and Fluid Flow* **94**, 108940.
- ALFREDSSON, P. H., ÖRLÜ, R., & SEGALINI, A. 2012 A new formulation for the stream-wise turbulence intensity distribution in wall-bounded turbulent flows. *European Journal of Mechanics-B/Fluids* **36**, 167–175.
- ASME 2009 Surface Texture (Surface Roughness, Waviness, and Lay). *Revision of ANSI/ASME B46.1-1995. Standard. ASME* .
- AVER'YANOVA, I. O., BOGOMOLOV, D. Y., & POROSHIN, V. V. 2017 ISO 25178 standard for three-dimensional parametric assessment of surface texture. *Russian Engineering Research* **37** (6), 513–516.
- BAI, H., KEVIN, HUTCHINS, N., & MONTY, J. 2018 Turbulence modifications in a turbulent boundary layer over a rough wall with spanwise-alternating roughness strips. *Physics of Fluids* **30** (5), 055105.
- BRERETON, G., JOUYBARI, M. A., & YUAN, J. 2021 Toward modeling of turbulent flow over surfaces of arbitrary roughness. *Physics of Fluids* **33** (6), 065121.
- CASTRO, I. P. 2007 Rough-wall boundary layers: mean flow universality. *Journal of Fluid Mechanics* **585**, 469–485.

- CHAN, C. I., SCHLATTER, P., & CHIN, R. C. 2021 Interscale transport mechanisms in turbulent boundary layers. *Journal of Fluid Mechanics* **921**, A13.
- CHAN, L., MACDONALD, M., CHUNG, D., HUTCHINS, N., & OOI, A. 2015 A systematic investigation of roughness height and wavelength in turbulent pipe flow in the transitionally rough regime. *Journal of Fluid Mechanics* **771**, 743–777.
- CHIN, C. C., HUTCHINS, N., OOI, A. S. H., & MARUSIC, I. 2009 Use of direct numerical simulation (DNS) data to investigate spatial resolution issues in measurements of wall-bounded turbulence. *Measurement Science and Technology* **20**, 115401.
- CLAUSER, F. H. 1956 The turbulent boundary layer. *Advances in Applied Mechanics* **4**, 1–51.
- DE MARCHIS, M., SACCONI, D., MILICI, B., & NAPOLI, E. 2020 Large eddy simulations of rough turbulent channel flows bounded by irregular roughness: advances toward a universal roughness correlation. *Flow, Turbulence and Combustion* **105**, 627–648.
- DJENIDI, L., TALLURU, K. M., & ANTONIA, R. A. 2018 Can a turbulent boundary layer become independent of the Reynolds number? *Journal of Fluid Mechanics* **851**, 1–22.
- DJENIDI, L., TALLURU, K. M., & ANTONIA, R. A. 2019 A velocity defect chart method for estimating the friction velocity in turbulent boundary layers. *Fluid Dynamics Research* **51**, 045502.
- FLACK, K. A., SCHULTZ, M. P., & BARROS, J. M. 2020 Skin Friction Measurements of Systematically-Variied Roughness: Probing the Role of Roughness Amplitude and Skewness. *Flow, Turbulence and Combustion* **104** (2), 317–329.
- FLACK, K. A., SCHULTZ, M. P., BARROS, J. M., & KIM, Y. C. 2016 Skin-friction behavior in the transitionally-rough regime. *International Journal of Heat and Fluid Flow* **61**, 21–30.
- FOROOGHI, P., STROH, A., MAGAGNATO, F., JAKIRLIĆ, S., & FROHNAPFEL, B. 2017 Toward a universal roughness correlation. *Journal of Fluids Engineering* **139** (12).
- FOROOGHI, P., YANG, X. I., & ABKAR, M. 2020 Roughness-induced secondary flows in stably stratified turbulent boundary layers. *Physics of Fluids* **32** (10), 105118.
- GHANADI, F. & DJENIDI, L. 2021 Spatial resolution effects on measurements in a rough wall turbulent boundary layer. *Experiments in Fluids* **62** (8), 1–6.
- GUL, M. & GANAPATHISUBRAMANI, B. 2022 Experimental observations on turbulent boundary layers subjected to a step change in surface roughness. *Journal of Fluid Mechanics* **947**, A6.
- HAMA, F. R. 1954 Boundary layer characteristics for smooth and rough surfaces. *Trans. Soc. Nav. Arch. Marine Engrs.* **62**, 333–358.
- HAMED, A. M., KAMDAR, A., CASTILLO, L., & CHAMORRO, L. P. 2015 Turbulent boundary layer over 2D and 3D large-scale wavy walls. *Physics of Fluids* **27** (10), 106601.
- HAMED, A. M., PETERLEIN, A. M., & RANDLE, L. V. 2019 Turbulent boundary layer perturbation by two wall-mounted cylindrical roughness elements arranged in tandem: Effects of spacing and height ratio. *Physics of Fluids* **31** (6), 065110.
- HUTCHINS, N., NICKELS, T. B., MARUSIC, I., & CHONG, M. S. 2009 Hot-wire spatial resolution issues in wall-bounded turbulence. *Journal of Fluid Mechanics* **635**, 103–136.

- JIMÉNEZ, J. 2004 Turbulent flows over rough walls. *Annual Review of Fluid Mechanics* **36**, 173–196.
- JOUBYARI, M. A., YUAN, J., BRERETON, G. J., & MURILLO, M. S. 2021 Data-driven prediction of the equivalent sand-grain height in rough-wall turbulent flows. *Journal of Fluid Mechanics* **912**, A08.
- LIGRANI, P. M. & BRADSHAW, P. 1987 Spatial resolution and measurement of turbulence in the viscous sublayer using subminiature hot-wire probes. *Experiments in Fluids* **5** (6), 407–417.
- LIGRANI, P. M. & MOFFAT, R. J. 1986 Structure of transitionally rough and fully rough turbulent boundary layers. *Journal of Fluid Mechanics* **162**, 69–98.
- MAREC, J. P. 2001 Drag reduction: a major task for research. In *Aerodynamic Drag Reduction Technologies*, pp. 17–27. Springer.
- MARUSIC, I., MONTY, J. P., HULTMARK, M., & SMITS, A. J. 2013 On the logarithmic region in wall turbulence. *Journal of Fluid Mechanics* **716**, R3.
- MEDJNOUN, T., RODRIGUEZ-LOPEZ, E., FERREIRA, M., GRIFFITHS, T., MEYERS, J., & GANAPATHISUBRAMANI, B. 2021 Turbulent boundary-layer flow over regular multiscale roughness. *Journal of Fluid Mechanics* **917**.
- MOODY, L. F. 1944 Friction factors for pipe flow. *Trans. ASME* **66**, 671–684.
- NAPOLI, E., ARMENIO, V., & DE MARCHIS, M. 2008 The effect of the slope of irregularly distributed roughness elements on turbulent wall-bounded flows. *Journal of Fluid Mechanics* **613**, 385–394.
- NICKELS, T. B., MARUSIC, I., HAFEZ, S., & CHONG, M. S. 2005 Evidence of the k_1^{-1} law in a high-Reynolds-number turbulent boundary layer. *Physical Review Letters* **95**, 074501.
- NIKURADSE, J. 1933 Laws of flow in rough pipes. *Translation from German published 1950 as NACA Tech. Memo. 1292* .
- NUGROHO, B., BAIDYA, R., NURROHMAN, M. N., YUSIM, A. K., PRASETYO, F. A., YUSUF, M., SUASTIKA, I. K., UTAMA, I. K. A. P., MONTY, J. P., HUTCHINS, N., ET AL. 2017 *In situ* turbulent boundary layer measurements over freshly cleaned ship-hull under steady cruising. In *Proceeding of International Conference on Ship and Offshore Technology (ICSOT), Royal Institution of Naval Architects (RINA) Conference*.
- NUGROHO, B., HUTCHINS, N., & MONTY, J. P. 2013 Large-scale spanwise periodicity in a turbulent boundary layer induced by highly ordered and directional surface roughness. *International Journal of Heat and Fluid Flow* **41**, 90–102.
- PERRY, A. E. & CHONG, M. S. 1982 On the mechanism of wall turbulence. *Journal of Fluid Mechanics* **119**, 173–217.
- PERRY, A. E. & JOUBERT, P. N. 1963 Rough-wall boundary layers in adverse pressure gradients. *Journal of Fluid Mechanics* **17** (02), 193–211.
- PERRY, A. E. & LI, J. D. 1990 Experimental support for the attached-eddy hypothesis in zero-pressure-gradient turbulent boundary layers. *Journal of Fluid Mechanics* **218**, 405–438.

- PLACIDI, M. & GANAPATHISUBRAMANI, B. 2018 Turbulent flow over large roughness elements: effect of frontal and plan solidity on turbulence statistics and structure. *Boundary-Layer Meteorology* **167** (1), 99–121.
- RAMANI, A., NUGROHO, B., BUSSE, A., MONTY, J. P., HUTCHINS, N., & JELLY, T. O. 2020 The Effects of Anisotropic Surface Roughness on Turbulent Boundary-Layer Flow. In *22nd Australasian Fluid Mechanics Conference, AFMC 2020*. The University of Queensland.
- SCHLICHTING, H. & KESTIN, J. 1961 *Boundary layer theory*. vol. 121, New York: McGraw-Hill.
- SCHULTZ, M. P. & FLACK, K. A. 2009 Turbulent boundary layers on a systematically varied rough wall. *Physics of Fluids* **21**, 015104.
- SILLERO, J. A., JIMÉNEZ, J., & MOSER, R. D. 2014 Two-point statistics for turbulent boundary layers and channels at Reynolds numbers up to $\delta^+ = 2000$. *Physics of Fluids* **26**, 105109.
- SQUIRE, D. T., HUTCHINS, N., MORRILL-WINTER, C., SCHULTZ, M. P., KLEWICKI, J. C., & MARUSIC, I. 2017 Applicability of Taylor’s hypothesis in rough-and smooth-wall boundary layers. *Journal of Fluid Mechanics* **812**, 398–417.
- SQUIRE, D. T., MORRILL-WINTER, C., HUTCHINS, N., SCHULTZ, M. P., KLEWICKI, J. C., & MARUSIC, I. 2016 Comparison of turbulent boundary layers over smooth and rough surfaces up to high Reynolds numbers. *Journal of Fluid Mechanics* **795**, 210–240.
- TALLURU, K., KULANDAIVELU, V., HUTCHINS, N., & MARUSIC, I. 2014 A calibration technique to correct sensor drift issues in hot-wire anemometry. *Measurement Science and Technology* **25** (10), 105304.
- TAYLOR, G. I. 1938 The spectrum of turbulence. *Proceedings of the Royal Society of London. Series A-Mathematical and Physical Sciences* **164** (919), 476–490.
- UTAMA, I. K. A. P., NUGROHO, B., CHIN, C., HAKIM, M. L., PRASETYO, F. A., YUSUF, M., SUASTIKA, I. K., MONTY, J., HUTCHINS, N., & GANAPATHISUBRAMANI, B. 2017 A study of skin friction drag from realistic roughness of a freshly cleaned and painted ship hull. In *International Symposium on Marine Engineering (ISME)*.
- VANDERWEL, C. & GANAPATHISUBRAMANI, B. 2015 Effects of spanwise spacing on large-scale secondary flows in rough-wall turbulent boundary layers. *Journal of Fluid Mechanics* **774**, R2.
- ZHENG, Y. & ANDERSON, W. 2021 Flow-roughness heterogeneity: critical obliquity and salient parameters. *Journal of Fluid Mechanics* **913**.

Chapter 7

Roughness Skewness Effect on Turbulent Boundary Layers

7.1 CHAPTER OVERVIEW

In the previous chapter 6, the effects of varying streamwise and spanwise effective slopes on turbulence statistics were investigated, whereas this chapter focuses on the effect of varying roughness skewness on turbulence statistics. The study utilized single hotwire anemometry to conduct zero pressure gradient turbulent boundary layer measurements over 3D sinusoidal rough walls with positive, zero, and negative roughness skewness values.

The results show that all rough surfaces cause a downward shift of the wall-unit normalized streamwise mean velocity profiles in comparison to smooth walls. The roughness function ΔU^+ and the friction coefficient C_f increase as roughness skewness increases, with the positive roughness skewness surfaces causing the greatest drag and downward shift. Interestingly, the percentage of increase of C_f and ΔU^+ is greater when the roughness skewness increases from negative to zero than from zero to positive values. An exponential function $k_s = f(k_{sk})$ was found to accurately predict the equivalent sand grain roughness k_s for these 3D sinusoidal rough surfaces when the roughness skewness parameter was varied and other roughness parameters were kept constant.

The velocity defect, velocity rms, and higher order turbulence statistics, such as velocity skewness (S_u) and velocity kurtosis factor (K_u), normalized by δ , collapse between the smooth and various 3D sinusoidal rough surfaces, supporting the outer layer similarity hypothesis, even for smaller values of δ/k and Re_τ , regardless of the surface and flow conditions.

This study emphasises the significance of higher-order topographical parameters, especially skewness, in influencing near-wall flow behaviour.

7.2 INFLUENCE OF SKEWED THREE-DIMENSIONAL SURFACE ROUGHNESS ON TURBULENT BOUNDARY LAYERS

This section consists of the following submitted journal article:

Cite as: Phys. Fluids **35**, 055143 (2023); <https://doi.org/10.1063/5.0152391>

Submitted: 29 March 2023 • Accepted: 8 May 2023 • Published Online: 24 May 2023

Misarah Abdelaziz, L. Djenidi, Mergen H. Ghayesh, and Rey Chin.

The article is identical to its submitted format with the following exceptions:

- The numbering of figures, tables and equations has been altered to include the chapter number.
- The position of some figures and tables has been changed to improve the article's legibility.
- References style has been changed to be consistent with the thesis style.

The image shows the cover of a research article. On the left, there is a dark blue vertical banner with the text 'Physics of Fluids' in white. To the right of the banner, the text reads: 'RESEARCH ARTICLE | MAY 24 2023', followed by the title 'Influence of skewed three-dimensional sinusoidal surface roughness on turbulent boundary layers' with a green checkmark icon. Below the title, the authors are listed: 'Misarah Abdelaziz', 'L. Djenidi', 'Mergen H. Ghayesh', and 'Rey Chin'. There is a 'Check for updates' button. At the bottom left, it says 'Physics of Fluids 35, 055143 (2023)' and provides the DOI link 'https://doi.org/10.1063/5.0152391'. At the bottom right, there are icons for 'View Online' (a globe) and 'Export Citation' (a document), along with the 'CrossMark' logo.

Statement of Authorship

Title of paper	Influence of skewed three-dimensional sinusoidal surface roughness on turbulent boundary layers
Publication status	Published
Publication details	Misarah Abdelaziz, L. Djenidi, Mergen H. Ghayesh, and Rey Chin. Influence of skewed three-dimensional sinusoidal surface roughness on turbulent boundary layers <i>Physics of Fluids</i> , 35 , 055143 (2023); https://doi.org/10.1063/5.0152391

Principal Author

Name of principal author (candidate)	Misarah Abdelaziz		
Contribution to the paper	Conception, acquiring data, knowledge, analysis and drafting		
Certification	This paper reports on original research I conducted during the period of my Higher Degree by Research candidature and is not subject to any obligations or contractual agreements with a third party that would constrain its inclusion in this thesis. I am the primary author of this paper.		
Signature:		Date:	05/07/2023

Co-author contributions

By signing the Statement of Authorship, each author certifies that:

- i.* the candidate's stated contribution to the publication is accurate (as detailed above)
- ii.* permission is granted for the candidate to include the publication in the thesis; and
- iii.* the sum of all co-author contributions is equal to 100% less the candidate's stated contribution.

Name of co-author	Lyazid Djenidi		
Contribution to the paper	Conception, knowledge, analysis and drafting		
Signature:		Date:	27/06/2023

Name of co-author	Mergen H. Ghayesh		
Contribution to the paper	Conception, knowledge, and drafting		
Signature:		Date:	04/07/2023

Name of co-author	Rey Chin		
Contribution to the paper	Conception, knowledge, analysis and drafting		
Signature:		Date:	04/07/2023

Influence of skewed three-dimensional sinusoidal surface roughness on turbulent boundary layers

Cite as: Phys. Fluids **35**, 055143 (2023); <https://doi.org/10.1063/5.0152391>

Submitted: 29 March 2023. Accepted: 8 May 2023.

Published Online: 24 May 2023

Misarah Abdelaziz,^{1,a)} L. Djenidi,² Mergen H. Ghayesh,¹ and Rey Chin¹

AFFILIATIONS

¹School of Electrical and Mechanical Engineering, University of Adelaide, Adelaide, South Australia, 5005, Australia

²Department of Mechanical Engineering, Indian Institute of Technology - Bombay, Powai, Mumbai 400076, India

^{a)} Author to whom correspondence should be addressed: misarah.abdelaziz@adelaide.edu.au

ABSTRACT

The impact of roughness skewness (k_{sk}) on turbulent boundary layer (TBL) flow with a zero pressure gradient (ZPG) over three-dimensional (3D) sinusoidal rough surfaces was experimentally investigated using a single hotwire anemometer. Nine 3D sinusoidal profiles were manufactured with positive, negative, and zero roughness skewness values. Measurements were taken at three different freestream velocities for each surface and compared with smooth wall TBL results. This study covered a range of friction Reynolds numbers (Re_τ) from approximately 1000 to 4000, with a $\delta/k \approx 20 \pm 2$, where δ represents the local boundary layer thickness, and k is the maximum height of the roughness, measured from the valley to peak. The results indicate that the wall-unit normalized streamwise mean velocity profiles for all rough surfaces exhibit a downward shift compared to the smooth wall profiles. Surfaces with positive roughness skewness produced the highest drag, leading to the largest downward shift. The friction coefficient (C_f) decreased as k_{sk} decreased. The percentage increase in C_f and ΔU^+ (the roughness function) was much larger when moving from negative to zero roughness skewness than when moving from zero to positive roughness skewness. The small differences in turbulence intensity profiles and higher-order turbulence statistics in the outer region of the TBL support the outer layer similarity hypothesis for the roughness considered in this study. The autocorrelation study revealed that surfaces with positive roughness skewness tend to shorten the average length of turbulence structures in the near-wall region.

Published under an exclusive license by AIP Publishing. <https://doi.org/10.1063/5.0152391>

7.3 INTRODUCTION

Turbulent boundary layers (TBLs) are a widely studied phenomenon in fluid dynamics, occurring in a range of applications such as aeroplane design and the growth of bio-fouling on ship hulls, even recently cleaned ship-hulls (Utama *et al.* 2021). Roughness is a common characteristic of wall-bounded fluid flows, and its impact on boundary layer flow has been studied since the early work of Darcy (1857) who showed that roughness affects the pressure drop in pipe flows. The roughness of a surface can have a significant effect on heat and momentum transfer in TBLs.

A long-standing goal in the study of TBLs over rough surfaces is to predict friction drag based solely on the surface's roughness topography. However, this is a challenging task due to the wide range of existing roughness geometries and sizes. Therefore, finding a length scale or roughness parameter that best characterizes a surface and correlates with the friction drag is non-trivial and potentially of paramount importance from an engineering point of view. This study focuses on the effect of roughness skewness in three-dimensional sinusoidal surfaces on turbulent boundary layers. While related studies on surface roughness and turbulent flows are briefly mentioned, readers seeking more information on these topics are directed to appropriate sources.

Nikuradse (1933) first introduced an equivalent sand grain roughness k_s in an attempt to quantify the roughness effect. Subsequently, roughness height was thus defined as the average diameter of a sand grain. A rough surface's friction coefficient C_f is generally larger than that of a smooth wall. ($C_f = 2U_\tau^2/U_\infty^2$, where U_τ is the friction velocity, and U_∞ is the freestream velocity, and $U_\tau = \sqrt{\tau_w/\rho}$, where τ_w is the wall shear stress, and ρ is the fluid density). The increase in C_f for a rough surface TBL is reflected in the downward shift in the wall-unit normalized mean velocity profile compared to that of a smooth wall (**Hama 1954**). This shift is known as the Hama roughness function, ΔU^+ . **Schlichting & Kestin (1961)** expressed ΔU^+ as a function of k_s^+ in the fully rough regime as follows:

$$\Delta U^+ = \frac{1}{\kappa} \log(k_s^+) + B - 8.5, \quad (7.1)$$

where κ is the von Kármán constant ≈ 0.41 , and B is an additive constant ≈ 5.0 . There are three flow regimes. The first regime is called the dynamically smooth flow regime or hydraulically smooth regime, where the wall roughness does not affect the flow at all and $\Delta U^+ = 0$ at different Re_τ values. The second regime is a transitionally rough flow regime when both pressure and viscous drags contribute to the total drag. The third regime is the fully rough flow regime when the viscous drag becomes negligible or zero. There is no clear evidence for the start of these regimes. However, it is commonly considered that the hydraulically smooth regime is for $k_s^+ < 5$, and the fully rough regime begins when $k_s^+ > 70$ (**Ligrani & Moffat 1986; Jiménez 2004**).

Unfortunately, k_s is not a real roughness parameter that can be determined from the topology of the roughness; it has no physical meaning. Thus, after conducting experiments, ΔU^+ is calculated by measuring the vertical shift of the log region between the smooth and rough wall-unit normalized velocity profiles. Although ΔU^+ can be predicted directly from the surface topology with some limitations. This approach is more challenging as, so far, there has been no definite consensus on what is the best roughness parameter to characterise roughness. This is due to the many different surface parameters such as the mean roughness height k_a , root mean square height k_q , maximum peak to valley height k_t , average peak to valley height k_z , streamwise and spanwise effective slopes ES_x and ES_z , solidarity λ_f , skewness k_{sk} , and flatness k_{ku} . Over the last decades, a large body of work has been undertaken to address this issue (among many others, **Napoli et al. 2008; Yuan & Piomelli 2014; Chan et al. 2015; Forooghi et al. 2017; Barros et al. 2018; Flack et al. 2020a; Jouybari et al. 2021; Abdelaziz et al. 2022a**).

The concept of mean absolute roughness gradient, referred to as ES , was initially introduced by **Napoli et al. (2008)**. Their study revealed that there is a linear relationship between ΔU^+ and ES when $ES \leq 0.15$, and a non-linear relationship for higher ES values. **Schultz & Flack (2009)** conducted a study on turbulent boundary layer (TBL) flow over close-packed pyramid roughness and varied both the height and slope of the pyramid edges. They found that the relationship between ΔU^+ and the roughness parameter k_t was consistent, except for very

small slopes, where the roughness was considered as waviness and the relationship was no longer valid.

Chan *et al.* (2015) performed direct numerical simulations (DNS) of a turbulent pipe flow with a 3D sinusoidal roughness surface, where both k_t and ES were systematically varied. The results of their study showed that ΔU^+ had a strong dependence on both k_t and ES , and was only marginally affected by the Reynolds number.

The roughness skewness, represented by k_{sk} , was not considered in previously mentioned studies due to the nature of the roughness examined. However, Flack & Schultz (2010) found that k_s could be predicted based on k_q and k_{sk} for 3D irregular roughness in the fully rough regime. Flack *et al.* (2020a) conducted a study on the influence of roughness height and roughness skewness on the friction coefficient and found that there is a relationship between k_s and both k_q and k_{sk} , with the friction coefficients being divided into three categories based on the roughness skewness (negative, positive, and zero values). Their results also showed that negative roughness skewness surfaces produce a smaller C_f than positive roughness skewness surfaces.

Forooghi *et al.* (2017) proposed a more complex function that incorporated additional roughness parameters in their DNS of fully rough regime channel flows at $Re_\tau \approx 500$ over different wall geometries. They showed that k_s could be predicted based on k_t , k_{sk} , and ES . Abdelaziz *et al.* (2022a) also found that these three parameters had a significant impact on the turbulence statistics and drag coefficient of TBL flows over both 2-D and 3D roughness surfaces. Their study indicated that a universal scaling for roughness is unlikely to exist and that each family of roughness, such as 2-D and 3D roughness, may have its own scaling.

Over the past few decades, significant progress has been made in understanding the correlation between the roughness parameter k_s and real roughness parameters. However, a universal correlation remains elusive. Multiple major roughness parameters, such as k_t , ES , and k_{sk} , must be considered to predict drag accurately. It is imperative to independently investigate the impact of each parameter on turbulence statistics and drag reduction in order to understand the nature of the relationship between k_s and the roughness parameter. A better understanding of the behaviour of turbulent boundary layer (TBL) over rough surfaces is essential to help develop a strategy for controlling these flows.

In a recent study, Abdelaziz *et al.* (2023) have examined the effect of ES_x and ES_z on turbulence statistics and the coefficient of drag. The results showed that ES_x has a more pronounced effect on ΔU^+ and C_f than ES_z . The study aims to isolate and examine the impact of the roughness skewness parameter on TBLs while keeping all other roughness parameters constant. The experiment was performed on 3D sinusoidal roughnesses with systematically varied k_{sk} values from negative to positive to determine the roughness skewness effect on C_f for this rough wall family.

To the best of the authors' knowledge, no previous studies have investigated the influence of skewed three-dimensional sinusoidal surface roughness on both lower and higher-order statistics of turbulent boundary layers. One advantage of employing such surfaces is the capacity to methodically manipulate one or two roughness parameters while maintaining other parameters constant. In this paper, x , y and z are the streamwise, wall-normal and spanwise directions, respectively, while u denotes the streamwise fluctuating velocity component and U denotes the mean streamwise velocity component. Quantities with the superscript (+) are normalized by viscous velocity scale U_τ or length scale ν/U_τ , where ν is the kinematic viscosity. The friction Reynolds number, $Re_\tau = \delta U_\tau/\nu$, where δ is the thickness of the boundary layer, defined as the distance from the wall to the point at which the mean streamwise velocity reaches 99% of the freestream velocity.

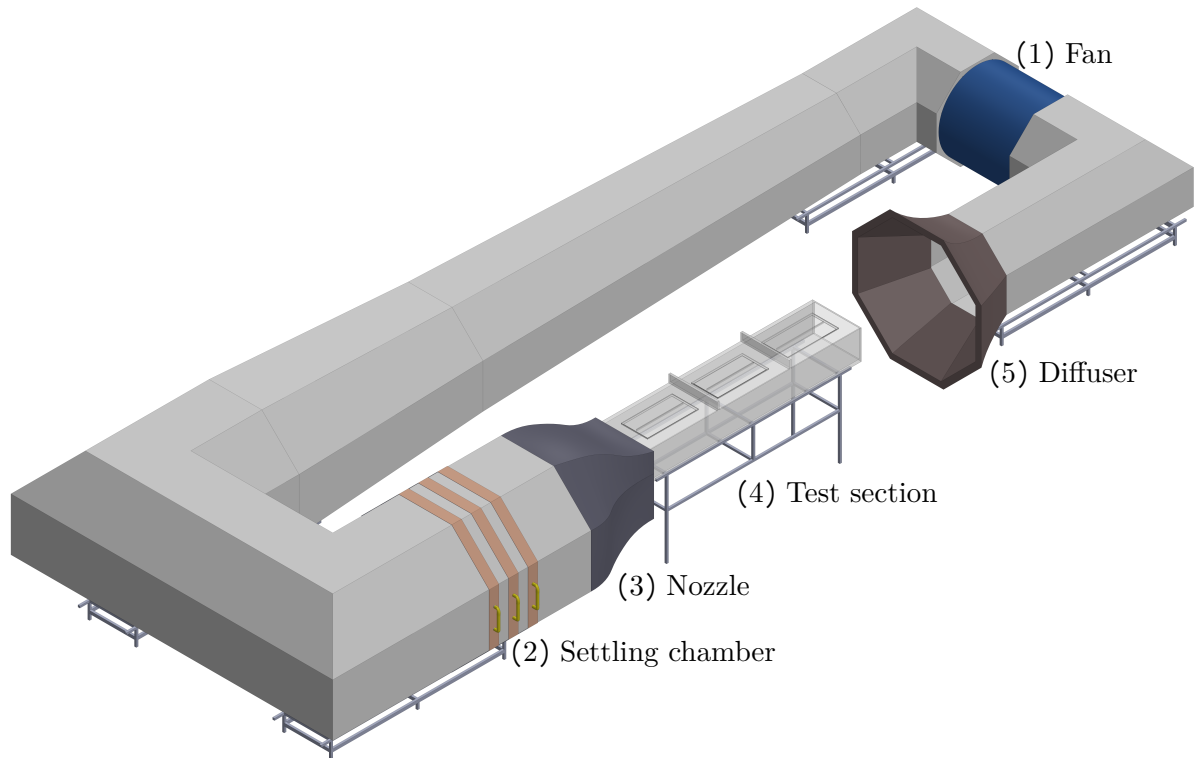


FIGURE 7.1: A schematic of the University of Adelaide wind tunnel. The air is guided from (1) the fan through a series of turning vanes into (2) the settling chamber consists of a honeycomb flow straightener, and three screens, then enter (3) the nozzle and (4) the test section before redirecting back through (5) the diffuser to the fan.

7.4 EXPERIMENTAL DETAILS

7.4.1 Wind tunnel and test section facilities

The experiments were conducted in a closed-return wind tunnel at the University of Adelaide, using a two-meter-long test section with a rectangular cross-section of 0.5 m by 0.3 m. To maintain a uniform flow across the entire cross-section, a honeycomb straightener and three screens were installed in the settling chamber downstream of the octagonal contraction of the wind tunnel. This allowed for an air velocity of up to 30 m/s to be achieved within the test section, with a turbulence intensity of approximately 0.5%. To ensure the development of a two-dimensional boundary layer, the 0.5 m width of the test section was selected to be wider than the recommended threshold value given by [Nickels *et al.* \(2005\)](#). To maintain a ZPG flow along the whole test section, a maximum value of 3×10^{-8} acceleration parameter $K = (\nu/U_\infty^2)(dU_\infty/dx)$ is generated by the adjustable sidewalls installed in the test section. To ensure a turbulent boundary layer, the flow was tripped upstream with a 3 mm diameter threaded rod and a 100 mm rough sandpaper strip. A simple illustration of the wind tunnel is shown in Figure 7.1.

7.4.2 3D Sinusoidal roughness and roughness parameters

The rough surfaces utilized in this study were computer-numerically controlled (CNC) machined acrylic sheets of 6 mm thickness. The roughness profiles were generated using 3D sinewave functions with a maximum height from the lowest valley to the highest peak of $k = 2.4$ mm and similar wavelengths in the streamwise and spanwise directions of approximately six times the maximum height ($s_x = s_z \approx 6k$). The fabrication of these surfaces was carried out using a Multicam M1212 Router machine with a 0.4 mm stepover and a 12 mm ball nose cutter. The roughness profiles were defined as follows:

$$Y(x, z) = \begin{cases} a \frac{k}{2} \sin\left(\frac{2\pi x}{s_x}\right) \sin\left(\frac{2\pi z}{s_z}\right) & Y(x, z) > 0.00, \\ b \frac{k}{2} \sin\left(\frac{2\pi x}{s_x}\right) \sin\left(\frac{2\pi z}{s_z}\right) & Y(x, z) < 0.00, \end{cases} \quad (7.2)$$

where a and b are constants and varied to get different roughness skewness values. For example, $a = b = 1$ represents a surface with zero roughness skewness characterised by equal areas of peaks and valleys around the mean line, while $a = 5/3$ and $b = 1$ represent *S24-06-06P48* surface. The surfaces are defined by the first letter of the shape name: *S* for a sinewave, followed by $10k$, then the streamwise and spanwise spacing to height ratios between two consecutive roughness peaks, respectively, and finally, $k_{sk} \times 100$ (if $k_{sk} \neq 0$), *P* and *N* represent positive and negative, respectively. For instance, *S24-06-06P48* represents a 3D sinusoidal surface with 2.4 mm roughness height from peak to valley, with a streamwise and spanwise spacing to height ratio of 6 and a positive roughness skewness value of 0.48. The sinewave surface and the tripping strip of sandpaper were fixed onto a 2.4 m long aluminium sheet. A schematic representation of the various 3D roughness profiles utilized in the experiments is provided in Figure 7.2. The surface plots were generated with consistent axis and contour limits to facilitate easy comparison.

ASME (2009) defined the average roughness height k_a , and the root-mean-square height k_q , respectively on a sampling area A_s as:

$$k_a = \frac{1}{A_s} \int \int_{A_s} |Y(x, z)| dx dz, \quad (7.3)$$

$$k_q = \sqrt{\frac{1}{A_s} \int \int_{A_s} Y(x, z)^2 dx dz}. \quad (7.4)$$

The roughness skewness k_{sk} as defined in Aver'Yanova *et al.* (2017) is the asymmetry of the height distribution. This roughness parameter is crucial, as it indicates the morphology of the surface texture (see Flack *et al.* 2016). Positive roughness skewness values indicate that the height distribution is skewed above the mean plane, while negative roughness skewness values are skewed below the mean plane. Zero roughness skewness values occur when peaks and valleys are symmetrical around the mean plane. Contrary to k_a and k_q , k_{sk} does not provide any information about the roughness height of the surface and is defined on a sampling area A_s as:

$$k_{sk} = \frac{1}{k_q^3 A_s} \int \int_{A_s} Y(x, z)^3 dx dz. \quad (7.5)$$

The roughness kurtosis k_{ku} refers to how sharp is the roughness height distribution. $k_{ku} = 3$ is the normal distribution. $k_{ku} > 3$ indicates the presence of spikes (high peaks/ deep

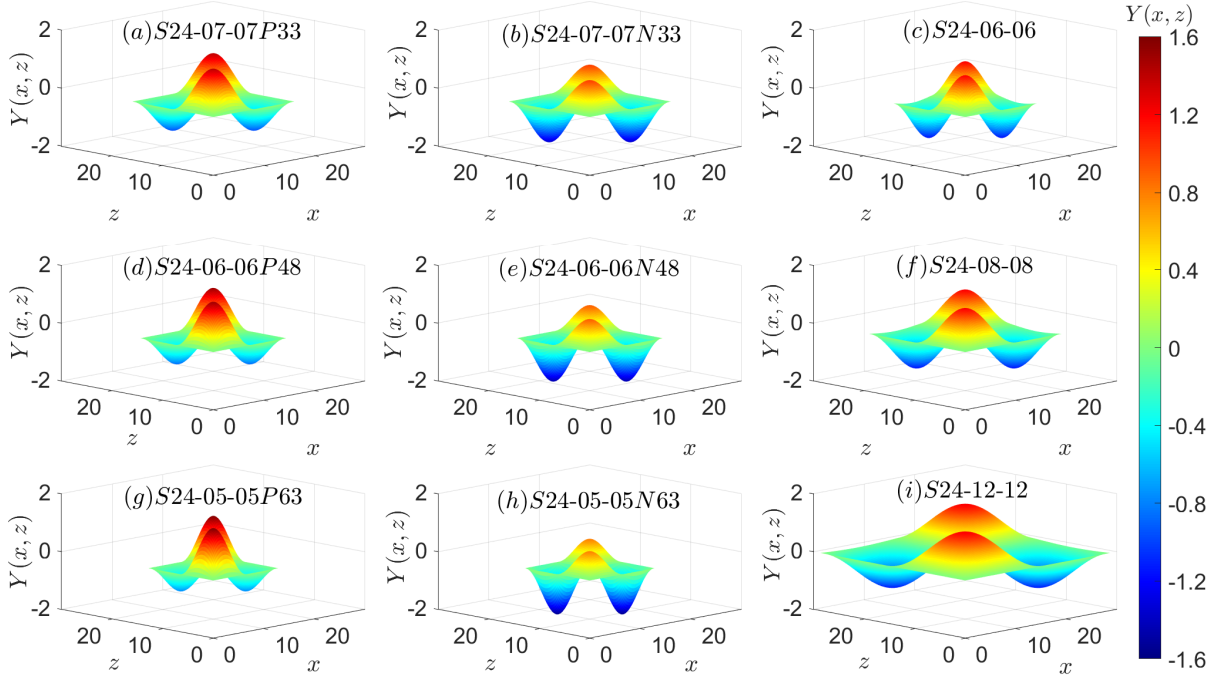


FIGURE 7.2: A schematic of different 3D sinewave rough surfaces. Plots on the left column are Positive roughness skewness, while plots on the middle column are negative roughness skewness, and the zero roughness skewness are plotted on the right column. Units of x , z and Y are in mm.

valleys), while $k_{ku} < 3$ indicates gradually varying rough surfaces. k_{ku} defined in [Aver'Yanova et al. \(2017\)](#) on the sampling area as:

$$k_{ku} = \frac{1}{k_q^4 A_s} \iint_{A_s} Y(x, z)^4 dx dz, \quad (7.6)$$

[Napoli et al. \(2008\)](#) defined the effective slope parameter, which is the mean absolute roughness gradient on a sampling area A_s as:

$$ES = \frac{1}{A_s} \iint_{A_s} \left| \frac{dY(x, z)}{dx} \right| dx dz, \quad (7.7)$$

and the increasing ES value indicates a denser rough surface. $ES \approx 0.35$, is a critical value that separate the waviness regime ($ES < 0.35$) and roughness regime ($ES > 0.35$). Different statistical parameters used to characterise different rough surfaces are detailed in [Table 7.1](#).

7.4.3 Hotwire and measurements apparatus

A minimum length-to-diameter ratio of 200 for the hotwire is required to minimize the end-conduction effects of a hotwire probe. The viscous-scaled wire length l^+ should be 20 or less to minimize the spatial attenuation of the hotwire probe, as recommended in ([Ligrani & Bradshaw 1987](#); [Hutchins et al. 2009](#)). Hence, a 1.5 mm Wollaston wire with a pure Platinum core is soldered on the prongs of a single hotwire probe, and then a length of $l = 0.5$ mm is itched to expose a 2.5 μm diameter Platinum wire for our measurements. An in-house constant temperature anemometer is connected to the probe, and an overheat ratio of 1.8 is applied. [Ardekani & Farhani \(2009\)](#) investigated the effect of changing the overheat ratio experimentally

TABLE 7.1: Statistical parameters of roughness topography for each surface. The surfaces are defined by the first letter of the geometry: S for a sinewave, followed by ten times the maximum peak-to-valley height k , then the streamwise spacing to height ratio and the spanwise spacing to height ratio for 3D roughness and followed by the roughness skewness value if it is not equal zero (P for positive and N for negative). For all the 3D sinewave surfaces, $k_t = k_p - k_v = 2.4$ mm, where k_p is the maximum peak height and k_v is the minimum valley height, and $k_a = 0.47$ mm and $k_q = 0.60$ mm.

Surface	Symbol	k_p (mm)	k_v (mm)	k_{sk}	k_{ku}	ES
$S24-07-07P33$	\triangle	1.4	-1.0	0.33	2.36	0.18
$S24-07-07N33$	∇	1.0	-1.4	-0.33	2.36	0.18
$S24-06-06P48$	\triangle	1.5	-0.9	0.48	2.43	0.20
$S24-06-06N48$	∇	0.9	-1.5	-0.48	2.43	0.20
$S24-05-05P63$	\triangle	1.6	-0.8	0.63	2.53	0.22
$S24-05-05N63$	∇	0.8	-1.6	-0.63	2.53	0.22
$S24-06-06$	\blacklozenge	1.2	-1.2	0.00	2.30	0.20
$S24-08-08$	\bullet	1.2	-1.2	0.00	2.30	0.15
$S24-12-12$	\blacksquare	1.2	-1.2	0.00	2.30	0.10

on the response of hotwire anemometers. They showed that the error in the constant temperature anemometer response decreased with an increasing overheat ratio. A T-type thermocouple is used to record the mean temperature during the experiments, and the temperature variation was less than $\pm 0.5^\circ\text{C}$ during each measurement. The hotwire probe was statically calibrated before and after each experiment using a Pitot-static tube located in the freestream, and measurements were repeated if the pre- and post-calibrations did not match within an error of 1%. A polynomial of order six-degree is used to map the hotwire output voltage and the actual velocity measured with the Pitot-static tube. The hotwire probe is attached to a 2-D traverse capable of moving $50\ \mu\text{m}$ and $5\ \mu\text{m}$ in the z and y axis, respectively, with closed feedback from two linear glass encoders with $10\ \mu\text{m}$ and $1\ \mu\text{m}$ resolution in the z and y axis, respectively, to minimize the movement error of the 2-D traverse. A simple schematic of the tripping devices and the rough surface inserted in the test section is shown in Figure 7.3.

The assessment reveals that calculating C_f is subject to a range of sources of error. The errors resulting from the hotwire calibration process are due to a variety of factors, including hotwire attachment, anemometer adjustment, isothermal flow conditions, velocity measurement with a pitot-static tube, calibration data reduction process, and the resulting errors from a six-order polynomial fit. Other sources of error include those due to data acquisition, data filtering, and cut-off frequencies. Furthermore, uncertainties arise due to the movement of the traverse in a wall-normal direction and accurately determining the first measurement point offset from the wall, as well as calculating the friction velocity and zero point in the wall-normal direction for rough surfaces. Collectively, these sources of error contribute to an estimated 10% uncertainty in determining C_f .

7.4.4 Experiments

In this experiment, a smooth wall turbulence boundary layer (TBL) measurement was performed at three different freestream velocities U_∞ : 10, 15, and 20 m/s. The measurement was taken at a streamwise location approximately 1.8 meters downstream from the tripping sandpaper.

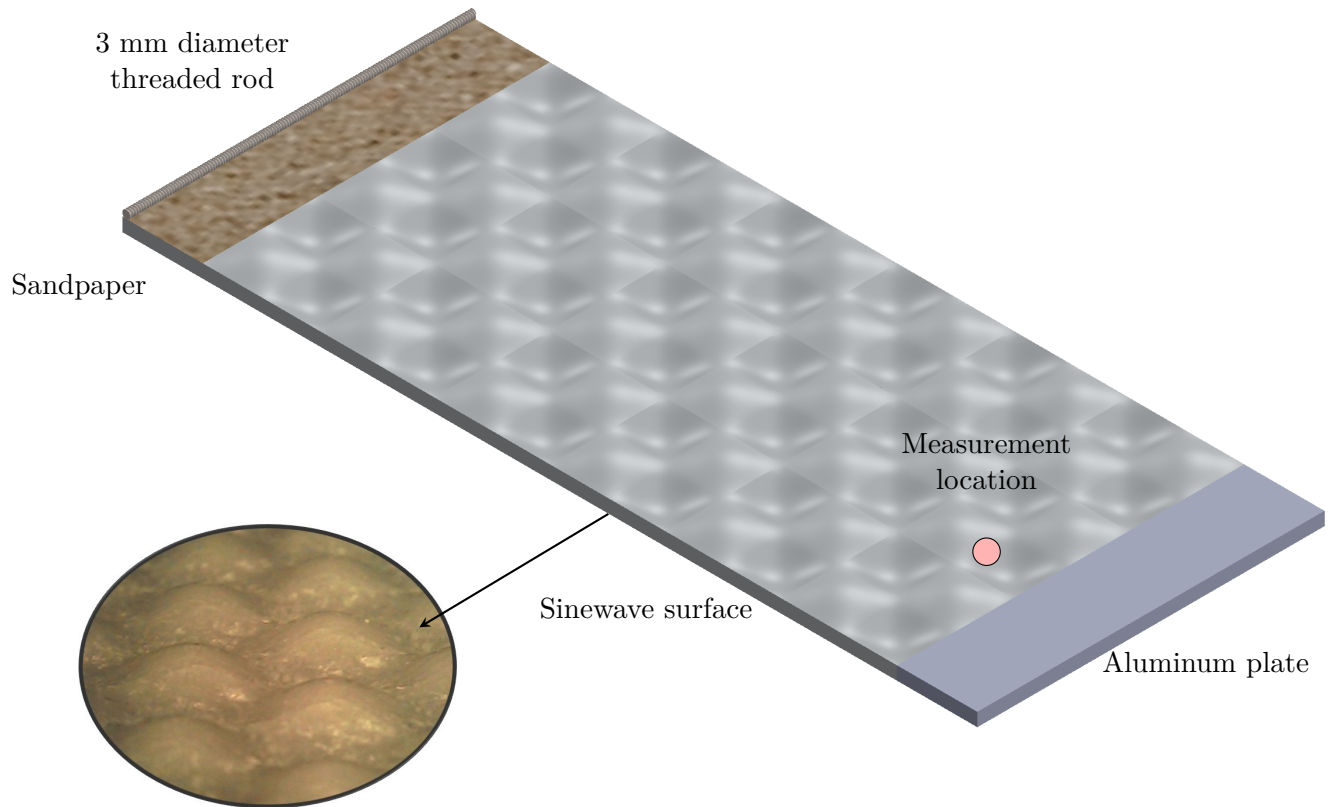


FIGURE 7.3: A simple schematic of the tripping devices and the rough surface inserted in the test section. This schematic is not to scale. The insert figure is a local view of the sinewave roughness taken by a high-magnification microscope

Nine different 3D sinusoidal surfaces were tested in the experiment, and measurements were recorded at the same three freestream velocities for each surface. The experiment aimed to compare the TBL flows over surfaces with positive roughness skewness values (0.33, 0.48, and 0.63) with those over surfaces with negative roughness skewness values of the same magnitude. Additionally, the effect of roughness skewness on TBL flows was also studied by testing surfaces with zero roughness skewness values.

In this study, a high-speed data acquisition system was utilized to obtain measurements at a sampling rate of 51.2 kHz for a duration of 120 s per measurement point. It is necessary to select a cutoff frequency that is lower than the Nyquist frequency to prevent aliasing distortions from manifesting in the collected signal. To this end, the hotwire cutoff frequency was adjusted to 22 kHz through a dynamic calibration procedure utilising a square wave test. Subsequently, a -3 dB drop-off was detected at a frequency of approximately 20 kHz. The streamwise velocity fluctuations were sampled at 48 logarithmically spaced points along the y axis at three different spanwise locations (over the 3D sinewave peak, valley, and mid-plane). The spanwise-averaged values were obtained and are presented in Table 7.2.

TABLE 7.2: Details of the experimental data sets. H is the shape factor.

Surface	Symbol	U_∞ (m/s)	δ (m)	Re_τ	l^+	H	C_f	k_s^+	ΔU^+
Smooth	×	10	0.042	1120	13	1.37	0.0031	-	-
	×	15	0.046	1740	19	1.35	0.0028	-	-
	×	20	0.045	2190	24	1.33	0.0026	-	-
S24-07-07P33	△	10	0.053	1840	18	1.54	0.0052	062	6.8
	△	15	0.053	2720	26	1.55	0.0051	090	7.7
	△	20	0.056	3650	32	1.57	0.0050	125	8.6
S24-07-07N33	▽	10	0.050	1650	18	1.51	0.0047	036	5.5
	▽	15	0.050	2380	26	1.49	0.0046	046	6.1
	▽	20	0.054	3360	32	1.53	0.0045	067	7.0
S24-06-06P48	△	10	0.054	1890	18	1.57	0.0054	075	7.3
	△	15	0.054	2810	26	1.58	0.0054	116	8.4
	△	20	0.055	3710	32	1.59	0.0052	147	9.0
S24-06-06N48	▽	10	0.049	1590	18	1.50	0.0046	032	5.1
	▽	15	0.049	2300	26	1.47	0.0045	042	5.8
	▽	20	0.051	3180	32	1.52	0.0044	061	6.8
S24-05-05P63	△	10	0.055	1910	18	1.59	0.0056	084	7.6
	△	15	0.055	2870	26	1.60	0.0055	135	8.8
	△	20	0.057	3880	32	1.61	0.0054	185	9.6
S24-05-05N63	▽	10	0.048	1500	18	1.49	0.0045	024	4.5
	▽	15	0.049	2290	26	1.46	0.0044	040	5.7
	▽	20	0.052	3200	32	1.52	0.0043	058	6.7
S24-06-06	◆	10	0.047	1640	16	1.53	0.0050	047	6.1
	◆	15	0.048	2390	25	1.52	0.0050	073	7.2
	◆	20	0.048	3180	31	1.54	0.0050	103	8.1
S24-08-08	●	10	0.046	1510	18	1.58	0.0048	037	5.5
	●	15	0.046	2270	26	1.53	0.0047	053	6.4
	●	20	0.048	3030	32	1.59	0.0046	073	7.2
S24-12-12	■	10	0.043	1350	18	1.52	0.0042	018	3.8
	■	15	0.044	1970	26	1.54	0.0041	029	4.9
	■	20	0.044	2750	32	1.57	0.0040	035	5.4

7.5 RESULTS AND DISCUSSION

7.5.1 Friction Velocity

TBL measurements are challenging, especially when it comes to friction velocity calculations. Clauser (1956) forces the log region of the mean streamwise velocity profile to adhere to a predefined logarithmic law as,

$$U^+ = \frac{1}{\kappa} \ln y^+ + B. \quad (7.8)$$

Prerequisite knowledge of the log region boundaries, if one exists, and κ and B values limit this method and increase its uncertainty. Coles (1956) adds an additional wake function to cover the defect layer, not only the logarithmic region, as follows:

$$U^+ = \frac{1}{\kappa} \ln y^+ + B + \frac{\Pi}{\kappa} \omega\left(\frac{y}{\delta}\right), \quad (7.9)$$

where Π is a profile parameter that depends on the pressure gradient and ω is the wake function. More recently, Chauhan *et al.* (2009) suggested a complete mean streamwise velocity profile called a composite profile that forces not only the log region but the whole velocity profile from the inner to the outer layer to adhere to the predefined composite profile as follows:

$$U^+ = U_{inner}^+ + \frac{2\Pi}{\kappa} \omega\left(\frac{y}{\delta}\right), \quad (7.10)$$

where U_{inner}^+ is a long function of y^+ (see Chauhan *et al.* (2009) for more details).

For rough surface TBLs, the friction velocity calculations are more challenging as two more parameters are introduced; ϵ the origin offset and ΔU^+ . The law of the wall becomes as follows:

$$U^+ = \frac{1}{\kappa} \ln \frac{(z + \epsilon)U_\tau}{\nu} + B - \Delta U^+. \quad (7.11)$$

Perry & Li (1990) introduced the modified Clauser method used for rough surface TBLs. However, fitting three different parameters U_τ , ϵ and ΔU^+ to a predefined logarithmic region give an infinite number of solutions that can be fitted with a minimal error; thus, increasing the uncertainty of the estimation of those three parameters. Djenidi *et al.* (2019) recently, proposed a new method for estimating U_τ that is valid for both smooth and rough wall TBLs. This method utilizes the outer layer similarity over the smooth and rough flow by collapsing the velocity profiles in defect form. An advantage of this new method is that it eliminates the uncertainties of determining κ and the log region boundaries. In this method, one uses a trial and error to adjust U_τ until the experimental data match a universal velocity defect profile expressed as:

$$f(x) = \frac{p_1 x^5 + p_2 x^4 + p_3 x^3 + p_4 x^2 + p_5 x + p_6}{x^5 + q_1 x^4 + q_2 x^3 + q_3 x^2 + q_4 x + q_5}, \quad (7.12)$$

where the coefficients are: $p_1 = 110.50$, $p_2 = -230.50$, $p_3 = 114.50$, $p_4 = 7.24$, $p_5 = -0.00638$, $p_6 = -0.0000460$; $q_1 = -10.07$, $q_2 = 15.56$, $q_3 = 0.4466$, $q_4 = -0.000820$ and $q_5 = -0.000001789$.

In the present study, both the modified Clauser chart method by Perry & Li (1990), and the velocity defect chart of Djenidi *et al.* (2019) methods are used to calculate U_τ . For the modified Clauser chart method, we used the $\kappa = 0.41$ and $B = 5$. We followed Marusic *et al.* (2013) recommendations for the boundaries of the log region to be $(3\sqrt{Re_\tau}) \leq y^+ \leq (y/\delta = 0.15)$.

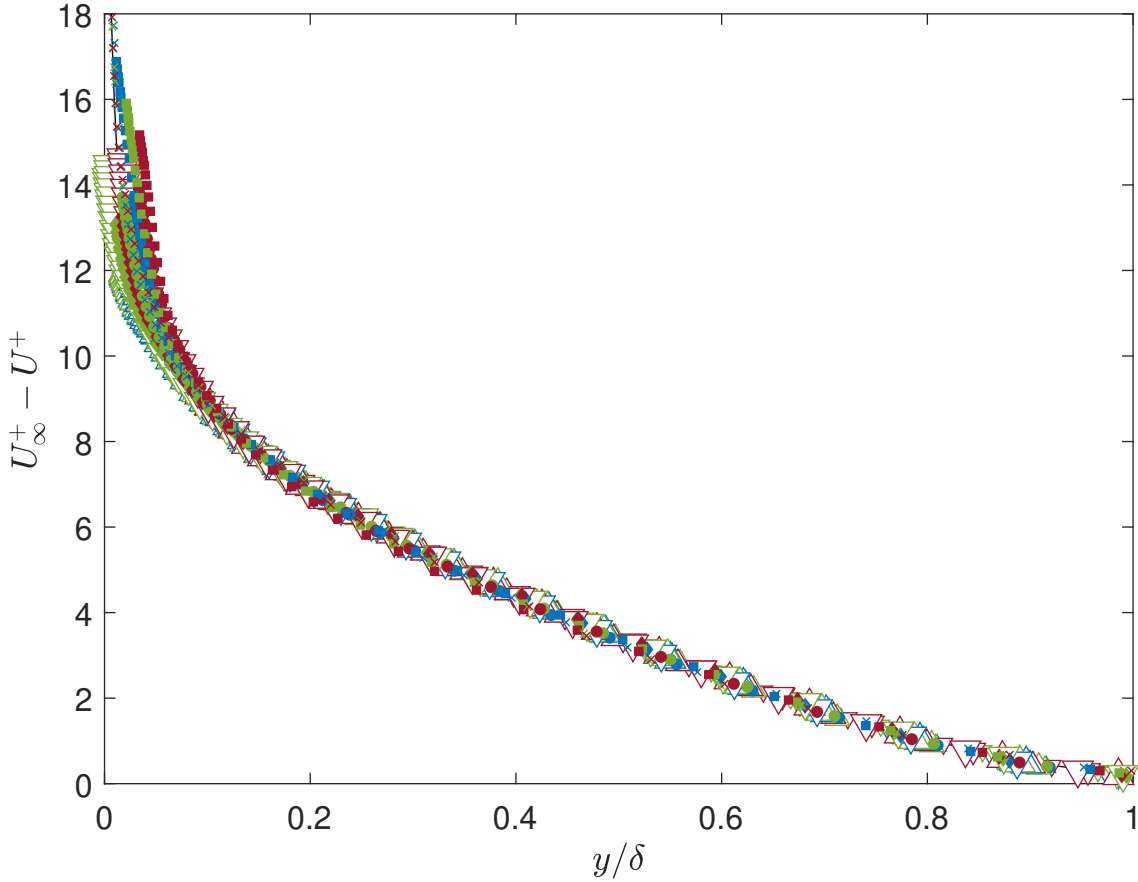


FIGURE 7.4: Streamwise mean velocity deficit profiles over smooth and rough wall surfaces for all the profiles at different Re_τ . The symbols of our measurements are detailed in Table 7.2. Solid black line: DNS smooth TBL data from Chan *et al.* (2021).

For the velocity defect chart method by Djenidi *et al.* (2019), we calculate the U_τ by fitting the velocity defect profile to the universal profile equation 7.12 from $0.1 \leq y/\delta \leq 1$ with the least square error technique. We fix $\epsilon = k/2$ in this method. Since the U_τ values obtained from both methods (the modified Clauser and the velocity defect) show good agreement, with less than 2 % difference in all our measurements, U_τ from the velocity defect chart is used in the subsequent tables and figures presented here. Refer to Abdelaziz *et al.* (2022a) for further details. Figure 7.4 shows the collapse of the deficit velocity profiles for all the surfaces in Table 7.2.

7.5.2 Mean velocity profile

By referring to Table 7.1, the effect of the roughness skewness parameter on turbulence statistics can be isolated as the surfaces S24-06-06P48, S24-06-06N48 and S24-06-06 share similar roughness parameters except for the skewness value. The positive roughness skewness value of S24-06-06P48 is 0.48, whereas S24-06-06N48 has a negative roughness skewness of the same value of 0.48, and S24-06-06 has a zero roughness skewness value. Figure 7.5 demonstrates that all rough wall surfaces exhibit higher drag compared to a smooth wall, which is reflected in the downward shift of the mean streamwise velocity profiles over the three-dimensional sinusoidal roughnesses in comparison with a smooth wall.

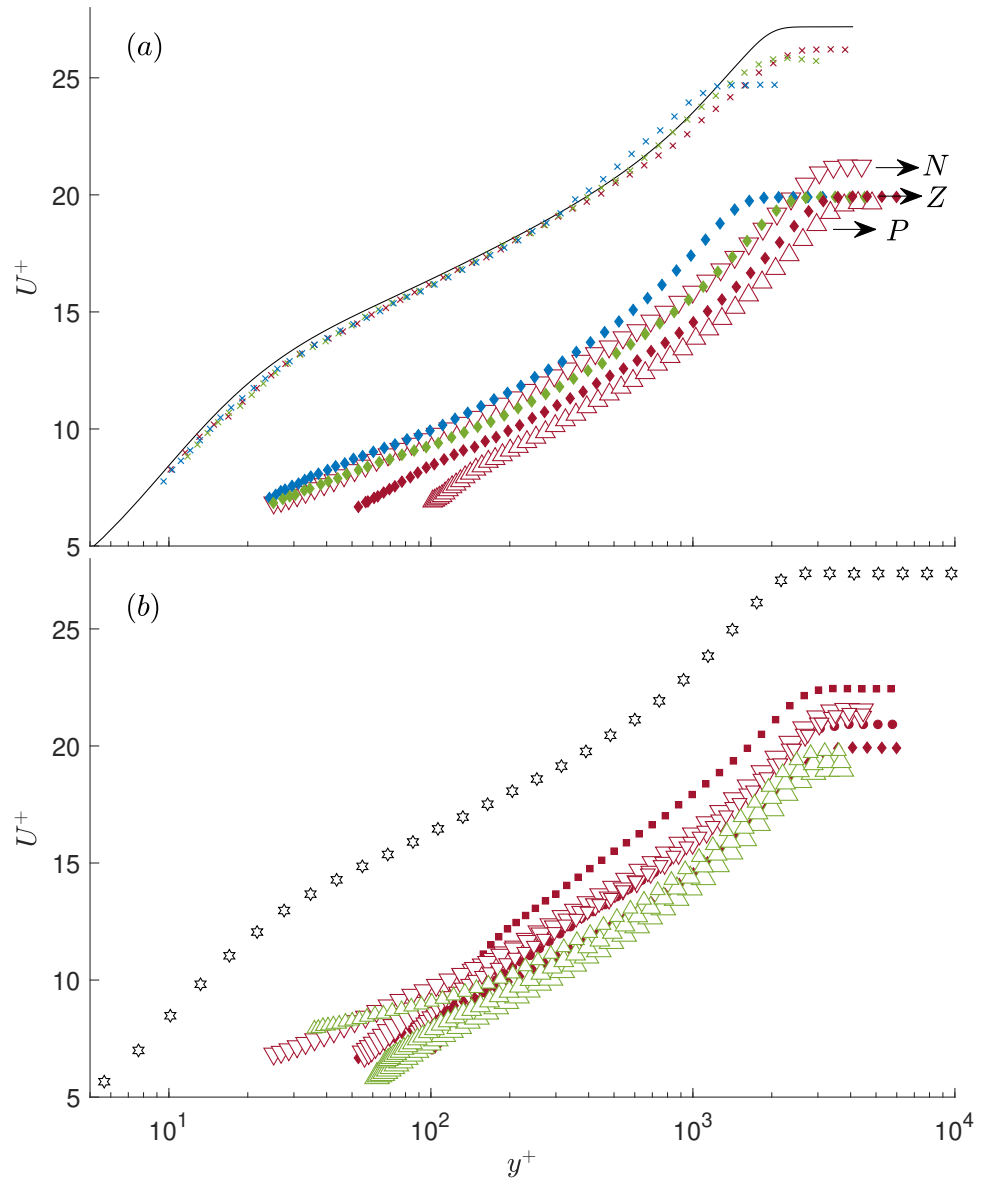


FIGURE 7.5: (a) Mean streamwise velocity profiles over our smooth wall data and 3D sinewave surfaces with constant $ES = 0.2$. The profiles over smooth and $S24-06-06$ surfaces at three different freestream velocities U_∞ are shown with the same symbols and different colours. Solid black line: DNS smooth TBL data from Chan *et al.* (2021) at $Re_\tau \approx 2000$. (b) Comparison with velocity profiles over a smooth wall data of Marusic *et al.* (2015), (the black hexagram) at matched $Re_\tau = 3000 \pm 300$. The symbols of our measurements are detailed in Table 7.2. N for negative k_{sk} , Z for zero k_{sk} and P for positive k_{sk} . The blue symbols are at $U_\infty = 10$ m/s. The green symbols are at $U_\infty = 15$ m/s. The red symbols are at $U_\infty = 20$ m/s.

Figure 7.5(a) illustrates the U^+ profiles over the three rough surfaces and compares them with the smooth wall TBL in Chan *et al.* (2021). The profiles over $S24-06-06P48$ and $S24-06-06N48$ are only displayed at the highest Re_τ values. Increasing Reynolds number, by raising the freestream velocity U_∞ , reduces the skin friction coefficient and extends the log region in the smooth wall TBL. However, for a given 3D sinusoidal surface, C_f is almost constant with increasing Reynolds number, and the profiles are shifted to the right to a larger y^+ . This indicates that a fully rough regime has been achieved, and the drag is predominantly caused by pressure drag. Figure 7.5(a) shows the profiles over $S24-06-06$ at three different Reynolds numbers for clarity of the figure, as the other profiles follow the same trend. The profiles of $S24-06-06P48$, $S24-06-06$ and $S24-06-06N48$ are compared, depicted as red symbols in Figure 7.5(a), to investigate the effect of the roughness skewness on the roughness function ΔU^+ . C_f and ΔU^+ increase when roughness skewness increases from negative to positive values. $S24-06-06P48$, with a positive roughness skewness value, has the largest ΔU^+ . ΔU^+ decreases slightly in $S24-06-06$, which has a zero roughness skewness value, and decreases further in $S24-06-06N48$, which has a negative roughness skewness value. The increase is more pronounced when moving from a negative to zero roughness skewness value than from zero to a positive one. ΔU^+ increases by 20% from $S24-06-06N48$ to $S24-06-06$, whereas the increase is only 10% from $S24-06-06$ to $S24-06-06P48$.

Figure 7.5(b) displays U^+ profiles over all the rough surfaces at matched Reynolds number $Re_\tau = 3000 \pm 300$. The profiles are compared with a smooth wall of Marusic *et al.* (2015). Due to wind tunnel constraints, the same Reynolds number could not be achieved in our smooth wall measurements. Figure 7.5(b) highlights the significant influence of ES on ΔU^+ reflected in the downward shift of the profiles when ES increases from 0.1 in $S24-12-12$ to 0.2 in $S24-06-06$ (filled symbols). The figure also demonstrates the effect of roughness skewness on ΔU^+ when the roughness skewness is the dominant roughness parameter and the changes in other parameters are neglected. Increasing k_{sk} from negative to positive values increases the downward shift of the velocity profiles. The lowest k_{sk} value of the surface $S24-05-05N63$, plotted in large red inverted triangles, has the minimum ΔU^+ of 6.7. However, the highest k_{sk} value of the surface $S24-05-05P63$, plotted in large green triangles, has the maximum ΔU^+ of 8.8.

The relationship between the shape factor H and C_f as a function of k_{sk} is plotted in Figures 7.6(a) and 7.6(b), respectively, in order to investigate the effect of k_{sk} on H and C_f . All of the 3D sinusoidal surfaces listed in Table 7.2 are plotted except for $S24-12-12$, which has a significantly lower ES compared to the other surfaces. The ES of all other surfaces is approximately 0.18 ± 0.4 .

As demonstrated in Figure 7.6(a), increasing k_{sk} from negative to positive values leads to an increase in H . It is noted that for negative and zero roughness skewness, H is higher at the lowest Re_τ value compared to moderate Re_τ for the same surface (the green symbols are higher than the blue symbols). This could indicate that the flow regime is still in a transitional stage for the lowest and middle Re_τ values for negative and zero roughness skewness. However, for positive roughness skewness, the fully rough regime is achieved at lower Re_τ values and H increases with increasing Re_τ for the same surface.

It is also found that in the fully rough regime and with a constant ES , the percent change of H from negative roughness skewness to zero roughness skewness is relatively small, around 1.5%. This value doubles from the zero roughness skewness value to the positive roughness skewness value, with an increase of around 3%.

The results in Figure 7.6(b) demonstrate that the increase in k_{sk} from negative to positive values leads to an increase in the value of C_f . For a constant roughness surface, an increase in

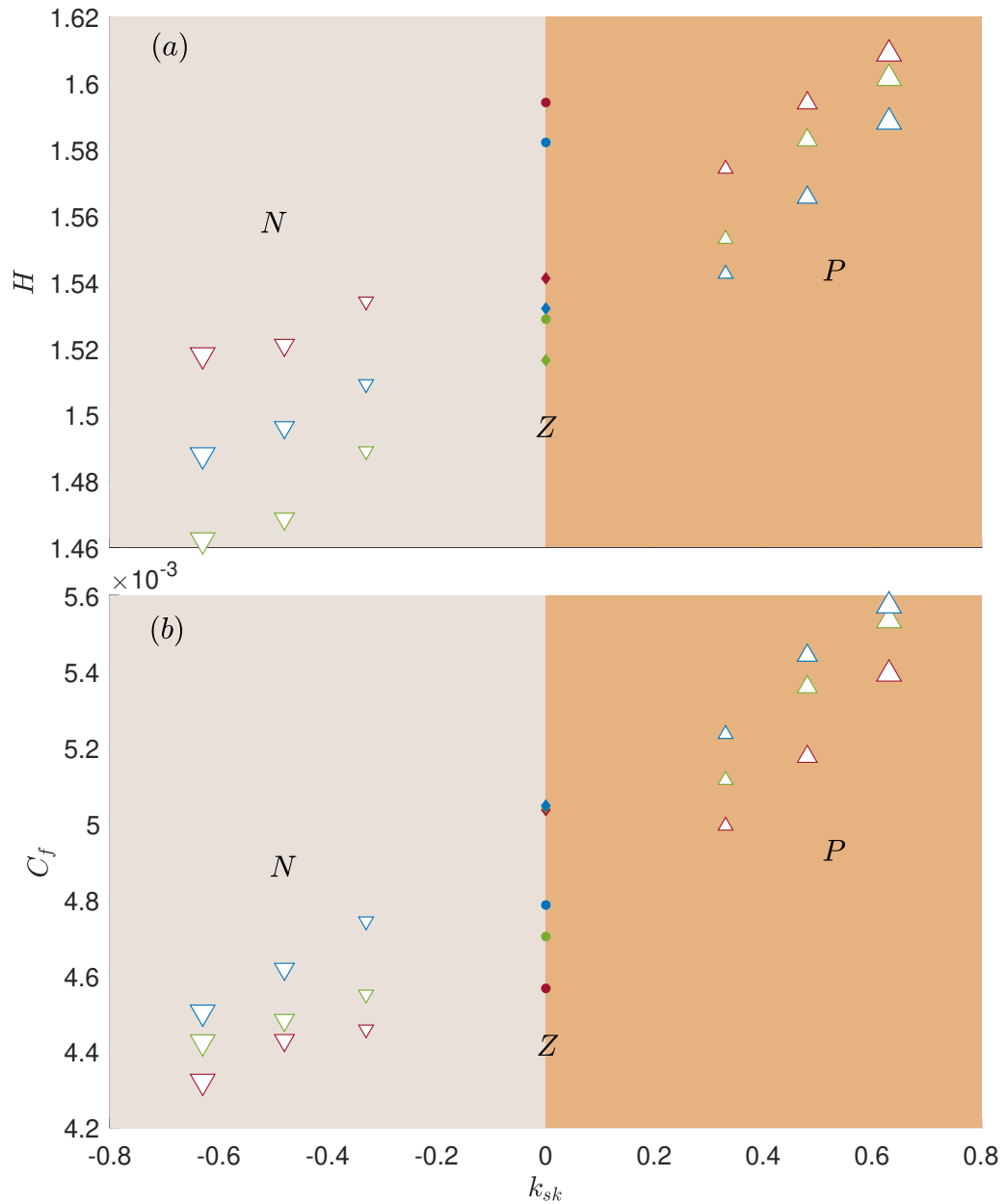


FIGURE 7.6: (a) The relation between H and k_{sk} for the different 3D sinewave surfaces that have $ES \approx 0.18 \pm 0.4$ at the three different Re_τ values. (b) The relation between C_f and k_{sk} for the different 3D sinewave surfaces with $ES \approx 0.18 \pm 0.4$ at the three different Re_τ values. The symbols of the rough surface are indicated in Table 7.2. N for negative k_{sk} , Z for zero k_{sk} and P for positive k_{sk} . the left area is for negative roughness skewness, while the right one is for positive roughness skewness values. The blue symbols are at $U_\infty = 10$ m/s. The green symbols are at $U_\infty = 15$ m/s. The red symbols are at $U_\infty = 20$ m/s.

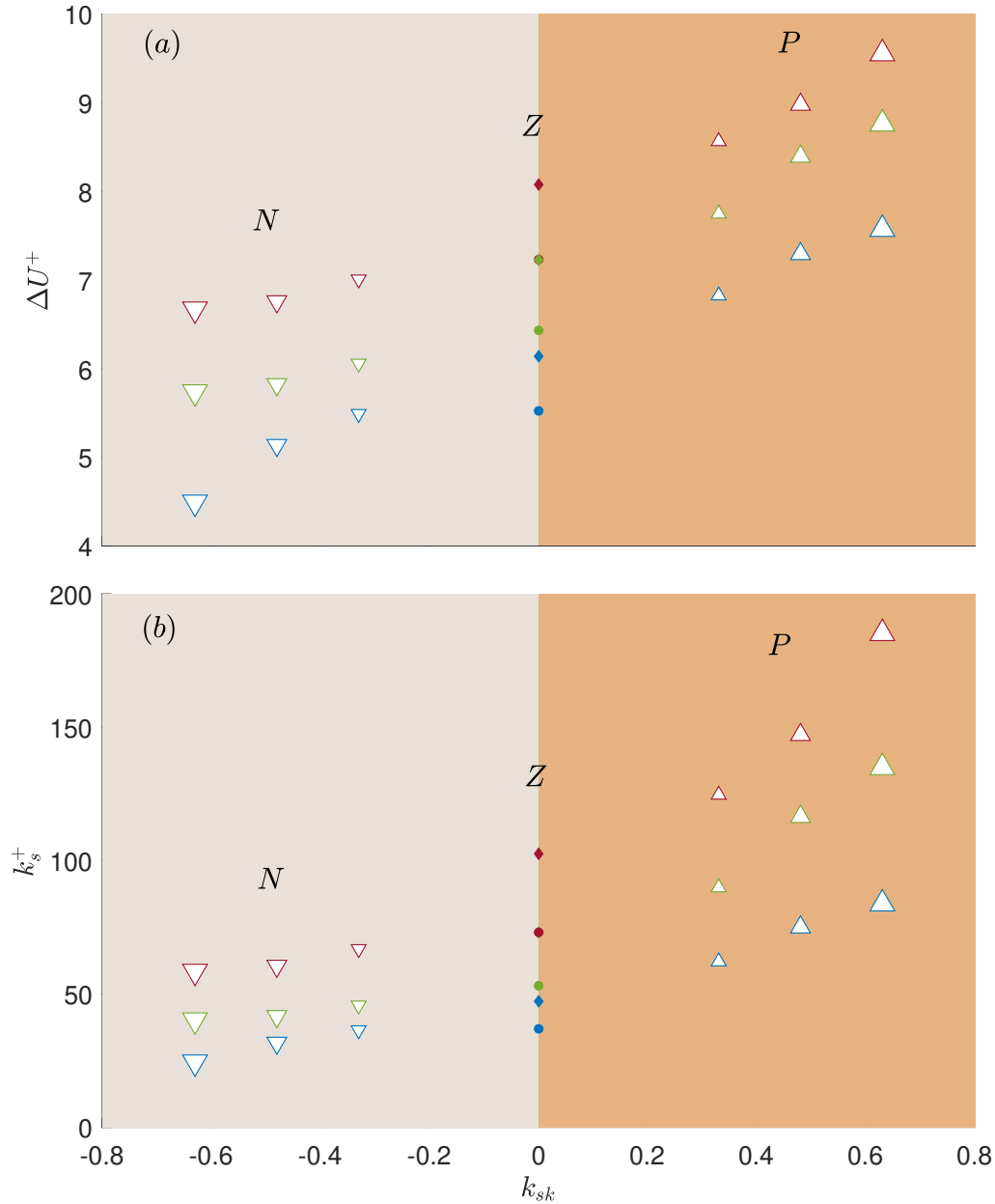


FIGURE 7.7: (a) The relation between ΔU^+ and k_{sk} for the different 3D sinewave surfaces that have $ES \approx 0.18 \pm 0.4$ at the three different Re_τ values. (b) The relation between k_s^+ and k_{sk} for the different 3D sinewave surfaces with $ES \approx 0.18 \pm 0.4$ at the three different Re_τ values. The symbols of the rough surface are indicated in Table 7.2. N for negative k_{sk} , Z for zero k_{sk} and P for positive k_{sk} . the left area for negative roughness skewness, while the right one is positive roughness skewness values. The blue symbols are at $U_\infty = 10$ m/s. The green symbols are at $U_\infty = 15$ m/s. The red symbols are at $U_\infty = 20$ m/s.

Re_τ slightly decreases C_f , regardless of the value of the roughness skewness. It is noted that in the fully rough regime and when ES is held constant, the percentage increase in C_f as k_{sk} transitions from negative to zero is more than three times the percentage increase in C_f as k_{sk} increases from zero to positive values.

The relationship between the roughness function ΔU^+ and the normalized equivalent sand grain roughness k_s^+ with respect to the roughness skewness k_{sk} are presented in Figures 7.7(a) and 7.7(b), respectively. The figures exclude the 3D sinusoidal surface $S24-12-12$, which has a significantly lower ES than the other surfaces. As shown in Figure 7.7(a), there is a

positive correlation between k_{sk} and ΔU^+ . Additionally, the figure reveals that increasing Re_τ leads to an increase in ΔU^+ for the same rough surface (represented by symbols of different colours). When k_{sk} increases from negative to zero values in the fully rough regime and with constant ES ($S24-06-06N48$, $S24-06-06$ and $S24-06-06P48$), ΔU^+ increases by 20%, whereas when k_{sk} increases from zero to positive values, ΔU^+ increases by only 10%.

The relationship between k_s^+ and k_{sk} is shown in Figure 7.7(b), which demonstrates a nearly exponential increase in k_s^+ as k_{sk} changes from negative to positive values. For a given surface, an increase in Re_τ leads to an increase in k_s^+ , and this increase becomes more pronounced as k_{sk} shifts from negative to positive values. An analysis of the fully rough regime with constant ES ($S24-06-06N48$, $S24-06-06$ and $S24-06-06N48$) shows that there was a 70% increase in k_s^+ when k_{sk} changed from negative to zero, compared to only a 40% increase when k_{sk} changed from zero to positive.

The observations from Figures 7.6 and 7.7 demonstrate an increase in C_f , ΔU^+ , and k_s as k_{sk} increases. Furthermore, the impact of k_{sk} increasing from negative to zero is greater than when k_{sk} increases from zero to positive. These findings align with previous experimental studies. For example, Flack *et al.* (2020b) found that an increase in drag is larger from negative to zero roughness skewness compared to from zero to positive roughness skewness. Additionally, these results are consistent with numerical studies such as Jelly & Busse (2018), which found that surfaces with more peaks than valleys (positive roughness skewness) produce more drag than negative ones.

The roughness skewness plays a crucial role in impacting turbulence statistics and drag reduction and should not be overlooked in any relationship linking k_s to real roughness parameters. In some cases where the roughness skewness is the dominant roughness parameter and changes in other roughness parameters are negligible, k_s can be directly correlated with k_{sk} . This relationship is demonstrated in Figure 7.8, which depicts that the exponential equation $k_s = a \times e^{b \times k_{sk}}$ with $a = 0.0015$ and $b = 0.8385$ accurately predicts k_s for this particular family of roughness with a statistical measure of goodness of fit, R^2 , of 0.97. However, this equation is suitable only for this family of roughness where k_{sk} is the only variable roughness parameter. Nevertheless, it provides a concept of the correlation between k_s and k_{sk} and what type of regression equation best describes this relationship.

7.5.3 Turbulence intensity profiles

Figure 7.9 shows the profiles of the root mean square (rms) of the mean streamwise velocity fluctuations, u' , over both smooth and rough surfaces. The profiles are normalized by the friction velocity U_τ , while the wall-normal distance y is normalized by the inner length scale ν/U_τ in panels (a) and (c) and by the outer length scale δ in panels (b) and (d). The profiles over surfaces $S24-06-06P48$, $S24-06-06N48$, and $S24-06-06$ are compared with those over a smooth wall in panels (a) and (b), similar to Figure 7.5. Additionally, the profiles over all the rough surfaces in Table 7.2 at a matched Reynolds number $Re_\tau \approx 3000 \pm 300$ are compared with the smooth wall data of Marusic *et al.* (2015) in panels (c) and (d).

In Figure 7.9(a), the small differences between our smooth wall data and DNS smooth wall data in the inner region are attributed to the length of our hotwire sensing element in wall units l^+ . The attenuation of the hotwire measurements is more pronounced in the near-wall region and decreases gradually as we move further from the wall until it is neglected from $y/\delta > 0.6$. This has been observed in a previous study by Chin *et al.* (2009) who investigated the effect of using different spatial resolutions of hotwire probes on TBL measurements.

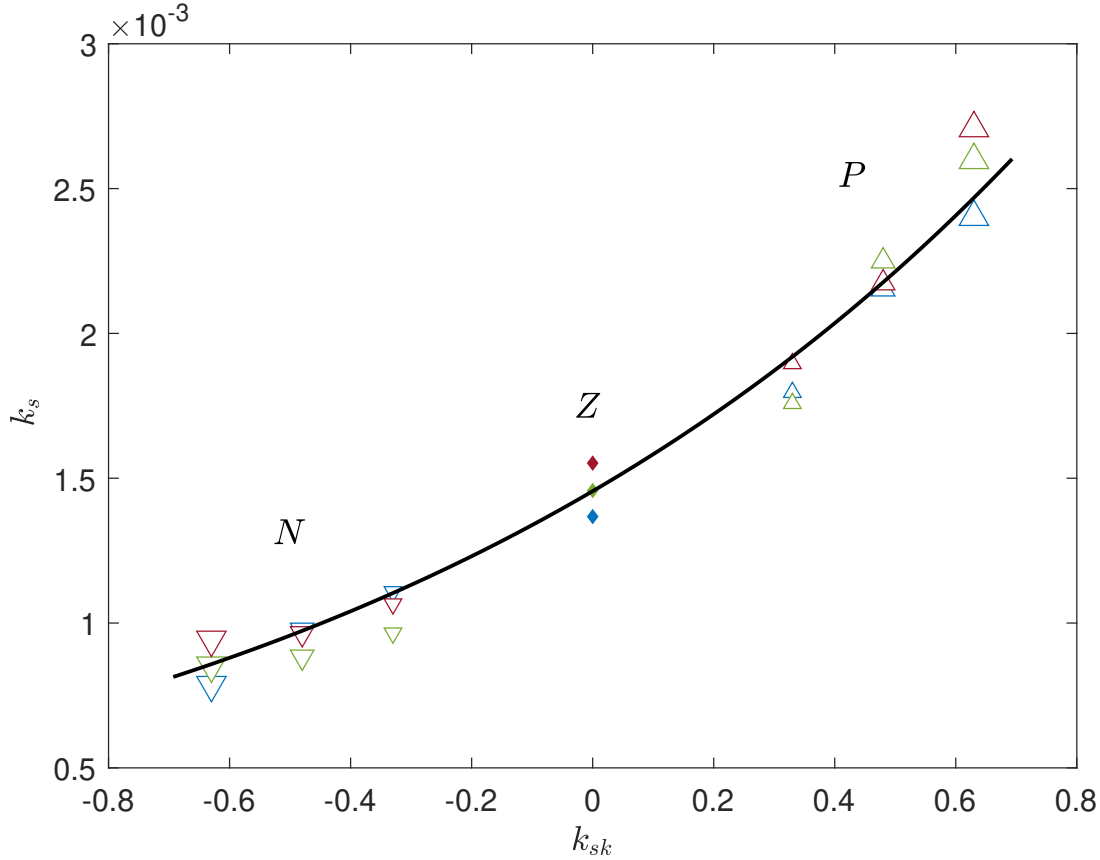


FIGURE 7.8: Equivelant sand grain roughness k_s as a function of roughness skewness k_{sk} for the different 3D sinewave surfaces that have $ES = 0.2 \pm 0.2$ at the three different Re_τ values. The solid black line represents the exponential fitting of the data. The symbols of the rough surface are indicated in Table 7.2. N for negative k_{sk} , Z for zero k_{sk} and P for positive k_{sk} . The blue symbols are at $U_\infty = 10$ m/s. The green symbols are at $U_\infty = 15$ m/s. The red symbols are at $U_\infty = 20$ m/s.

Increasing Re_τ for the same rough surface reduces the inner peak value of u'^+ and shifts the profiles to the right to larger y^+ , which is attributed to the transition from the transitionally rough to the fully rough regime. This reduction of the inner peak has been observed by [Ligrani & Moffat \(1986\)](#) when the flow is in a transitionally rough regime until it is fully removed in the fully rough regime.

For better comparison of the u' profiles for different rough surfaces, we plot the profiles over all the rough surfaces at matched $Re_\tau \approx 3000 \pm 300$ in Figures 7.9(c) and 7.9(d). These figures show that the zero roughness skewness has slightly lower turbulence intensities than positive and negative roughness skewness from the inner region up to $y/\delta < 0.6$. However, from Figures 7.9(b) and 7.9(d), it can be observed that these small differences can be neglected, and an outer layer similarity can still be valid for this family of roughness.

To investigate the impact of k_{sk} on turbulence intensities, we employed the diagnostic plot, introduced by [Alfredsson et al. \(2011\)](#), which plots u'/U against (U/U_∞) . This approach avoids the use of the friction velocity U_τ and the wall-normal position y and reduces measurement uncertainties. We plotted the diagnostic plot for smooth and rough wall surfaces, as shown in Figures 7.10(a) and 7.10(b). The same profiles used in Figures 7.9(a) and 7.9(b) are used here. The linear relationship $u'/U = 0.286 - 0.255 U/U_\infty$, which matches the smooth wall data for $U/U_\infty > 0.6$, was used as a reference. All the rough wall profiles were found to be higher than

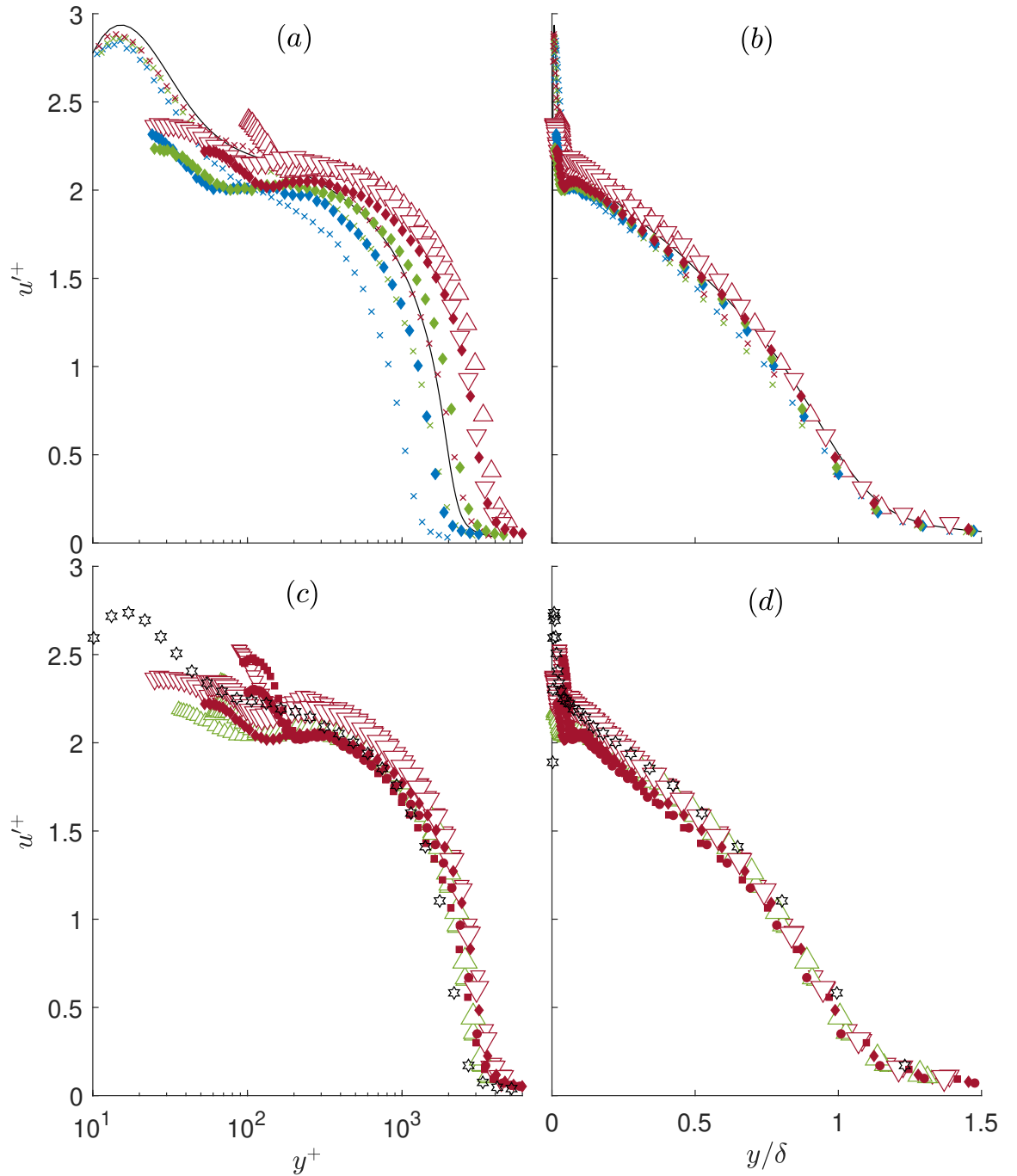


FIGURE 7.9: Mean streamwise turbulence intensity profiles over smooth and rough surfaces normalized by inner scaling in (a) and (c) and outer scaling in (b) and (d). The same surfaces used in Figure 7.5(a) are plotted in (a) and (b). The same surfaces used in Figure 7.5(b) are plotted in (c) and (d). The symbols of our measurements are detailed in Table 7.2. Solid black line in (a) and (b): DNS smooth TBL data from Chan *et al.* Chan *et al.* (2021) at $Re_\tau \approx 2000$. The smooth wall data of Marusic *et al.* Marusic *et al.* (2015) is plotted with a black hexagram in (c) and (d).

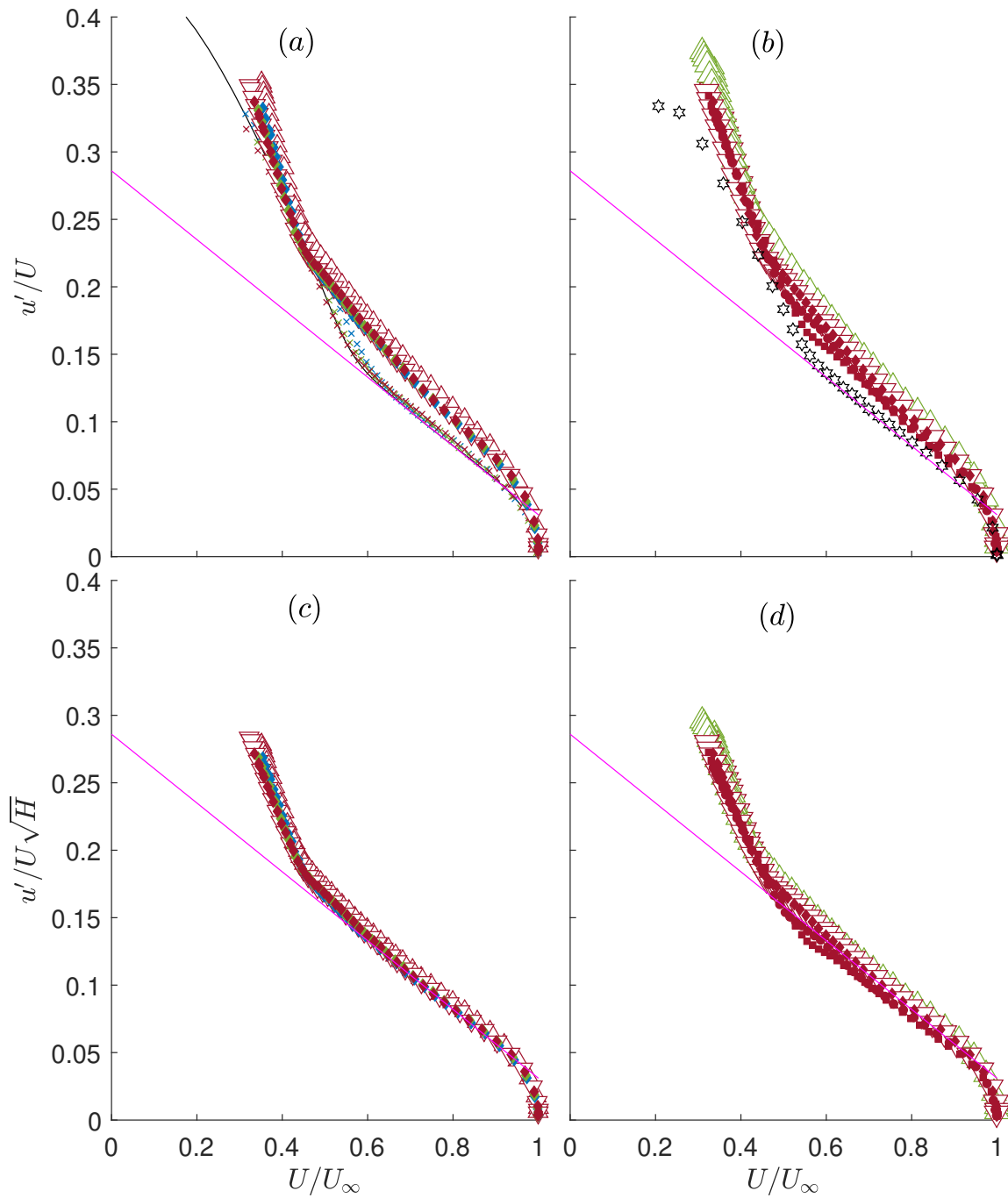


FIGURE 7.10: (a) and (b): u' is normalized by U and plotted against U normalized by U_∞ . (c) and (d): u' is normalized by $U\sqrt{H}$ and plotted against U normalized by U_∞ . The symbols of our measurements are detailed in Table 7.2. The smooth wall data of Marusic *et al.* (2015) is plotted with a black hexagram in (b). Solid black line in (a): DNS smooth TBL data from Chan *et al.* (2021) at $Re_\tau \approx 2000$. The solid straight magenta line corresponds to the linear relationship $u'/U = 0.286 - 0.255 U/U_\infty$ (Alfredsson *et al.* 2012).

the smooth wall profiles. [Djenidi *et al.* \(2018\)](#) also noticed differences among smooth, 2-D bars and sand-grain roughness in the outer region of TBL when the diagnostic plots were used.

Our results revealed that rough surfaces with zero roughness skewness have the lowest u'/U , while those with positive roughness skewness have the highest u'/U . To improve the collapse of smooth and rough wall data in the diagnostic plot, we employed the shape factor, H , which was shown by [Abdelaziz *et al.* \(2022b\)](#) to better collapse the data. In [Figures 7.10\(c\)](#) and [7.10\(d\)](#), we used the parameter $1/\sqrt{H}$ to “weight” the u'/U profiles, resulting in a much better collapse. Although the physical explanation of why \sqrt{H} enhances the collapse of different surfaces is yet to be determined and requires further investigation, this approach can be used to present u' conveniently for different rough surfaces.

7.5.4 Velocity skewness and kurtosis factor

Knowledge of the skewness distribution S_u is important as it directly influences the generation of turbulent quadrant events. The sweep event has positive streamwise and negative wall-normal fluctuations, while the ejection event has negative streamwise and positive wall-normal fluctuations. Both events share the same importance in turbulent production in ZPG TBL flows. [Drózdź \(2014\)](#) showed that S_u is a good indicator of the convection velocity of coherent structures. [Figure 7.11](#) shows the distributions of the streamwise velocity skewness, S_u , and kurtosis factor, K_u , for all TBL measurements and compared to the smooth DNS TBL data from [Chan *et al.* \(2021\)](#). Similar to the velocity defect profiles shown previously in [Figure 7.4](#), a variation in the S_u and K_u distribution between smooth and rough surfaces are observed near the wall up to $y/\delta = 0.07$ ([Figures 7.11\(a\)](#) and [\(b\)](#)). Beyond this region, the distributions collapse relatively well.

7.5.5 Autocorrelations

[Figure 7.12\(a\)](#) shows the outer-scaled autocorrelation of streamwise velocity fluctuations R_{uu} as a function of $\Delta x/\delta$ at $y/\delta = 0.1$ over a smooth wall and 3D sinewave surfaces with constant $ES = 0.2$. R_{uu} provides a statistical characterisation of the average half-length of the turbulence structure. For the smooth wall, increasing Re_τ increases the streamwise length of the positively correlated regions normalized by δ from 2.3 to 2.6 at the cutoff R_{uu} of 0.05. The negative and zero roughness skewness values almost have the same length normalized by δ of 2.4, as both profiles collapse, and they are slightly larger than the positive roughness skewness one which equals 2.1. [Figure 7.12\(b\)](#) shows R_{uu} as a function of $\Delta x/\delta$ at $y/\delta = 0.1$ over all the 3D sinewave surfaces at matched Re_τ . The figure shows that the surface *S24-12-12* has the largest streamwise length of the positively correlated regions normalized by δ of 2.65. This may be due to its much lower ES value than other surfaces. [Figure 7.12\(b\)](#) shows that the three negative roughness skewness and the zero roughness skewness that have comparable ES almost have the same streamwise length of the positively correlated regions normalized by δ of 2.4. The three positive roughness skewness surfaces collapse on each other and have shorter streamwise lengths of the positively correlated regions normalized by δ than the negative and zero roughness skewness surfaces. This indicates that positive roughness skewness surfaces tend to break the turbulence structure and shorten its length in the near-wall region.

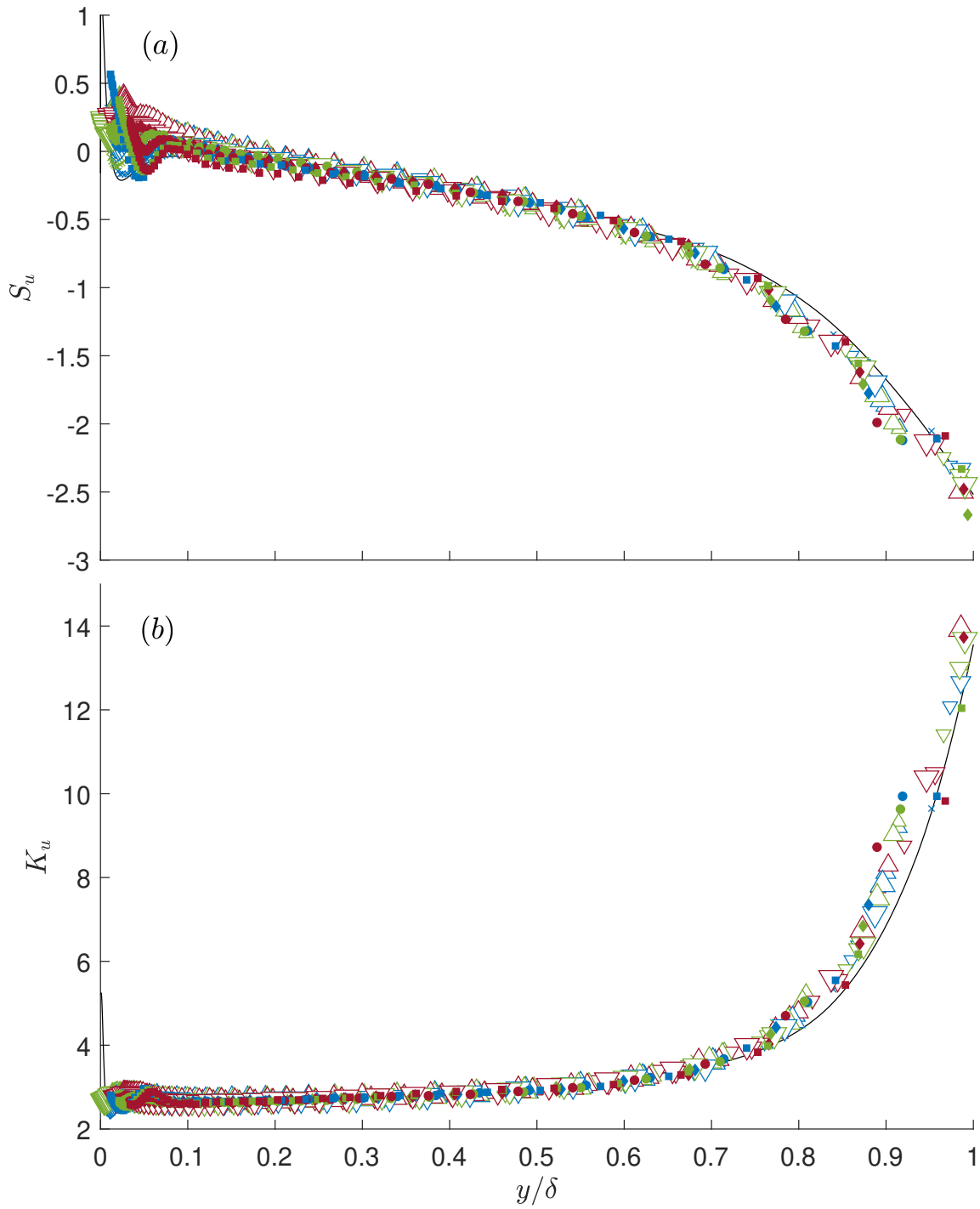


FIGURE 7.11: (a) Streamwise velocity skewness over smooth and rough wall surfaces at different Re_τ . (b) Streamwise velocity kurtosis over smooth and rough wall surfaces at different Re_τ . The symbols of our measurements are detailed in Table 7.2. Solid black line: DNS smooth TBL data from Chan *et al.* (2021). The wall-normal position y is normalized by the outer length scale δ .

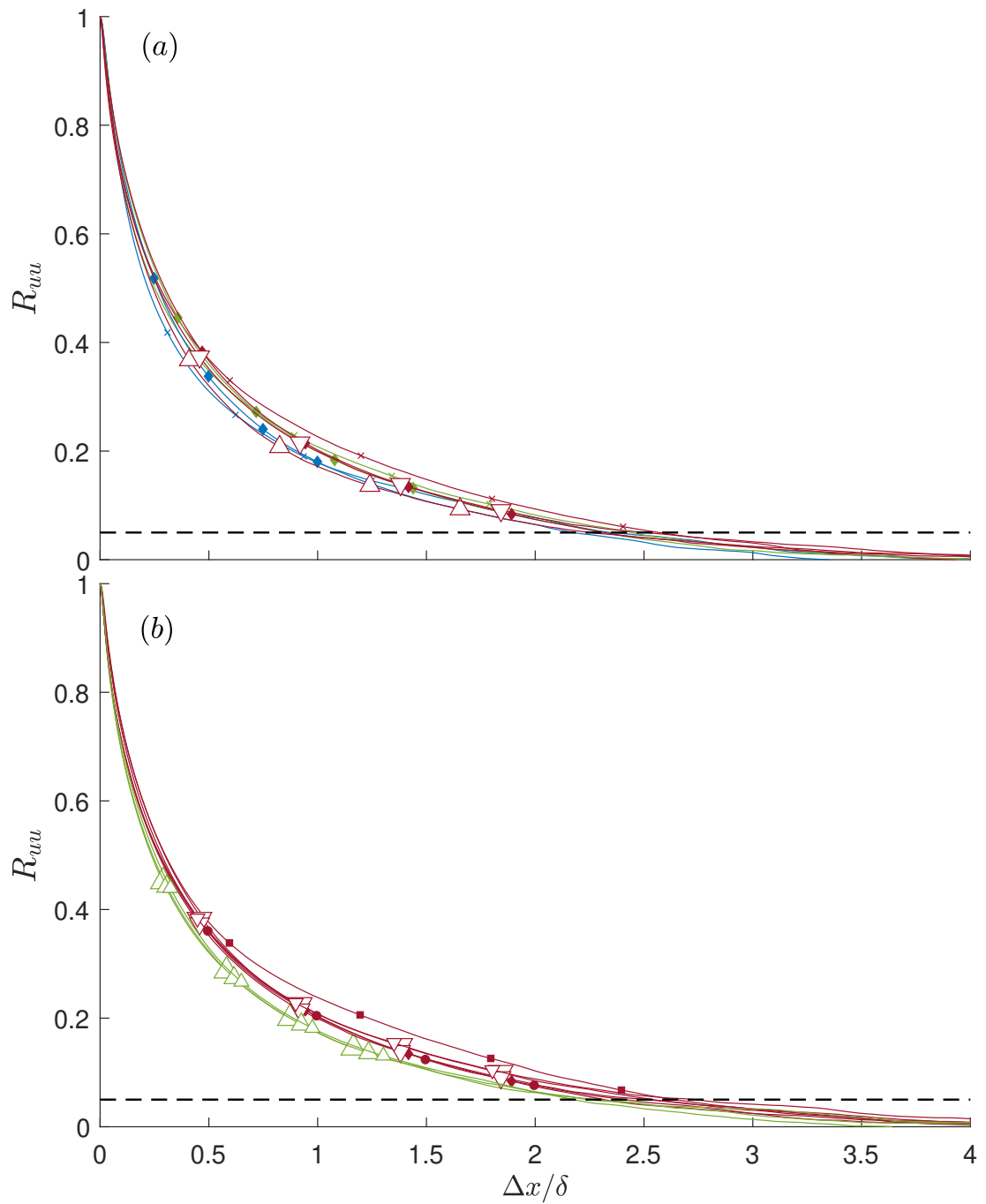


FIGURE 7.12: Autocorrelation R_{uu} of streamwise velocity fluctuations at $y/\delta = 0.1$ for different smooth and rough surfaces. The same surfaces used in Figures 7.5 (a) and (b) are plotted here in (a) and (b), respectively. The symbols of our measurements are detailed in Table 7.2. Marks are only for surface differentiation and do not indicate any specific data. The black dashed line represents $R_{uu} = 0.05$ as the cutoff R_{uu} .

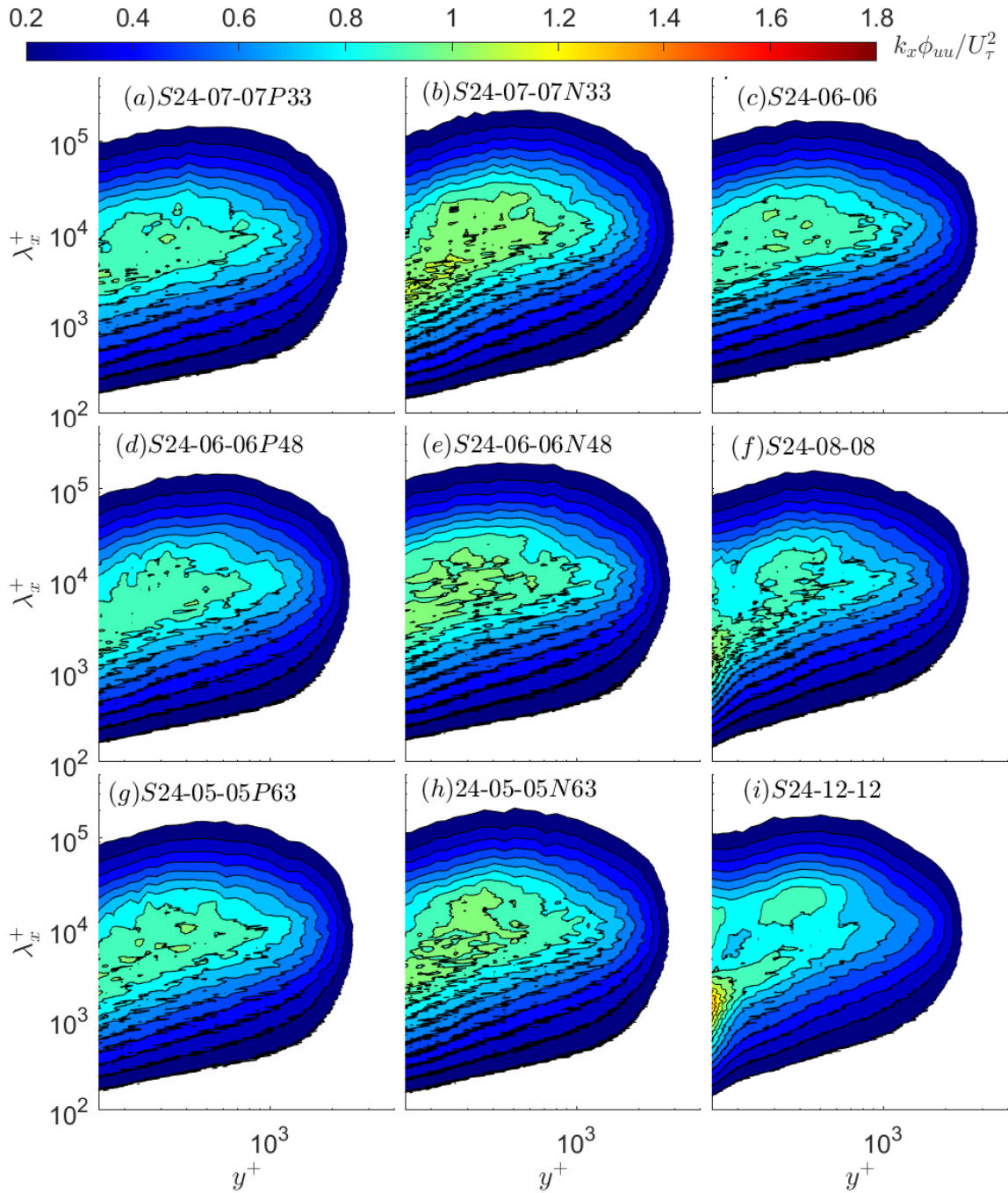


FIGURE 7.13: The premultiplied streamwise energy spectrograms contours at approximately matched $Re_\tau = 3000 \pm 300$, for the nine 3D sinusoidal surfaces. The positive roughness skewness rough surfaces are shown in the left column, (a) *S24-07-07P33*, (d) *S24-06-06P48* and (g) *S24-05-05P63*. The negative roughness skewness rough surfaces are shown in the middle column, (b) *S24-07-07N33*, (e) *S24-06-06N48* and (h) *S24-05-05N63*. The right column shows the three zero-roughness skewness rough surfaces, (c) *S24-06-06*, (f) *S24-08-08* and (i) *S24-12-12*.

7.5.6 Energy Spectra

The effect of roughness skewness on different length scales of TBL over 3D sinusoidal roughness can be investigated by spectral analysis. The contours of $k_x \phi_{uu} / U_\tau^2$, which are the premultiplied streamwise energy spectrogram normalized by inner scaling of various 3D sinusoidal roughness are shown in Figure 7.13. The left column of the figure depicts positive roughness skewness surfaces, while the middle depicts negative ones. The magnitude of the roughness skewness increases from the top to the bottom of the figure. The right column of the figure depicts the zero roughness skewness and the ES decreases from the top to the bottom of the figure. All the spectrogram contours are plotted with the same contour levels where the solid black lines separate the values from 0.2 to 1.8 with 0.1 steps. Here, $k_x = 2\pi/\lambda_x$ is the streamwise wavenumber, λ_x is the streamwise wavelength, and ϕ_{uu} is the spectral density of the streamwise velocity fluctuations. All the spectrogram contours are also plotted for y^+ varying from 1.5×10^2 to 4×10^3 and λ_x^+ varying from 10^2 to 5×10^5 in log scales for ease of comparison. The frequency spectra are converted to a spatial domain utilising Taylor’s frozen field hypothesis with convection velocity equal to the local mean one (Taylor 1938). Then a fast Fourier transform (FFT) algorithm is used to evaluate the streamwise velocity signal’s power spectral density. Squire *et al.* (2017) investigated the range where Taylor’s frozen field hypothesis is applicable for TBL flows. They revealed that Taylor’s hypothesis is applicable to the streamwise velocity component from $y/\delta > 0.02$, which equals to $y^+ > 60$ in our cases. Ghanadi & Djenidi (2021) showed that Taylor’s frozen field hypothesis is applicable on TBL over rod roughness surface with local wall suction from $z/k > 1$, which equals to $y^+ \approx 150$ in our cases. Hence, The premultiplied streamwise energy spectrograms contours plotted here started from $y^+ = 150$.

Figures 7.13(c), 7.13(d) and 7.13(e) show the countours for the $S24-06-06$, $S24-06-06P48$ and $S24-06-06N48$, respectively. Those three surfaces, as mentioned before, have the same ES and almost the same roughness parameters except roughness skewness. The figures show that the surface with negative roughness skewness $S24-06-06N48$ has the highest energy content in the outer layer among the three surfaces. In contrast, $S24-06-06P48$, which has positive roughness skewness, has the lowest energy content in the outer layer. The zero roughness skewness surface has a slightly larger energy content than the positive one. However, those small differences may be due to the small variation of U_τ , which is doubled, (U_τ^2) to normalise the premultiplied energy spectra, and the outer layer similarity is not affected much by roughness skewness. To investigate the effect of different roughness skewness values on the outer layer similarity, the contours for the three positive roughness skewness $S24-07-07P33$, $S24-06-06P48$ and $S24-05-05P63$ are shown in Figures 7.13(a), 7.13(d) and 7.13(g), respectively. However, Figures 7.13(b), 7.13(e) and 7.13(h) show the contours for the three negative roughness skewness $S24-07-07N33$, $S24-06-06N48$ and $S24-05-05N63$, respectively. The three positive roughness skewness surfaces have almost the same energy content and are always lower than the negative roughness skewness surfaces. The differences in energy content for the negative roughness skewness surfaces are more pronounced. $S24-07-07N33$ has a little larger energy content than the other two surfaces. Again, those differences are small and within the uncertainty in the hotwire measurements. Flack *et al.* (2020b) also showed that turbulence statistics vary only near the wall, and the outer layer is not affected by roughness skewness. The effect of ES on premultiplied streamwise energy spectrograms contours is shown in Figures 7.13(c), 7.13(f) and 7.13(i), for the three zero roughness skewness surfaces $S24-06-06$, $S24-08-08$ and $S24-12-12$ respectively. ES has a much larger effect on the energy content than the k_{sk} . $S24-06-06$ has the largest energy content in the outer layer among the three zero roughness skewness surfaces, and this energy content decreases with decreasing ES from 0.2 to 0.1.

7.6 CONCLUSIONS

Experiments were carried out for a zero pressure gradient rough wall turbulent boundary layer to investigate the effect of roughness skewness on turbulence statistics and drag coefficient. Nine 3D sinusoidal profiles of roughness were machined on acrylic plates using computerized control. The maximum height from the lowest valley to the highest peak is $k = 2.4$ mm with positive, negative and zero roughness skewness values (± 0.33 , ± 0.48 , ± 0.63 and zero). For each surface, single hotwire measurements were carried out at three different freestream velocities $U_\infty = 10$, 15 and 20 m/s and the results were compared with those of smooth wall TBL measurements at similar velocities. The range of Re_τ is from about 1000 to 4000 with a $\delta/k \approx 20 \pm 2$.

The results show the expected behaviour of the downward shift of the wall-unit normalized streamwise mean velocity profiles for all rough surfaces compared with the smooth wall profiles. The roughness function ΔU^+ and the friction coefficient C_f increase with increasing k_{sk} . The peak-dominated surfaces (positive roughness skewness) produce the highest drag, leading to the largest downward shift. However, the percentage of increase of C_f and ΔU^+ is larger when the roughness skewness increases from negative values to zero than when it increases from zero to positive values. The reduction in drag penalty observed for surfaces with negative skewness may be attributed to the flow gliding over the surface indentations. The absence of peaks on the surface results in weakened form-induced shear stress, which further contributes to the decrease in ΔU^+ observed above the surface. It is found that an exponential function $k_s = f(k_{sk})$ accurately predicts the equivalent sand grain roughness k_s for these 3D sinusoidal rough surfaces only when the roughness skewness parameter is varied and other roughness parameters are kept constant. However, different features of surface texture can affect the near-wall flow. Therefore, to establish predictive correlations of drag, a minimum of three surface parameters, namely k_{sk} , a surface height (probably k_t), and a measure of surface slope (likely ES) should be considered.

The collapse between the smooth and various 3D sinusoidal rough surfaces in the velocity defect, the velocity rms, and higher order turbulence statistics, such as the velocity skewness, S_u , and the velocity kurtosis factor, K_u , normalized by δ , support the outer layer similarity hypothesis, even for smaller values of δ/k and Re_τ , regardless of the surface and flow conditions. The shape factor H exhibits a better collapse for both the smooth and rough wall data in the diagnostic plot. The autocorrelation analysis shows that positive roughness skewness surfaces tend to shorten the average length of the turbulence structures in the near-wall region. However, the positive roughness skewness surfaces have significantly higher drag than the negative roughness skewness surfaces. The premultiplied streamwise energy spectrogram contours showed that the roughness skewness has a neglected effect on the turbulence structures far from the wall. However, ES has a much larger effect on the energy content than the k_{sk} , and the energy content increases with increasing ES from 0.1 to 0.2.

In general, this study highlights the significance of higher-order topographical parameters, specifically skewness, in influencing near-wall flow behaviour. The investigation provides a comprehensive analysis of the impact of positive, negative, and zero roughness skewness values on turbulence statistics, including ΔU^+ . Future research should consider additional surface texture characteristics that can affect near-wall flow behaviour to develop more robust predictive correlations for drag.

ACKNOWLEDGMENTS

The authors acknowledge the financial support of the Australian Research Council.

AUTHOR DECLARATIONS

Conflict of Interest

The authors have no conflicts to disclose.

Author Contributions

Misarah Abdelaziz: Conceptualization (equal). **Lyazid Djenidi:** Conceptualization (equal). **Mergen Ghayesh:** Conceptualization (equal). **Rey Chin:** Conceptualization (equal).

DATA AVAILABILITY

The data that support the findings of this study are available from the corresponding author upon reasonable request.

Bibliography

- ABDELAZIZ, M., DJENIDI, L., GHAYESH, M., & CHIN, R. 2023 On the effect of streamwise and spanwise spacing to height ratios of three-dimensional sinusoidal roughness on turbulent boundary layers. *Physics of Fluids* **35** (2).
- ABDELAZIZ, M., DJENIDI, L., GHAYESH, M. H., & CHIN, R. 2022a A new equivalent sand grain roughness relation for two-dimensional rough wall turbulent boundary layers. *Journal of Fluid Mechanics* **940**, A25.
- ABDELAZIZ, M., DJENIDI, L., GHAYESH, M. H., & CHIN, R. 2022b Outer turbulent boundary layer similarities for different 2d surface roughnesses at matched reynolds number. *International Journal of Heat and Fluid Flow* **94**, 108940.
- ALFREDSSON, P. H., ÖRLÜ, R., & SEGALINI, A. 2012 A new formulation for the streamwise turbulence intensity distribution in wall-bounded turbulent flows. *European Journal of Mechanics-B/Fluids* **36**, 167–175.
- ALFREDSSON, P. H., SEGALINI, A., & ÖRLÜ, R. 2011 A new scaling for the streamwise turbulence intensity in wall-bounded turbulent flows and what it tells us about the “outer” peak. *Physics of Fluids* **23** (4), 041702.
- ARDEKANI, M. & FARHANI, F. 2009 Experimental study on response of hot wire and cylindrical hot film anemometers operating under varying fluid temperatures. *Flow Measurement and Instrumentation* **20** (4-5), 174–179.
- ASME 2009 Surface Texture (Surface Roughness, Waviness, and Lay). *Revision of ANSI/ASME B46.1-1995. Standard. ASME* .
- AVER'YANOVA, I. O., BOGOMOLOV, D. Y., & POROSHIN, V. V. 2017 ISO 25178 standard for three-dimensional parametric assessment of surface texture. *Russian Engineering Research* **37** (6), 513–516.
- BARROS, J. M., SCHULTZ, M. P., & FLACK, K. A. 2018 Measurements of skin-friction of systematically generated surface roughness. *International Journal of Heat and Fluid Flow* **72**, 1–7.

- CHAN, C., SCHLATTER, P., & CHIN, R. 2021 Interscale transport mechanisms in turbulent boundary layers. *Journal of Fluid Mechanics* **921**, A13.
- CHAN, L., MACDONALD, M., CHUNG, D., HUTCHINS, N., & OOI, A. 2015 A systematic investigation of roughness height and wavelength in turbulent pipe flow in the transitionally rough regime. *Journal of Fluid Mechanics* **771**, 743–777.
- CHAUHAN, K. A., MONKEWITZ, P. A., & NAGIB, H. M. 2009 Criteria for assessing experiments in zero pressure gradient boundary layers. *Fluid Dynamics Research* **41** (2), 021404.
- CHIN, C., HUTCHINS, N., OOI, A., & MARUSIC, I. 2009 Use of direct numerical simulation (dns) data to investigate spatial resolution issues in measurements of wall-bounded turbulence. *Measurement Science and Technology* **20** (11), 115401.
- CLAUSER, F. H. 1956 The turbulent boundary layer. *Advances in Applied Mechanics* **4**, 1–51.
- COLES, D. 1956 The law of the wake in the turbulent boundary layer. *Journal of Fluid Mechanics* **1** (2), 191–226.
- DARCY, H. 1857 *Recherches expérimentales relatives au mouvement de l'eau dans les tuyaux*. vol. 1., Mallet-Bachelier.
- DJENIDI, L., TALLURU, K., & ANTONIA, R. 2018 Can a turbulent boundary layer become independent of the reynolds number? *Journal of Fluid Mechanics* **851**, 1–22.
- DJENIDI, L., TALLURU, K., & ANTONIA, R. 2019 A velocity defect chart method for estimating the friction velocity in turbulent boundary layers. *Fluid Dynamics Research* **51** (4), 045502.
- DRÓZDŹ, A. 2014 Influence of pressure gradient on streamwise skewness factor in turbulent boundary layer. In *Journal of Physics: Conference Series*. vol. 530, P. 012061, IOP Publishing.
- FLACK, K., SCHULTZ, M., & BARROS, J. 2020a Skin friction measurements of systematically-varied roughness: probing the role of roughness amplitude and skewness. *Flow, Turbulence and Combustion* **104**, 317–329.
- FLACK, K. A. & SCHULTZ, M. P. 2010 Review of hydraulic roughness scales in the fully rough regime. *Journal of Fluids Engineering* **132** (4).
- FLACK, K. A., SCHULTZ, M. P., BARROS, J. M., & KIM, Y. C. 2016 Skin-friction behavior in the transitionally-rough regime. *International Journal of Heat and Fluid Flow* **61**, 21–30.
- FLACK, K. A., SCHULTZ, M. P., & VOLINO, R. J. 2020b The effect of a systematic change in surface roughness skewness on turbulence and drag. *International Journal of Heat and Fluid Flow* **85**, 108669.
- FOROOGHI, P., STROH, A., MAGAGNATO, F., JAKIRLIĆ, S., & FROHNAPFEL, B. 2017 Toward a universal roughness correlation. *Journal of Fluids Engineering* **139** (12).
- GHANADI, F. & DJENIDI, L. 2021 Spatial resolution effects on measurements in a rough wall turbulent boundary layer. *Experiments in Fluids* **62**, 1–6.
- HAMA, F. R. 1954 Boundary layer characteristics for smooth and rough surfaces. *Trans. Soc. Nav. Arch. Marine Engrs.* **62**, 333–358.

- HUTCHINS, N., NICKELS, T. B., MARUSIC, I., & CHONG, M. 2009 Hot-wire spatial resolution issues in wall-bounded turbulence. *Journal of Fluid Mechanics* **635**, 103–136.
- JELLY, T. O. & BUSSE, A. 2018 Reynolds and dispersive shear stress contributions above highly skewed roughness. *Journal of Fluid Mechanics* **852**, 710–724.
- JIMÉNEZ, J. 2004 Turbulent flows over rough walls. *Annual Review of Fluid Mechanics* **36**, 173–196.
- JOUYBARI, M. A., YUAN, J., BRERETON, G. J., & MURILLO, M. S. 2021 Data-driven prediction of the equivalent sand-grain height in rough-wall turbulent flows. *Journal of Fluid Mechanics* **912**, A8.
- LIGRANI, P. & BRADSHAW, P. 1987 Spatial resolution and measurement of turbulence in the viscous sublayer using subminiature hot-wire probes. *Experiments in Fluids* **5** (6), 407–417.
- LIGRANI, P. M. & MOFFAT, R. J. 1986 Structure of transitionally rough and fully rough turbulent boundary layers. *Journal of Fluid Mechanics* **162**, 69–98.
- MARUSIC, I., CHAUHAN, K., KULANDAIVELU, V., & HUTCHINS, N. 2015 Evolution of zero-pressure-gradient boundary layers from different tripping conditions. *Journal of Fluid Mechanics* **783**, 379–411.
- MARUSIC, I., MONTY, J. P., HULTMARK, M., & SMITS, A. J. 2013 On the logarithmic region in wall turbulence. *Journal of Fluid Mechanics* **716**, R3.
- NAPOLI, E., ARMENIO, V., & DE MARCHIS, M. 2008 The effect of the slope of irregularly distributed roughness elements on turbulent wall-bounded flows. *Journal of Fluid Mechanics* **613**, 385–394.
- NICKELS, T., MARUSIC, I., HAFEZ, S., & CHONG, M. 2005 Evidence of the k^{-1} law in a high-reynolds-number turbulent boundary layer. *Physical Review Letters* **95** (7), 074501.
- NIKURADSE, J. 1933 Laws of flow in rough pipes. *Translation from German published 1950 as NACA Tech. Memo. 1292* .
- PERRY, A. & LI, J. D. 1990 Experimental support for the attached-eddy hypothesis in zero-pressure-gradient turbulent boundary layers. *Journal of Fluid Mechanics* **218**, 405–438.
- SCHLICHTING, H. & KESTIN, J. 1961 *Boundary layer theory*, 9th edn. vol. 121, New York: McGraw-Hill.
- SCHULTZ, M. P. & FLACK, K. A. 2009 Turbulent boundary layers on a systematically varied rough wall. *Physics of Fluids* **21** (1), 015104.
- SQUIRE, D., HUTCHINS, N., MORRILL-WINTER, C., SCHULTZ, M., KLEWICKI, J., & MARUSIC, I. 2017 Applicability of Taylor’s hypothesis in rough-and smooth-wall boundary layers. *Journal of Fluid Mechanics* **812**, 398–417.
- TAYLOR, G. I. 1938 The spectrum of turbulence. *Proceedings of the Royal Society of London. Series A-Mathematical and Physical Sciences* **164** (919), 476–490.
- UTAMA, I., NUGROHO, B., YUSUF, M., PRASETYO, F., HAKIM, M., SUASTIKA, I., GANAPATHISUBRAMANI, B., HUTCHINS, N., & MONTY, J. P. 2021 The effect of cleaning and repainting on the ship drag penalty. *Biofouling* **37** (4), 372–386.

YUAN, J. & PIOMELLI, U. 2014 Estimation and prediction of the roughness function on realistic surfaces. *Journal of Turbulence* **15** (6), 350–365.

Chapter 8

A New Equivalent Sand Grain Roughness Relation For 3D Rough Surfaces

8.1 CHAPTER OVERVIEW

One of the longstanding goals of rough wall fluid dynamics research is to determine the drag penalty of surfaces based solely on their topographical parameters. While previous chapters have investigated the effects of different roughness parameters on turbulence statistics, this chapter compiles a chronological record of roughness correlations, detailing the parameter ranges and types of roughness used in their development.

To evaluate the effectiveness of previous predictive correlations, this chapter examines over 120 distinct 3D surface textures available in the literature. The previous correlations showed only moderate precision, achieving an accuracy of approximately $R^2 \approx 0.5$ when applied to a range of irregular roughness. The coefficient of determination R^2 is used as a statistical measure to assess the proximity of data to the regression line.

Furthermore, a new correlation model is introduced based on surface height skewness (k_{sk}) and streamwise effective slope (ES_x), which can predict k_s normalised with root mean square roughness height (k_q) for 3D roughness in the fully rough regime. This model demonstrated a high level of accuracy in predicting k_s with a coefficient of determination (R^2) of 0.96.

8.2 ON PREDICTIVE MODELS FOR THE EQUIVALENT SAND GRAIN ROUGHNESS FOR WALL-BOUNDED TURBULENT FLOWS

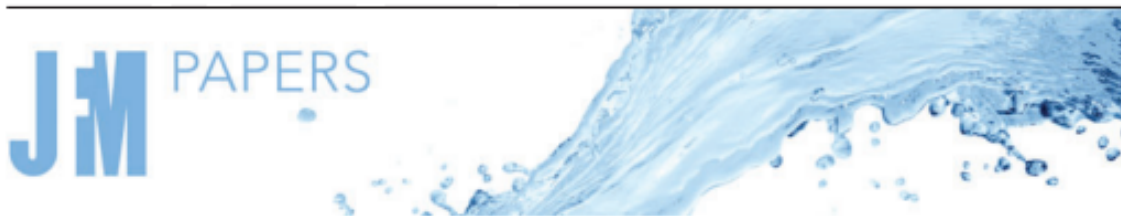
This section consists of the following submitted journal article:

To be submitted to Journal of Fluid Mechanics

Misarah Abdelaziz, L. Djenidi, Mergen H. Ghayesh, and Rey Chin.

The article is identical to its submitted format with the following exceptions:

- The numbering of figures, tables and equations has been altered to include the chapter number.
- The position of some figures and tables has been changed to improve the article's legibility.
- References style has been changed to be consistent with the thesis style.



Statement of Authorship

Title of paper	On predictive models for the equivalent sand grain roughness for wall-bounded turbulent flows
Publication status	Submitted
Publication details	Misarah Abdelaziz, L. Djenidi, Mergen H. Ghayesh, and Rey Chin. On predictive models for the equivalent sand grain roughness for wall-bounded turbulent flows

Principal Author

Name of principal author (candidate)	Misarah Abdelaziz
Contribution to the paper	Conception, acquiring data, knowledge, analysis and drafting
Certification	This paper reports on original research I conducted during the period of my Higher Degree by Research candidature and is not subject to any obligations or contractual agreements with a third party that would constrain its inclusion in this thesis. I am the primary author of this paper.
Signature:	Date: 05/07/2023

Co-author contributions

By signing the Statement of Authorship, each author certifies that:

- i.* the candidate's stated contribution to the publication is accurate (as detailed above)
- ii.* permission is granted for the candidate to include the publication in the thesis; and
- iii.* the sum of all co-author contributions is equal to 100% less the candidate's stated contribution.

Name of co-author	Lyazid Djenidi
Contribution to the paper	Conception, knowledge, analysis and drafting
Signature:	Date: 27/06/2023

Name of co-author	Mergen H. Ghayesh
Contribution to the paper	Conception, knowledge, and drafting
Signature:	Date: 04/07/2023

Name of co-author	Rey Chin
Contribution to the paper	Conception, knowledge, analysis and drafting
Signature:	Date: 04/07/2023

On predictive models for the equivalent sand grain roughness for wall-bounded turbulent flows

Misarah Abdelaziz,^{1,a)} L. Djenidi,² Mergen H. Ghayesh,¹ and Rey Chin¹

AFFILIATIONS

¹School of Electrical & Mechanical Engineering, University of Adelaide, Adelaide, South Australia, 5005, Australia

²Department of Mechanical Engineering, Indian Institute of Technology - Bombay, Powai, Mumbai 400076, India

^{a)} Author to whom correspondence should be addressed: misarah.abdelaziz@adelaide.edu.au

ABSTRACT

One of the longstanding goals of rough wall fluid dynamics research is to determine the drag penalty of surfaces based solely on their topographical parameters. The most important length scale or roughness parameter that best describes a surface in relation to friction drag has not been agreed upon. Over the years, many studies have attempted to identify the most important surface parameter. The concept of the equivalent sand-grain roughness (k_s) was introduced to standardise different types of roughness in wall-bounded turbulence, serving as an input parameter for predictions. To anticipate the amount of drag generated by a rough surface under turbulent flow conditions, experts use roughness correlations that establish a correspondence between the topographical characteristics of the surface and k_s . Therefore, a chronological compilation of roughness correlations is presented, detailing the parameter ranges and types of roughness used in their development. This study evaluates the effectiveness of predictive correlations and aims to formulate a universal one by exploring a comprehensive assortment of three-dimensional (3D) surface textures available in the literature. The results suggest that a correlation based on surface height skewness (k_{sk}) and streamwise effective slope (ES_x) can predict k_s normalised with root mean square roughness height (k_q) for 3D roughness in the fully rough regime. Despite the fact that the correlation is restricted to 3D surface roughness, which is a more realistic representation, the model demonstrated a high level of accuracy in predicting k_s for over 120 distinct rough surfaces, with a coefficient of determination (R^2) of 0.96, a statistical measure for assessing the proximity of data to the regression line.

8.3 INTRODUCTION

The turbulent boundary layer (TBL) constitutes a fundamental phenomenon in the realm of fluid dynamics, describing fluid motion in close proximity to a solid boundary. TBL behaviour has a paramount impact on a wide range of engineering applications, including but not limited to aerodynamics, heat transfer, and drag reduction. While TBL research has traditionally relied on smooth surfaces, real-life surfaces tend to be rough, and roughness elements can exert a considerable influence on TBL dynamics, including alterations to flow structures, turbulence intensity, and drag forces. For instance, a single large container ship may release pollutants equivalent to those discharged by 50 million cars within a year. Even after cleaning, ship hulls still exhibit significant drag increases compared to their smooth counterparts due to imperfections and biofouling (Nugroho *et al.* 2017; Utama *et al.* 2017). Skin friction drag alone accounts

for roughly 50% of the total drag in commercial aircraft, while it may account for up to 80-90% in large carrier ships. Consequently, a thorough understanding of the various roughness parameters and their impact on drag coefficients is critical. One of the longstanding goals of rough wall fluid dynamics research is to determine the drag penalty on surfaces based solely on their topographical parameters.

Despite its importance, several questions and knowledge gaps remain concerning TBL over rough surfaces. For instance, the effects of different types of roughness, such as shape, size, and arrangement, on TBL behaviour are still not fully comprehended. Moreover, the minimum Reynolds number and maximum relative roughness required to achieve wall similarity in data are still a subject of debate. Lastly, the dominant roughness parameters that impact turbulence statistics and drag coefficients across various flow regimes, from hydrodynamically smooth to fully rough regimes, remain unknown.

8.3.1 Motivation

Accurately predicting fluid motion over uneven surfaces is of significant importance in engineering design, given that surfaces in engineering flows are typically rough, resulting from a range of factors, including surface imperfections, corrosion, erosion, and fouling processes (Kuwata *et al.* 2019). These rough surfaces can decrease performance due to an increase in wall friction, which has been extensively documented. The study of roughness in turbulent flows dates back over two centuries, beginning with Darcy (1857) on the effect of roughness in pipe flow. Nikuradse (1933) furthered the study of the impact of sand roughness on turbulent pipe flow, with Moody (1944) subsequently developing a chart to estimate head losses in smooth and rough pipes, which has become a cornerstone of hydraulic engineering.

The concept of k_s was proposed by Schlichting (1937) based on the classic experiments of Nikuradse (1933) to standardise different types of roughness in wall-bounded turbulence. However, it is important to note that k_s is not a measure of roughness elevation but a measure of the height of a hypothetical roughness element that would produce the same frictional resistance as the actual roughness elements on the surface. Researchers aim to develop a deeper understanding of the relationship between surface characteristics and the resistance they pose to fluid flow, particularly in terms of the point at which roughness begins to have a greater impact on wall shear stress than a smooth surface.

Roughness on these surfaces can significantly affect boundary layer flow, impacting heat and momentum transfer and causing an increase in drag. This increase in drag can result in higher fuel consumption and emissions in transportation, such as ships and aeroplanes. By understanding the effect of roughness on boundary layer flows, it is possible to develop methods for controlling and reducing drag, leading to substantial cost savings and environmental benefits.

There is no consensus on which length scale or roughness parameter best describes a surface in relation to friction drag. Over the years, many studies have attempted to identify the most important surface parameter. Mean roughness height (k_a), root-mean-square height (k_q), maximum peak to valley height (k_t), average peak to valley height (k_z), effective slope (ES), solidarity (λ), skewness (k_{sk}), and kurtosis (k_{ku}) are among the various parameters that have been examined. However, none of these parameters has been found to be universally applicable to all types of roughness.

This study makes a significant contribution to the field of rough bounded flow by comprehensively evaluating a range of 3D surface textures to identify more universal correlations between surface parameters and friction drag. Despite extensive research in this area, there

remains a lack of consensus regarding which surface parameter is the most important in relation to friction drag. To address this issue, the authors introduce a new equation for normalised k_s , which incorporates the physical roughness parameters of surface height skewness k_{sk} , stream-wise effective slope ES_x , and the root mean square roughness height k_q . The proposed equation demonstrates a high level of accuracy in predicting k_s for both regular and irregular 3D roughness in the fully rough regime. The authors' comprehensive approach and novel equation make a valuable contribution to the ongoing effort to enhance our understanding of friction drag prediction.

8.3.2 Roughness function

The roughness function ΔU^+ , is defined as $\Delta U^+ = \Delta U / U_\tau$, where U is the mean streamwise velocity and U_τ is the friction velocity $U_\tau = \sqrt{\tau_w / \rho}$; the superscript, $(^+)$ means normalisation by the wall units U_τ or ν / U_τ , where ν is the kinematic viscosity, is a valuable tool for describing the log-law intercept in rough-wall flows. This function was independently defined by Hama (1954) and is calculated as the shift at matched y^+ of the rough-wall log law relative to that of the smooth wall. The formula for ΔU^+ is given by:

$$\Delta U^+ = \frac{1}{\kappa} \ln k^+ + B - C, \quad (8.1)$$

where κ is the von Kármán constant, B is a universal constant, and C is a constant that equals 8.5 for Nikuradse sand grain roughness in the fully rough regime. The roughness function quantifies the increase in drag due to surface roughness and represents the difference in coefficient of friction between smooth and rough walls at the same matched Reynolds number $Re_\tau = \delta U_\tau / \nu$, where δ is the thickness of the boundary layer, defined as the distance from the wall to the point at which the mean streamwise velocity reaches 99% of the freestream velocity. It is particularly useful in scaling up experimental or numerical data obtained at lower outer Reynolds numbers and in specific geometries to predict drag at higher Reynolds numbers and in other geometries. However, it should be noted that at low Re_τ and low boundary layer to roughness height ratio (δ/k), the distorted log region is not fully formed, leading to some Re_τ dependence in ΔU^+ . This dependence has been observed by Chan *et al.* (2015) and may cause an overestimation of ΔU^+ .

8.3.3 Equivalent sand grain roughness height, k_s

The concept of equivalent sand grain roughness is a crucial aspect of hydraulic engineering that has its origins in the early studies of open channel flow. The roughness of a channel bed was recognised to affect the rate of flow and sediment transport. Manning *et al.* (1890) developed an empirical formula to calculate the flow rate in an open channel, which included a coefficient called the Manning roughness coefficient to account for the effects of bed roughness on the flow. However, the coefficient was initially determined through trial and error, and only later attempts were made to link it with the physical characteristics of the bed material.

Emile Bazin, a French engineer, developed a formula similar to Manning's for computing the flow rate in open channels with a roughness coefficient that was intended to be more physically based. Bazin's formula proposed that the roughness coefficient should be proportional to the size of the bed material, and he developed a series of experiments to determine the relationship between the coefficient and the size of the sand grains in a riverbed. Later, the French engineer Albert Darcy extended Bazin's work and developed a formula for the friction factor in

pipe flow based on the roughness of the pipe wall. Darcy's formula relates the pressure or head loss resulting from friction along a specific pipe length to the mean velocity of an incompressible fluid flow.

The equivalent sand grain roughness was first introduced by Johann Nikuradse, a German hydraulic engineer in the 1930s. [Nikuradse \(1933\)](#) conducted experiments to measure the effect of surface roughness on the frictional resistance of fluid flow in pipes. Nikuradse created a range of different surface roughnesses on the interior walls of pipes, pumped water through them, and measured the frictional resistance of the flow at different Reynolds numbers. Nikuradse found that the friction factor increased as the surface roughness increased, which became known as the Nikuradse experiment.

Nikuradse's experiments revealed that the relationship between surface roughness and friction factor could be described by a single parameter known as the equivalent sand grain roughness. This parameter represented the height of an imaginary layer of sand grains that would create the same level of surface roughness as the actual rough surface of the pipe. The concept of the equivalent sand grain roughness was later refined and expanded upon by other researchers. In particular, Lewis Moody, a mathematician from the United Kingdom, was instrumental in creating a popular empirical formula for computing the friction factor in pipes, which is commonly referred to as the Moody chart ([Moody 1944](#)). The Moody chart incorporates the equivalent sand grain roughness as a variable to factor in the impact of surface roughness on frictional resistance.

8.3.4 Rough flow regimes

In the field of fluid dynamics, the presence of wall roughness alters the law of the wall used to describe the viscous sublayer. To account for this effect, the roughness Reynolds number k_s^+ is introduced as $k_s^+ = k_s U_\tau / \nu$, where U_τ is the friction velocity and ν is the kinematic viscosity of the fluid. Based on this number, three distinct regimes of roughness are identified, each corresponding to a different region of the wall affected by the turbulent boundary layer. These regimes are classified as hydraulically smooth, transitionally rough, and fully rough regimes. The onset of the transitionally rough and fully rough regimes is defined by $k_{s-Smooth}^+$ and $k_{s-Rough}^+$, respectively. Table 8.1 provides different reported values of these parameters in the literature. The hydraulically smooth regime, occurs when $k_s^+ < k_{s-Smooth}^+$, where the roughness elements are completely embedded in the viscous sublayer, and as a result, skin friction and the drag coefficient remain unchanged. In the transitionally rough regime, which occurs when $k_{s-Smooth}^+ < k_s^+ < k_{s-Rough}^+$, both viscous and pressure forces influence the skin friction and drag coefficient, making it a more complex regime. Finally, the fully rough regime occurs when $k_s^+ > k_{s-Rough}^+$, where rough elements penetrate into the fully turbulent region, causing the destruction of the viscous sublayer and a shift in the logarithmic profile downward. This regime causes a significant increase in friction drag due to pressure force on the roughness, and the pressure loss becomes independent of the molecular viscosity of the fluid and velocity.

Predicting the drag of rough surfaces is a complex task, mainly due to the distinct characteristics of each rough surface in relation to ΔU^+ as a function of $f(k_s^+)$. In these scenarios, the skin friction and drag coefficients are influenced by both viscous and pressure forces. The transitional rough regime presents complex behaviour that can exhibit a step behaviour, similar to the Nikuradse-type roughness function, or gradual behaviour, similar to the Colebrook-type roughness function, as represented in Figure 8.1.

[Bradshaw \(2000\)](#) provided a theoretical explanation for the dissimilarity between Nikuradse-type and Colebrook-type behaviours, which is grounded on the Oseen solution for roughness

Authors and year	Roughness type	Range
Nikuradse (1933)	Sand grain	$5 < k_s^+ < 70$
Schlichting & Kestin (1961)	Sand grain	$5 < k_s^+ < 70$
Cebeci & Bradshaw (1977)	Sand grain	$2.25 < k_s^+ < 90$
Lewkowicz & Musker (1978)	Ship hull roughness	$2.25 < k_q^+ < 90$
Ligrani & Moffat (1986)	Sand grain	$2.25 < k_s^+ < 90$
	Uniform spheres	$15 < k_s^+ < 55$
Bandyopadhyay (1987)	k -type roughness	$f(Re_\tau, s_x/k) < k_t^+ < f(Re_\tau, s_x/k)$
Shockling <i>et al.</i> (2006)	Honed pipes	$3.5 < k_s^+ < 30$
Schultz & Flack (2007)	3D roughness similar to the honed pipes of Shockling <i>et al.</i> (2006)	$2.5 < k_s^+ < 25$
Langelandsvik <i>et al.</i> (2008)	Commercial steel pipes	$1.4 \pm 0.2 < k_s^+ < 18 \pm 4$
Flack <i>et al.</i> (2012)	Sandpapers	$5 < k_s^+ < -$
	Ship painted surface	$10 < k_t^+ < -$

TABLE 8.1: Previous research on the onsets of transitionally rough and fully rough regimes

elements (Oseen 1910). However, recent studies have suggested that irregular surfaces with multiple scales of roughness follow Nikuradse-type behaviour more closely than Colebrook-type behaviour. This behaviour is observed in various surfaces, including honed surfaces, commercial steel pipes, painted and sanded surfaces, grit-blasted surfaces, and sparsely biofouled surfaces, where a sudden departure from the hydraulically smooth regime occurs, and inflectional behaviour in the C_f transitionally rough regime is observed (Shockling *et al.* 2006; Langelandsvik *et al.* 2008; Flack *et al.* 2012, 2016; Monty *et al.* 2016). As the roughness height k_s^+ increases, the contribution of the viscous stress to skin friction becomes negligible compared to the form drag on individual roughness elements. As demonstrated in Figure 8.1, both Nikuradse-type and Colebrook-type roughness approach the fully-rough asymptote.

8.3.5 k_s predictive correlations based on roughness parameters

The challenge of accurately predicting drag in various applications is hindered by the lack of a reliable approach to associating k_s with topographical features. Numerous studies have attempted to establish correlations between topographical features and k_s to develop a universal model that captures the behaviour of rough surfaces. The primary focus is identifying which topographical characteristics influence flow and determining the minimum set of features needed to estimate drag. This section reviews previous studies aimed at attributing k_s solely based on topographical characteristics.

Over the past few decades, numerous studies have attempted to identify the dominant surface parameters affecting friction drag. Several parameters have been explored, including k_a ,

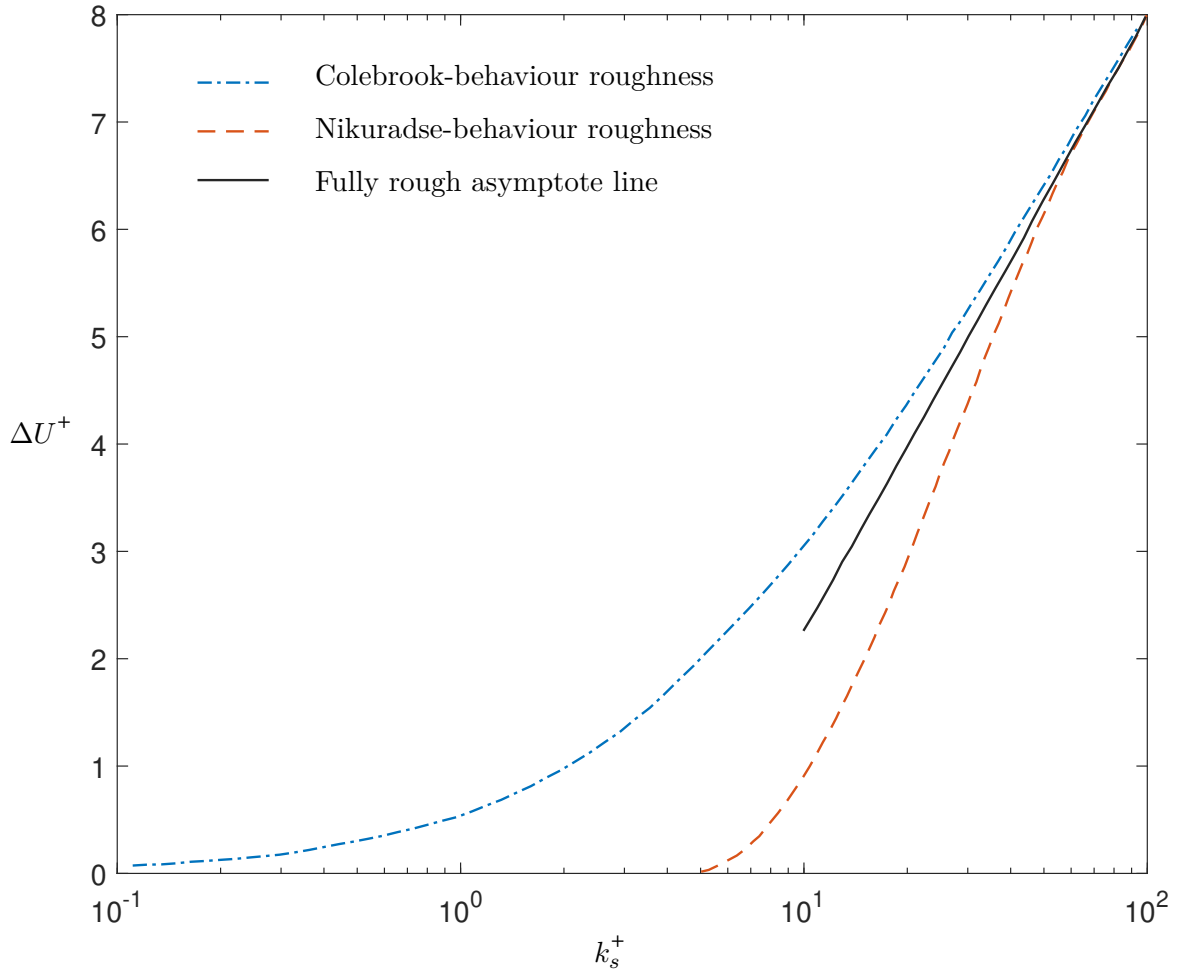


FIGURE 8.1: The roughness function ΔU^+ as a function of the roughness Reynolds number k_s^+ for Nikuradse and Colebrook behaviour roughness.

k_q , k_t , k_z , ES , λ , k_{sk} , and k_{ku} as previously mentioned. Despite extensive exploration, none of these parameters, when considered independently, is sufficient to be generalised for all types of roughness. Further discussion on surface roughness parameters will be presented in section 8.4.

The impact of surface finish on nozzle and blade efficiency was studied in Forster (1966), which found that the equivalent sand grain roughness could be correlated using ratios of $k_s = a.k_t$, where a is a constant dependent on the surface finish. Dvorak (1969) expanded upon this work by proposing equations for ΔU^+ based on roughness density parameter λ_p , which is the ratio of total surface area to roughness area, and dimensionless roughness height k^+ . The study by Simpson (1973) generalised the roughness density correlations proposed by Dvorak (1969) for various other roughness element geometries, using the more widely applicable roughness density parameter λ_f which is the ratio of the total surface area to the total roughness frontal area normal to the flow.

Dirling (1973) presented a correlation to determine the equivalent sand grain roughness of rough surfaces with arbitrary shape and spacing, and Koch & Smith Jr (1976) determined a reference value of $k_s/k_a = 6.2$ for emery paper. Bammert & Sandstede (1976) investigated the effect of blade manufacturing tolerances and surface roughness on turbine performance and recommended converting the centre-line-average value to the sand roughness height using the

relationship $k_s \approx 2.19k_a^{0.877}$.

Musker (1980) investigated the effect of ship-hull roughness on the roughness function using air pipelines. They proposed a modified roughness Reynolds number, which takes into account the standard deviation of the surface roughness (k_q) and simple geometric statistics of naturally occurring surfaces such as k_{sk} and k_{ku} . They found that their modified roughness Reynolds number better fits roughness functions associated with natural surfaces.

Sigal & Danberg (1990) proposed a new parameter to characterise roughness density that takes into account the angle of inclination of the windward surface of roughness elements Λ_s . They suggested this new parameter as an improvement to the existing roughness density parameter proposed by **Dirling (1973)**. They also provided an equation for the equivalent sand roughness of two-dimensional roughness that depends on the density parameter. **Bogard et al. (1996)** investigated the impact of surface roughness on flow and heat transfer in turbine vanes used in aircraft engines. They found that the conventional centerline average measurement was insufficient to predict these effects and instead recommended the use of the correlation between the equivalent sand grain roughness and the roughness shape/density parameter proposed by **Sigal & Danberg (1990)** as a more accurate predictor.

Waigh & Kind (1998) proposed an equation to estimate the equivalent sand grain roughness of a regular 3D rough surface. They suggested that the roughness function of a 3D rough surface is mainly determined by the bluntness of an element and its aspect ratio in the spanwise direction. Their equation takes into account these parameters and gives a roughness constant that can be used to calculate the equivalent sand grain roughness.

The article by **Van Rij et al. (2002)** built on the work of **Sigal & Danberg (1990)** by incorporating irregular, three-dimensional surface roughness into the analysis of the relationship between two-dimensional, regular surface roughness and equivalent sand grain roughness. They proposed a correlation equation between equivalent sand grain roughness and roughness shape/-density parameter Λ_s . **Bons (2002)** introduced a new approach for determining the equivalent sand grain roughness of actual turbine surfaces, which relied on the root-mean-square slope angle of the surface. They also proposed a new correlation equation that was later adjusted by normalising the equivalent sand grain roughness height with mean roughness height based on the five largest peak-to-valley (k_z), and by making it a function of the surface slope angle α_{rms} (**Bons 2005**).

Napoli et al. (2008) introduced a new roughness parameter called the effective slope ES , which represents the average absolute gradient of the roughness over a surface. They found that ES played a critical role in determining the roughness function, with the transitionally rough regime being separated from the fully rough regime at approximately $ES = 0.15$. Additionally, this value represented the threshold between linear and nonlinear behaviour of the roughness function. **Schultz & Flack (2009)** investigated the impact of close-packed pyramid roughness on flow dynamics and found that the velocity change ΔU^+ was primarily determined by the height of the roughness. They also identified a range of effective slopes (ES) where the roughness function was significantly influenced by ES values. When ES was below this range $ES \approx 0.35$, the surface could be classified as wavy, rather than rough.

Boyle & Stripf (2009) proposed a new correlation for calculating the equivalent sand grain roughness of turbine vane roughness, based on two parameters: the roughness skewness (k_{sk}) and the root-mean-square roughness (k_q). **Flack & Schultz (2010)** conducted a study to determine the relevant roughness scales for three-dimensional roughness in the fully rough regime. They found that the root-mean-square roughness (k_q) and roughness skewness (k_{sk}) of the surface elevation probability density function were the most effective parameters in characterising a

surface hydraulically. Based on these parameters, they proposed a similar correlation to that proposed by [Boyle & Stripf \(2009\)](#), but with a power equation instead of a linear equation.

[Yuan & Piomelli \(2014\)](#) used large-eddy simulations to investigate the roughness of sand-grain and realistic roughness mimicking hydraulic turbine blades in open channel flows. They found that the fully rough regime began at different k_s^+ values depending on the type of roughness, and that the equivalent sand-grain roughness height was highly dependent on the surface topography. Moreover, the researchers also discovered that the realistic rough surfaces had a higher critical value of effective slope ($ES \approx 0.7$) that distinguished between the waviness and roughness regimes, compared to the values obtained for uniform roughness types investigated in a previous study by [Schultz & Flack \(2009\)](#). [Chan et al. \(2015\)](#) used direct numerical simulation (DNS) to study the effects of 3D sinusoidal roughness on turbulent flow through pipes. They found that the effect of low Reynolds numbers on the change in velocity was minimal, and that both roughness height and effective slope had a strong influence on the change in velocity.

[Ünal \(2015\)](#) focused on analysing the turbulent boundary layer in the presence of different rough surfaces, such as marine antifoulings and other engineering surfaces with irregular roughness. The researchers proposed a new roughness length scale k as a function of surface parameters, k_q , k_{sk} and Sd_4 , capable of accurately representing the roughness functions in both the transitionally and fully rough flow regimes, where Sd_4 is the mean spacing of roughness elements between the zero-crossings. [Flack et al. \(2016\)](#) established a correlation between the equivalent sand grain roughness height and the root-mean-square parameter of the roughness element (grit blasted surfaces) for fully developed turbulent channel flow. The findings revealed that it is possible to estimate the equivalent height of sand-grain roughness by utilising the parameters k_q and k_{sk} .

[Botros \(2016\)](#) established a correlation between the equivalent sand grain roughness height, denoted as k_s , and the root-mean-square (rms) parameter of the roughness element, k_q , for fully developed turbulent pipe flow in commercial steel pipes. By investigating eleven steel pipes obtained from different mills and using the measured friction factor and the Colebrook or Nikuradse rough functions. The study conducted by [Goodhand et al. \(2016\)](#) points out the insufficiency of the current roughness criteria that rely on a single amplitude parameter, such as k_a , for describing surface finish. The research examines the impact of roughness on drag by modifying the roughness on a single symmetrical aerofoil. The results indicate that the ratio of the roughness amplitude to its wavelength, a topographical parameter, is an essential factor and can be correlated with the equivalent sand grain roughness height, k_s . The study conducted by [De Marchis \(2016\)](#) aimed to estimate energy losses in roughened channel flows by performing large-eddy simulations (LES). The authors proposed a new mathematical logarithmic law, comparable to the one previously suggested using the equivalent sand grain roughness, to describe the results obtained from resolved LES on regular triangular rough surfaces and analysed in relation to irregular rough surfaces.

[Stimpson et al. \(2017\)](#) investigated the roughness of channels manufactured through direct metal laser sintering (DMLS) with different hydraulic length scales. The study found a significant correlation between the relative arithmetic mean roughness and the relative equivalent sand grain roughness, expressed as $k_s/D_h = 18k_a/D_h - 0.05$, where D_h is the hydraulic diameter. The authors noted that this relationship only applies to randomly rough surfaces with $k_a/D_h > 0.028$ as lower values will result in a negative k_s/D_h . The study by [Thakkar et al. \(2017\)](#) used DNS to investigate the effect of various parameters on the roughness function of 17 irregular rough surfaces under the transitionally rough regime. The study found that the roughness function ΔU^+ was influenced by frontal solidity, skewness, streamwise correlation length, and

root-mean-square roughness height. The study introduced a new parameter λ_0 as a function of these parameters to estimate the roughness function. [Forooghi *et al.* \(2017\)](#) used DNS to investigate the relationship between various roughness parameters and equivalent sand grain roughness (k_s) in fully rough channel flows with a friction Reynolds number of around 500. They varied the moments of the surface height probability density function, the effective slope of the random roughness, and the size distribution of the roughness peaks to generate roughness geometries. The authors established a correlation between k_s and the roughness parameters k , k_{sk} , and ES . The correlation is expressed as $k_s/k = F(k_{sk}) \cdot G(ES)$, where $F(k_{sk})$ and $G(ES)$ are functions of k_{sk} and ES , respectively. The study found that this correlation accurately predicted k_s for randomly distributed roughness in the fully rough regime of channel flows.

[Placidi & Ganapathisubramani \(2018\)](#) proposed a new parameter named “shelter solidity” (λ_s) to address non-similarity in surface morphology features. The authors conducted experiments using uniform LEGO bricks to test the new parameter and found that it could be applied to address differences in surface drag. A linear correlation was discovered between λ_s and roughness function, with an inverse relationship. Meanwhile, [Barros *et al.* \(2018\)](#) examined the relationship between roughness length scales in the wavy flow regime and found that k_s could be predicted from k_q and k_{sk} using a correlation equation.

[Kuwata & Kawaguchi \(2019\)](#) used a Lattice Boltzmann direct numerical simulation to investigate the impact of roughness parameters on turbulence in open-channel flows. The study examined the effect of root-mean-square roughness and skewness on the skin friction coefficient by analysing the triple-integrated double-averaged Navier-Stokes equation. The authors varied statistical moments of roughness elevation, such as mean height, standard deviation, skewness, and kurtosis, by altering the number and diameter of hemispheres. The paper found that the roughness function can be accurately predicted using a correlation between k_q and k_{sk} , which was expressed as $k_s/k_q = 4(1 + 0.17k_{sk})^4$.

[De Marchis *et al.* \(2020\)](#) used large eddy simulations to investigate the impact of different surface geometries on the roughness function in transitional and fully rough regimes. The researchers generated rough surfaces using sinusoidal functions with random amplitudes and established a relationship between the roughness function and statistical moments of roughness elevation such as mean height and standard deviation. The roughness function was expressed as a function of the friction Reynolds number and the chosen statistical moment. The study found that the roughness function could be predicted using the product of the equivalent sand grain roughness parameter and the statistical moment, with an additive constant to fit the data. [Flack *et al.* \(2020\)](#) investigated the impact of roughness height and skewness on friction coefficients. The authors found that surfaces with negative skewness led to lower friction coefficients compared to those with positive skewness. They established a correlation between k_s , k_q , and k_{sk} , and classified friction coefficients into three categories based on the roughness skewness (positive, negative, and zero). The study’s results provide valuable insights into the interplay between roughness height, skewness, and friction coefficients.

[Ramani *et al.* \(2020\)](#) examined the effects of effective slopes on turbulent boundary layer flows in both the streamwise and spanwise directions. The research found that the streamwise effective slope had a greater influence on the drag coefficient than the spanwise effective slope, although the study concluded that the latter should not be ignored as it plays a significant role in determining the drag coefficient. The study by [Abdelaziz *et al.* \(2020\)](#) investigated the impact of roughness parameters on the turbulence statistics and drag coefficient of turbulent boundary layer flows over 2D surfaces with circular rods and sine-waves of different heights and streamwise spacing to height ratios. The authors identified the roughness parameters k_t , ES , and k_{sk} as

primary factors that influence the flow. They proposed an equation to predict roughness height k_s based on these parameters.

The study by [Jouybari et al. \(2021\)](#) proposes a novel machine learning approach to predict the Nikuradse equivalent sand-grain roughness k_s . The authors employed Direct Numerical Simulations (DNS) on 45 different rough surfaces, and a combination of these DNS results and experimental data sets from literature to train Deep Neural Network (DNN) and Gaussian Process Regression (GPR) models. The models outperformed existing correlations in the literature, with an rms error of less than 10% and a maximum error of less than 30%. The study provides valuable insights into predicting k_s for turbulent flows over a wide range of rough surfaces, but did not propose new correlations for computing k_s . The study by [Medjnoun et al. \(2021\)](#) investigated the effects of roughness hierarchy on turbulent boundary layers over multiscale rough surfaces consisting of regular cuboid elements. The authors found that the aerodynamic roughness length scale varied linearly between subsequent iterations of smaller cuboids added uniformly to a first iteration of large-scale cuboids. Furthermore, they observed that a geometrical parameter that was proportional to the frontal solidity of the roughness could accurately describe this relationship.

The study by [Abdelaziz et al. \(2022\)](#) investigated the effects of 2D surface roughness on turbulent boundary layer flows by introducing new surface geometries such as triangular ribs and sine waves in addition to circular rods of varying heights and five different streamwise spacing to height ratios. The authors developed a new equation for predicting the Nikuradse equivalent sand-grain roughness for 2D uniformly distributed roughness in the fully rough regime. The study also found that due to the complex nature of roughness topography involving multiple parameters, each family of roughness has its own unique scaling law, suggesting the need for separate scaling laws for 2D and 3D roughness. The authors established an empirical correlation for both 2D and 3D data based on supplementary data on roughness.

The study by [Sarakinis & Busse \(2022\)](#) investigated the effect of barnacle-like rough surfaces on wall-bounded turbulence through direct numerical simulations, while [Busse & Zhdanov \(2022\)](#) studied the impact of the orientation of ratchet-type rough surfaces on the roughness function through direct numerical simulations. [Sarakinis & Busse \(2022\)](#) found that the barnacle-like roughness affects wall-bounded turbulence, and [Busse & Zhdanov \(2022\)](#) found that the roughness function depends on the orientation of the ratchet. The study evaluated existing empirical equations used to estimate the roughness function or the equivalent sand-grain roughness, but these equations failed to predict the differences accurately between ratchet surfaces with high windward slopes and those with high leeward slopes, suggesting the need for developing new empirical relationships or modifying existing ones to account for the orientation-dependency effect.

The study by [Jelly et al. \(2022\)](#) aimed to investigate the impact of varying ES_z on roughness drag penalty using ten irregular surfaces generated by a surface generation algorithm. The study showed that changes in ES_z can significantly affect roughness drag, especially for low- ES_x surfaces. The study builds upon the previous work of [Ramani et al. \(2020\)](#) and used near-Gaussian roughness profiles with a common mean peak-to-valley height while holding other roughness parameters constant. The study by [Abdelaziz et al. \(2023\)](#) investigated the impact of streamwise and spanwise spacing to height ratio on the drag coefficient (C_f) and roughness function ΔU^+ in turbulent boundary layer flows. The study examined seven sinewave profiles with different streamwise and spanwise spacing to height ratios to evaluate their impact on C_f and ΔU^+ . The study showed that streamwise spacing to height ratio had a more significant impact on C_f and ΔU^+ compared to spanwise spacing to height ratio.

The previous extensive literature discussed the challenge of estimating the roughness function or equivalent sand-grain roughness for modelling turbulent flows over rough surfaces, and the absence of a universal correlation due to the intricate nature of roughness topography. Table 8.2 summarises the existing correlations proposed by different researchers. To add to this body of literature, this research aims to develop a universal correlation for estimating k_s of 3D surface textures based solely on roughness parameters using our experimental data and existing published data.

TABLE 8.2: Previous research on k_s correlations

Correlation	Notes	Roughness type	Researchers
$k_s = a.k_t$	$a = 0.625$, Spheres $a = 2$, Fences $a = 1.4$, Hemispheres $a = 0.4$, Machined surfaces	Various grades of emery paper	Forster (1966)
$\Delta U^+ = \begin{cases} a \log k^+ + b(c \log \lambda_p - 1), & 1 < \lambda_p < 4.68 \\ a \log k^+ - d(e \log \lambda_p - 1), & \lambda_p > 4.68 \end{cases}$	$a = 5.6$ $b = 17.35$ $c = 1.625$ $d = 5.95$ $e = 1.103$	2D & 3D roughness	Dvorak (1969)
$\Delta U^+ = \begin{cases} a \log k^+ + b(c \log \lambda_f - 1), & 1 < \lambda_f < 4.68 \\ a \log k^+ - d(e \log \lambda_f - 1), & \lambda_f > 4.68 \end{cases}$	$a = 5.6$ $b = 17.35$ $c = 1.625$ $d = 5.95$ $e = 1.103$	2D & 3D roughness	Simpson (1973)
$\frac{k_s}{k_a} = \begin{cases} 0.0164 \lambda_D^{3.78} & \lambda_D < 4.93 \\ 139 \lambda^{-1.9} & \lambda_D > 4.93 \end{cases}$	$\lambda_D = \frac{D}{k} \left(\frac{A_p}{A_w} \right)^{-4/3}$	Arbitrarily rough surfaces	Dirling (1973)
$\frac{k_s}{k_a} = 6.2$	NA	Emery paper	Koch & Smith Jr (1976)

Continued on next page

TABLE 8.2: Previous research on k_s correlations (continued)

Correlation	Notes	Roughness type	Researchers
$\frac{k_s}{k_t} = \begin{cases} 0.4 & \text{Flow } \perp \text{ milling grooves} \\ 0.2 & \text{Flow } \parallel \text{ milling grooves} \end{cases}$	NA	Manufacturing tolerances of turbines blades	Bammert & Sandstede (1976)
$k_s^+ = \frac{k_q U_\tau}{\nu} (1 + aES)(1 + bk_{sk}k_{ku})$	a and b are constants chosen to provide the best fit for roughness functions	Naturally occurring surfaces	Musker (1980)
$\frac{k_s}{k} = \begin{cases} 0.003215\Lambda_s^{4.925} & 1.4 \leq \Lambda_s \leq 4.89 \\ 8 & 4.89 < \Lambda_s < 13.25 \\ 139\Lambda_s^{-1.9} & 13.25 \leq \Lambda_s \leq 100 \end{cases}$	$\Lambda_s = \frac{S_t}{S_f} \left(\frac{A_f}{A_w} \right)^{-1.6}$	2D & 3D roughness	Sigal & Danberg (1990)
$\frac{k_s}{k} = e^{(C+4)/0.41}$ $C = \begin{cases} a \log \left[\left(\frac{1}{\lambda_f} \frac{k}{b_m} \right)^{0.87} \left(\frac{A_w}{A_f} \right)^{0.44} \right] - b & \Lambda < 6 \\ c \log \left[\left(\frac{1}{\lambda_f} \frac{k}{b_m} \right)^{0.55} \left(\frac{A_w}{A_f} \right)^{1.38} \right] + d & \Lambda > 6 \end{cases}$	$\Lambda = \lambda_f k / s_m$ $\lambda_f = A_f / A_t$ $a = 10.56$ $b = 7.59$ $c = -5.57$ $d = 5.78$	Regular 3D roughness	Waigh & Kind (1998)
$\frac{k_s}{k} = \begin{cases} 1.583 \times 10^{-5} \Lambda_s^{5.683} & \Lambda_s \leq 7.842, \\ 1.802 \Lambda_s^{0.03038} & 7.842 < \Lambda_s < 28.12 \\ 255.5 \Lambda_s^{-1.454} & 28.12 \leq \Lambda_s \end{cases}$	NA	Nonuniform, 3D roughness with irregular geometry	Van Rij <i>et al.</i> (2002)
$\log \left(\frac{k_{s,adj}}{k} \right) = -0.43 \log \Lambda_s + 0.82$ $k_{s,adj} = 0.0138 \alpha_{rms}^2 - 0.0261 \alpha_{rms}$	NA	Real turbine blade roughness	Bons (2002)

Continued on next page

TABLE 8.2: Previous research on k_s correlations (continued)

Correlation	Notes	Roughness type	Researchers
$\log\left(\frac{k_{s,adj}}{k}\right) = -0.43\log\Lambda_s + 0.82$ $\frac{k_{s,adj}}{k_z} = 0.0191\alpha_{rms}^2 + 0.0736\alpha_{rms}$	NA	Real turbine blade roughness	Bons (2005)
$\Delta U^+ = f(ES)$	$ES \approx 0.15$ separates the linear and nonlinear behaviour of ΔU^+	2D corrugated walls	Napoli <i>et al.</i> (2008)
$k_s = 4.3k_q(1 + C_{sk}k_{sk})$	C_{sk} is slightly less than 1	Turbine vane roughness	Boyle & Stripf (2009)
$k_s = 4.43k_q(1 + k_{sk})^{1.37}$	NA	3D roughness	Flack & Schultz (2010)
$\Delta U_{est}^+ = \alpha \log k_a^+ + \beta \log ES + \gamma$	$\alpha = 1/\kappa$ $\beta = 1.12$ $\gamma = 1.47$	Egg cartoon 3D roughness	Chan <i>et al.</i> (2015)
$k = 15.77k_q^2(1 + k_{sk})^{0.862}/sd_4$ $\Delta U^+ = \ln(k^+ + 1)/\kappa$	sd_4 is mean spacing between the zero-crossings	Marine anti-fouling irregular roughness.	Ünal (2015)
$\frac{k_s}{k_q} = 3.47(2 + k_{sk})^{-0.405}$	NA	Grit blasting with various types and sizes of media.	Flack <i>et al.</i> (2016)

Continued on next page

TABLE 8.2: Previous research on k_s correlations (continued)

Correlation	Notes	Roughness type	Researchers
$k_s(\text{Colebrook}) = 0.078k_q^2 + 1.306k_q$ $k_s(\text{Nikuradse}) = 2.294k_q$	Units in μm	Commercial steel pipes	Botros (2016)
$\Delta U^+ = \frac{1}{\kappa} \ln(ES^2) - B + C$	$B = 6.5$ & $C = 8.5$	Regular & irregular rough surfaces	De Marchis (2016)
$\frac{k_s}{D_h} = 18 \frac{k_a}{D_h} - 0.05$	Valid for $\frac{k_a}{D_h} > 0.028$	Additive manufactured random roughness	Stimpson et al. (2017)
$\Delta U^+ = 1.47\lambda_3 + 8$ $\lambda_3 = \lambda_f \left[1 + 0.09 \ln \left(\frac{L_x^{cor}}{k_z} \right) \right]$ $\left(\frac{4k_q}{k_z} \right)^{-0.44} e^{-0.074k_{sk}}$	NA	Irregular roughness	Thakkar et al. (2017)
$\begin{cases} k_s/k = F(k_{sk}) \cdot G(ES), \\ F(k_{sk}) = 0.67k_{sk}^2 + 0.93k_{sk} + 1.3, \\ G(ES) = 1.07 \cdot (1 - e^{-3.5ES}). \end{cases}$	NA	Random roughness	Forooghi et al. (2017)
$\Delta U^+ = f(\lambda_s)$	$\lambda_s = \frac{A_t - A_{sh}}{A_t}$	LEGO bricks	Placidi & Ganapathisubramani (2018)
$\frac{k_s}{k_q} = 3.41(1 + k_{sk})^{0.61}$	NA	3D random roughness	Barros et al. (2018)

Continued on next page

TABLE 8.2: Previous research on k_s correlations (continued)

Correlation	Notes	Roughness type	Researchers
$\frac{k_s}{k_q} = 4(1 + 0.17k_{sk})^4$	NA	Randomly distributed hemispheres	Kuwata & Kawaguchi (2019)
$\Delta U^+ = \frac{1}{\kappa} \ln(ES.k^*) + B$	If $k^* = k_a^+$ $B = 3.5$, If $k^* = k_q^+$ $B = 4$	Superimposing sinusoidal functions	De Marchis et al. (2020)
$k_s = \begin{cases} 2.48k_q(1 + k_{sk})^{2.24} & k_{sk} > 0.00, \\ 2.11k_q & k_{sk} = 0.00, \\ 2.73k_q(2 + k_{sk})^{-0.45} & k_{sk} < 0.00. \end{cases}$	NA	3D random roughness	Flack et al. (2020)
$k_s = a + b(k_t) + c(s_x) + d(ES)(k_{sk})$	$a = 0.001$ $b = 2.029$ $c = -0.114$ $d = 0.013$	2D regular roughness Units in mm	Abdelaziz et al. (2020)
$k_s = a + b(k_t) + c\left(\frac{2k_t}{ES}\right) + d\left(\frac{2k_t}{ES}\right)^2 + e\left(e^{f(ES)(k_{sk})}\right)$	$a = -0.002$ $b = 0.93$ $c = 0.28$ $d = -4.93$ $e = 0.001$ $f = 3.66$	2D & 3D roughness Units in mm	Abdelaziz et al. (2022)

8.4 SURFACE ROUGHNESS

Surface roughness is characterised by small, irregular deviations on a material's surface that cause it to deviate from a perfect plane. It can arise from various mechanisms such as erosion, corrosion, deposition processes, manufacturing processes, and normal wear and tear. The presence of roughness can compromise system safety, efficiency, and performance by altering the momentum and energy transfer and turbulent structure. While natural degradation and

deposition processes decrease compressor and turbine performance in gas turbines (Bons 2010), intentionally manufactured roughness features such as dimples on golf balls and sharkskin denticles on aircraft surfaces are used for drag reduction and aerodynamic enhancement (Soleimani & Eckels 2021). However, due to the diverse forms, types, and textures of roughness, it is challenging to describe it using only one physical parameter. Therefore, it is crucial to identify the primary roughness parameters that affect drag to understand its impact fully. Additionally, combining these crucial parameters can create a formula for the equivalent sand grain roughness denoted as k_s .

In the field of roughness characterisation, height is commonly used as the primary parameter for measurement. Different types of height parameters, including average roughness height (k_a), root-mean-square roughness height (k_q), and maximum peak to valley roughness height (k_t), can be obtained from roughness topography. However, no single parameter can fully describe roughness due to its diverse forms, types and textures. Among these parameters, k_a is one of the most widely used and is directly proportional to the drag experienced by an object in a fluid flow. k_a is the average distance between the roughness profile and the mean line shown in Figure 8.2. k_q and k_t are measures of the entire roughness profile, taking into account the root-mean-square and maximum roughness height, respectively. These parameters are used to characterise surfaces with varying degrees of irregularity and are directly proportional to drag experienced in fluid flow. Figure 8.2 shows the main roughness heights parameters on a sampling length L_s .

The roughness height parameter alone is insufficient to fully characterise the roughness of a surface. Other roughness categories must be employed to evaluate the effect of surface roughness on fluid flow. Roughness frontal solidity λ_f is a dimensionless value that represents the ratio of the frontal projected roughness area A_f to the total roughness area A_t . A high roughness frontal solidity indicates that the roughness elements are closely spaced and are likely to have a significant effect on the fluid flow, while a low roughness frontal solidity indicates that the roughness elements are widely spaced and are likely to have a minimal effect.

Another roughness parameter used to characterise the roughness of a surface is the effective slope ES . The ES is a dimensionless value that represents the average slope of the roughness elements on a surface. It is also known as the average slope of the roughness profile or the average inclination angle of the roughness elements. A high ES indicates that the roughness elements are steep and are likely to have a significant effect on the fluid flow, while a low ES indicates that the roughness elements are gentle and are likely to have a minimal effect. Figure 8.3 shows a simple schematic of different configurations of 3D isotropic sinusoidal surfaces with

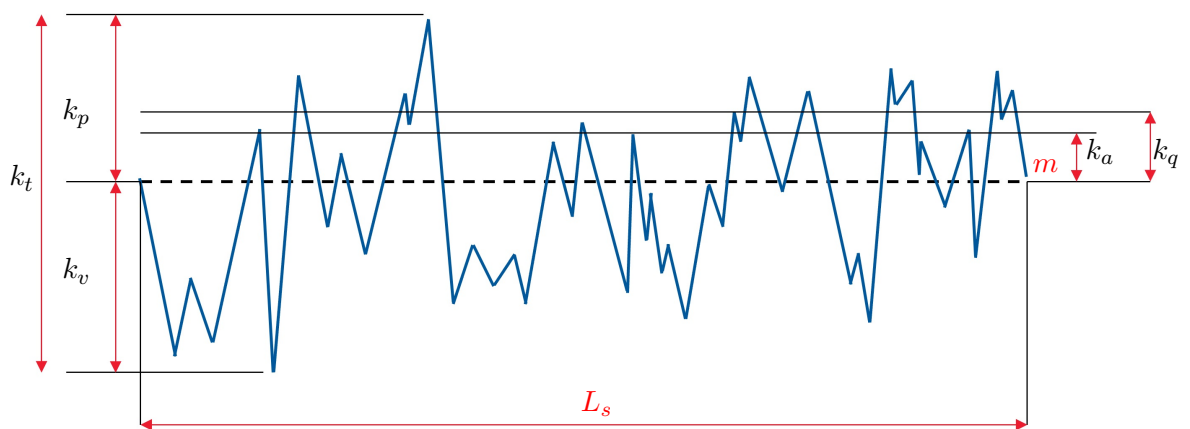


FIGURE 8.2: The main roughness heights parameters on a sampling length L_s . The dashed line represents the mean line m , the reference line about which the profile deviations are measured.

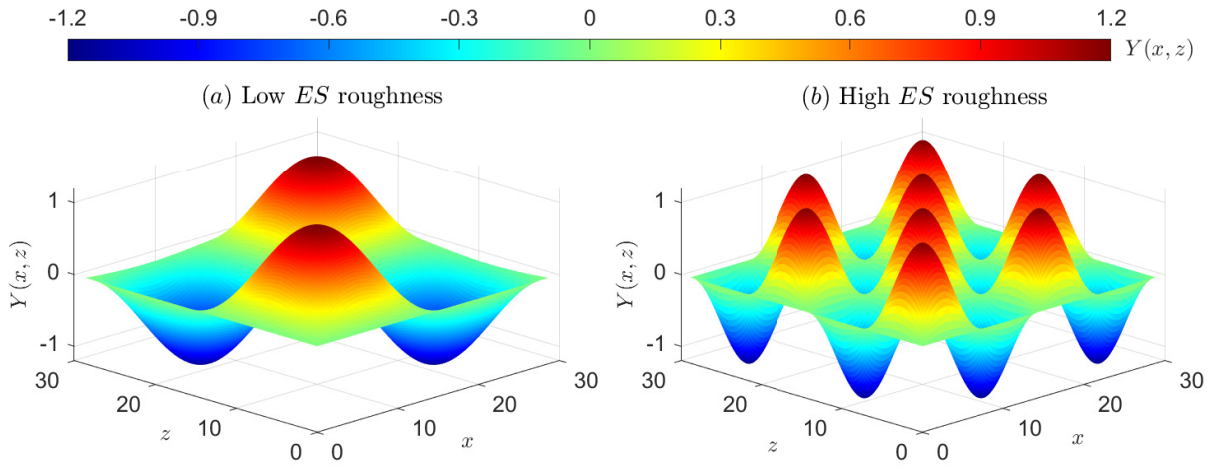


FIGURE 8.3: Sketches of different configurations of 3D isotropic sinusoidal surfaces with equal streamwise and spanwise roughness effective slopes. (a) Low ES value. (b) High ES value. The contours are plotted with the same coordinates for ease of comparison.

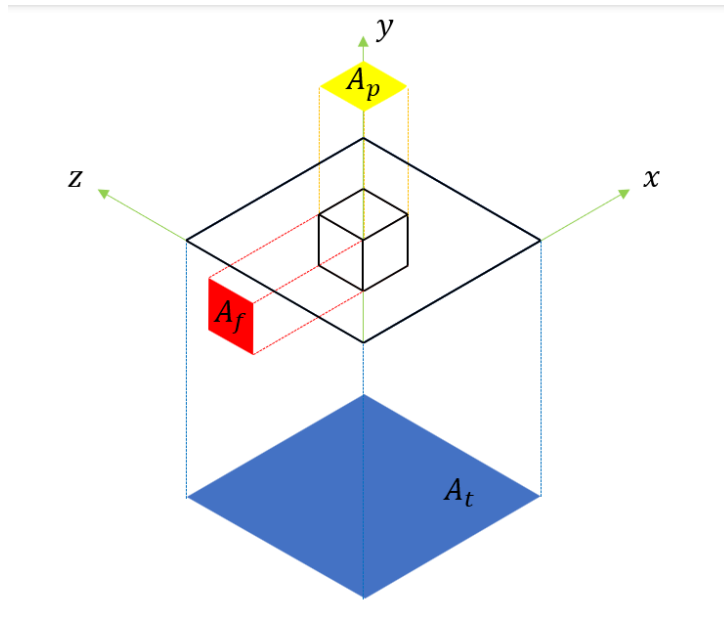


FIGURE 8.4: Sketch of rough surface illustrates how frontal and plan solidity are calculated. The red area is the frontal projection of the rough element. The yellow area represents the plan projection of the rough element. The blue area is the projection of the total area of the surface.

the roughness profile with the centerline at different points along the surface. A positive value indicates that the roughness profile has more peaks than valleys, while a negative value indicates the opposite. This parameter plays a crucial role in understanding the impact of roughness on fluid flow, particularly in turbulent flows. A high positive roughness skewness implies that the roughness elements are steep and can have a significant effect on fluid flow, whereas a low or negative roughness skewness implies that the roughness elements are gentle and have a minimal impact on fluid flow. Figure 8.5 shows a simple schematic of different configurations of 3D isotropic sinusoidal surfaces with negative, zero and positive skewness values.

The roughness kurtosis k_{ku} is an important parameter used in fluid flow studies to assess the impact of surface roughness. It is a dimensionless value that quantifies the peakedness or flatness of the roughness profile of a surface. If the roughness kurtosis value is less than 3, the height distribution of the roughness profile tends to have light tails or lack of outliers, whereas a

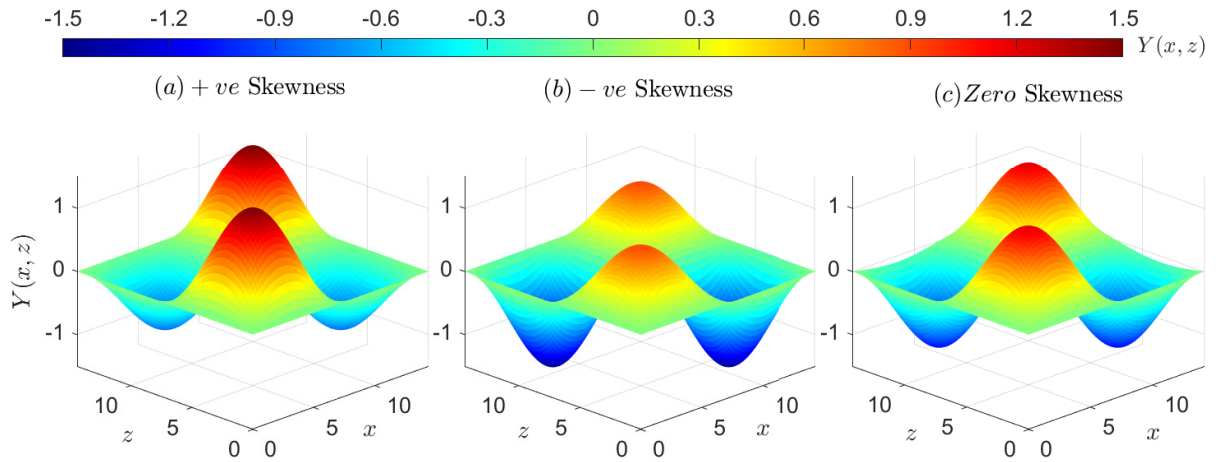


FIGURE 8.5: Sketches of different configurations of 3D isotropic sinusoidal surfaces with equal streamwise and spanwise roughness skewness. (a) Positive skewness value. (b) Negative skewness value. (c) Zero skewness roughness. The contours are plotted with the same coordinates for ease of comparison.

TABLE 8.3: Different roughness parameters and their corresponding equations.

Roughness parameter	Equation
k_a	$\frac{1}{A_s} \iint_{A_s} Y(x, z) dx dz$
k_q	$\sqrt{\frac{1}{A_s} \iint_{A_s} Y(x, z)^2 dx dz}$
k_t	$k_p - k_v$
λ_f	$\frac{A_f}{A_t}$
λ_p	$\frac{A_p}{A_t}$
ES_x	$\frac{1}{A_s} \iint_{A_s} \left \frac{dY(x, z)}{dx} \right dx dz$
ES_z	$\frac{1}{A_s} \iint_{A_s} \left \frac{dY(x, z)}{dz} \right dx dz$
k_{sk}	$\frac{1}{k_q^3 A_s} \iint_{A_s} Y(x, z)^3 dx dz$
k_{ku}	$\frac{1}{k_q^4 A_s} \iint_{A_s} Y(x, z)^4 dx dz$

value greater than 3 indicates a spike height distribution. A value of 3 corresponds to a normal distribution of the roughness height. The various roughness parameters and their respective equations are summarised in Table 8.3.

8.5 RESULTS AND DISCUSSION

In order to effectively describe a rough surface, a combination of the three roughness categories, namely height, slope, and asymmetry, is considered to be the most appropriate approach. In order to understand the impact of these roughness parameters on a turbulent boundary layer (TBL) and identify the specific parameters that influence turbulence statistics and drag coefficient.

The present study explores a comprehensive assortment of 3D surface textures available in the literature to evaluate the efficacy of predictive correlations and to formulate more universal ones. The roughness data utilised for this analysis is primarily obtained from our experiments and from the Roughness Database (Roughnessdatabase.org). The classification scheme employed to categorise the roughness patterns incorporates the following criteria: regular roughness (Reg.) represented by unfilled symbols or irregular roughness (Irreg.) depicted by filled symbols, flow configuration in the form of channel flows (Cha.) represented by square symbols or turbulent boundary layer (TBL) indicated by triangle symbols, study method with experimental investigations (Exp.) indicated by larger symbols and numerical investigations (Sim.) represented by smaller symbols, and authorship with different symbol colours assigned to the common authors. Table 8.4 presents a synopsis of the statistical properties of diverse rough surface topographies and their corresponding k_s values attributed to various studies. A total of approximately 120 distinct 3D surface textures were compiled through the following classification scheme: roughly 80 instances of irregular patterns and 40 instances of regular patterns, around 80 instances of channel flows and 40 instances of turbulent boundary layer (TBL) flows, with nearly equal representation between experimental investigations and numerical investigations, totalling roughly half of the cases for each.

8.5.1 Existing k_s correlations

To commence, an assessment will be conducted to evaluate the effectiveness of current predictive correlations on both regular and irregular 3D roughness. The outcome of this evaluation will provide insights into the crucial roughness parameters capable of establishing a correlation with k_s , and further examine if any of the existing correlations are suitable for various types of 3D roughness.

In Figure 8.6, the predicted k_s values using six distinct correlations for different regular 3D roughness are plotted against the actual k_s values. The first correlation, proposed by [Boyle & Stripf \(2009\)](#), utilises truncated cone roughness elements with different arrangements to derive a k_s correlation from k_q and k_{sk} . The application of this correlation equation on different regular roughness cases resulted in a relatively accurate predicted k_s value with an R^2 value of 0.78, as depicted in Figure 8.6(a). The coefficient of determination (R^2) is used as a statistical metric to evaluate the proximity of the data to the fitted regression line. The second correlation was developed by [Flack *et al.* \(2016\)](#) using fifteen surfaces produced by grit blasting with various types and sizes of media. The correlation equation proposed by [Flack *et al.* \(2016\)](#) was applied to diverse regular roughness cases, resulting in a predicted k_s value with an R^2 of 0.45, as illustrated in Figure 8.6(b). The third correlation was formulated by [Forooghi *et al.* \(2017\)](#) using DNS of channel flow and three parameters, namely k_t , ES , and k_{sk} , where roughness elements of random sizes and prescribed shapes were randomly distributed on different wall geometries. The application of the correlation equation proposed by [Forooghi *et al.* \(2017\)](#) on various regular roughness cases resulted in a remarkably accurate predicted k_s value with an R^2 of 0.98, as depicted in Figure 8.6(c). The fourth correlation was developed by [Barros](#)

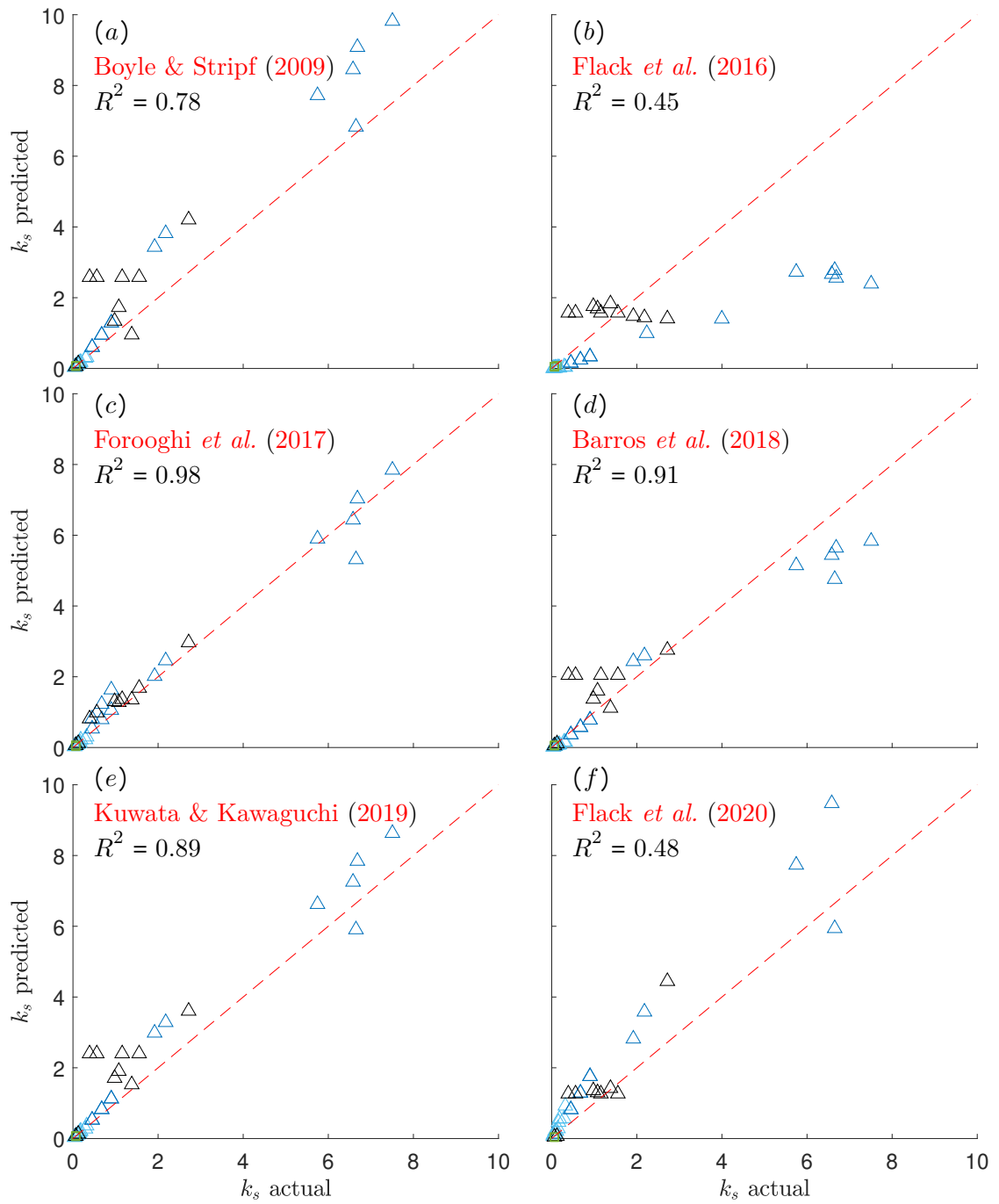


FIGURE 8.6: Comparison between actual k_s and predicted k_s for regular 3D roughnesses using different correlation from literature: (a) correlation from Boyle & Stripf (2009), (b) correlation from Flack *et al.* (2016), (c) correlation from Forooghi *et al.* (2017), (d) correlation from Barros *et al.* (2018), (e) correlation from Kuwata & Kawaguchi (2019) and (f) correlation from Flack *et al.* (2020).

TABLE 8.4: The statistical characteristics of different rough surface topographies and k_s values, gathered from literature, are presented. Both experimental and numerical data have been utilised, and the measurements are given in millimetres.

Author	Sym.	Type	Study	Flow type	k_t	k_a	k_q	k_{sk}	k_{ku}	ES_x	ES_z	k_s
Schultz & Flack 2003	▲	Irreg.	Exp.	TBL	0.02-0.98	0.002-0.130	0.003-0.150	-0.27-0.34	3.07-4.20	0.06-1.40	-	0.02-0.51
Boyle & Stripf 2009	△	Reg.	Exp.	TBL	0.01-0.60	0.002-0.120	0.003-0.150	1.00-2.87	3.0-8.7	0.15-0.60	0.15-0.60	0.04-0.90
Flack <i>et al.</i> 2016	■	Irreg.	Exp.	Cha.	0.13-0.36	0.005-0.016	0.007-0.020	-1.44-1.00	3.0-22.2	0.39-0.74	0.45-0.87	0.02-0.07
Forooghi <i>et al.</i> 2017	■	Irreg.	Sim.	Cha.	0.14-0.23	0.032-0.037	0.039-0.044	-0.40-0.68	1.8-2.8	0.17-0.93	0.17-0.90	0.07-0.50
Barros <i>et al.</i> 2018	■	Irreg.	Exp.	Cha.	0.23-0.34	0.020-0.360	0.025-0.045	0.10-0.30	2.9	0.15-0.18	0.14-0.19	0.02-0.05
Flack <i>et al.</i> 2020	■	Irreg.	Exp.	Cha.	0.23-0.89	0.020-0.090	0.025-0.110	-0.66-0.81	2.8-3.6	0.15-0.56	0.14-0.56	0.02-0.44
Jouybari <i>et al.</i> 2021	■ □	Irreg. -Reg.	Sim.	Cha.	0.06-0.17	0.010-0.060	0.010-0.040	-0.65-2.14	1.5-7.3	0.10-1.13	0.08-0.76	0.02-0.54
Womack <i>et al.</i> 2022	▲ △	Irreg. -Reg.	Exp.	TBL	3.15	0.160-1.530	0.590-1.210	0.04-3.96	1.5-18.0	0.08-0.63	0.60-0.07	2.12-8.10
Yang <i>et al.</i> 2022	■	Irreg.	Sim.	Cha.	0.12	0.016	0.020	-0.49-0.49	3.0	0.36-0.57	0.36-0.56	0.003-0.009
Sarakinos & Busse 2022	■	Irreg.	Sim.	Cha.	0.13	0.009-0.030	0.018-0.034	0.40-4.10	2.1-19.5	0.07-0.55	-	0.07-0.24
Flack & Schultz 2023	■	Irreg.	Exp.	Cha.	0.19-0.25	0.015-0.020	0.019-0.027	-0.08-0.48	2.7-3.2	0.35-0.65	0.35-0.63	0.07-0.14
Abdelaziz <i>et al.</i> 2023	△	Reg.	Exp.	TBL	2.40	0.470	0.600	0.00	2.3	0.08-0.20	0.08-0.20	0.39-2.37
Abdelaziz <i>et al.</i> 2023	△	Reg.	Exp.	TBL	2.40	0.470	0.600	-0.63-0.63	2.3-2.5	0.10-0.22	0.10-0.22	0.56-2.72

et al. (2018) using three controlled roughness surfaces produced by a high-resolution 3D printer. The application of the correlation equation proposed by Barros *et al.* (2018) on diverse regular roughness cases resulted in a relatively accurate prediction of k_s values with an R^2 of 0.91, as shown in Figure 8.6(d). The fifth correlation proposed by Kuwata & Kawaguchi (2019) was based on k_q and k_{sk} obtained using DNS of channel flow over randomly distributed hemispheres. The accuracy of this correlation equation was evaluated by applying it to various regular roughness cases, resulting in a reasonably precise prediction of k_s values with an R^2 of 0.89, as presented in Figure 8.6(e). The sixth correlation was developed by Flack *et al.* (2020), aiming to investigate channel flows over random roughnesses with a Gaussian power spectral density distribution of surface elevations. The correlation equation proposed by Flack *et al.* (2020) utilised k_q and k_{sk} to predict the roughness coefficient (k_s). The proposed correlation equation was applied to

various regular roughness cases, resulting in a prediction of k_s values with an R^2 value of 0.45, as demonstrated in Figure 8.6(f).

Figure 8.6 illustrates that the correlations proposed by [Forooghi *et al.* \(2017\)](#), [Barros *et al.* \(2018\)](#), and [Kuwata & Kawaguchi \(2019\)](#) exhibit a high degree of accuracy in predicting k_s values for various regular roughness cases. These correlations are formulated based on the roughness parameters k_t , k_q , k_{sk} , and ES , which appear to be significant factors in correlating k_s for regular roughness. The next step involves evaluating the efficacy of the same set of six predictive correlations on irregular 3D roughness, which is a more realistic representation of surface roughness.

In Figure 8.7, the predicted k_s values obtained from each correlation of the same six distinct correlations are compared with the actual values when applied for different types of irregular 3D roughness. The first correlation proposed by [Boyle & Stripf \(2009\)](#) yielded an R^2 value of 0.56 when applied to different types of irregular roughness cases, as illustrated in Figure 8.7(a). Similarly, the second correlation developed by [Flack *et al.* \(2016\)](#) resulted in an R^2 value of 0.33 when applied to diverse types of irregular roughness, as shown in Figure 8.7(b). The third correlation proposed by [Forooghi *et al.* \(2017\)](#) was applied to various types of irregular roughness and yielded an R^2 value of 0.49, as depicted in Figure 8.7(c). The fourth correlation developed by [Barros *et al.* \(2018\)](#) yielded an R^2 value of 0.52 when applied to different types of irregular roughness, as shown in Figure 8.7(d). The fifth correlation proposed by [Kuwata & Kawaguchi \(2019\)](#) resulted in an R^2 value of 0.48 when applied to various types of irregular roughness, as presented in Figure 8.7(e). Finally, the sixth correlation developed by [Flack *et al.* \(2020\)](#) yielded an R^2 value of 0.55 when applied to different types of irregular roughness, as demonstrated in Figure 8.7(f).

The results presented in Figure 8.7 suggest that the majority of the predictive correlations demonstrate comparable levels of precision in forecasting k_s values for a range of irregular roughness cases, with an accuracy of around 50%. The ultimate phase of the assessment of the predictive correlations involves their application to all the 3D cases, comprising both regular and irregular 3D roughness, as depicted in Figure 8.8.

Figure 8.8 presents a comparison of the predicted k_s values obtained from the six distinct correlations against the actual values when applied to different types of regular and irregular 3D roughness surfaces. The first correlation proposed by [Boyle & Stripf \(2009\)](#) yielded an R^2 value of 0.75 when applied to various types of regular and irregular 3D roughness cases, as depicted in Figure 8.8(a). For the second correlation developed by [Flack *et al.* \(2016\)](#), the R^2 value was 0.56 when applied to diverse types of regular and irregular roughness, as shown in Figure 8.8(b). The third, fourth, and fifth correlations proposed by [Forooghi *et al.* \(2017\)](#), [Barros *et al.* \(2018\)](#), and [Kuwata & Kawaguchi \(2019\)](#), respectively, were applied to different types of regular and irregular roughness, resulting in an R^2 value of approximately 0.80, as illustrated in Figures 8.8(c)-8.8(e). Lastly, the sixth correlation developed by [Flack *et al.* \(2020\)](#) yielded an R^2 value of 0.69 when applied to various types of regular and irregular roughness, as demonstrated in Figure 8.8(f).

Based on the preceding discussion, it appears that the correlation proposed by [Forooghi *et al.* \(2017\)](#) shows the highest R^2 value for predicting k_s for regular, irregular, and both regular and irregular roughness. This correlation employs significant parameters such as k_t , k_{sk} , and ES to establish correlations with k_s . However, it appears that there is scope for enhancing the accuracy of this correlation, which is discussed in the subsequent section.

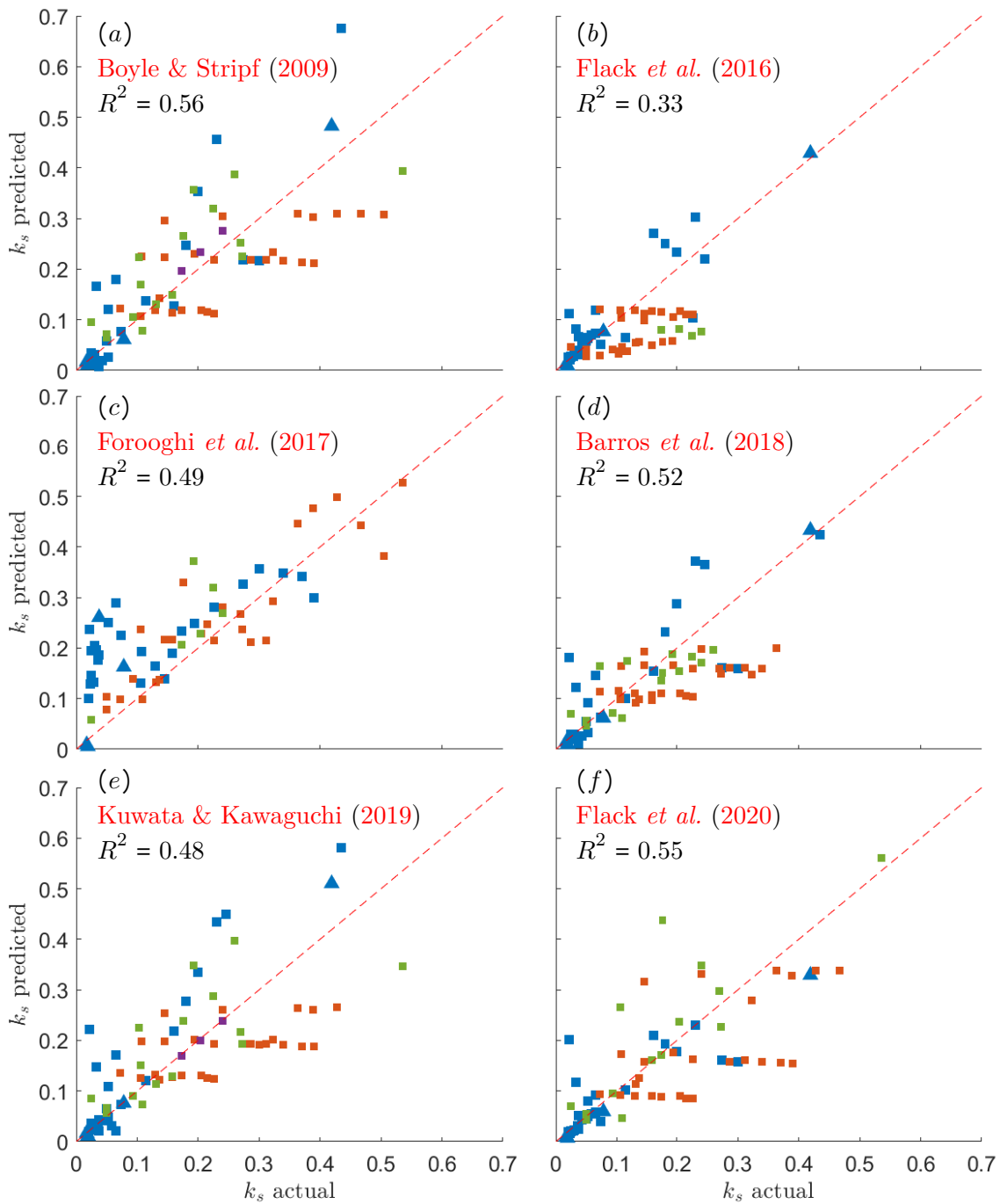


FIGURE 8.7: Comparison between actual k_s and predicted k_s for irregular 3D roughnesses using different correlation from literature: (a) correlation from Boyle & Stripf (2009), (b) correlation from Flack *et al.* (2016), (c) correlation from Forooghi *et al.* (2017), (d) correlation from Barros *et al.* (2018), (e) correlation from Kuwata & Kawaguchi (2019) and (f) correlation from Flack *et al.* (2020).

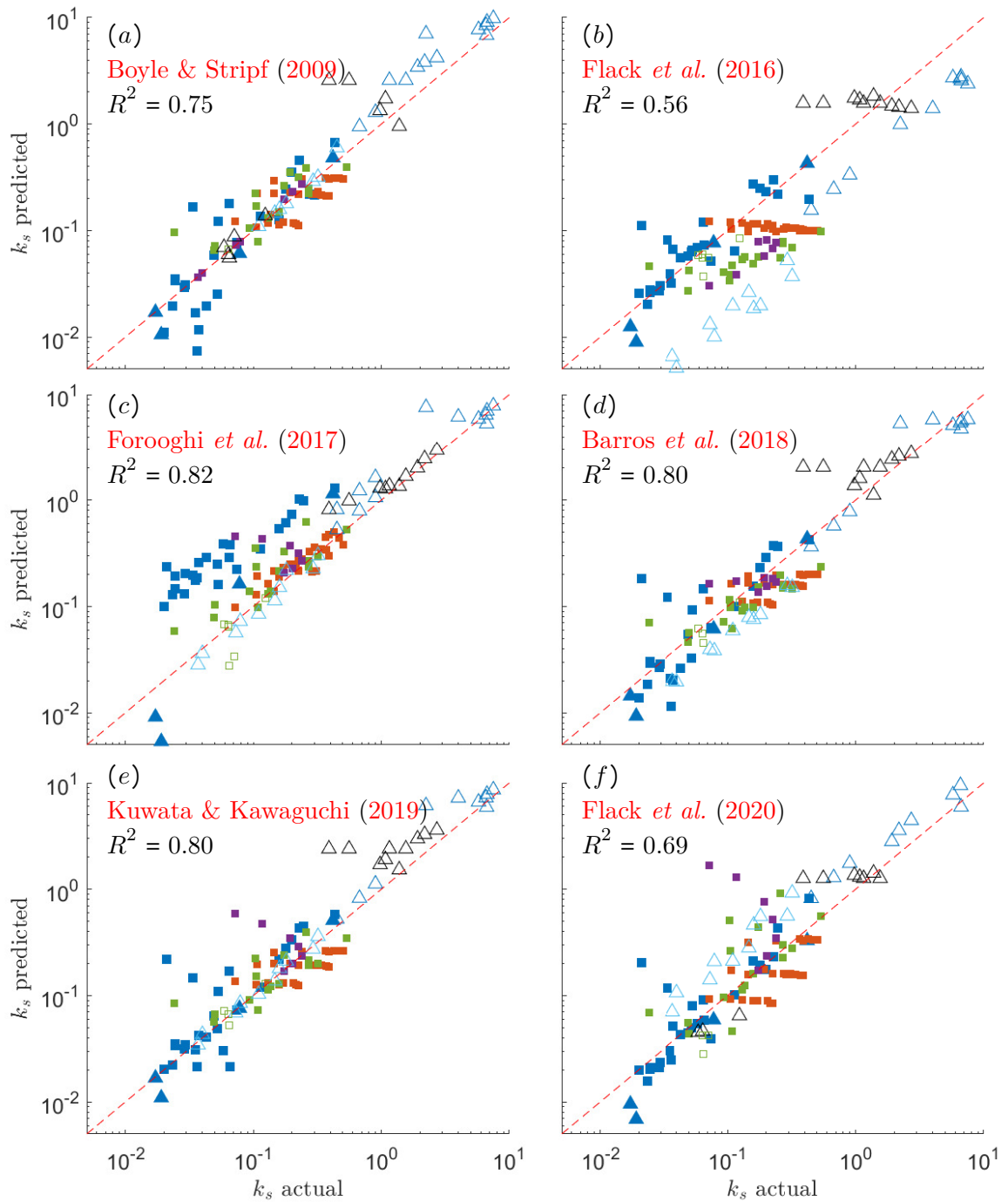


FIGURE 8.8: Comparison between actual k_s and predicted k_s for all 3D roughnesses using different correlation from literature: (a) correlation from Boyle & Stripf (2009), (b) correlation from Flack *et al.* (2016), (c) correlation from Forooghi *et al.* (2017), (d) correlation from Barros *et al.* (2018), (e) correlation from Kuwata & Kawaguchi (2019) and (f) correlation from Flack *et al.* (2020).

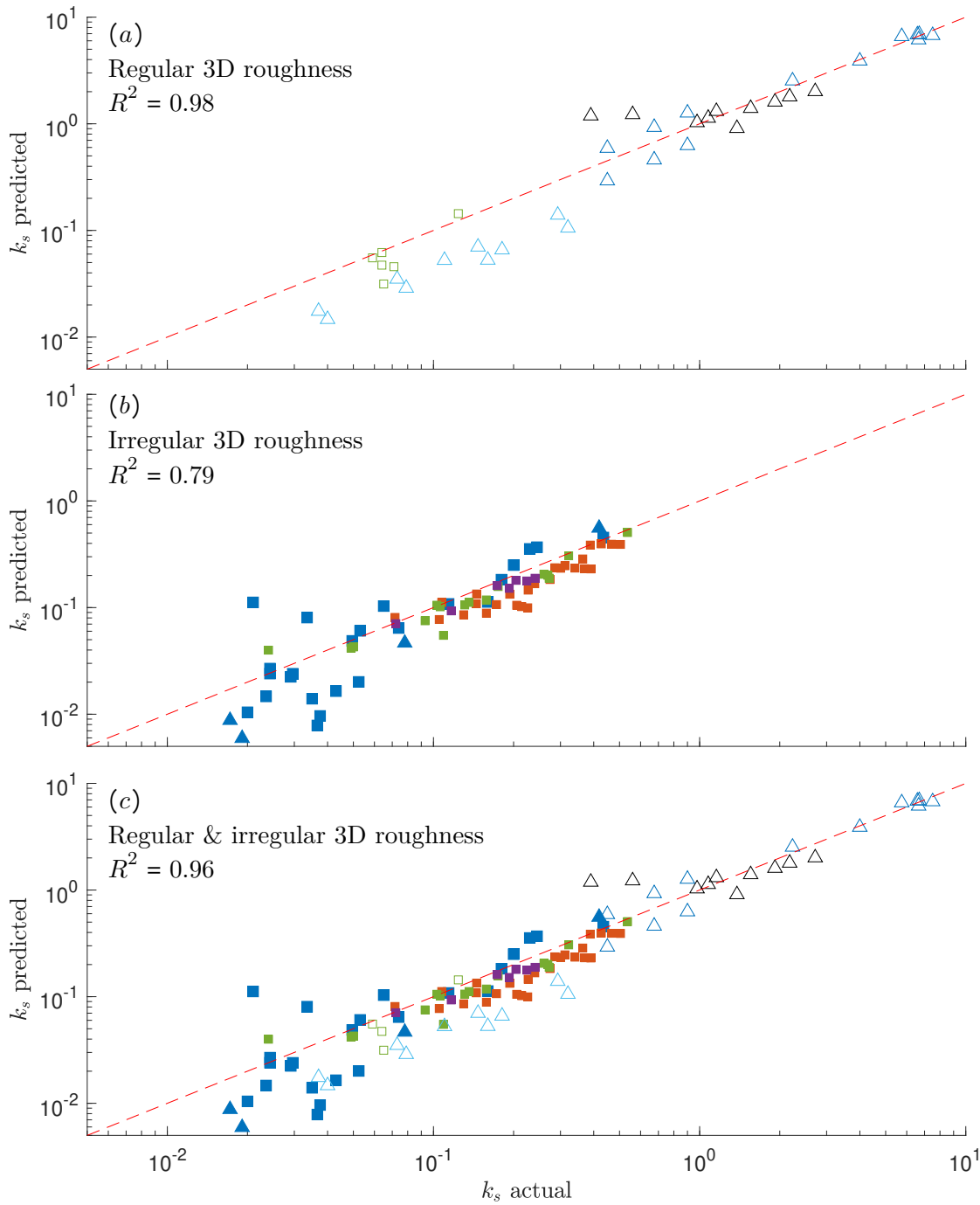


FIGURE 8.9: Comparison between actual k_s and predicted k_s using the new predicted correlation 8.2 for (a) regular 3D roughnesses, (b) irregular 3D roughnesses, (c) regular and irregular 3D roughnesses.

8.5.2 New k_s correlation

The current findings provide an opportunity to develop predictive correlations for the normalised equivalent sand grain roughness height, expressed as $k_s/k_* = f(k_{sk}, ES)$, where k_* denotes the roughness height parameter such as k_t , k_q , or k_a . To accomplish this, various non-linear regression analyses using different relationships, including exponential, power,

and polynomial functions, were explored with different roughness parameters. As a result, the following correlation was derived:

$$\frac{k_s}{k_q} = a + bk_{sk} + cES_x + de^{ek_{sk}ES_x}, \quad (8.2)$$

where $a = -7.65$, $b = -0.0013$, $c = 2.90$, $d = 9.40$ and $e = 0.705$.

The procedure for evaluating the effectiveness of the newly proposed predictive correlation on both regular and irregular 3D roughness is identical to the one discussed previously. Figure 8.9 depicts the comparison between the predicted k_s values obtained from the new correlation and the actual values when applied to different types of regular and irregular 3D roughness. When applied to different types of regular roughness cases, the correlation generated an R^2 value of 0.98, as presented in Figure 8.9(a). In contrast, when applied to diverse types of irregular roughness, the correlation yielded an R^2 value of 0.83, as depicted in Figure 8.9(b). Finally, when the correlation was employed to various types of regular and irregular roughness, the predicted k_s value was remarkably accurate, with an R^2 of 0.96, as shown in Figure 8.9(c).

It is important to note that the newly proposed correlation for k_s is limited to 3D roughness in a fully rough regime. The range of roughness parameters examined in the approximately 120 cases are as follows: $0.01 < k_t < 3.2$ mm, $0.002 < k_a < 1.3$ mm, $0.003 < k_q < 1.2$ mm, $-1.5 < k_{sk} < 4.0$, $1.5 < k_{ku} < 22$, $0.06 < ES_x < 1.4$, and $0.08 < ES_y < 0.9$. Further experiments on a wider range of roughness parameters are necessary to validate this correlation. Such studies will help in developing a more generalised correlation for k_s , if such generalisation is possible.

8.6 CONCLUSIONS

The study focuses on the aim of determining the drag penalty on surfaces solely based on their topographical parameters. In order to standardise different types of roughness in wall-bounded turbulence and provide an input parameter for predictions, the concept of equivalent sand-grain roughness k_s was introduced by Nikuradse (1933). However, despite the usefulness of this parameter, it is not an actual roughness parameter and there is still a lack of consensus on which length scale or roughness parameter is most effective in describing a surface in relation to friction drag.

To address the lack of consensus on the most effective method of characterising surface roughness in relation to friction drag, we compiled a table of roughness correlations available in the literature that lists the parameter ranges and roughness types used in their development. Table 8.2 includes multiple equations for estimating k_s using various approaches to roughness characterisation. The variability in the proposed equations in the table demonstrates that no single correlation can accurately estimate the equivalent roughness height for all types of roughness.

To assess the efficacy of various predictive correlations, we conducted an evaluation of six recently proposed methods. Our analysis encompassed a comprehensive range of three-dimensional (3D) surface textures, as documented in the literature. The roughness data utilised in this study was predominantly obtained from our own experiments, as well as from the Roughness Database (Roughnessdatabase.org). Based on our findings, it was found that the predictive correlations proposed by Forooghi *et al.* (2017), Barros *et al.* (2018), and Kuwata & Kawaguchi (2019) exhibit a high degree of accuracy in predicting k_s for regular roughness. However, when applied to a range of irregular roughness, these correlations showed similar levels of precision, achieving an accuracy of only approximately $R^2 \approx 0.5$.

In order to address the need for more accurate predictions of k_s , we introduced a new equation for normalised k_s that involves the physical roughness parameters of surface height skewness k_{sk} , streamwise effective slope ES_x , and the root mean square roughness height k_q . This new expression was found to be effective in predicting k_s for regular and irregular 3D roughness in the fully rough regime. It should be noted that this relation is limited to the roughness parameters examined in this study, with the following ranges: $0.01 < k_t < 3.2$ mm, $0.002 < k_a < 1.3$ mm, $0.003 < k_q < 1.2$ mm, $-1.5 < k_{sk} < 4.0$, $1.5 < k_{ku} < 22$, $0.06 < ES_x < 1.4$, and $0.08 < ES_y < 0.9$. Further experiments on wider ranges of roughness parameters are needed to develop a more generalised relation for k_s .

ACKNOWLEDGMENTS

The authors acknowledge the financial support of the Australian Research Council.

AUTHOR DECLARATIONS

Conflict of Interest

The authors have no conflicts to disclose.

Bibliography

- ABDELAZIZ, M., DJENIDI, L., GHAYESH, M., & CHIN, R. 2020 Turbulent boundary layer over various 2d uniform distributed roughness elements. In *22nd Australasian Fluid Mechanics Conference, AFMC 2020*. The University of Queensland.
- ABDELAZIZ, M., DJENIDI, L., GHAYESH, M., & CHIN, R. 2023 On the effect of streamwise and spanwise spacing to height ratios of three-dimensional sinusoidal roughness on turbulent boundary layers. *Physics of Fluids* **35** (2).
- ABDELAZIZ, M., DJENIDI, L., GHAYESH, M. H., & CHIN, R. 2022 A new equivalent sand grain roughness relation for two-dimensional rough wall turbulent boundary layers. *Journal of Fluid Mechanics* **940**, A25.
- BAMMERT, K. & SANDSTEDT, H. 1976 Influences of manufacturing tolerances and surface roughness of blades on the performance of turbines. *Journal of Engineering for Power* **98** (1), 29–36.
- BANDYOPADHYAY, P. R. 1987 Rough-wall turbulent boundary layers in the transition regime. *Journal of Fluid Mechanics* **180**, 231–266.
- BARROS, J. M., SCHULTZ, M. P., & FLACK, K. A. 2018 Measurements of skin-friction of systematically generated surface roughness. *International Journal of Heat and Fluid Flow* **72**, 1–7.
- BOGARD, D. G., SCHMIDT, D. L., & TABBITA, M. 1996 Characterization and laboratory simulation of turbine airfoil surface roughness and associated heat transfer. In *Turbo Expo: Power for Land, Sea, and Air, Turbo Expo: Power for Land, Sea, and Air*, vol. Volume 4: Heat Transfer; Electric Power; Industrial and Cogeneration. American Society of Mechanical Engineers.

- BONS, J. 2005 A critical assessment of reynolds analogy for turbine flows. *Journal of Heat Transfer* **127** (5), 472–485.
- BONS, J. P. 2002 S_t and C_f augmentation for real turbine roughness with elevated freestream turbulence. *Turbo Expo: Power for Land, Sea, and Air*, vol. Volume 3: Turbo Expo 2002, Parts A and B, pp. 349–363.
- BONS, J. P. 2010 A review of surface roughness effects in gas turbines. *Journal of Turbomachinery* **132** (2).
- BOTROS, K. 2016 Experimental investigation into the relationship between the roughness height in use with nikuradse or colebrook roughness functions and the internal wall roughness profile for commercial steel pipes. *Journal of Fluids Engineering* **138** (8).
- BOYLE, R. J. & STRIPF, M. 2009 Simplified approach to predicting rough surface transition. *Journal of Turbomachinery* **131** (4).
- BRADSHAW, P. 2000 A note on “critical roughness height” and “transitional roughness”. *Physics of Fluids* **12** (6), 1611–1614.
- BUSSE, A. & ZHDANOV, O. 2022 Direct numerical simulations of turbulent channel flow over ratchet roughness. *Flow, Turbulence and Combustion* **109** (4), 1195–1213.
- CEBECI, T. & BRADSHAW, P. 1977 *Momentum transfer in boundary layers*. Hemisphere Publishing Corporation: New York, NY, USA.
- CHAN, L., MACDONALD, M., CHUNG, D., HUTCHINS, N., & OOI, A. 2015 A systematic investigation of roughness height and wavelength in turbulent pipe flow in the transitionally rough regime. *Journal of Fluid Mechanics* **771**, 743–777.
- DARCY, H. 1857 *Recherches expérimentales relatives au mouvement de l’eau dans les tuyaux*. vol. 1., Mallet-Bachelier.
- DE MARCHIS, M. 2016 Large eddy simulations of roughened channel flows: Estimation of the energy losses using the slope of the roughness. *Computers & Fluids* **140**, 148–157.
- DE MARCHIS, M., SACCONI, D., MILICI, B., & NAPOLI, E. 2020 Large eddy simulations of rough turbulent channel flows bounded by irregular roughness: advances toward a universal roughness correlation. *Flow, Turbulence and Combustion* **105**, 627–648.
- DIRLING, JR, R. 1973 A method for computing rough wall heat transfer rates on reentry nosetips. In *8th Thermophysics Conference*, p. 763.
- DVORAK, F. 1969 Calculation of turbulent boundary layers on rough surfaces in pressure gradient. *AIAA Journal* **7** (9), 1752–1759.
- FLACK, K. A. & SCHULTZ, M. P. 2010 Review of hydraulic roughness scales in the fully rough regime. *Journal of Fluids Engineering* **132** (4).
- FLACK, K. A. & SCHULTZ, M. P. 2023 Hydraulic characterization of sandpaper roughness. *Experiments in Fluids* **64** (1), 3.
- FLACK, K. A., SCHULTZ, M. P., & BARROS, J. M. 2020 Skin friction measurements of systematically-varied roughness: Probing the role of roughness amplitude and skewness. *Flow, Turbulence and Combustion* **104** (2), 317–329.

- FLACK, K. A., SCHULTZ, M. P., BARROS, J. M., & KIM, Y. C. 2016 Skin-friction behavior in the transitionally-rough regime. *International Journal of Heat and Fluid Flow* **61**, 21–30.
- FLACK, K. A., SCHULTZ, M. P., & ROSE, W. B. 2012 The onset of roughness effects in the transitionally rough regime. *International Journal of Heat and Fluid Flow* **35**, 160–167.
- FOROOGHI, P., STROH, A., MAGAGNATO, F., JAKIRLIĆ, S., & FROHNAPFEL, B. 2017 Toward a universal roughness correlation. *Journal of Fluids Engineering* **139** (12).
- FORSTER, V. 1966 Performance loss of modern steam-turbine plant due to surface roughness. *Proceedings of the Institution of Mechanical Engineers* **181** (1), 391–422.
- GOODHAND, M. N., WALTON, K., BLUNT, L., LUNG, H. W., MILLER, R. J., & MARSDEN, R. 2016 The limitations of using “Ra” to describe surface roughness. *Journal of Turbomachinery* **138** (10), 101003.
- HAMA, F. R. 1954 Boundary layer characteristics for smooth and rough surfaces. *Trans. Soc. Nav. Arch. Marine Engrs.* **62**, 333–358.
- JELLY, T., RAMANI, A., NUGROHO, B., HUTCHINS, N., & BUSSE, A. 2022 Impact of spanwise effective slope upon rough-wall turbulent channel flow. *Journal of Fluid Mechanics* **951**, A1.
- JOUYBARI, M. A., YUAN, J., BRERETON, G. J., & MURILLO, M. S. 2021 Data-driven prediction of the equivalent sand-grain height in rough-wall turbulent flows. *Journal of Fluid Mechanics* **912**, A08.
- KOCH, C. & SMITH JR, L. 1976 Loss sources and magnitudes in axial-flow compressors. *Journal of Engineering for Power* **98** (3), 411–424.
- KUWATA, Y. & KAWAGUCHI, Y. 2019 Direct numerical simulation of turbulence over systematically varied irregular rough surfaces. *Journal of Fluid Mechanics* **862**, 781–815.
- KUWATA, Y., SUGA, K., & KAWAGUCHI, Y. 2019 An extension of the second moment closure model for turbulent flows over macro rough walls. *International Journal of Heat and Fluid Flow* **77**, 186–201.
- LANGELANDSVIK, L., KUNKEL, G., & SMITS, A. J. 2008 Flow in a commercial steel pipe. *Journal of Fluid Mechanics* **595**, 323–339.
- LEWKOWICZ, A. & MUSKER, A. 1978 The surface roughness on ship hulls: interaction in the viscous sublayer. In *Proceedings of the International Symposium on Ship Viscous Resistance-SSPA*.
- LIGRANI, P. M. & MOFFAT, R. J. 1986 Structure of transitionally rough and fully rough turbulent boundary layers. *Journal of Fluid Mechanics* **162**, 69–98.
- MANNING, R., GRIFFITH, J. P., PIGOT, T., & VERNON-HARCOURT, L. F. 1890 *On the flow of water in open channels and pipes*.
- MEDJNOUN, T., RODRIGUEZ-LOPEZ, E., FERREIRA, M., GRIFFITHS, T., MEYERS, J., & GANAPATHISUBRAMANI, B. 2021 Turbulent boundary-layer flow over regular multiscale roughness. *Journal of Fluid Mechanics* **917**, A1.

- MONTY, J., DOGAN, E., HANSON, R., SCARDINO, A., GANAPATHISUBRAMANI, B., & HUTCHINS, N. 2016 An assessment of the ship drag penalty arising from light calcareous tubeworm fouling. *Biofouling* **32** (4), 451–464.
- MOODY, L. F. 1944 Friction factors for pipe flow. *Trans. ASME* **66**, 671–684.
- MUSKER, A. J. 1980 Universal roughness functions for naturally-occurring surfaces. *Transactions of the Canadian Society for Mechanical Engineering* **6** (01), 1–6.
- NAPOLI, E., ARMENIO, V., & DE MARCHIS, M. 2008 The effect of the slope of irregularly distributed roughness elements on turbulent wall-bounded flows. *Journal of Fluid Mechanics* **613**, 385–394.
- NIKURADSE, J. 1933 Laws of flow in rough pipes. *Translation from German published 1950 as NACA Tech. Memo. 1292* .
- NUGROHO, B., BAIDYA, R., NURROHMAN, M. N., YUSIM, A. K., PRASETYO, F. A., YUSUF, M., SUASTIKA, I. K., UTAMA, I. K. A. P., MONTY, J. P., HUTCHINS, N., ET AL. 2017 In-situ turbulent boundary layer measurements over freshly cleaned ship-hull under steady cruising. In *Proceeding of International Conference on Ship and Offshore Technology (ICSOT), Royal Institution of Naval Architects (RINA) Conference*.
- OSEEN, C. W. 1910 Uber die stokes' sche formel und uber eine verwandte aufgabe in der hydrodynamik. *Arkiv Mat., Astron. och Fysik* **6**, 1.
- PLACIDI, M. & GANAPATHISUBRAMANI, B. 2018 Turbulent flow over large roughness elements: effect of frontal and plan solidity on turbulence statistics and structure. *Boundary-Layer Meteorology* **167** (1), 99–121.
- RAMANI, A., NUGROHO, B., BUSSE, A., MONTY, J. P., HUTCHINS, N., & JELLY, T. O. 2020 The effects of anisotropic surface roughness on turbulent boundary-layer flow. In *22nd Australasian Fluid Mechanics Conference, AFMC 2020*. The University of Queensland.
- SARAKINOS, S. & BUSSE, A. 2022 Investigation of rough-wall turbulence over barnacle roughness with increasing solidity using direct numerical simulations. *Physical Review Fluids* **7** (6), 064602.
- SCHLICHTING, H. 1937 *Experimental investigation of the problem of surface roughness*. National Advisory Committee for Aeronautics.
- SCHLICHTING, H. & KESTIN, J. 1961 *Boundary layer theory*, 9th edn. vol. 121, New York: McGraw-Hill.
- SCHULTZ, M. & FLACK, K. 2007 The rough-wall turbulent boundary layer from the hydraulically smooth to the fully rough regime. *Journal of Fluid Mechanics* **580**, 381–405.
- SCHULTZ, M. P. & FLACK, K. A. 2003 Turbulent boundary layers over surfaces smoothed by sanding. *Journal of Fluids Engineering* **125** (5), 863–870.
- SCHULTZ, M. P. & FLACK, K. A. 2009 Turbulent boundary layers on a systematically varied rough wall. *Physics of Fluids* **21**, 015104.
- SHOCKLING, M., ALLEN, J., & SMITS, A. 2006 Roughness effects in turbulent pipe flow. *Journal of Fluid Mechanics* **564**, 267–285.

- SIGAL, A. & DANBERG, J. E. 1990 New correlation of roughness density effect on the turbulent boundary layer. *AIAA Journal* **28** (3), 554–556.
- SIMPSON, R. L. 1973 A generalized correlation of roughness density effects on the turbulent boundary layer. *AIAA Journal* **11** (2), 242–244.
- SOLEIMANI, S. & ECKELS, S. 2021 A review of drag reduction and heat transfer enhancement by riblet surfaces in closed and open channel flow. *International Journal of Thermofluids* **9**, 100053.
- STIMPSON, C. K., SNYDER, J. C., THOLE, K. A., & MONGILLO, D. 2017 Scaling roughness effects on pressure loss and heat transfer of additively manufactured channels. *Journal of Turbomachinery* **139** (2).
- THAKKAR, M., BUSSE, A., & SANDHAM, N. 2017 Surface correlations of hydrodynamic drag for transitionally rough engineering surfaces. *Journal of Turbulence* **18** (2), 138–169.
- ÜNAL, U. O. 2015 Correlation of frictional drag and roughness length scale for transitionally and fully rough turbulent boundary layers. *Ocean Engineering* **107**, 283–298.
- UTAMA, I. K. A. P., NUGROHO, B., CHIN, C., HAKIM, M. L., PRASETYO, F. A., YUSUF, M., SUASTIKA, I. K., MONTY, J., HUTCHINS, N., & GANAPATHISUBRAMANI, B. 2017 A study of skin friction drag from realistic roughness of a freshly cleaned and painted ship hull. In *International Symposium on Marine Engineering (ISME)*.
- VAN RIJ, J. A., BELNAP, B., & LIGRANI, P. 2002 Analysis and experiments on three-dimensional, irregular surface roughness. *Journal of Fluids Engineering* **124** (3), 671–677.
- WAIGH, D. R. & KIND, R. J. 1998 Improved aerodynamic characterization of regular three-dimensional roughness. *AIAA Journal* **36** (6), 1117–1119.
- WOMACK, K. M., VOLINO, R. J., MENEVEAU, C., & SCHULTZ, M. P. 2022 Turbulent boundary layer flow over regularly and irregularly arranged truncated cone surfaces. *Journal of Fluid Mechanics* **933**, A38.
- YANG, J., STROH, A., CHUNG, D., & FOROOGHI, P. 2022 Direct numerical simulation-based characterization of pseudo-random roughness in minimal channels. *Journal of Fluid Mechanics* **941**, A47.
- YUAN, J. & PIOMELLI, U. 2014 Estimation and prediction of the roughness function on realistic surfaces. *Journal of Turbulence* **15** (6), 350–365.

Chapter 9

Conclusions

This thesis has provided valuable insights into the impact of various two-dimensional (2D) and three-dimensional (3D) roughness geometries on turbulence statistics and drag coefficients in a zero pressure gradient turbulent boundary layer (ZPG-TBL). The findings have important implications for enhancing energy efficiency and decreasing environmental impact across multiple industries. In particular, the research highlights the significance of understanding the influence of surface roughness on boundary layer flow in engineering applications, such as ships and aeroplanes. The existence of surface roughness significantly influences the boundary layer flow and affects the heat and momentum transfer. The increase in drag caused by roughness leads to greater fuel consumption and emissions in transportation.

The study focuses on the impact of three types of 2D roughness, including circular rods, 3D-printed triangular ribs, and CNC-machined sinewave surfaces, each with varying heights and streamwise spacings. Additionally, three types of 3D sinewave roughness are examined, including isotropic 3D sinewave surfaces with equal streamwise and spanwise wavelengths, anisotropic 3D sinewave surfaces with different streamwise and spanwise wavelengths, and isotropic 3D sinewave surfaces with varying roughness skewness values (positive, negative, and zero). The turbulence statistics and drag coefficient are analysed to determine the effects of these 2D and 3D roughness geometries in ZPG-TBL flows.

This study has contributed towards the ongoing efforts to determine the most significant surface roughness parameters in wall-bounded turbulence. The concept of equivalent sand-grain roughness k_s was introduced by [Schlichting \(1937\)](#) based on the data of [Nikuradse \(1933\)](#) to standardise different types of roughness and serve as an input parameter for predictions of the roughness function and drag coefficient. The chronological compilation of roughness correlations presented in this study provides details on the parameter ranges and types of roughness used during their development. These findings and TBL experiments performed in this thesis contribute to the development of a more accurate and reliable k_s correlation.

The results show that in the fully rough regime, the friction Reynolds number Re_τ no longer affects the drag coefficient C_f . Compared to smooth wall profiles, all types of roughness cause a downward shift in the wall-unit normalised streamwise mean velocity profile. When the roughness height and streamwise spacing are the same, 2D roughness has higher drag coefficients and roughness functions than 3D roughness. This is due to the larger blockage area imposed by 2D roughness, which forces the fluid to flow over the roughness elements. Conversely, the fluid can flow around and above the roughness elements of 3D roughness.

The robust agreement observed in the velocity defect profiles of the smooth and rough turbulent boundary layer flows, indicates the universality and similarity of velocity distributions.

This finding is supported by the remarkable level of similarity observed in the velocity profiles between the smooth and rough walls. The results suggest that Townsend's similarity hypothesis is applicable to mean velocity distributions, even for smaller values of $\delta/k > 20$ and $Re_\tau > 2000$, under different surface or flow conditions. The introduction of surface roughness results in the attenuation of the inner peak that is observable in the mean streamwise turbulence intensity profiles of smooth walls. As the value of k_s^+ increases in the transitionally rough regime, a progressive decrease in the inner peak is observed. In the fully rough regime, the mean streamwise turbulence intensity profiles exhibit only one outer peak, which occurs at approximately the same location, around $y/\delta = 0.06$. The graphs of $u'/(U\sqrt{H})$ versus U/U_∞ , which is a slightly modified diagnostic plot, demonstrate that all the rough wall profiles in the outer layer of the turbulent boundary layer collapse reasonably with the linear relationship introduced by Alfredsson *et al.* (2012).

The study also found that the streamwise spacing-to-height ratio s_x/k has a greater impact on the roughness function ΔU^+ and drag coefficient C_f than the spanwise spacing-to-height ratio s_y/k for 3D sinewave roughness. However, s_y/k substantially affects streamwise turbulence intensities in the logarithmic and outer layer. Surfaces with positive roughness skewness k_{sk} exhibit higher drag, resulting in a more significant downward shift compared with zero and negative roughness skewness. The friction coefficient decreases as the roughness skewness decreases. The increase in the percentage of C_f and ΔU^+ is significantly higher when moving from negative to zero roughness skewness than when moving from zero to positive roughness skewness. These findings provide important insights into the influence of surface roughness parameters on the drag coefficient and turbulence statistics.

Finally, the study identified the roughness skewness k_{sk} and streamwise effective slope ES_x as significant parameters that influence the drag coefficient for 2D roughness in the fully rough regime. These parameters have been incorporated into a new expression for k_s that is normalised with the maximum peak-to-valley roughness height k_t . Similarly, for 3D roughness in the fully rough regime, a correlation has been developed based on k_{sk} and ES_x to predict k_s normalised with the root mean square roughness height k_q . These correlations provide important tools for predicting the drag coefficient and improving the design of surfaces for engineering applications. For the 2D roughness correlation, the coefficient of determination ($R^2 = 0.93$, where R^2 is a statistical metric that quantifies the extent to which the variation in the dependent variable can be accounted for by the independent variable(s) in a regression model. For the 3D roughness correlation, the model demonstrated a very high level of accuracy in predicting k_s over 120 distinct rough 3d surfaces with $R^2 = 0.96$.

9.1 FUTURE WORK

Flow over rough surfaces is a complex phenomenon that has been studied extensively in the past. However, there are still many unresolved questions and areas of interest that could be explored in future research. Below are some potential directions for future work:

- Investigating the effect of pressure gradients on the boundary layer: Pressure gradients can significantly influence the behaviour of the fluid in the boundary layer over curved surfaces. Future work could focus on understanding how these pressure gradients affect the behaviour of the boundary layer, and how they influence the overall flow behaviour.
- Analysing the impact of boundary layer separation: Boundary layer separation can occur when the pressure gradients within the boundary layer become too large, resulting in a

significant reduction in lift and an increase in drag. Future work could investigate the conditions under which boundary layer separation occurs and study the effects of different surface geometries and flow conditions on the likelihood of separation.

- Exploring techniques for controlling the boundary layer over rough surfaces: There are various techniques that can be used to control the behaviour of the boundary layer, such as suction or blowing of the boundary layer, riblets on the surface, or vortex generators. Future work could explore these techniques and investigate their effectiveness in controlling the behaviour of the boundary layer over rough surfaces in different flow conditions.
- Investigating the flow over rough surfaces using advanced measuring techniques: Advanced measuring techniques such as particle image velocimetry (PIV) or direct numerical simulation (DNS) can provide a more complete understanding of the flow behaviour over rough surfaces than traditional measuring techniques. Future work could use these advanced techniques to gain a more detailed view of the flow behaviour over rough surfaces and investigate the interactions between the surface and the turbulent flow.
- Investigating the flow over randomly rough surfaces using controlled roughness: Real-world surfaces are often irregular and random, which can complicate the understanding of the flow behaviour over rough surfaces. Future work could use controlled roughness to investigate the flow behaviour over randomly rough surfaces and identify the key mechanisms that govern the flow response. By investigating the flow over randomly rough surfaces using controlled roughness, researchers can gain a more realistic understanding of the flow behaviour in practical applications and can develop design guidelines for surfaces that are optimised for specific performance metrics such as drag reduction or heat transfer enhancement.
- In addition, the findings of this study suggest that further research is needed to refine and develop more accurate and reliable correlations for the equivalent sand-grain roughness parameter k_s , particularly in the fully rough regime. This could involve exploring the impact of additional surface roughness parameters or incorporating machine learning techniques to improve predictions.

In summary, these different directions of future work could deepen our understanding of the flow behaviour over rough surfaces and help to optimise the design of surfaces for a range of practical applications.

Bibliography

- ALFREDSSON, P. H., ÖRLÜ, R., & SEGALINI, A. 2012 A new formulation for the stream-wise turbulence intensity distribution in wall-bounded turbulent flows. *European Journal of Mechanics-B/Fluids* **36**, 167–175.
- NIKURADSE, J. 1933 Laws of flow in rough pipes. *Translation from German published 1950 as NACA Tech. Memo. 1292* .
- SCHLICHTING, H. 1937 *Experimental investigation of the problem of surface roughness*. National Advisory Committee for Aeronautics.